UNIVERSIDADE DE SANTIAGO DE COMPOSTELA

Departamento de Física de Partículas

An approach to new physics at LHCb:
study of penguin pollution to $\phi_s(B_s^0 \to J/\psi\phi)$ using $B_s^0 \to J/\psi\overline{K}^{*0}$ decays, and search for a light A_1^0 Higgs boson in the NMSSM

Carlos Vázquez Sierra

Tese de Doutoramento

Programa de Doutoramento
en Física Nuclear e de Partículas

Máximo Pló Casasús, Catedrático de Universidade do Departamento de Física de Partículas da Universidade de Santiago de Compostela,

Juan José Saborido Silva, Profesor Titular de Universidade do Departamento de Física de Partículas da Universidade de Santiago de Compostela,

Diego Martínez Santos, Investigador Asociado do Departamento de Física de Partículas da Universidade de Santiago de Compostela,

INFORMAN:

Que o presente traballo, titulado **"An approach to new physics at LHCb: study of penguin pollution to $\phi_s(B_s^0 \to J/\psi\phi)$ using $B_s^0 \to J/\psi\overline{K}^{*0}$ decays, and search for a light A_1^0 Higgs boson in the NMSSM"**, foi realizado por

Carlos Vázquez Sierra

baixo a súa dirección no Departamento de Física de Partículas da Universidade de Santiago de Compostela e no experimento LHCb do CERN. Así mesmo, **expresan a súa conformidade co mesmo** e **autorizan a súa presentación** diante da Comisión Examinadora do Programa de Doutoramento en Física Nuclear e de Partículas, constituíndo así a **Tese de Doutoramento** do seu autor para optar ó **Grao de Doutor en Física**.

E para que así conste, asinan en Santiago de Compostela, a 2 de setembro de 2016,

Máximo Pló Casasús

Juan José Saborido Silva

Diego Martínez Santos

Carlos Vázquez Sierra

Author: Carlos Vázquez Sierra

Supervisor: Máximo Pló Casasús
Supervisor: Juan José Saborido Silva
Supervisor: Diego Martínez Santos

Inform for European Mention: Paula Álvarez Cartelle
Inform for European Mention: Greig Cowan

Defense date: December 14, 2016
Jury: Vincenzo Vagnoni, Olivier Leroy, Martino Borsato

Printed on October, 2016. Last modification on April, 2017.

Acknowledgements

First of all, I would like to thank my supervisors for their dedication, time, and patience. Without Diego, Juan and Máximo, this work would not be possible. I'm sincerely grateful.

I would like to express my gratitude to my colleagues of the LHCb Collaboration, especially the VELO Upgrade group (the first people whom I worked with when I arrived at CERN for the first time as a summer student), the B decays to charmonia (B2CC) working group (where I spent most of my time as a PhD student), and the stripping group where I belonged to for a two-years period as the *stripping liaison* of the B2CC working group. Most of the knowledge I acquired during the last four years was obtained from fruitful discussions with their integrants. I also want to thank two of my Spanish LHCb colleagues, Pablo and Vicente. One can meet not only fellow scientists but also friends when working at such a big collaboration as LHCb.

Special thanks to Vincenzo, Olivier, Yasmine, Cibrán, Martino and Veronika, for kindly accepting being members of my thesis jury, and to Paula and Greig, for accepting the hard task of reading this work as referees for the European Mention.

Of course I want to thank my colleagues here at Santiago, as part of the Grupo de Física de Altas Enerxías (GAES). An special word for Xabi and his invaluable help during the analysis of $A_1^0 \to \mu^+\mu^-$ decays, and for my fellow PhD and postdoc students: Álvaro, Brais, María, Julián, Toño, Miguel, Miriam, Martino, Jessica and Veronika.

I thank the financial support provided by the Ministerio de Economía y Competitividad (MINECO) and by the European Research Council (ERC).

Agradecimientos

No podía faltar el más sincero agradecimiento a mi padre Carlos, a mi madre María Isabel y a mi tía Ángeles, por su apoyo, sus consejos y un cariño que no se puede describir con palabras. Gracias por haberme ayudado a llegar a ser lo que soy hoy en día.

También quiero agradecer a aquellos que son prácticamente parte de mi familia, Fran, Camilo y Xabier, a los que conozco ya hace más de una década y con los que he compartido buenos y malos momentos, aunque siempre con un denominador común y es el de haber sido memorables. Dentro de este grupo podría incluír también a aquellos que conocí cuando comencé la Licenciatura, y que aún conservo ya no sólo como compañeros de biblioteca sino como buenos amigos: Aarón, Alexis, Manoel y Yago. Agradezco también la amistad y apoyo de aquellos que no conocí al comienzo pero sí durante mis primeros años en la Universidad, y que aún conservo: Álvaro, Vila, Arribi, Alex, Tato, Yasser, Aida, Santiago, Adrián...

Por último, sería hipócrita por mi parte no dar las gracias a los que también son mis amigos, y que, tanto por su apoyo como por las noches de rock & roll que hemos vivido juntos, han ayudado de una forma u otra a conservar mi salud mental y han contribuido al éxito de mi período como estudiante de doctorado: Brais, Gonzalo, Hugo, Colinas, Hermida, Xosé... Y por supuesto, una especial nota de cariño y agradecimiento a mis tres grandes templos nocturnos de preferencia, Currúncho, Maycar y Ulises.

Espero no olvidarme de nadie, y de hacerlo, mis más sinceras disculpas: la memoria es, a veces, muy cruel de no tener en consideración a aquellos que de verdad se lo merecen.

Elementary particles are terribly boring, which is one reason why we are so interested in them.
Steven Weinberg

The imagination of nature is far, far greater than the imagination of man.
Richard Feynman

Homines, dum docent discunt.
Lucius Annaeus Seneca

Abstract

This thesis presents the analysis of $B_s^0 \to J/\psi \overline{K}^{*0}$ decays, using 3 fb^{-1} of data collected by the LHCb experiment during 2011 and 2012, from LHC pp collisions at centre-of-mass energies of 7 TeV and 8 TeV, respectively. The purpose of this analysis is to estimate the second order (penguin) contributions, which may be confused as possible new physics, to the CP-violating phase ϕ_s measured in $B_s^0 \to J/\psi\phi$ decays. First steps of the analysis of the $A_1^0 \to \mu^+\mu^-$ decay mode, using 2.97 fb^{-1} of Run I LHCb pp data, are also reported, along with the characterisation of silicon pixel detectors using SPS test beams consisting of charged hadrons with a momentum of 180 GeV/c, in the context of the upgraded LHCb VELO R&D programme. The excellent performance of the LHCb detector during 2011 and 2012, especially the muon and trigger systems, crucial for the reconstruction of muon tracks, has been also reported. Some details about the on-going upgrade of LHCb subsystems have been reviewed as well.

Limiar

Esta tese está adicada á analise dos decaementos $B_s^0 \to J/\psi \overline{K}^{*0}$, mediante o emprego de 3 fb^{-1} de datos tomados polo experimento LHCb durante 2011 e 2012, a partires de colisións pp no LHC a enerxías de centro de masas de 7 TeV e 8 TeV, respectivamente. O obxectivo desta análise é a estimación de contribucións de segunda orde (contaminación por pingüíns), as cales poden ser confundidas con posíbel nova física, á fase ϕ_s de violación CP medida na canle $B_s^0 \to J/\psi\phi$. Nesta tese recóllense tamén os primeiros pasos da análise do modo de decaimento $A_1^0 \to \mu^+\mu^-$, empregando 2.97 fb^{-1} de datos pp tomados durante o Run I de LHCb, así como a caracterización de detectores de píxeles de silicio empregando feixes de proba do SPS, compostos de hadróns cargados cun momento de 180 GeV/c, no contexto do programa de investigación e desenvolvemento da mellora do VELO de LHCb. Os excelentes resultados obtidos polo detector LHCb durante 2011 e 2012, especialmente polo sistema de muóns e o sistema de *trigger*, cruciais para a reconstrucción das trazas de muóns, móstranse neste traballo, xunto a algúns detalles sobre a mellora dos subsistemas de LHCb que se está a levar a cabo neste período.

Contents

Chapter 1

Introduction

The Standard Model (SM) of Particle Physics, based on strong, weak and electromagnetic (electroweak) interactions, is a very powerful and self-consistent model which has led to many successes in providing accurate descriptions of experimental measurements. As of today this theory is considered the benchmark model to classify subatomic particles and explain their interactions, except gravitation, which is not incorporated in the SM. However, as the scientific community knows very well, being successful is still far from being perfect: some tensions between results from several experiments and SM predictions have arisen in the previous years, such as the inability to find a proper SM candidate for dark matter in the Universe, the existence of neutrino masses, or the necessary imbalance between matter and antimatter in the Universe, among others. The SM is not able to explain these phenomena, which are intensively investigated in several High Energy Physics (HEP) experiments. Searching for both direct or indirect evidence of possible New Physics (NP), which may lead to the establishment of a new benchmark model able to explain all these tensions, can be considered as the *avant-garde* of HEP. A more detailed theory overview is given in Chapter 2.

Regarding indirect searches of possible NP, the violation of a certain discrete symmetry, the CP violation, is one of the ingredients necessary to explain the imbalance between matter and antimatter in the Universe, also known as the problem of the baryogenesis. However, experimental results have shown that the amount of CP violation predicted by the SM is not enough to satisfy the conditions needed to solve that baryogenesis puzzle: a search for new NP sources of CP violation is mandatory. The study of CP violation in the neutral B_s^0 meson system offers an excellent opportunity to detect possible deviations from SM predictions. A study of second order (penguin) contributions to the mixing-induced CP-violating phase ϕ_s in $b \to c\bar{c}s$ processes, which may be confused as a signal of NP, is presented in Chapter 4, while the results are discussed in Chapter 5. My contribution to this analysis is focused in the construction of the data samples, the event selection, the treatment of peaking backgrounds and the measurement of branching fractions.

As for direct searches of possible NP, one way to complement the SM are its supersymmetric extensions. Direct searches of possible new particles predicted by those extensions, such as in the Next-to-Minimal-Supersymmetric-SM (NMSSM), constitute a direct way

to test the robustness of the SM, where the observation of possible NP particles predicted by alternative candidate models, might be achieved. A search of the $A_1^0 \to \mu^+\mu^-$ decay mode, where A_1^0 is the light CP-odd Higgs boson in the NMSSM, is presented in Chapter 6, where the construction of the data samples, event selection and multivariate studies are my main contribution to this analysis.

The work of this thesis has been done using data recorded by the LHCb experiment, dedicated to Heavy Flavor (HF) physics at the Large Hadron Collider (LHC), which is located at CERN and is the most powerful hadron accelerator and collider ever built by humankind. The primary goal of the experiment is to look for indirect evidence of NP in CP violation and rare decays of beauty and charm hadrons. As of June 2016, the LHCb experiment is driven by a collaboration of 1199 members, from 69 institutes in 16 countries around the world. A 2% of the collaboration are part of the University of Santiago de Compostela, while 1.45% is the average contribution per institute. Data used for the studies described in this thesis were taken during 2011 and 2012, as part of the first LHC run period, named Run I. At the present moment, the LHCb experiment is taking data as well, as part of the second LHC run period, named Run II, which started at 2015 and will last until 2018. A more detailed description of the LHC and the LHCb experiment can be found in Chapter 3. However, the LHCb experiment is now going through an upgrade of its subdetectors and online infrastructure, the LHCb Upgrade, which will end after the second LHC long technical stop, the Long Shutdown 2 (LS2), with the start of Run III planned for 2021. Characterisation studies for a certain type of silicon pixel sensors, based on Medipix3 technology, in the context of the upgrade of the LHCb Vertex Locator are presented at the end of Chapter 3.3. My contribution to these studies is focused in the measurements performed with irradiated assemblies.

Apart from the contributions described in the previous paragraphs, during my PhD period at LHCb, I also worked as a piquet of the Silicon Tracker subdetector (see Chapter 3.2.1.2), and with the LHCb stripping team as the stripping *liaison* of the B meson to charmonia working group. Details about what the "stripping" is are given in Chapter 3.2.6.

In summary: after this brief introduction, a theory overview is presented in Chapter 2, a detailed description of the LHC machine and the LHCb experiment is given in Chapter 3, Chapter 4 contains the analysis of $B_s^0 \to J/\psi \overline{K}^{*0}$ decays while the results are discussed in Chapter 5, in Chapter 6 the study of the $A_1^0 \to \mu^+\mu^-$ decay mode is presented, and finally, Chapter 7 gives the conclusions and Chapter 8 (Chapter 9) contains a summary of this thesis in English (Galician).

Chapter 2

Theory overview

The Standard Model is a Quantum Field Theory (QFT) based on strong and ElectroWeak (EW) interactions [1–4]. It is characterised by a huge predictive power, leading to continued successes in providing accurate descriptions of experimental measurements. Due to this fact and to the theoretical self-consistency of the model itself, as of today this theory is considered the benchmark model to classify subatomic particles and explain their interactions, except gravitation, which is not incorporated in the SM. However, some phenomena are not incorporated in the SM, such as the possible presence of Dark Matter (DM) in the Universe, or the non-zero masses of the neutrinos [4].

The CP transformation combines charge conjugation C, which means that this operation changes one particle into its anti-particle, with parity P. If CP were an exact symmetry, the laws of Nature would be the same for matter and for antimatter [5]. It is observed that most phenomena are indeed CP-symmetric. In particular, this symmetry is respected by electromagnetic and strong interactions. The weak interactions, on the other hand, violate C, P [6, 7], and also CP [8]. This phenomenon of CP violation, discovered more than 50 years ago, is one of the three essential ingredients to explain the imbalance between matter and anti-matter in the Universe [9]. The existence of CP violation, along with the existence of B (baryonic number) violation and with the existence of interactions out of thermal equilibrium, are known as the "Sakharov conditions" (named after the Russian nuclear physicist and Nobel Peace Prize Andrei D. Sakharov) for the baryon asymmetry in the baryogenesis [10]. In the SM, CP violation arises in the Yukawa-sector via quark mixing and it is described by a complex parameter in the Cabibbo-Kobayashi-Maskawa (CKM) matrix [11, 12]. Current results in CP violation from various experiments do not contradict the unitarity of the CKM matrix [13], resulting in the statement that this single complex phase of the CKM is currently sufficient to describe the multitude of CP-violating phenomena observed by experiments [14]. However, CP violation in the Yukawa-sector is not sufficient to cope with the previously stated problem of the baryogenesis in the Universe [15]. This demands the existence of additional sources of CP violation Beyond the SM (BSM): finding such a source may not only fulfill one of the "Sakharov conditions", but also result in the detection of New Physics itself.

The study of CP violation in the B_s^0 system offers an excellent opportunity to detect

possible deviations from SM predictions. The current SM estimation for CP violation effects due to the intereference between mixing and decay in $b \to c\bar{c}s$ processes, taking only into account tree-level topologies, is [16]

$$-2\beta_s = -0.0376^{+0.0008}_{-0.0007} \text{ rad}, \tag{2.1}$$

where β_s is defined in terms of the Wolfenstein parametrisation of the CKM matrix (see Chapter 2.2). However, due to the outstanding precision of this estimation, contributions due to second-order topologies have to be taken into account to avoid confusing any possible significative deviation as an unambiguous signal of NP. These contributions, so-called "penguin pollution", are studied in Chapter 4 as a central part of this work. The latest experimental world average for the CP-violating phase ϕ_s (see Chapter 2.2 and Chapter 2.3), taking into account the results from several experiments, is [13]

$$\phi_s = -0.033 \pm 0.033 \text{ rad}. \tag{2.2}$$

As stated in Chapter 3, search for indirect evidence of NP in CP violation and rare decays of beauty and charm hadrons is the main objective of the LHCb experiment, which is an ideal laboratory for these kind of studies.

In Chapter 2.1, a phenomenological introduction to CP violation in the B_s^0 system is presented. In Chapter 2.2, the introduction in previous chapter is particularised to the measurement of CP violation due to the interference between mixing and decay for the $B_s^0 \to J/\psi\phi$ channel. Phenomenological characterisation of penguin pollution to previous case is explained in Chapter 2.3. Finally, a brief discussion about potential sources and searches of NP in these measuremrents is presented in Chapter 2.4.

2.1 CP violation in the B_s^0 system

In the system of neutral B_s^0 mesons, the quantum mechanical time evolution of a decaying B_s^0 meson, with mass and lifetime $\mathrm{m}_{B_s^0}$ and $\tau_{B_s^0} = 1/\Gamma_{B_s^0}$, respectively, is given by

$$|B_s^0(t)\rangle = e^{-i\left(2\mathrm{m}_{B_s^0} - i\Gamma_{B_s^0}\right)\frac{t}{2}}|B_s^0(0)\rangle, \tag{2.3}$$

where $\Gamma_{B_s^0}$ denotes the total decay rate of the B_s^0 meson. The time evolution of these states is governed by the Schrödinger equation

$$i\frac{d}{dt}\begin{pmatrix}|B_s^0(t)\rangle \\ |\overline{B}_s^0(t)\rangle\end{pmatrix} = \left(\boldsymbol{M} - i\frac{\boldsymbol{\Gamma}}{2}\right)\begin{pmatrix}|B_s^0(t)\rangle \\ |\overline{B}_s^0(t)\rangle\end{pmatrix}, \tag{2.4}$$

where $\mathbf{M}$ and $\mathbf{\Gamma}$ are 2×2 hermitian matrices. In the SM, $B_s^0 - \overline{B}_s^0$ oscillations are induced due to the flavour changing weak interaction described by the so-called "box diagrams" (see Figure 2.1). An initially produced B_s^0 or $\overline{B}_s^0$ meson evolves in time into a superposition of both states, causing off-diagonal elements of $\mathbf{M}$ and $\mathbf{\Gamma}$ matrices to be non-zero. Due

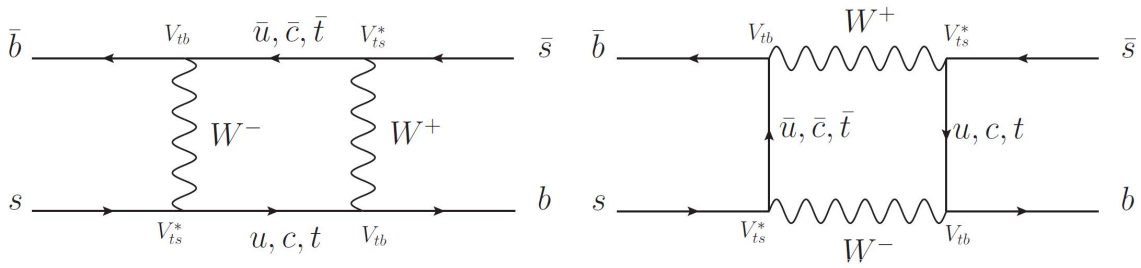

Figure 2.1: "box diagrams" related to $B_s^0 - \overline{B}_s^0$ mixing.

to the CPT theorem, their diagonal elements are equal, representing the mass $M_{B_s^0}$ and the decay rate $\Gamma_{B_s^0}$, respectively, of B_s^0 and $\overline{B}_s^0$ mesons. These mass eigenstates are

$$\begin{aligned} |B_L\rangle &= p|B_s^0\rangle + q|\overline{B}_s^0\rangle, \\ |B_H\rangle &= p|B_s^0\rangle - q|\overline{B}_s^0\rangle, \end{aligned} \tag{2.5}$$

with $|p|^2 + |q|^2 = 1$. Once the mass eigenstates $|B_L\rangle$ (light) and $|B_H\rangle$ (heavy) are defined, the mass difference $\Delta \mathrm{M}_{B_s^0}$ and the decay rate difference $\Delta\Gamma_{B_s^0}$ can be written as

$$\Delta \mathrm{M}_{B_s^0} = M_H - M_L, \qquad \Delta\Gamma_{B_s^0} = \Gamma_L - \Gamma_H, \tag{2.6}$$

followed by the time evolution of the flavour eigenstates as

$$\begin{aligned} |B_s^0(t)\rangle &= g_+(t)|B_s^0\rangle + \frac{q}{p} g_-(t)|\overline{B}_s^0\rangle, \\ |\overline{B}_s^0(t)\rangle &= \frac{p}{q} g_-(t)|B_s^0\rangle + g_+(t)|\overline{B}_s^0\rangle, \end{aligned} \tag{2.7}$$

with the coefficients

$$g_\pm(t) = \frac{1}{2}\left(e^{-iM_L t} e^{-\frac{1}{2}\Gamma_L t} \pm e^{-iM_H t} e^{-\frac{1}{2}\Gamma_H t}\right). \tag{2.8}$$

The decay amplitude describing the transition of the flavour eigenstate B_s^0 into the final state f (being $\bar{f}$ its CP-conjugated state) is denoted by A_f ($A_{\bar{f}}$); for the decay of a $\overline{B}_s^0$ state into f ($\bar{f}$) the notation $\bar{A}_f$ ($\bar{A}_{\bar{f}}$) is used,

$$\begin{aligned} A_f &= \langle f|\mathcal{H}|B\rangle, & A_{\bar{f}} &= \langle \bar{f}|\mathcal{H}|B\rangle, \\ \bar{A}_f &= \langle f|\mathcal{H}|\overline{B}\rangle, & \bar{A}_{\bar{f}} &= \langle \bar{f}|\mathcal{H}|\overline{B}\rangle, \end{aligned} \tag{2.9}$$

being the flavour changing weak transitions described by an effective Hamiltonian

$$\mathcal{H} = \boldsymbol{M} - i\frac{\boldsymbol{\Gamma}}{2}. \tag{2.10}$$

The amplitudes A_f and $\bar{A}_f$ are typically affected by hadronic effects and very difficult to be calculated reliably in theory. However, CP-symmetries are governed by a single complex quantity, λ_f, given by

$$\lambda_f = \frac{q}{p}\frac{\bar{A}_f}{A_f}, \tag{2.11}$$

whose argument is usually written as

$$\phi_s = -\arg(\lambda_f). \tag{2.12}$$

Defining the following abbreviations for direct, mixing-induced and $\Delta\Gamma$-correction-induced CP asymmetries, respectively,

$$\mathcal{A}_{CP}^{\text{dir}} = \frac{1-|\lambda_f|^2}{1+|\lambda_f|^2}, \qquad \mathcal{A}_{CP}^{\text{mix}} = \frac{2\Im(\lambda_f)}{1+|\lambda_f|^2}, \qquad \mathcal{A}_{\Delta\Gamma} = \frac{2\Re(\lambda_f)}{1+|\lambda_f|^2}, \tag{2.13}$$

which satisfy the closing relation

$$(\mathcal{A}_{CP}^{\text{dir}})^2 + (\mathcal{A}_{CP}^{\text{mix}})^2 + (\mathcal{A}_{\Delta\Gamma})^2 = 1, \tag{2.14}$$

the time dependent asymmetry due to the interference of both decay rates $\Gamma[B_s^0 \to \text{f}]$ and $\Gamma[\overline{B}_s^0 \to \text{f}]$ can be written as

$$\mathcal{A}_{CP,f(t)} = \frac{\Gamma[\overline{B}_s^0 \to \text{f}] - \Gamma[B_s^0 \to \text{f}]}{\Gamma[\overline{B}_s^0 \to \text{f}] + \Gamma[B_s^0 \to \text{f}]} = \frac{\mathcal{A}_{CP}^{\text{dir}}\cos(\Delta M_{B_s^0} t) + \mathcal{A}_{CP}^{\text{mix}}\sin(\Delta M_{B_s^0} t)}{\cosh\left(\Delta\Gamma_{B_s^0} t/2\right) - \mathcal{A}_{\Delta\Gamma}\sinh\left(\Delta\Gamma_{B_s^0} t/2\right)}. \tag{2.15}$$

From these considerations, three main cases can be studied: CP violation appearing in the mixing ($|q/p| \neq 1$), in the decay ($|\bar{A}_{\bar{f}}/A_f| \neq 1$), and induced due to the interference between the mixing and the decay. The latter case, which is the only relevant for the purpose of this work, is explained in detail in Chapter 2.2. A more detailed discussion about CP violation in the B_s^0 system can be found in [14], from where most of the details described here were extracted.

2.2 The ϕ_s phase in the $B_s^0 \to J/\psi\phi$ mode

As previously stated at the beginning of Chapter 2, CP violation due to the interference between mixing and decay in $b \to c\bar{c}s$ processes can be computed in the SM with high precision, constituting an excellent probe for the search of sources of possible NP. The golden mode for the measurement of this CP-violating phase $-2\beta_s$ is the $B_s^0 \to J/\psi\phi$ channel, which is mediated by a $b \to c\bar{c}s$ process. In this section, the formalism described in Chapter 2.1 will be particularised for this case. For this purpose, the following considerations should be made:

1. The final state f is a CP eigenstate: since in $B_s^0 \to J/\psi\phi$ decays, the final state $f = J/\psi\phi$ is a CP eigenstate, the relation

$$f \equiv f_{CP} = \eta_{CP}\bar{f}_{CP} \tag{2.16}$$

is satisfied. Consequently, to a good approximation, hadronic uncertainties cancel out in the ratio of decay amplitudes, only remaining a pure weak CKM phase ϕ_j^{CKM}, and being the ratio given by

$$\frac{\bar{A}_f}{A_f} = -\eta_{CP} e^{-2i\phi_j^{\mathrm{CKM}}}, \tag{2.17}$$

thus the parameter λ_f, given by (2.11), is now written as

$$\lambda_f = \frac{q}{p}\frac{\bar{A}_f}{A_f} = \left(-\frac{V_{ts}V_{tb}^*}{V_{ts}^*V_{tb}}\right)\left(-\eta_{CP} e^{-2i\phi_j^{\mathrm{CKM}}}\right) = \eta_{CP}\frac{V_{ts}V_{tb}^*}{V_{ts}^*V_{tb}} e^{-2i\phi_j^{\mathrm{CKM}}}, \tag{2.18}$$

where the CKM elements responsible for the mixing are explicitly shown.

2. Only one type of weak process contributes to the decay amplitude: the decay mode $B_s^0 \to J/\psi\phi$ is governed on quark-level by a $b \to c\bar{c}s$ transition, with a large tree-level contribution and a suppressed penguin contribution. Hence, it can be considered that $|\lambda_f| = 1$, and consequently, $\mathcal{A}_{CP}^{\mathrm{dir}} = 0$, $\mathcal{A}_{CP}^{\mathrm{mix}} = \sin\phi_s$ and $\mathcal{A}_{\Delta\Gamma} = -\cos\phi_s$. Then, the general expression of the time dependent asymmetry as given in (2.15), can be written as

$$\mathcal{A}_{CP,f(t)} \approx \frac{\sin(\phi_s)\cos(\Delta \mathrm{M}_{B_s^0} t)}{\cos(\phi_s)\sinh\left(\Delta\Gamma_{B_s^0} t/2\right) - \cosh\left(\Delta\Gamma_{B_s^0} t/2\right)}. \tag{2.19}$$

Since only one CKM process $b \to c\bar{c}s$ is contributing, the parameter $|\lambda_f|$ can be completely written in terms of elements of the CKM matrix and the corresponding CP eigenvalue. Hence, its argument ϕ_s previously written in (2.12) is, in the SM and considering only tree-level topologies, given by

$$\phi_s^{\mathrm{SM}} = -\arg\left(\eta_{CP}\frac{V_{ts}V_{tb}^*}{V_{ts}^*V_{tb}}\frac{V_{cb}V_{cs}^*}{V_{cb}^*V_{cs}}\right). \tag{2.20}$$

Following previous considerations, and using a convention which leads to a positive value of β_s, a positive CP eigenvalue $\eta_{CP} = +1$ is adopted. Therefore, the phase given by (2.20) can be finally re-written as

$$\phi_s^{\mathrm{SM}} = 2\arg\left(-\frac{V_{ts}V_{tb}^*}{V_{cb}V_{cs}^*}\right) = -2\beta_s, \tag{2.21}$$

where β_s is defined, using the Wolfenstein parametrisation of the CKM matrix, as $\beta_s = \eta\lambda^2 + \mathcal{O}(\lambda^4)$ [16–18]. Hereafter, the CP-violating phase ϕ_s in this particular case where $\phi_s^{\mathrm{SM}} = -2\beta_s$, will be simply referred to as ϕ_s.

The final state of the $B_s^0 \to J/\psi\phi$ decay mode is an admixture of CP eigenstates because of the relative angular momentum between J/ψ and ϕ mesons. Since both particles are spin-1 vector mesons, the angular momentum eigenvalue can run over three possible values, 0, 1 or 2. In other words, there are three possible linear polarisation states:

longitudinal (0), parallel ($1, \|$) and perpendicular ($2, \perp$). Of course, each one of these polarisation states corresponds to a *CP* eigenstate with an associated *CP* eigenvalue. Hence, it is neccesary to disentangle this admixture in order to distinguish among eigenstates, where parallel and longitudinal states are *CP*-even, and perpendicular state is *CP*-odd. *CP*-violating effects in the time-dependent angular distribution of the $B_s^0 \to J/\psi\phi$ decay products play a key role for the search of NP. Within the SM, these effects are expected to be small: a hypothetical discovery of *CP*-violating effects significantly larger than zero could lead to clear evidences of NP. But penguin topologies in the $B_s^0 \to J/\psi\phi$ channel (see Figure 2.2), which are doubly Cabibbo-suppressed and hence assumed to be negligible [19–22], cannot be calculated reliably from QCD [23] and could mimic *CP*-violating effects which might be misinterpreted as signals of NP in $B_s^0 - \overline{B}_s^0$ mixing with a small but sizeable *CP*-violating NP phase. This limits the theoretical accuracy of the benchmark for the search of NP and pollutes the efforts, probably leading to false evidences of NP.

Latest LHCb results from time-dependent tagged analysis of $B_s^0 \to J/\psi K^+K^-$ decays [24] show the following measurement for the *CP*-violating phase ϕ_s in this mode,

$$\phi_s(B_s^0 \to J/\psi K^+K^-) = -0.058 \pm 0.049 \text{ (stat)} \pm 0.006 \text{ (syst)}, \tag{2.22}$$

where the first uncertainty is statistical and the second is systematic. This value is in good agreement with the SM tree-level predicted value in (2.1). But this result could be affected by penguin pollution, leading to an avoidable imprecision in the systematic uncertainties. In consequence, it is strongly recommended to estimate this pollution in order to disentangle SM effects from possible NP and to obtain more precise values by decreasing statistical errors.

Theoretically, penguin effects are expected to interfere constructively with mixing-induced *CP* violation, leading to *CP* asymmetries significantly large. These effects can be controlled by means of an analysis of the angular distribution of the $B_s^0 \to J/\psi\overline{K}^{*0}$ channel (see Figure 2.3) and its *CP*-conjugate: applying $SU(3)$ flavour-symmetry arguments and neglecting penguin annihilation and exchange topologies (probed through $B^0 \to J/\psi\phi$ decays), the relevant hadronic parameters entering the $B_s^0 \to J/\psi\phi$ observables can be determined and taken into account in the extraction of ϕ_s. Using the $B_s^0 \to J/\psi\overline{K}^{*0}$ channel as a control channel for this purpose is possible because relevant hadronic parameters which can be used to estimate the penguin pollution in the extraction of ϕ_s from the $B_s^0 \to J/\psi\phi$ channel are not suppressed. A direct measurement of these hadronic parameters in the same $B_s^0 \to J/\psi\phi$ channel is almost impossible because they are strongly suppressed, around a 95% [19–22]. The formalism used in this work for the estimation of this penguin pollution is described in Chapter 2.3.

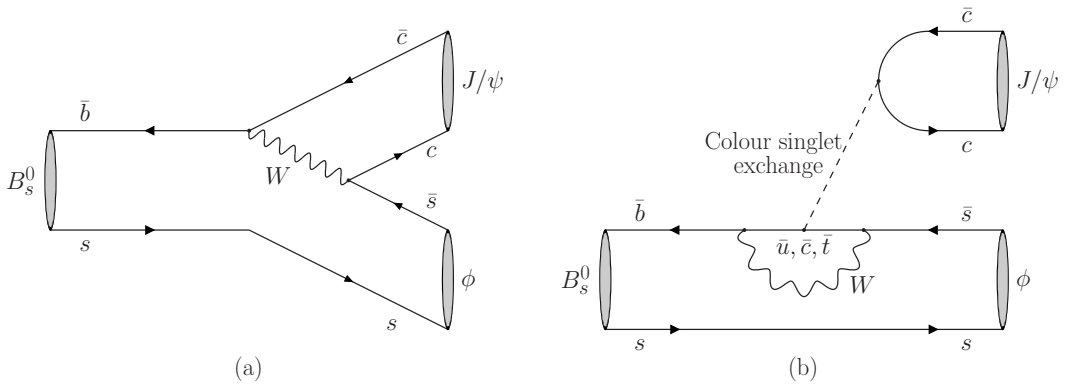

Figure 2.2: Tree-level (a) and penguin (b) diagrams (SM) contributing to $B_s^0 \to J/\psi\phi$.

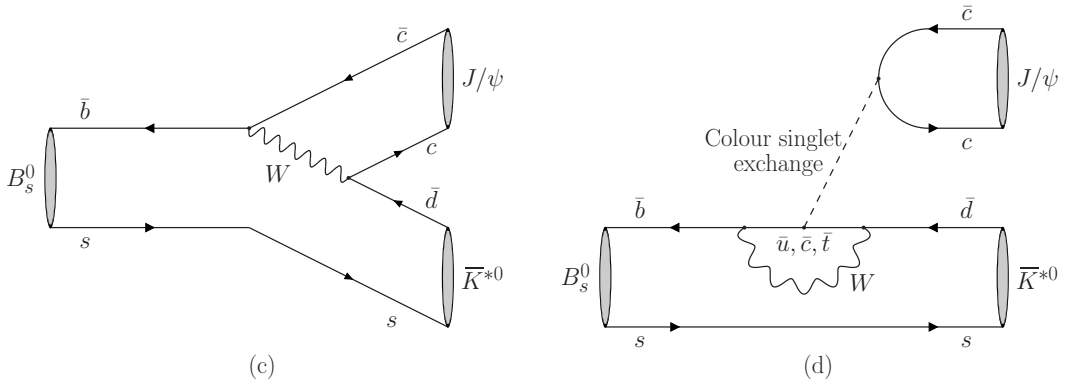

Figure 2.3: Tree-level (c) and penguin (d) diagrams (SM) contributing to $B_s^0 \to J/\psi\overline{K}^{*0}$.

2.3 Contribution to ϕ_s due to penguin diagrams

For neutral B_s^0 meson decays, the transition amplitudes A_f and $\bar{A}_f$ defined in Chapter 2.1, can be written in the following form [20, 21],

$$A_f = \mathcal{N}_f[1 - b_f e^{\rho_f} e^{+i\gamma}], \tag{2.23}$$
$$\bar{A}_f = \eta_f \mathcal{N}_f[1 - b_f e^{\rho_f} e^{-i\gamma}], \tag{2.24}$$

where η_f is the CP eigenvalue of the final state f, $\mathcal{N}_f$ is a CP-conserving normalisation factor representing the dominant tree-level topology, b_f parametrises the relative contribution from the penguin topologies, ρ_f is the CP-conserving phase difference between the tree and penguin contributions, whereas their relative weak phase is given by the Unitary Triangle (UT) angle γ.[1] The parameters $\mathcal{N}_f$ and b_f depend both on CKM factors and on

[1] Defined as $\gamma = \arg\left(-\frac{V_{ud}V_{ub}^*}{V_{cd}V_{cb}^*}\right)$ [25].

hadronic matrix elements of four-quark operators entering the corresponding low-energy effective Hamiltonian [19]. In the particular case of $B_s^0 \to J/\psi\phi$ decays, $\mathcal{N}_f = (1-\lambda^2/2)\mathcal{A}'_f$ and $b_f e^{\rho_f} = -\epsilon a'_f e^{i\theta'_f}$,[2] leading to [20]

$$A_f = (1-\lambda^2/2)\mathcal{A}'_f[1+\epsilon a'_f e^{i\theta'_f} e^{i\gamma}], \tag{2.25}$$

$$\bar{A}_f = \eta_f(1-\lambda^2/2)\mathcal{A}'_f[1+\epsilon a'_f e^{i\theta'_f} e^{-i\gamma}]. \tag{2.26}$$

where f can be any of the three final polarisation states of the $B_s^0 \to J/\psi\phi$ mode, which, as stated in Chapter 2.2, are pure CP eigenstates. Because of this and to avoid possible confussion, henceforth f will be replaced with the index i. Thus, CP asymmetries as given by (2.15) can be re-written, for each final polarisation state as

$$\mathcal{A}^{\rm dir}_{CP,i} = -2\epsilon a'_i \sin\theta'_i \sin\gamma/N_i, \tag{2.27}$$

$$\mathcal{A}^{\rm mix}_{CP,i} = +\eta_i[\sin\phi_s + 2\epsilon a'_i \cos\theta'_i \sin(\phi_s+\gamma) + \epsilon^2 a_i'^2 \sin(\phi_s+2\gamma)]/N_i, \tag{2.28}$$

$$\mathcal{A}_{\Delta\Gamma,i} = -\eta_i[\cos\phi_s + 2\epsilon a'_i \cos\theta'_i \cos(\phi_s+\gamma) + \epsilon^2 a_i'^2 \cos(\phi_s+2\gamma)]/N_i, \tag{2.29}$$

where $N_i \equiv 1 + 2\epsilon a'_i \cos\theta'_i \cos\gamma + \epsilon^2 a_i'^2$. Then, the following relation is derived [19, 26]

$$\frac{\eta_i \mathcal{A}^{\rm mix}_{CP,i}}{\sqrt{1-(\mathcal{A}^{\rm dir}_{CP,i})^2}} = \sin(\phi_s + \Delta\phi_s^i), \tag{2.30}$$

where

$$N_i\sqrt{1-(\mathcal{A}^{\rm dir}_{CP,i})^2}\sin\Delta\phi_s^i = 2\epsilon a'_i \cos\theta'_i \sin\gamma + \epsilon^2 a_i'^2 \sin 2\gamma, \tag{2.31}$$

$$N_i\sqrt{1-(\mathcal{A}^{\rm dir}_{CP,i})^2}\cos\Delta\phi_s^i = 1 + 2\epsilon a'_i \cos\theta'_i \cos\gamma + \epsilon^2 a_i'^2 \cos 2\gamma, \tag{2.32}$$

therefore a direct relation between the phase shift $\Delta\phi_s^i$ and the so-called "penguin parameters" (a'_i, θ'_i) can be established,

$$\tan(\Delta\phi_s^i) = \frac{2\epsilon a'_i \cos\theta'_i \sin\gamma + \epsilon^2 a_i'^2 \sin 2\gamma}{1 + 2\epsilon a'_i \cos\theta'_i \cos\gamma + \epsilon^2 a_i'^2 \cos 2\gamma}. \tag{2.33}$$

The phase shift $\Delta\phi_s^i$ measures the shift of the $B_s^0 - \overline{B}_s^0$ mixing phase ϕ_s due to the contribution of penguin topologies to the $B_s^0 \to J/\psi\phi$ channel. As we expect $\cos\theta_i < 0$ [20], the shift of ϕ_s is expected to be negative as well, interfering constructively with $-2\beta_s$. In order to obtain the penguin pollution shift $\Delta\phi_s^i$, the relevant penguin parameters a_i and θ_i need to be written in terms of measurable observables. Due to the doubly Cabibbo-suppression of these terms in the $B_s^0 \to J/\psi\phi$ decay (see Chapter 2.2), these parameters cannot be measured in this decay channel. Under certain assumptions, detailed in Chapter 5, this measurement can be performed via an angular analysis to $B_s^0 \to J/\psi\overline{K}^{*0}$ decays (see Chapter 4).

[2] Where ϵ is defined as $\lambda^2/(1-\lambda^2)$.

2.4 Implications on New Physics

As previously stated in Chapter 2.2, the CP violating phase ϕ_s is an excellent probe for the search of possible NP, where its latest world average value can be found in ref. [13]. However, prospects for several NP models can be studied if information from ϕ_s is combined with additional information from the very rare decay $B_s^0 \to \mu^+\mu^-$ [27], heavily suppressed in the SM and where contributions from NP models (see for example Figure 2.4) may change its branching fraction in a significant way [28]. Figure 2.5 shows many of those models plotted in the (ϕ_s, $\mathcal{B}(B_s^0 \to \mu^+\mu^-)$) plane.

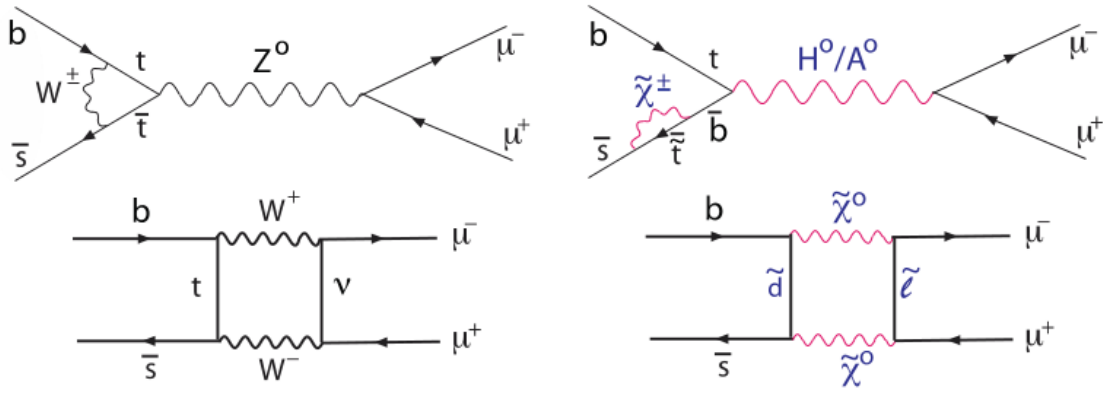

Figure 2.4: Decay diagrams for $B_s^0 \to \mu^+\mu^-$ in the SM (left) and in the Minimal-Supersymmetric-SM (MSSM) (right) [29].

Possible NP contributions to $B_s^0 \to \mu^+\mu^-$ decays from a certain SUSY model (which, in terms of decay diagrams, are essentially the same as those of the MSSM, see Figure 2.4), namely the Next-to-Minimal-Supersymmetric-SM [31,32], have been found to enhance or even suppress the predicted SM value of $\mathcal{B}(B_s^0 \to \mu^+\mu^-)$ by more than one order of magnitude [33]. This is due to the presence of the light CP-odd Higgs boson A_1^0, in the context of the NMSSM. Figure 2.6 shows the predicted branching ratio of $B_s^0 \to \mu^+\mu^-$ decays (left) and the expected shift in ϕ_s due to NP contributions (right), as a function of the mass hypothesis of the A_1^0 pseudoscalar.

Light spin-0 particles can arise in well-motivated NMSSM as well as in models with a dark sector [34, 35]. First steps of a model-independent search of this light pseudoscalar A_1^0 boson decaying to a pair of muons, $A_1^0 \to \mu^+\mu^-$, in a certain low-mass range between approximately $5\,\mathrm{GeV}/c^2$ and $15\,\mathrm{GeV}/c^2$, are presented in Chapter 6. The LHCb experiment can be an excellent laboratory, because of the efficient muon triggering and the excellent mass resolution (see Chapter 3.2.2.3), to search for these light pseudoscalars in the bottonium resonance region.

Other high-energy physics experiments already published results from a search of this NMSSM A_1^0 boson, in particular the CMS experiment [36]. Figure 2.7 shows a prediction

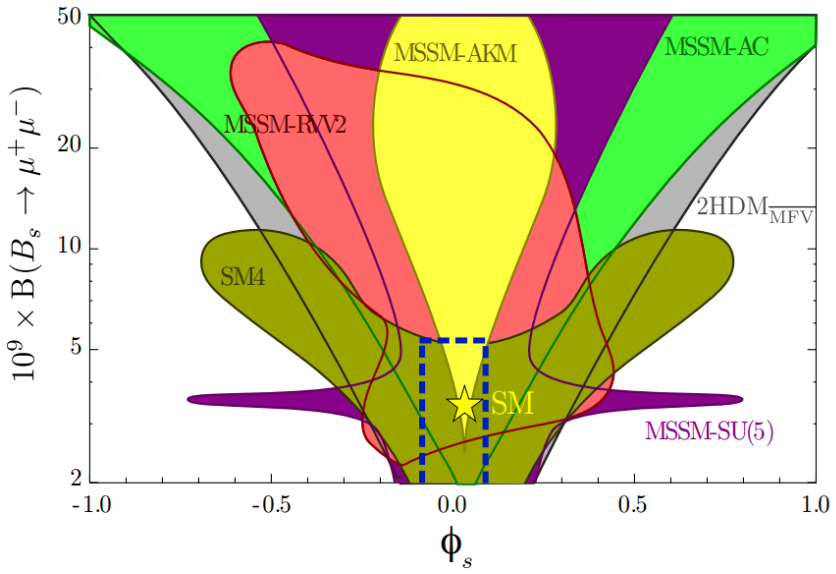

Figure 2.5: Several NP extensions of the SM plotted in the (ϕ_s, $\mathcal{B}(B_s^0 \to \mu^+\mu^-)$) plane. The SM point is marked by a star. The gray area is ruled out experimentally. Blue dashed region outlines the allowed region within one standard deviation of their measured values [29, 30].

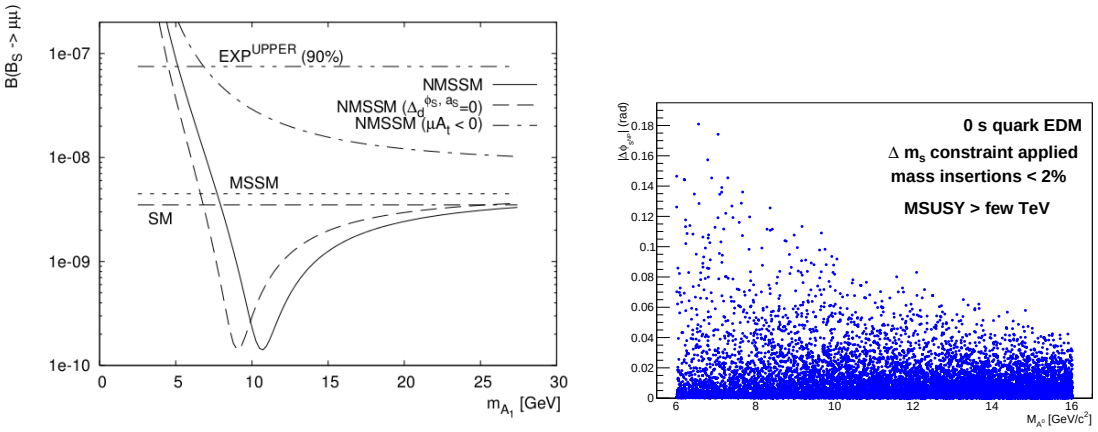

Figure 2.6: Branching fraction of the $B_s^0 \to \mu^+\mu^-$ decay mode (left) and expected shift in ϕ_s due to NP contributions (right) as a function of the mass of the A_1^0 boson. In the left plot, the solid dot-dashed curve shows the NMSSM prediction [33].

(where the 3% of LHCb *pp* data recorded during 2012 is used) of the universal pseudoscalar coupling strength $|\kappa_P|$ [35] as a function of the pseudoscalar mass hypothesis: LHCb seems to be favoured w.r.t. CMS in the mass region mentioned before. An aditional comparison with CMS is shown in Figure 2.8, where both CMS and LHCb acceptances are overlayed

on the pseudorapidity versus muon p_T distribution of $A_1^0 \to \mu^+\mu^-$ (at a certain A_1^0 mass hypothesis) simulated decays at generator level. LHCb can take advantange of the forward acceptance region and of a cleaner environment (no prescale, low p_T).

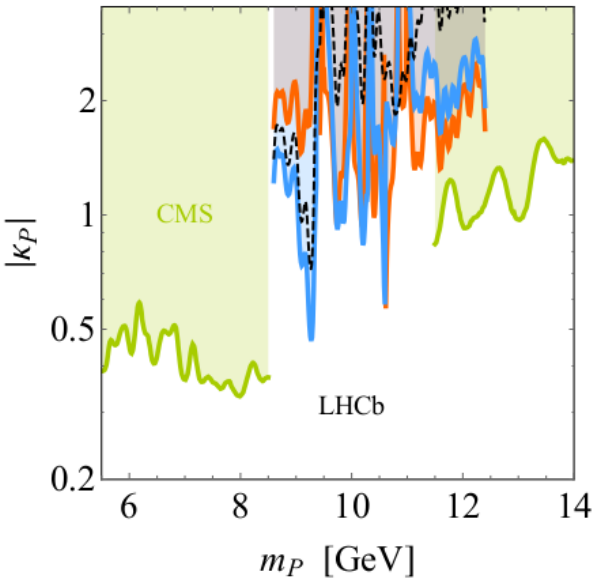

Figure 2.7: Universal pseudoscalar coupling strength $|\kappa_P|$, at 95% C.L., as a function of the pseudoscalar mass hypothesis m_P. For this estimation, 3% of LHCb pp data recorded during 2012 is used [35].

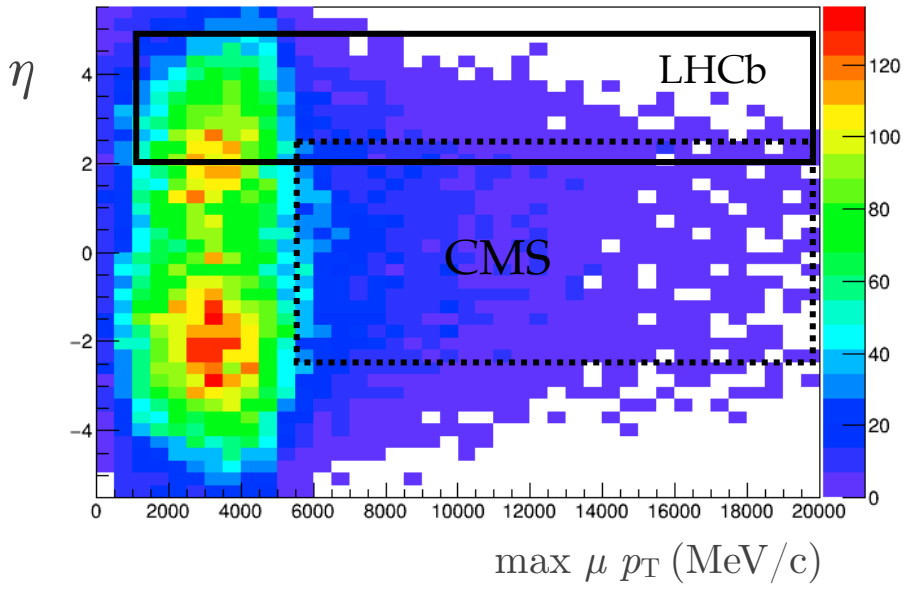

Figure 2.8: Distribution of pseudorapidity versus muon p_T of $A_1^0 \to \mu^+\mu^-$ simulated decays (at a generator level), at a certain A_1^0 mass hypothesis. Both CMS and LHCb acceptance regions are shown.

Chapter 3

The LHCb experiment

The LHCb (Large Hadron Collider beauty) experiment is dedicated to Heavy Flavor physics at the Large Hadron Collider [37] located at CERN[1] (Geneva, Switzerland). As of June 2016, the experiment is driven by a collaboration of 1199 members, from 69 institutes in 16 countries around the world.[2] The primary goal of the experiment is to look for indirect evidence of NP in *CP* violation and rare decays of beauty and charm hadrons.

As previously stated in Chapter 2, current results in HF physics are consistent with theoretical predictions of the CKM mechanism [38], but the level of *CP* violation predicted by the weak interactions of the Standard Model cannot explain the difference between matter and antimater in the Universe [10]. This puzzle motivates the search for a new source of *CP* violation beyond the SM which can explain these differences, and might be seen in HF physics in a further stage of development of beauty and charm experiments.

Rare decays and *CP* violation of B and D mesons are a protential probe for those NP searches: with the large $b\bar{b}$ production cross section of approximately 640 μb [39] expected at a centre-of-mass energy of 14 TeV, the LHC (described in Chapter 3.1) is the most copious source of B mesons in the world, producing also large quantities of b-baryons.

As already mentioned in Chapter 1, the two analyses described on this work are the study of $B_s^0 \to J/\psi \overline{K}^{*0}$ decays (see Chapter 4) and the study of the $A_1^0 \to \mu^+\mu^-$ mode (see Chapter 6). In both cases, a parent particle is reconstructed from a pair of muons: for this task, the role of the muon and the trigger system (described in Chapter 3.2.2.3 and Chapter 3.2.3, respectively) in order to obtain a muon sample of high purity, is essential. For the analysis of the $B_s^0 \to J/\psi \overline{K}^{*0}$ channel, it is also important a good hadronic identification, since the K^{*0} meson is reconstructed from a charged kaon and a charged pion. Consequently, having a proper separation (in terms of particle identification) between kaons and pions and avoiding possible mis-identification with other particles, such as protons, require a good performance of the calorimeter system and the Ring Imaging CHerenkov (RICH) detectors (see Chapter 3.2.2.2 and Chapter 3.2.2.1, respectively). For both analyses as well, good tracking and vertexing systems, described in Chapter 3.2.1,

[1] CERN, European Organization for Nuclear Research (a).
[2] The LHCb Collaboration (b).

are crucial.

After the description of the different subsystems of the LHCb detector, enumerated in more detail in Chapter 3.2, its DAta acQuisition (DAQ) sequence is described in Chapter 3.2.4, along with the simulation framework, in Chapter 3.2.5. A summary of the detector performance is presented in Chapter 3.2.6, followed by a description of the experimental conditions of LHCb Run I on Chapter 3.2.7. A final chapter describing the on-going upgrade of the LHCb detector in order to be able to cope with higher luminosities and higher centre-of-mass energies due to the upgrade of the LHC machine, can be found in Chapter 3.3. Some paragraphs and sentences in the following pages may be literally extracted from other LHCb theses, such as refs. [40–44], and also from certain technical design reports and performance publications, but appropriately cited in the latter case.

3.1 The Large Hadron Collider

The Large Hadron Collider, operating at CERN since September 2008, is the most powerful hadron accelerator and collider ever built by humankind. Installed in the 27 km circular tunnel built to house the Large Electron Positron (LEP) collider, it is located between 45 m and 170 m underneath surface at the French-Swiss border. The LHC machine was designed to accelerate proton beams up to an energy of 7 TeV per beam and to collide them with a centre-of-mass energy of 14 TeV [37].

Protons, obtained from hydrogen gas, are progressively accelerated up to 450 GeV through the chain of pre-accelerators shown in Figure 3.1. First, the LINear ACCelerator 2 (LINAC2) up to 50 MeV; second, the BOOSTER up to 1.4 GeV; third, the Proton Synchrotron up to 26 GeV; and finally, the Proton Synchrotron (SPS) up to 450 GeV. After being accelerated up to 450 GeV, each beam is injected in the LHC and accelerated using 16 radiofrequency (RF) cavities to the final collision energy. At these energies, 1232 superconducting Nb-Ti dipole magnets, cooled down to 1.9 K using super-fluid He, create a very intense magnetic field (8.33 T at a nominal centre-of-mass energy of 7 TeV) to bend and keep the two proton beams in opposite orbits around the LHC ring. The two beams are accomodated in the same cryostat with a common yoke, which provides the opposite magnetic fields. To focus the nominal proton beams, composed of bunches of 1.2 to 1.4×10^{11} protons with a separation of 25 ns (40 MHz of bunch crossing frequency), 392 quadrupole magnets are also located around the ring. A schematic of the cross-section of a LHC cryodipole, where all these elements are mecanically fit together, is shown in Figure 3.2.

The LHC was operated during 2011 and 2012 at centre-of-mass energies of 7 and 8 TeV (3.5 TeV and 4 TeV per beam), respectively, with bunches separated in time by 50 ns (20 MHz of bunch crossing frequency). Beams are collided in four interaction points (IPs) along the LHC ring. A total of seven detectors share these four IPs, as shown in Figure 3.3, to study the physics produced by the unprecedented high energy collisions at the TeV scale.

The two General Purpose Detectors (GPDs) ATLAS (A Toroidal LHC ApparatuS) [47]

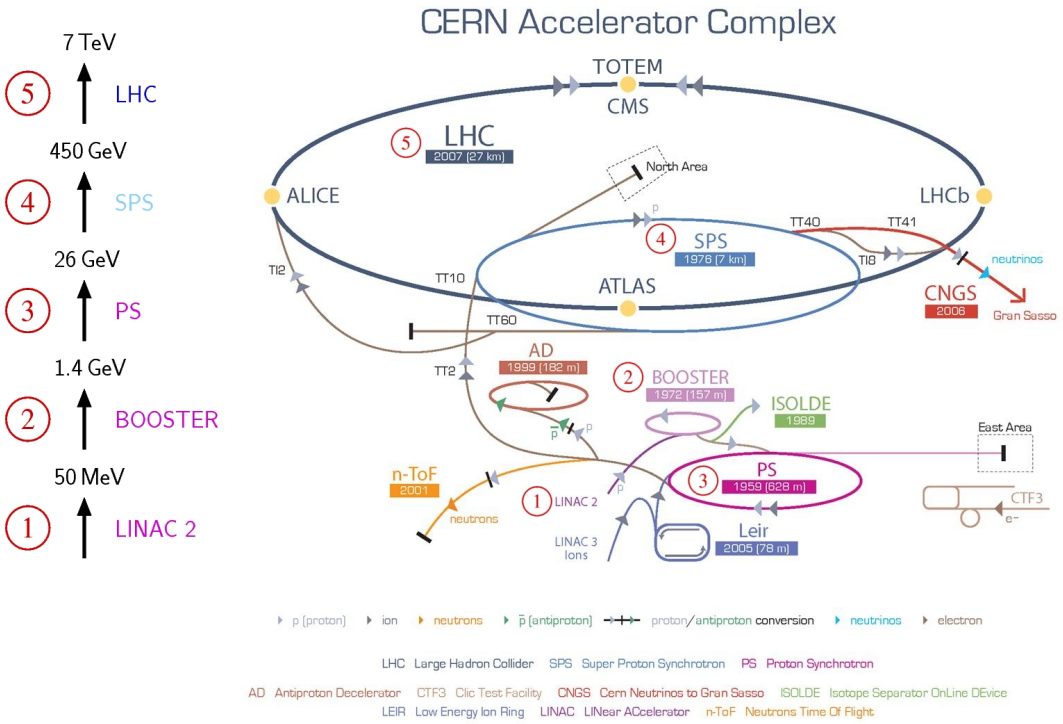

Figure 3.1: CERN accelerator complex layout (2008) [45]. On the left, the step-by-step acceleration sequence is shown.

and CMS (Compact Muon Solenoid) [48] are based on large central detectors, located at IPs 1 and 5 respectively, and designed to study collisions producing high tranverse momentum (p_T) particles. Both experiments develop a wide physics programme, which includes direct searches of NP particles, b and t quark physics, and the fundamental objective of the detection of the Higgs boson. The latter was reported to be successfully observed for the first time in 2012, in the mass region around 125 GeV [49, 50]. One year later, the Nobel Prize in Physics was awarded jointly to François Englert and Peter Higgs.[3] Now, a large part of ATLAS and CMS physics programme is devoted to a precision measurement of the properties of this recently discovered scalar boson.

Located at IP 2, ALICE (A Large Ion Collider Experiment) [51] is a dedicated heavy–ion experiment which studies quark-gluon plasma with data resulting from nucleus–nucleus collision. For this purpose, LHC is filled in with dedicated runs of heavy ions (Pb) instead of protons.

Finally, the LHCb (Large Hadron Collider beauty) [52] experiment (described more in

[3]The Nobel Prize in Physics 2013: François Englert and Peter Higgs (a, b, c)

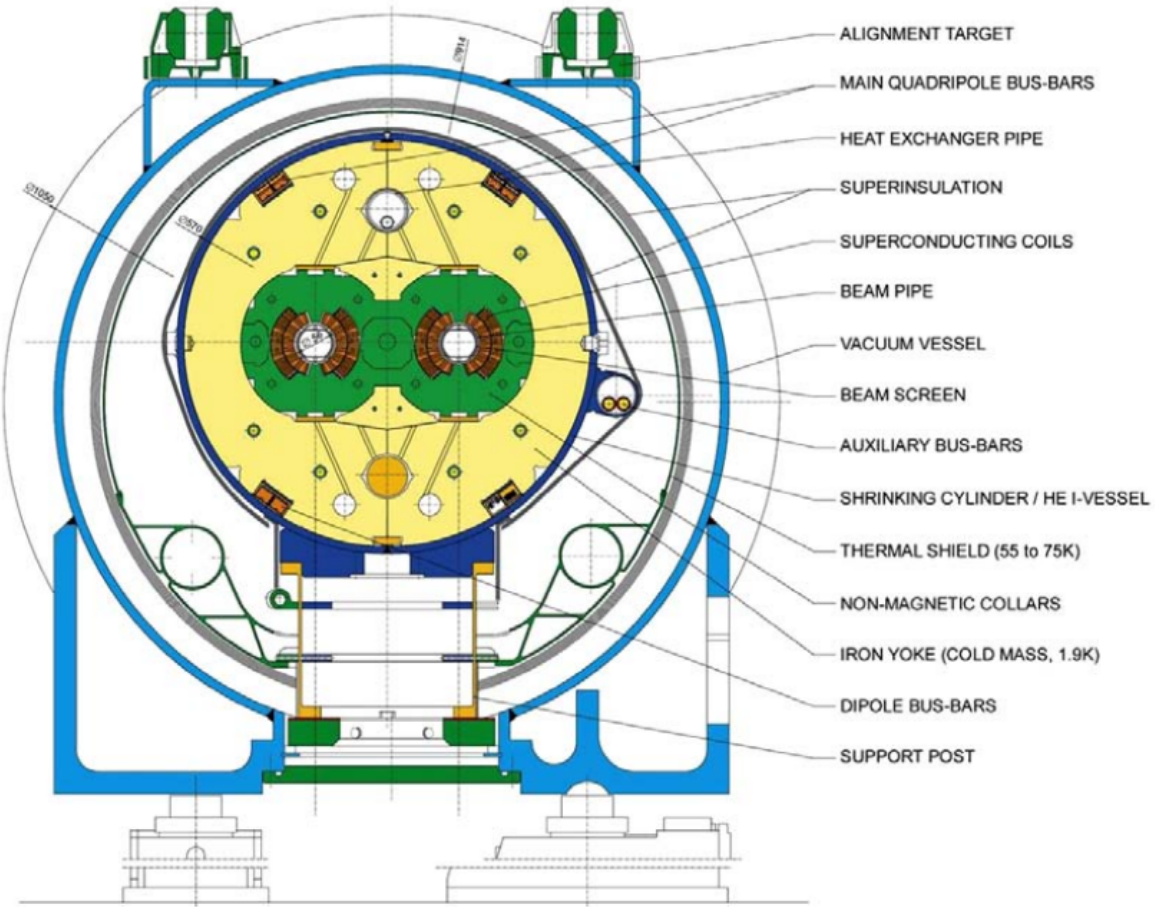

Figure 3.2: Cross-section of a LHC cryodipole [37]. Lengths are in mm.

detail in Chapter 3.2) at IP 8 was originally designed for the study of *CP* violation and rare decays focused in b and c quark physics. However, due to the excellent performance of the detector during the past years, the LHCb collaboration has been able to develop a wider physics programme obtaining successful results, such as the first observation of an exotic five-quark [53] and the observation of several exotic four-quark [54–56] hadronic structures, and studies of proton-nucleus collisions [57–61]. Because of these improvements, in the present years the LHCb detector started to be considered a forward GPD.

Other experiments as TOTEM (TOTal Elastic and diffractive cross section Measurement) [62], LHCf (Large Hadron Collider forward) [63] and MoEDAL (Monopole and Exotics Detector at the LHC) [64] are also being operated at the LHC. The LHCf experiment studies energy distributions of particles in the very forward region, and is placed at roughly ~ 140 m from the ATLAS IP. TOTEM is designed to measure the total elastic and diffractive cross section as its name indicates, and shares IP 5 with CMS. The MoEDAL, deployed at the opposite side of the LHCb detector at IP 8, is a pioneering

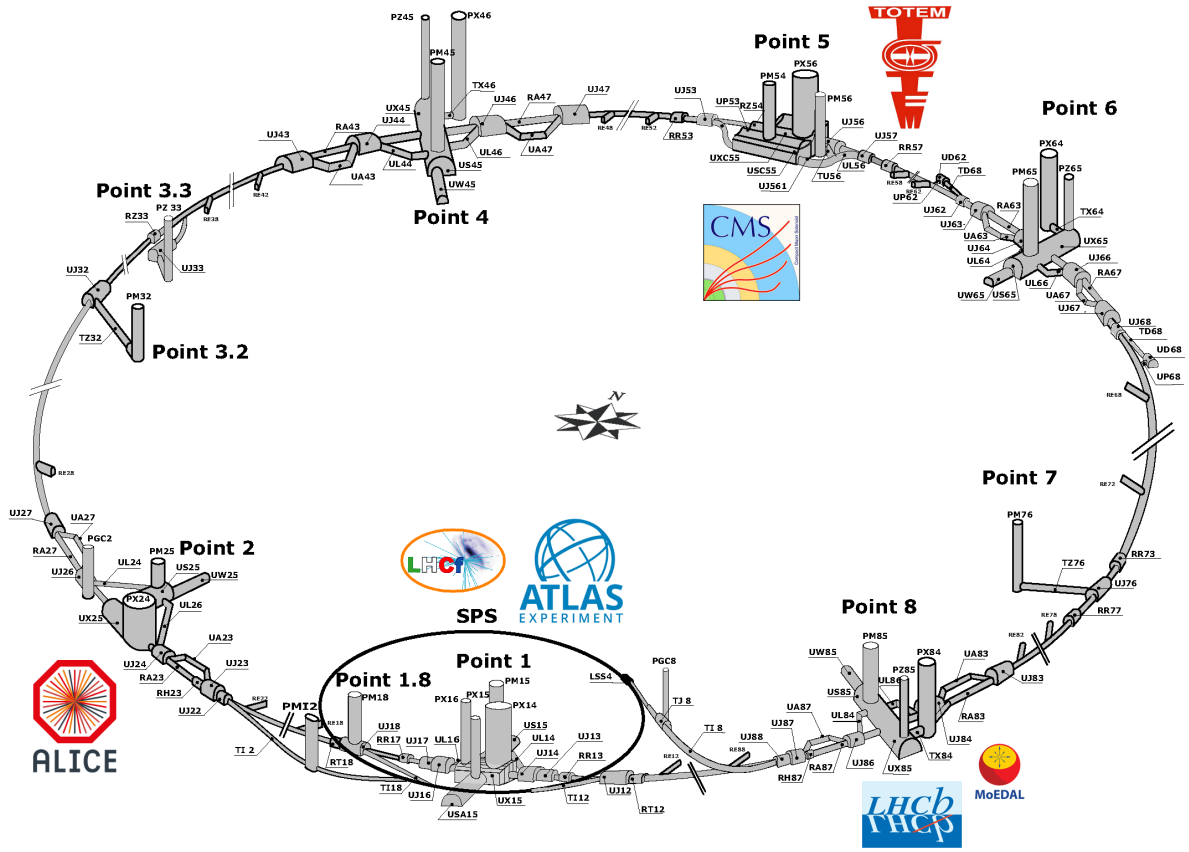

Figure 3.3: Detailed schematic of the LHC ring, adapted from ref. [46], showing the different interaction points, sectors and experiments.

experiment designed to search for highly ionizing avatars of new physics, such as magnetic monopoles or massive (pseudo)stable charged particles.

3.2 The LHCb detector

The LHCb detector is a single-arm spectrometer with a forward angular coverage, focused on the high rapidity region on one side of the IP. It approximately covers an angular range from 10 to 300 mrad in the bending plane. The angular coverage is smaller in the non-bending plane, from 10 to 250 mrad [52]. As shown in Figure 3.4,[4] the polar distribution of the $b\bar{b}$ pair production at the LHC justifies this design, because at high energies these pairs are predominantly produced in the same forward or backward cone.

The IP 8 of the LHC, previously used by the DELPHI experiment during the LEP

[4]These plots were created using PYTHIA8 [65] and CTEQ6 NLO [66] by Christian Elsasser (che@physik.uzh.ch). Here, pseudorapidity is defined as $\eta \equiv -\log\left[\tan\left(\frac{\theta}{2}\right)\right]$, where θ is the polar angle of the corresponding $b(\bar{b})$ quark.

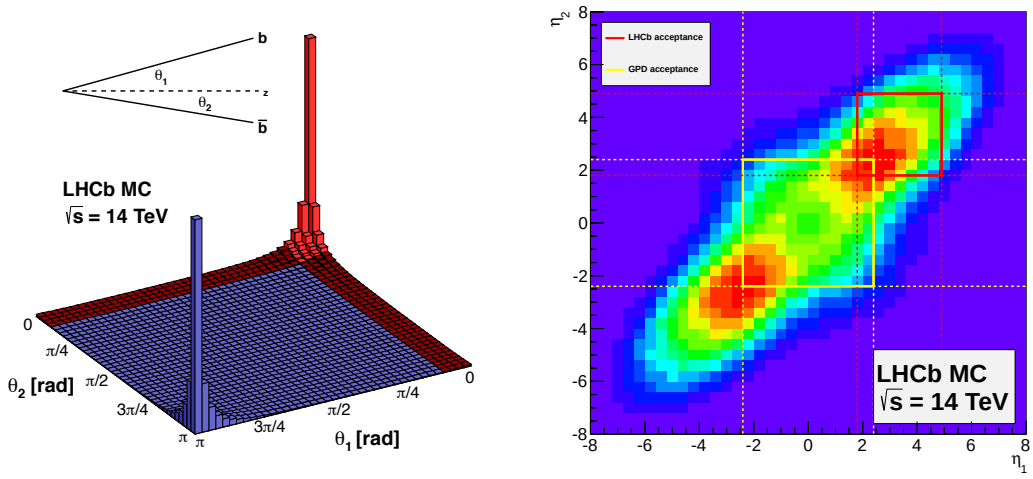

Figure 3.4: Angular $b\bar{b}$ production plots, from LHCb simulation, at a centre-of-mass energy of 14 TeV. Left: Polar distribution of the $b\bar{b}$ pair production in the forward region. Right: pseudorapidity distribution of the $b\bar{b}$ pair production, where one axis refers to one of the b-quarks and the other axis refers to the remaining one in the pair. A comparison between LHCb acceptance (defined as $1.8 < \eta < 4.9$) and other GPDs acceptance (defined as $|\eta| < 2.4$) is overlayed over the right plot, manifestly showing the forward design of the LHCb detector.

time, has been allocated to the LHCb detector. A modification to the LHC optics, displacing the interaction point by 11.25 m from the centre, has permitted maximum use of the existing cavern for the LHCb detector components. With a low occupancy and low radiation damage due to a modest luminosity of $2 \times 10^{32} cm^{-2} s^{-1}$, an amount of 10^{12} $b\bar{b}$ pairs would be produced in 10^7 s (see Chapter 3.2.7). Due to this lower luminosity, tuned independently from the other IPs, events are dominated by a single pp interaction per bunch crossing and hence simpler to analyse [52].

The layout of the LHCb spectrometer is shown in Figure 3.5. The right-handed coordinate system adopted has the z axis along the beam, and the y axis along the vertical. With an overall dimension of approximately 6 m $\times$ 5 m $\times$ 20 m, the detector is composed by the following main parts: the beam pipe, the magnet, the tracking and vertexing systems: VErtex LOcator, Silicon Tracker and Outer Tracker; and the particle identification systems: Ring Imaging CHerenkov detectors, the calorimeter system, and the muon system. Also, because of the relative high interaction rate and the low branching ratio of those rare decays of interest (as addressed at the beginning of Chapter 3), an efficient rejection of data is required. For this purpose a trigger system is built, consisting of a hardware based system (Level 0 or L0) and a pure software based trigger (High Level Trigger or HLT).

The beam pipe [52] is 19 m long and is divided in four conical sections, including the

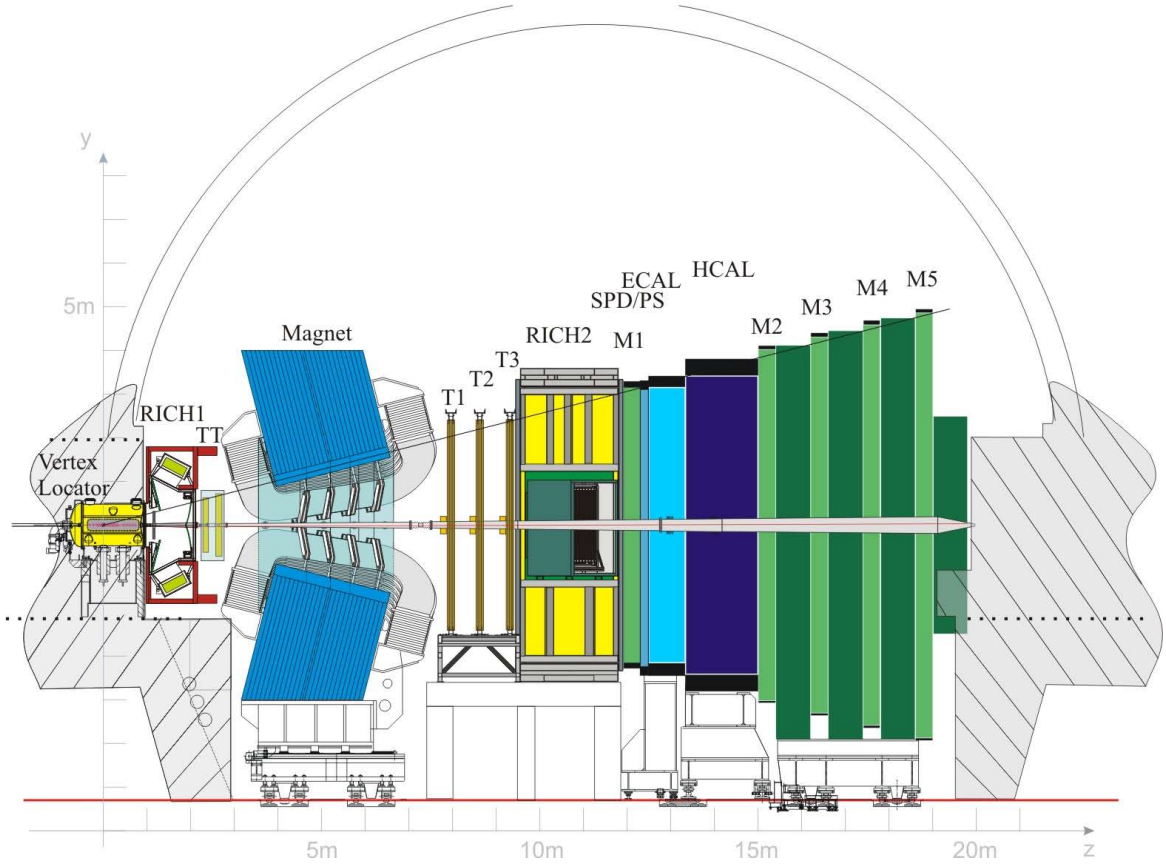

Figure 3.5: Schematic two-dimensional view of the LHCb detector [67]. The right-handed coordinate system adopted has the z axis along the beam, and the y axis along the vertical.

forward window of the VELO and covering the full LHCb acceptance. This design is particularly delicate since the LHCb experiment is focused on the high rapidity region, where the particle density is high: the mass of the beam pipe and the presence of flanges and bellows have a direct influence on the occupancy, in particular for the tracking system and the RICH detectors.

The momentum of charged particles is measured using a a dipole magnet, covering the forward acceptance of ± 250 mrad vertically and of ± 300 mrad horizontally. This dipole is composed by a Fe yoke surrounded by two identical coils of conical saddle shape produced of the metal alloy Al 99.7 [42, 68]. In average, the LHCb magnet has an integrated magnetic field of 4 T $\times$ m. The relative precision obtained after a field mapping is about 4×10^{-4}, enough to achieve the required momentum resolution for charged particles. Figure 3.6 shows on the left a picture of the dipole installed at the LHCb experimental site, while on the right the B_y magnetic field component as a function of the z coordinate is presented. For the measurement of CP asymmetries it is important to control the systematic effects of the detector, by periodically changing the direction of the magnetic field.

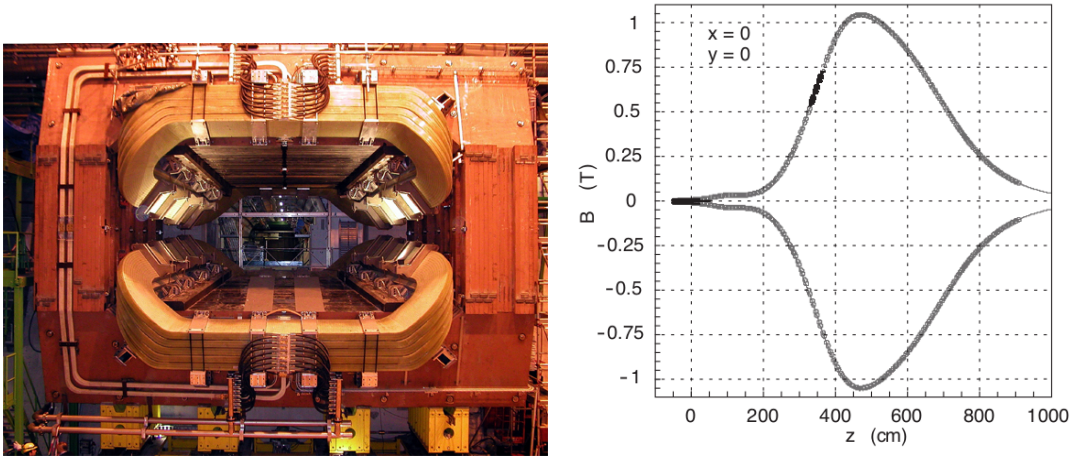

Figure 3.6: LHCb magnet dipole. Left: picture of the dipole installed at the LHCb experimental site (2004). Right: B_y magnetic field component as a function of the z coordinate [52].

As stated at the beginning of Chapter 3, without an appropriate vertex reconstruction, particle identification and an efficient rejection of background data, the physical studies described in this work could not be done. Hence, tracking and vertexing systems, particle identification systems and trigger systems are described in the following paragraphs with more detail, followed by a description of the LHCb DAQ sequence, the simulation framework and a summary of the detector performance during the Run I.

3.2.1 Tracking and vertexing systems

The LHCb tracking and vertexing systems consists of the VErtex LOcator system, the Tracker Turicensis (TT) and the Inner Tracker (IT) developed as a common project called the Silicon Tracker (ST), and the Outer Tracker (OT) located at the outer region of the IT. Each one of the ST and OT stations has four detection layers in a x-u-v-x arrangement with vertical strips in each of the two x layers, and strips rotated by $\pm 5^{o}$ in the u and v layers, in order to get a stereo-view of the particle trajectory.

3.2.1.1 VErtex LOcator

The VErtex LOcator, has a critical importance for the experiment: to study different b-hadron decays like those involving short-lived resonances, a precise vertex reconstruction which allows to distinguish between primary and secondary vertices (see Chapter 3.2.6.1) is imperative. As a consequence, high background rejection and a precise measurement of lifetimes (not only required to resolve short-lived resonances but also to resolve the fast oscillation of the B_s^0 meson system) are achieved.

LHCb VELO contains 21 stations, positioned along and perpendicular to the beam

axis with an r-ϕ geometry: with this design, forward-going tracks with a high impact parameter with respect to the production vertex are easily identified. It covers the pseudorapidity range $1.6 < \eta < 4.9$ for particles coming from primary vertices in the range -10.6 cm < z < 10.6 cm. Each disc, with a radius of $\sim$ 42 mm, is composed of two types of half-disc silicon sensors: r-type sensors (circular strips centered around the beam axis, measuring the r polar coordinate) and ϕ-type sensors (straight and almost radial strips, measuring the ϕ polar coordinate). These half-disc sensors, are arranged in pairs of r-type and ϕ-type, mounted back-to-back to reduce thickness. At innermost radius, the minimum strip pitch in the sensors is 38 μm, increasing up to 101.6 μm. The sensitive area of the sensors starts at 8 mm from the beam axis, such that the first measurement of the track is as close to the primary vertex as possible: the shorter the extrapolation of a track from its first measurement to the interaction region, the smaller is the error on the reconstructed position of the vertex [52, 69]. A modelled view of the VELO, and a real picture of one of the modules, are shown in Figure 3.7.

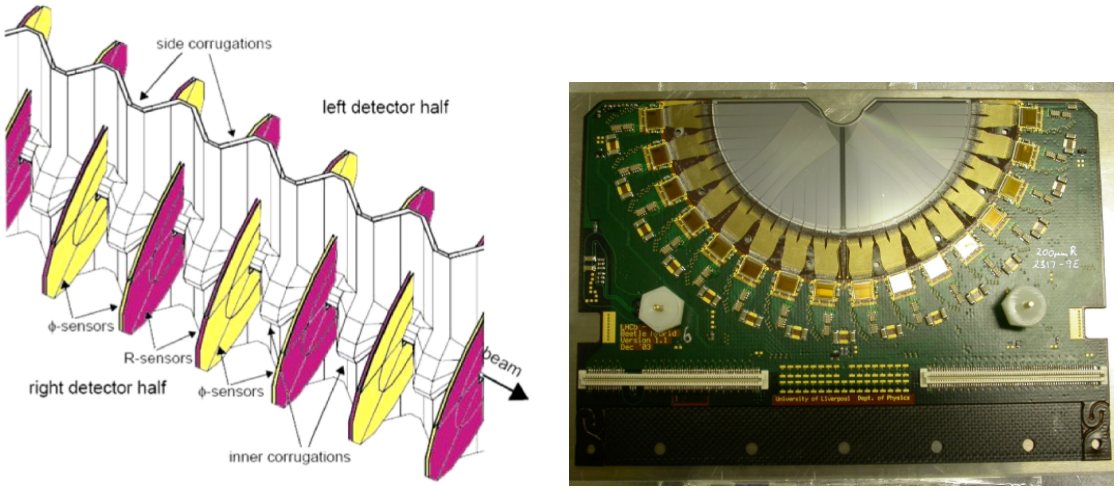

Figure 3.7: LHCb VErtex LOcator. Left: modelled view of the VELO. Right: a VELO module [52].

3.2.1.2 Silicon Tracker

The Silicon Tracker is composed by two detectors: the Tracker Turicensis [70] and the Inner Tracker [71]. Both use silicon microstrip sensors with a strip pitch size (or distance between the centre-of-mass of neighboring strips) of about 200 μm. Housed in separated light tight, thermally and electrically insulated detector volumes, both detectors are mantained at a temperature below 5 °C, being these volumes continuously flushed with nitrogen to avoid condensation on cold surfaces. Design choices for the ST were mainly driven by considerations of spatial resolution, hit occupancy, signal shaping time,

single hit-efficiency and radiation damage, among others. An important contribution[5] from the University of Santiago de Compostela to the construction of the ST has to be remarked.

The four detection layers of the TT are located upstream of the LHCb magnet dipole (see Figure 3.5) covering the full acceptance of the experiment. The TT has a width of 150 cm and a height of 130 cm, with a total active area of 8.4 m^2.

The IT, composed by four detector boxes arranged around the beam pipe and located downstream of the magnet, is 120 cm wide and 40 cm high. It has an active area of 4.0 m^2 [52]. Figure 3.8 shows the layouts of a TT layer and a IT module, as described before.

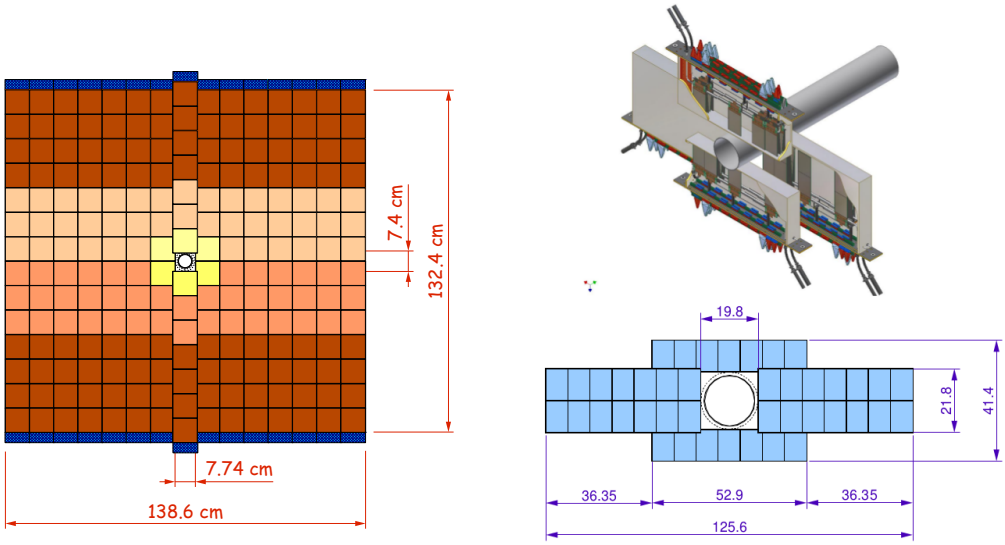

Figure 3.8: LHCb Silicon Tracker. Left: schematic layout of one of the TT layers. Right: view (top) and schematic (bottom) layout of an IT module [52, 70, 71].

3.2.1.3 Outer Tracker

The Outer Tracker [72] is a drift-time detector, designed for the tracking of charged particles and the measurement of their momentum over a large acceptance area. An excellent momentum resolution is required for a precise determination of the invariant mass of reconstructed b-hadrons. High tracking efficiency (95%) and a low fraction of wrongly reconstructed tracks ($\leq$ 15%) is demanded by the reconstruction of high multiplicity B decays.

This detector is designed as an array of individual, gas (70% Argon, 20% CO_2) straw-tube modules (see Figure 3.9), arranged in three stations (as the external part of T1, T2 and T3 in Figure 3.5) of four layers each one. Rigidity, electrical shielding and radiation hardness were main requirements during its design [52].

[5]Grupo de Física de Altas Enerxías (GAES): LHCb Silicon Tracker Construction (a)

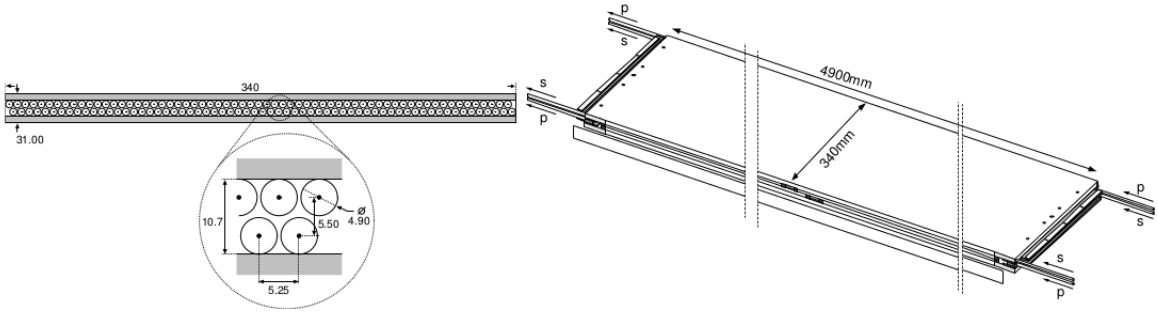

Figure 3.9: LHCb Outer Tracker. Left: cross section of a straw-tubes module. Right: overview of a straw-tubes module design [52, 72].

3.2.2 Particle identification system

The particle identification systems consists of three well-separated parts: the RICH detectors, the calorimeter system, and the muon system.

3.2.2.1 Ring Imaging CHerenkov detectors

It is essential for the goals of the experiment to separate pions from kaons in selected B hadron decays (see Chapter 4.2). This task is performed by the RICH detectors: this system consists of two RICH (RICH1 and RICH2) detectors to cover the full momentum range.

The upstream RICH1 covers the full LHCb angular acceptance, from ±25 mrad to ±300 mrad (horizontal) and ±250 mrad (vertical), and the low momentum charged particle range, from ∼1 to 60 GeV/c, using aerogel and C_4F_{10} radiators. The downstream RICH2 covers a limited angular acceptance, from ±25 mrad to ±120 mrad (horizontal) and ±100 mrad (vertical), and the high momentum charged particle range, from ∼15 GeV/c up to and beyond 100 GeV/c, using a CF_4 radiator. Both RICH detectors [73] (see Figure 3.10) are composed by a combination of spherical and flat mirrors which reflect and focus Cherenkov light out of the spectrometer acceptance, and Hybrid Photon Detectors (HPDs) to detect Cherenkov photons in the wavelength range from 200 to 600 nm, surrounded by external iron shields.

3.2.2.2 Calorimeter system

The calorimeter system [74] provides the identification of electrons, photons and hadrons as well as the measurement of their energies and positions. This system is also essential for the study of B meson decays. It selects the transverse energy of hadron, electron and photon candidates for the first trigger level (L0), too (see Chapter 3.2.3). This system is composed by a Scintillator Pad Detector (SPD) and a PreShower (PS) detector, followed by an Electromagnetic CALorimeter (ECAL) and a Hadron CALorimeter (HCAL). The

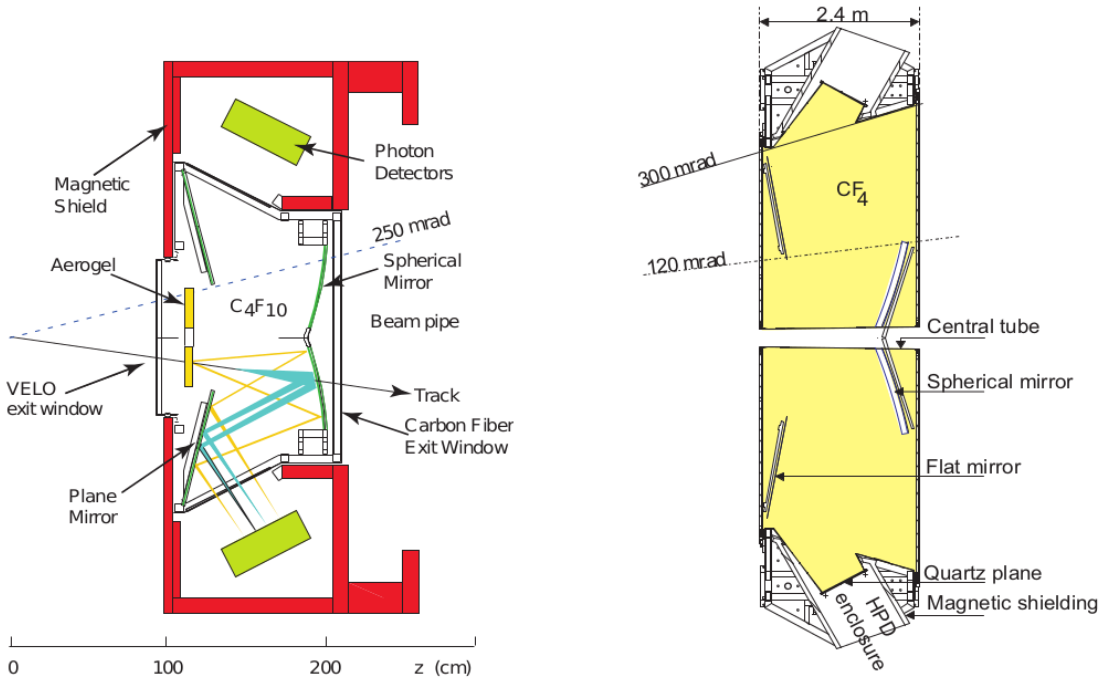

Figure 3.10: LHCb Ring Imaging CHerenkov. Left: layout of RICH1. Right: layout of RICH2 [52, 73].

purpose of this structure is to be able to properly discriminate between hadrons, electrons/positrons and photons, since the energy deposition in each part of the calorimeter components will depend on the nature of the particles passing through.

The SPD and PS, consisting of a 15 mm lead converter enclosed between two almost identical planes of rectangular scintillator pads, help to differentiate between charged and neutral particles, and the electron trigger to reject a background of pions with large transverse energy, E_T, respectively. With a thickness of 2.5 radiation lengths, its sensitive area is 7.6 m wide and 6.2 m high. The ECAL, is composed by a scintillator/lead structure with overall dimensions 7.8×6.3 m, and placed at 12.5 m from the interaction point with a thickness of 25 radiation lengths. It enables the reconstruction of photons, electrons and neutral pions. An optimal energy resolution requires the full containment of the showers from high energy photons. On the other hand, the HCAL is composed by iron and scintillating tiles parallel to beam pipe, with overall dimensions of 8.4×6.8 m, and has a thickness of 5.6 interaction lengths, due to space limitations. The trigger requirements on the HCAL resolution do not impose a stringent hadronic shower containment condition. In the whole calorimeter system (see Figure 3.11), the scintillation light is transmitted to PhotoMultiplier Tubes (PMTs), that turn this light into an electric signal.

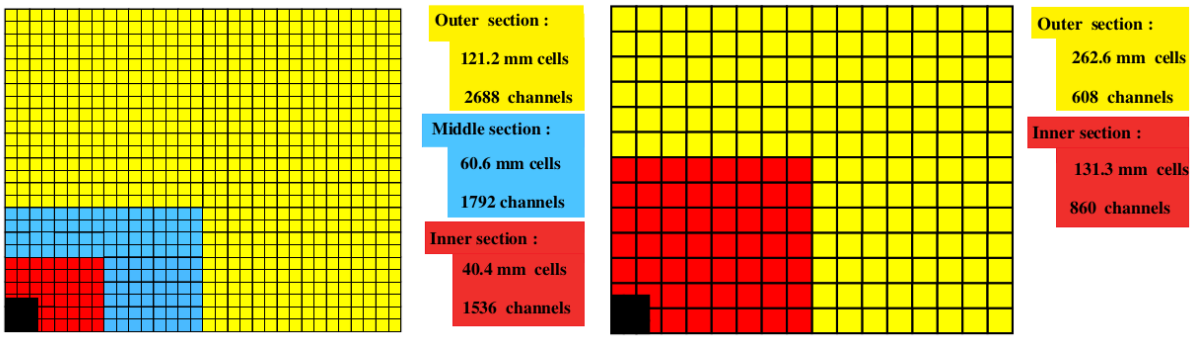

Figure 3.11: LHCb calorimeter system. Left: segmentation of the SPD, PS and ECAL. Right: segmentation of the HCAL [52].

3.2.2.3 Muon system

The muon system [75] for the LHCb experiment consists of five tracking stations placed along the beam axis. The first station (M1) is placed in front of the PS detector, while the remaining four stations (M2, M3, M4 and M5) are located downstream the calorimeter, interleaved with three iron filters.

The inner and outer angular acceptances of the muon system are 20 (16) mrad and 306 (258) mrad in the bending (non-bending) plane. This provides a geometrical acceptance of about $\sim$ 20 % for muons from b decays relative to the full solid angle. Each station is subdivided in four regions with dimensions and logical pad size which scales a factor of two from one region to the next, see Figure 3.12.

The muon stations are equipped with Multi Wire Proportional Chambers (MWPCs) operating with an Ar:CO_2:CF_4 gas mixture. The only exception to the MWPCs is the innermost region R1 of the station M1, in which the high rate of particles requires the use of a triple-GEM detector, which consists of three Gas Electron Multiplier (GEM), using the same gas mixture with different relative proportions.

3.2.3 Trigger system

The LHCb trigger system [76] filters information collected by the different substations of the experiment, reducing the collected amount of data to the maximum allowed by the long-term data storage resources, retaining as much interesting b decays as possible. At the 2012 luminosity and pile-up running conditions, the rate of visible beam crossings in LHCb is about 10 MHz. Thus, the practical purpose of the LHCb trigger system is to reduce the rate down to about 5 kHz (the highest that can be written to storage) while efficiently selecting events suitable for LHCb physics analyses. This system searchs for events with relatively high p_T and vertex displacement respect to the primary vertex: main signatures which identify events originated during b decays. The LHCb trigger system is composed of two levels: L0 (Level 0) and HLT (High Level Trigger). After the trigger,

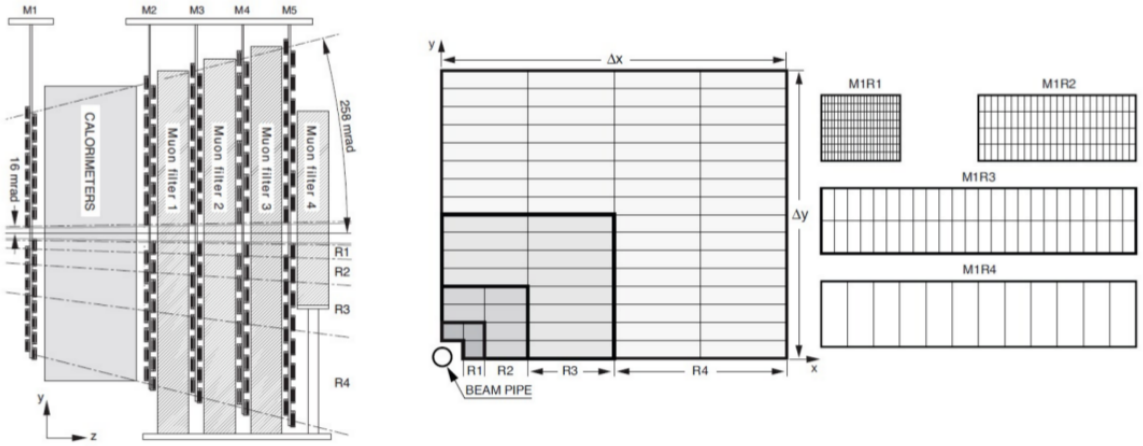

Figure 3.12: LHCb muon system. Left: schematic cross section of the muon system. Middle: a quadrant of one of the muon stations with the four separated regions R1-4, where each square represents a muon chamber. Right: segmentation of the four types of muon chambers installed in the different regions R1-4 [52].

events are stored for offline data analysis. Trigger configuration information is embedded into an hexadecimal word called Trigger Configuration Key (TCK), that identifies the set of trigger decisions, the algorithms run in the trigger and the cuts applied to trigger the events in a given run.

The L0 trigger is the logical OR of several decisions and vetoes. It reduces the event rate to 1 MHz. The main physics triggers in L0 are `L0Hadron`, `L0Electron`, `L0Photon` (based on signatures in the calorimeter system), `L0Muon` and `L0Dimuon`. `L0Muon` is based on a standalone track, reconstructed in the muon system. Using the muon chambers alone, the transverse momentum can be reconstructed with a precision of 20%. Under 2011 (2012) conditions, the muon candidates are required to have $p_T > 1.48$ GeV/c ($p_T > 1.76$ GeV/c). On the other hand, `L0Dimuon` is based on two muon candidates where the product of the p_T of the two is required to satisfy a minimum ${p_T}^2 > (1.3 \text{ GeV}/c)^2$ (${p_T}^2 > (1.6 \text{ GeV}/c)^2$) under 2011 (2012) conditions. All the L0 p_T thresholds applied during Run I are shown in Table 3.1.

The HLT is a software trigger continuously running and forming the EFF (Event Filter Farm). For the decays studied in this thesis (see Chapter 4 and Chapter 6), which have two muons in the final state, the HLT1 dimuon triggers serve as the adequated signal trigger. The HLT1 di-muon triggers require the logical OR of `L0Muon` and `L0DiMuon`, described before [52].

Table 3.1: L0 thresholds in LHCb Run I [77].

	2011	2012
single muon	$1.48\,\text{GeV}/c$	$1.76\,\text{GeV}/c$
dimuon $p_{T1} \times p_{T2}$	$(1.30\,\text{GeV}/c)^2$	$(1.60\,\text{GeV}/c)^2$
hadron	$3.50\,\text{GeV}/c$	$3.70\,\text{GeV}/c$
electron	$2.50\,\text{GeV}/c$	$3.00\,\text{GeV}/c$
photon	$2.50\,\text{GeV}/c$	$3.00\,\text{GeV}/c$

3.2.4 Online system

The task of the LHCb online system is to ensure the transfer of data from the front-end electronics to permanent storage under known and controlled conditions. The LHCb Online system (see Figure 3.13) consists of three components, the DAQ system, the Timing and Fast Control (TFC) system, and the Experiment Control System (ECS).

The purpose of the DAQ system is the transport of the data belonging to a given bunch crossing, and identified by the trigger, from the detector front-end electronics to permanent storage. Data from the front-end electronics are collected in LHCb-wide standardized readout boards, named TELL1. In the CPU farm, the HLT algorithm selects interesting interactions; upon a positive decision, the data are subsequently sent to permanent storage. The quality of the acquired data is checked in a separate monitoring farm that receive events accepted by the HLT and house user-defined algorithms to determine, for example, the efficiencies of detector channels or the mass resolution of the detector.

The TFC system drives all stages of the data readout of the LHCb detector between the front-end electronics and the online processing farm by distributing the beam-synchronous clock, the L0 trigger, synchronous resets and fast control commands. The system is a combination of electronic components common to all LHC experiments and LHCb custom electronics.

The ECS ensures the control and monitoring of the operational state of the entire LHCb detector. This encompasses not only the traditional detector control domains, such as high and low voltages, temperatures, gas flows, or pressures, but also the control and monitoring of the Trigger, TFC, and DAQ systems. The hardware components of the ECS are somewhat diverse, mainly as a consequence of the variety of the equipment to be controlled, ranging from standard crates and power supplies to individual electronics boards. The distributed components of the ECS system are connected with a large Ethernet network consisting of several hundred Gigabit and Fast Ethernet links [52, 78].

3.2.5 Simulation

To generate (simulated) Monte Carlo (MC) samples as those described in this thesis, a full simulation of collisions and of the LHCb detector response is needed. Collisions are generated using Pythia [65] with a specific LHCb configuration [79]. For this task, the following LHCb software packages, based on Gaudi [80] architecture and not used only

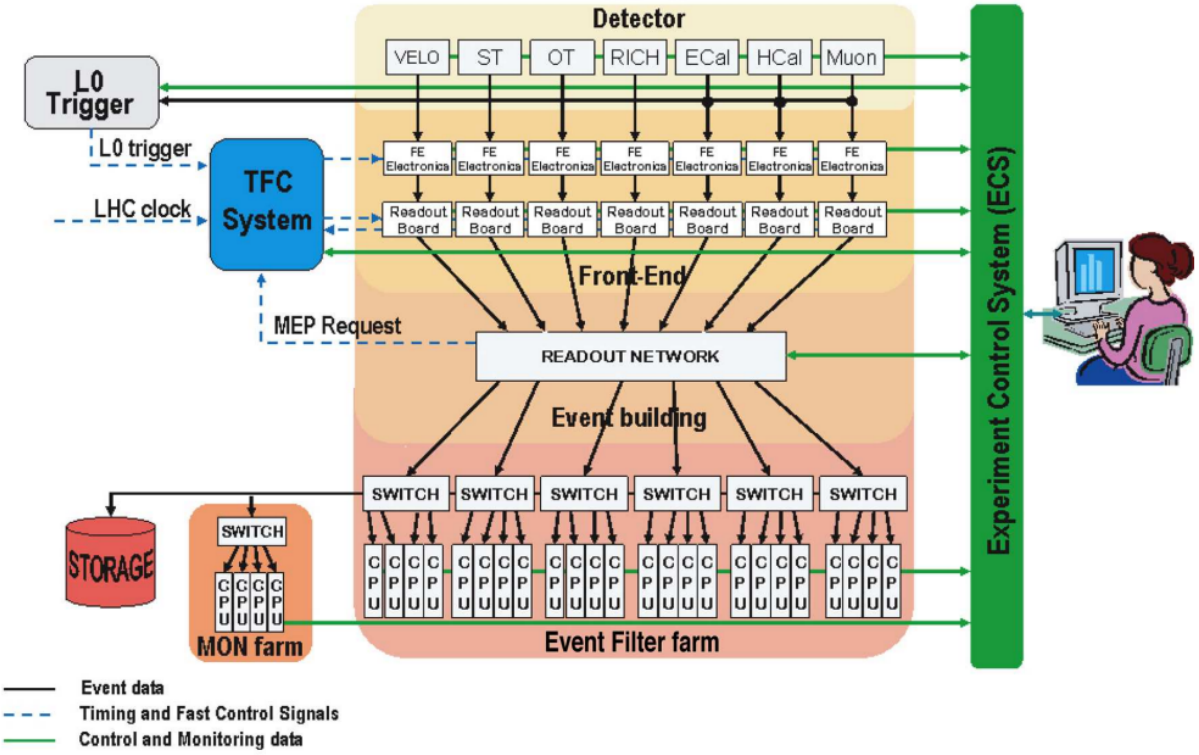

Figure 3.13: General architecture of the LHCb Online system with its three major components: TFC, DAQ and ECS [52].

for simulation but also to process information taken by the detector, are used:

1. Gauss [81], which is a collection of libraries for event generation and detector simulation based on Gaudi and with specialised algorithms and tools for generators, such as Pythia, Herwig [82], HepMC [83] and EvtGen [84] for event generation, PHOTOS [85] for final-state radiation simulation, or Geant4 [86] for detector simulation.

2. Boole,[6] used to digitalize the data from Gauss to model the detector response.

3. Moore,[7] used to run the HLT in the LHCb online system, processing a given set of input data or taken from the output of Boole (or processing real data from the DAQ system).

4. Brunel,[8] which takes care of the reconstruction from the output of Boole (or real data from the DAQ system as well).

[6]The Boole project (a).
[7]The Moore project (a).
[8]The Brunel project (a).

5. Finally, the physics analysis is carried out by the DaVinci[9] application. Certain DaVinci-dependant packages, such as Bender[10] or Erasmus[11], are also used.

Some differences between simulated and real data remain, such as the average event multiplicity and the particle identification efficiency, which however can be easily kept under control in physics analyses. Table 3.2 summarizes the software versions considered to generate the simulated samples described in this thesis.

Table 3.2: Software versions used for simulation in Chapter 4.1.2 and Chapter 6.1.2.

		`Sim08a`	`Sim08b`	`Sim08c`	`Sim08h`
Gauss		v45r3	v45r4	v45r5	v45r10p1
	Geant4	v95r2p5	v95r2p5	v95r2p5	v95r2p7
	HepMC	2.06.05	2.06.05	2.06.05	2.06.05
	Pythia	8.175	8.175	8.175	8.175
	LHCb	v35r4	v35r4	v35r4	v35r4
	Gaudi	v23r6	v23r6	v23r6	v23r6
Boole		v26r3	v26r3	v26r3	v26r3
Moore	`0x40760037`	v12r8g3	v12r8g3	v12r8g3	v12r8g3
	`0x409f0045`	v14r8p1	v14r8p1	v14r8p1	v14r8p1
Brunel		v43r2p7	v43r2p7	v43r2p7	v43r2p11
DaVinci	`Stripping20r1`	v32r2p3	v32r2p3	v32r2p3	v32r2p3
	`Stripping20`	v32r2p1	v32r2p1	v32r2p1	v32r2p1

3.2.6 Performance

Data taken by LHCb from collisions at the LHC, at a rate of several million events per second, need to be selected, prepared and distributed in the most possible efficient way for its subsequent analysis. This process is performed using several `C++` tools and algorithms, grouped in different projects (see Chapter 3.2.5). The different steps leading the raw detected data to the physics results can be summarised as follows:

1. The amount of raw data generated by LHC collisions is too high to be directly stored. In this way, it becomes necessary an initial and fast selection which allows to discard most of the events that are not interesting for the physics analysis, this is, the LHCb trigger (see Chapter 3.2.3). The trigger is considered an online process, in the sense that it takes place almost at the same time that the data is being recorded by the detector, and reduces the rate from several millions of events per second to just a few thousand.

[9]The DaVinci project (a).
[10]The Bender project (a).
[11]The Erasmus project (a).

2. Data selected by the trigger, pure electronic signals recorded by the different subdetectors, are transformed by different mathematical algorithms in an ensemble of tracks and vertices. Tracks correspond to the charged particles trajectories produced in the collisions (or from decays of other particles) and which go through the detector, while vertices correspond to the point where the collisions (Primary Vertices, PVs) or the decay of a particle in two or more daughter tracks (Secondary Vertices, SVs) took place. In practice, vertices are built from the crossing point of two or more tracks. The reconstruction of tracks and vertices is mainly done by the tracking and vertexing system (see Chapter 3.2.1). The information from the particle identification system (see Chapter 3.2.2) is then added to identify the nature of the tracks, distinguishing, for instance, muons from other particles. This whole process is called reconstruction. Figure 3.14 displays a LHCb $B_s^0 \to J/\psi\phi$ reconstructed event using the Panoramix[12] application.

3. Once all the triggered events have been reconstructed, it becomes mandatory to separate them according to their physics content. This is done by selecting the different decays using their particular features. For instance, $B_s^0 \to \mu^+\mu^-$ or $A_1^0 \to \mu^+\mu^-$ decays, with the same final state, have different mass and decay time of the parent particle. With these selections, the splitting of the data is performed, with a procedure called "stripping" in the framework of LHCb.[13] Thus, each one of these selections is embedded in a "stripping line". These selections, performed with the data already on tape, are called "offline".

4. The triggered, reconstructed and stripped dataset has to be then distributed to a series of computing centers spread worldwide. A copy of the raw data from detectors is also saved, with the idea of allowing a later re-reconstruction and stripping once the relevant algorithms have been improved. The process of distributing the data has a double intention. On the one hand, it ensures that the data cannot be lost, regardless any possible technical problem appearing. On the other hand, it allows physicists an easy access to a distributed computing system of huge power. This distributed system is called Grid [87], used via the DIRAC framework [88].

Details about the performance of tracking and vertexing, particle identification and trigger systems are given in Chapter 3.2.6.1, Chapter 3.2.6.2 and Chapter 3.2.6.3, respectively.

3.2.6.1 Tracking and vertexing

As already stated, one of the key points for the reconstruction of events at LHCb is the determination of the trajectories of all charged particles (tracks) and the position where they were generated (vertices) both if this was a collision (PVs) or the decay point of some other particle (SVs). During the event reconstruction stage, the following types of tracks, as shown in Figure 3.15, are considered [89]:

[12] The Panoramix project (a).
[13] The Stripping project (a).

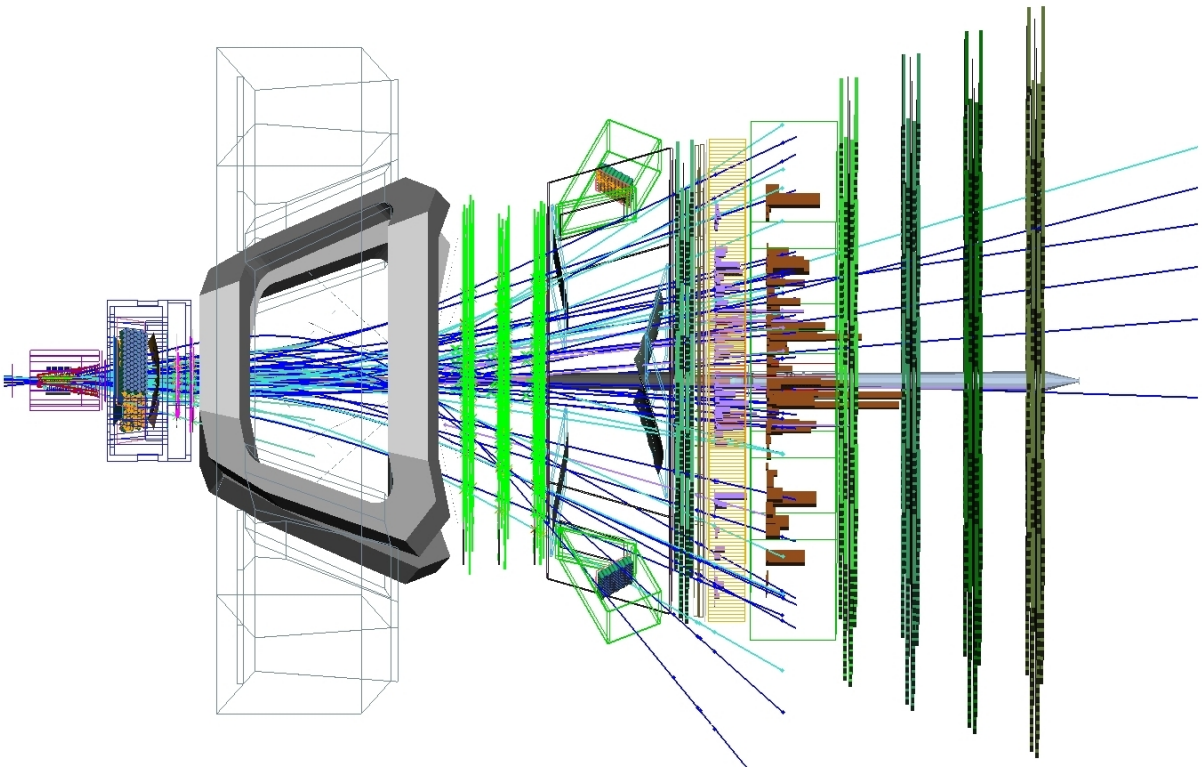

Figure 3.14: Event reconstruction of a LHCb simulated $B_s^0 \to J/\psi\phi$ event.

- Long tracks: tracks traversing the full tracking system. They have hits in both the VELO and the T-stations of the OT, and optionally in the TT. As they traverse the full magnetic field they have the most precise momentum estimate and therefore are the most important set of tracks for physics analyses.

- Upstream track: tracks passing only through the VELO and TT stations. In general their momentum is too low to traverse the magnet and reach the T-stations. However, they pass through the RICH1 detector and may generate Cherenkov photons if they have $p > 1\,\mathrm{GeV}/c^2$. They are therefore also used to understand backgrounds in the particle identification algorithm of the RICH.

- Downstream tracks: tracks passing only through the TT and T-stations. They are important for the reconstruction of long lived particles, such as K_s^0 and Λ, that decay outside the VELO acceptance.

- VELO tracks: tracks passing only through the VELO and are typically large-angle or backward tracks, which are useful for the primary vertex reconstruction.

- T tracks: tracks passing only through the T-stations. They are typically produced

in secondary interactions, but are still useful during the treatment of RICH2 data for particle identification.

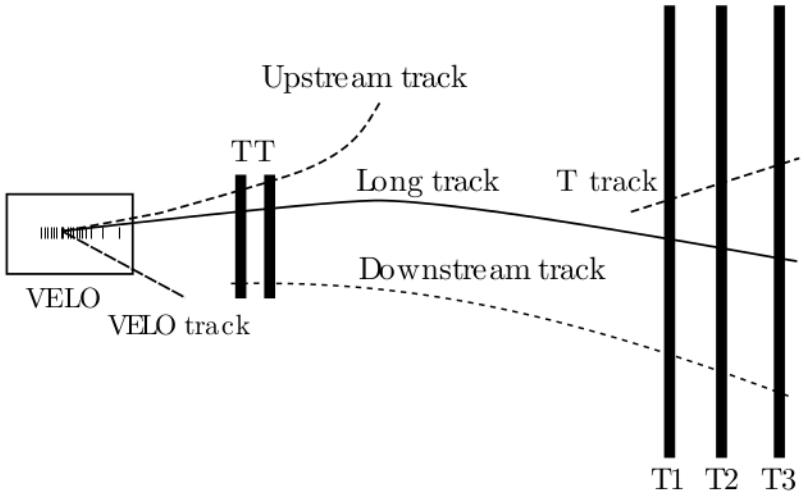

Figure 3.15: Various types of tracks considered for the event reconstruction [52].

The capability of assigning a track to the right vertex and of distinguishing secondary vertices is given by the resolution on the Impact Parameter (IP), or the distance of closest approach of a track to a vertex. The VELO detector provides very good IP resolution (see Figure 3.16) thanks to thin silicon strips placed as close as 8 mm from the beam axis. The LHCb tracking system gave very good performances as well: a relative momentum resolution below 0.5% at low momenta and 0.9% at 100 GeV/c, and as a consequence, a very good di-muon relative mass resolution of about 5 per mille all the way up to the masses of the Υ resonances (see Figure 3.17). Thus, the best performances in terms of momentum resolution for long tracks are achieved.

3.2.6.2 Particle identification

The particle identification is the last step of the LHCb event reconstruction. Once all the tracks have been built, the information from the particle identification system (RICH, calorimeter and muon systems) is added in order to establish hypotheses about the nature of the particles (pion, kaon, proton, muon or electron). Similarly, the energy deposited at the calorimeters may be related to photons, even if these particles cannot be associated to tracks since they are neutral (see Figure 3.18). As previously stated in Chapter 3.2.5, differences in particle identification efficiencies between simulated and real data samples may appear and therefore need to be corrected for: a software package developed by the LHCb global PID team, PIDCalib [91], is used by LHCb physicists for this task.

The LHCb PID information from the different subdetectors is linearly combined in a common likelihood to maximise the efficiency and minimise the mis-identification rate,

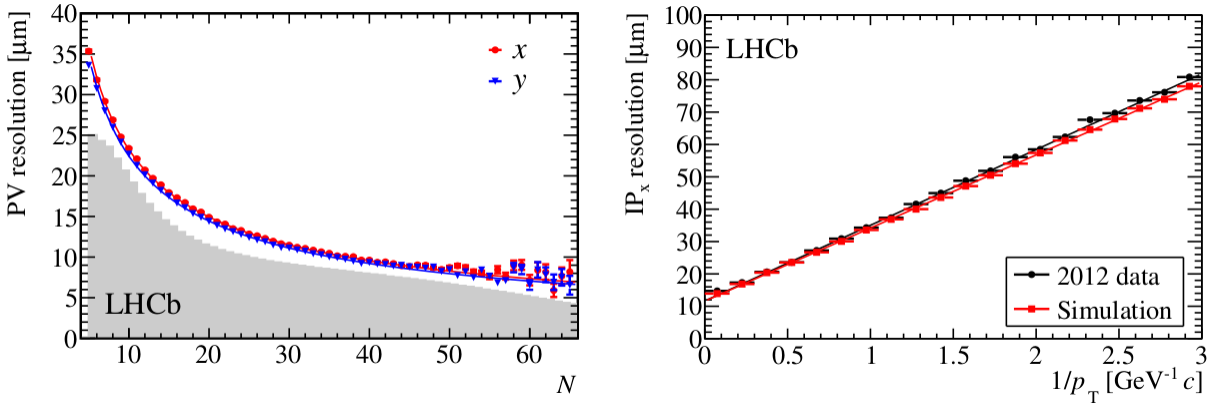

Figure 3.16: Performance of the LHCb VELO detector. Left: PV resolution as a function of the number of tracks composing the vertex. The x (red) and y (blue) resolutions are separately shown while the overlayed histogram (grey) shows the distribution of number of tracks per reconstructed primary vertex for events passing the high level trigger. Right: impact parameter in x resolution as a function of $1/p_T$. Both plots are made using LHCb data collected in 2012 [89, 90].

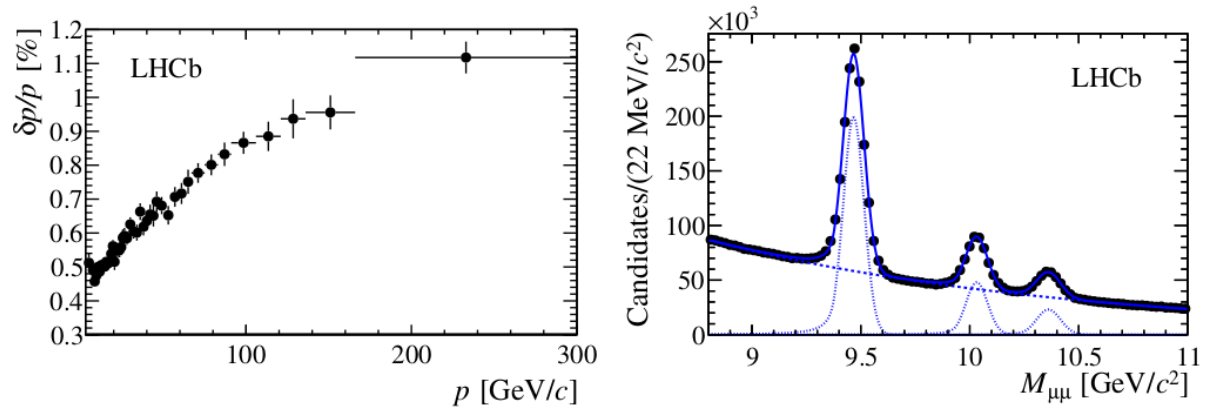

Figure 3.17: Left: relative momentum resolution versus momentum for long tracks from $J/\psi \to \mu^+\mu^-$ events. Right: mass distribution for the Υ resonances, showing the excellent relative mass resolution of LHCb of about 5 per mille [89].

ΔLLxy, being this variable the likelihood of the considered particle to be x, with respect to the hypothesis of being y instead (this "normalisation" hypothesis y is chosen by default to be the pion hypothesis). However, another approach which takes into account correlations between subdetectors and additional information is replacing (or used with) the previous likelihood: the output of a MultiLayer Perceptron Neural Network (MLPNN) named ProbNNx, which is simply the probability of the studied particle to be x. However, the identification of each particle is typically dominated by one of the subdetectors. The PID

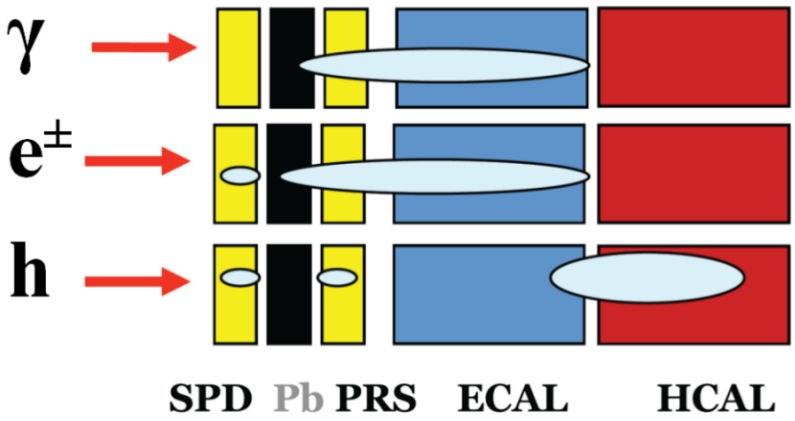

Figure 3.18: Energy deposition on the different elements of the calorimeter system, depending on the nature of the considered particle, where h refers to hadrons.

algorithms for calorimeter, RICH and muon systems, together with their performances, are presented next.

The calorimeter system (or simply CALO) PID uses the energy deposited in the different regions (see Figure 3.18) of the LHCb calorimeter to identify the particles having gone through its different parts. As muons are Minimum Ionizing Particles (MIPs), they are capable of going through the detector losing a characteristic energy on it which can also help on their identification. Similarly to the RICH case, but using the energy deposited in the different calorimeter elements, these algorithms use the information to obtain PID variables for the different particle hypotheses. Efficiency and mis-identification rate for electrons in 2011 data as a function of track momentum are shown in Figure 3.19.

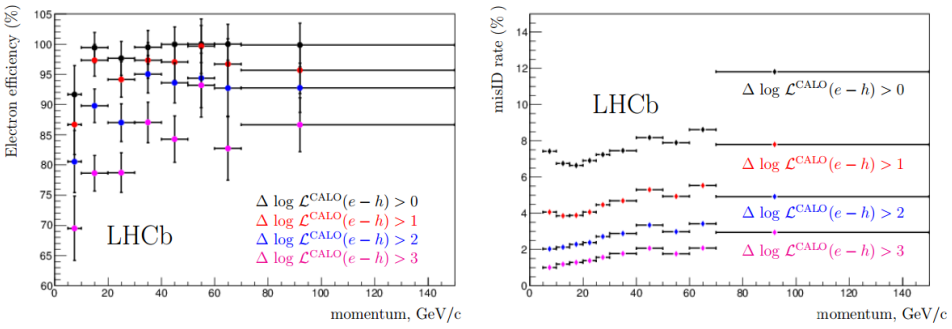

Figure 3.19: LHCb CALO electron identification performances on 2011 data. Left: electron efficiency as a function of the track momentum. Right: electron mis-identification rate as a function of track momentum [89].

The RICH PID is based on the difference in the expected Cherenkov angle [92] (angle of

the radiated photons) between protons, kaons and pions. The low mass difference between pions and muons makes the Cherenkov angle very similar in both of these particles, so RICH PID is not efficient separating them (see Figure 3.20). Using the RICH information, PID variables can be built for tracks in order to establish the probabilities of different particle hypotheses [52]. Figure 3.21 shows the kaon efficiency (kaons identified as kaons) and pion mis-identification (pions mis-identified as kaons) fraction on 2012 data, as a function of momentum and for one of the LHCb dipole magnet polarities. Proton efficiency and pion mis-identification fraction as a function of momentum for the complementary LHCb magnet polarity and for 2012 data are also shown.

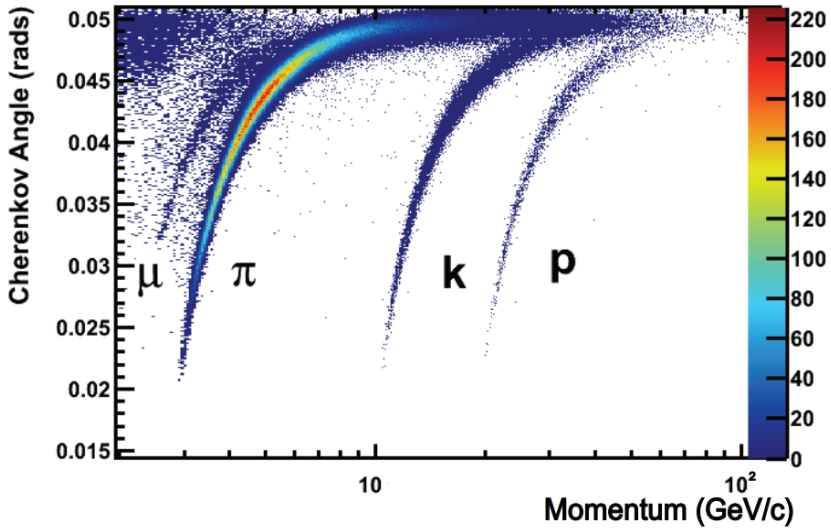

Figure 3.20: Reconstructed Cherenkov angle as a function of track momentum in the C_4F_{10} radiator [93].

Muon identification uses the fact that muons are the only particles (except for punch-through hadrons, which are rather unlikely) able to go through the calorimeter and hit the muon system stations. For any reconstructed track, a field of interest at the muon stations is built and muon hits are searched for. The identity and location of these hits allows the calculation of a muon PID variable that is later used to discriminate between muons and other particles [94]. Figure 3.22 shows the muon PID efficiency and mis-identification probabilities for protons, pions and kaons as a function of the particle momentum [52]. A di-muon invariant mass reconstruction after imposing trigger requirements, showing the excellent performance of LHCb muon and trigger systems, is presented in next Chapter 3.2.6.3.

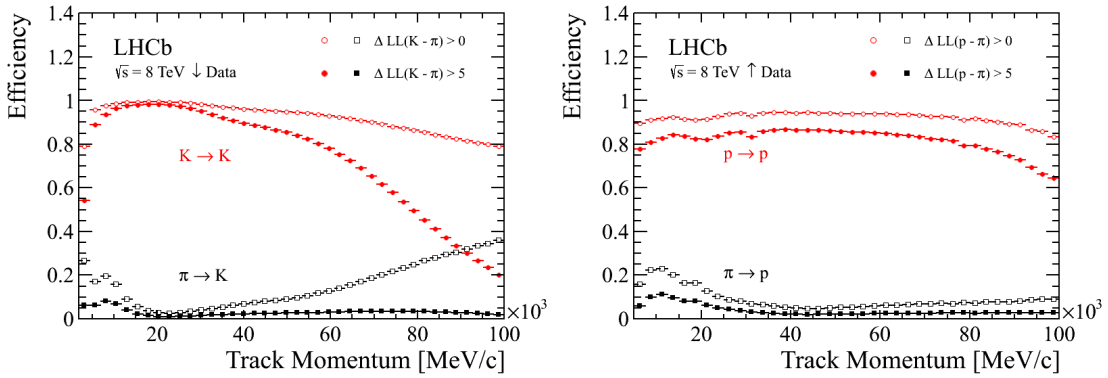

Figure 3.21: LHCb RICH system performance. Left: kaon efficiency and pion mis-identification fraction on 2012 data, as a function of track momentum and for LHCb magnet down polarity. Right: proton efficiency and pion mis-identification fraction on 2012 data, as a function of track momentum and for LHCb magnet up polarity.

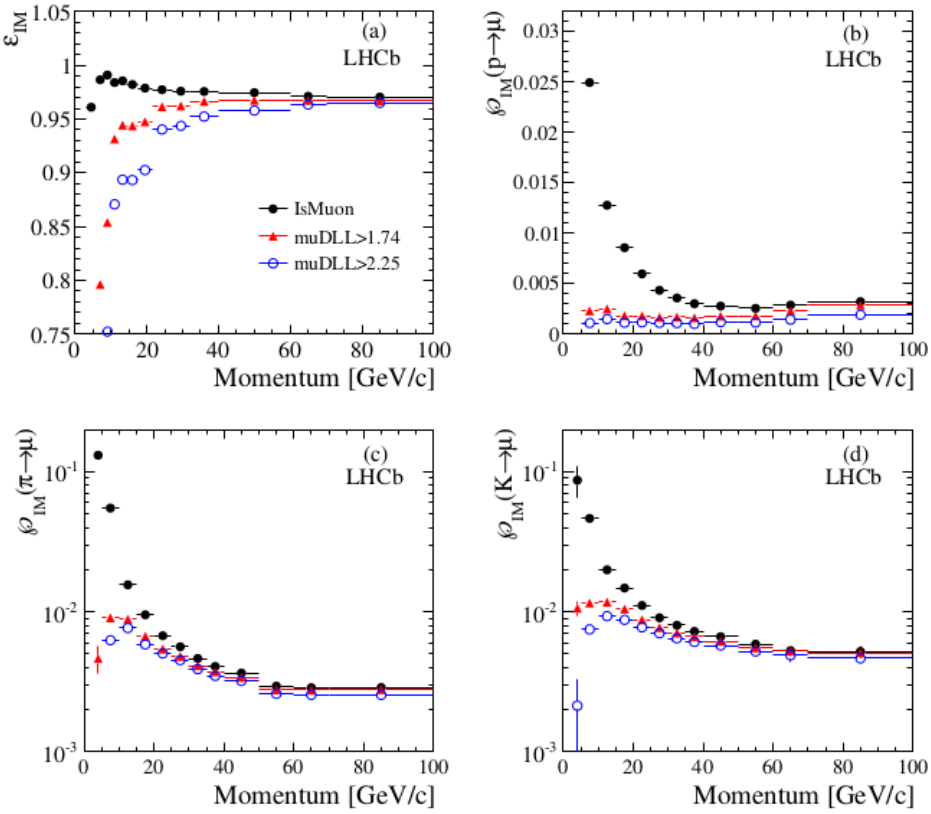

Figure 3.22: Muon efficiency (a) and misidentification probabilities for protons (b), pions (c) and kaons (d) as a function of particle momentum [94].

3.2.6.3 Trigger performance

For the analyses described in this thesis, of $B_s^0 \to J/\psi \overline{K}^{*0}$ (see Chapter 4) and $A_1^0 \to \mu^+\mu^-$ (see Chapter 6) decay modes, the most relevant LHCb trigger lines are those related to the reconstruction of single muons and di-muon resonances. A reconstruction of the di-muon invariant mass of LHCb data taken during Run I is presented in Figure 3.23, showing the excellent performance of the LHCb combined muon and trigger systems in the context of muon searches.

In the LHCb trigger context, an event is classified as TOS (Trigger On Signal) if the trigger objects that are associated with the signal are sufficient to trigger the event. TOS efficiencies for L0, HLT1 and HLT2 muon trigger lines are presented in Figure 3.24. The integrated efficiency for both L0 single muon and di-muon triggers is evaluated to be 89%, while for HLT1, single muon and di-muon trigger efficiencies are 90% and 69%, respectively. The total output rate of all single muon and di-muon trigger lines is about 1 kHz [77, 95]. Trigger efficiencies obtained for the analysis of $B_s^0 \to J/\psi \overline{K}^{*0}$ decays are calculated in Appendix D.2.

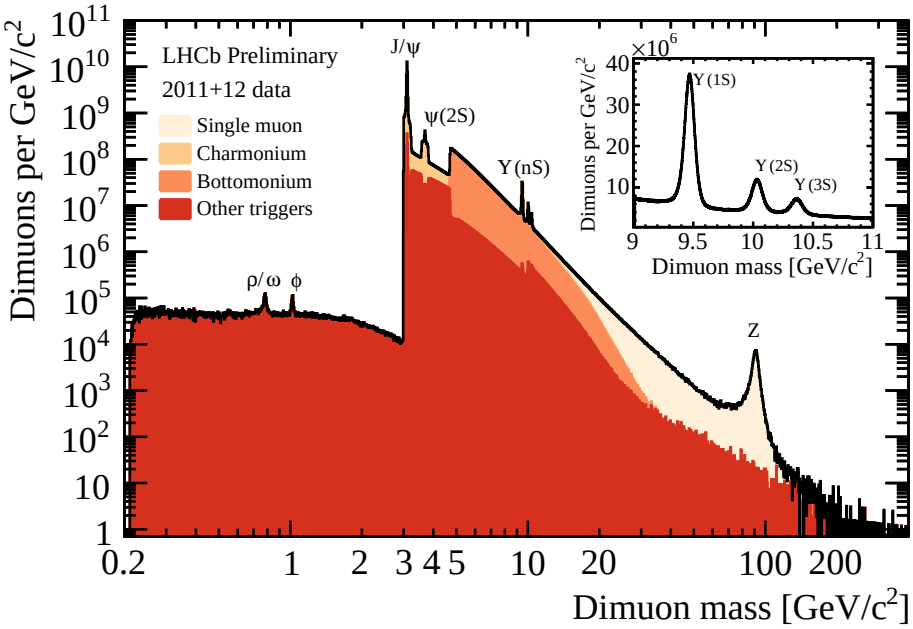

Figure 3.23: Di-muon mass distribution divided by trigger groups of LHCb Run I data. An inset plot with a zoom on the bottomonium region is shown on the top right corner [96].

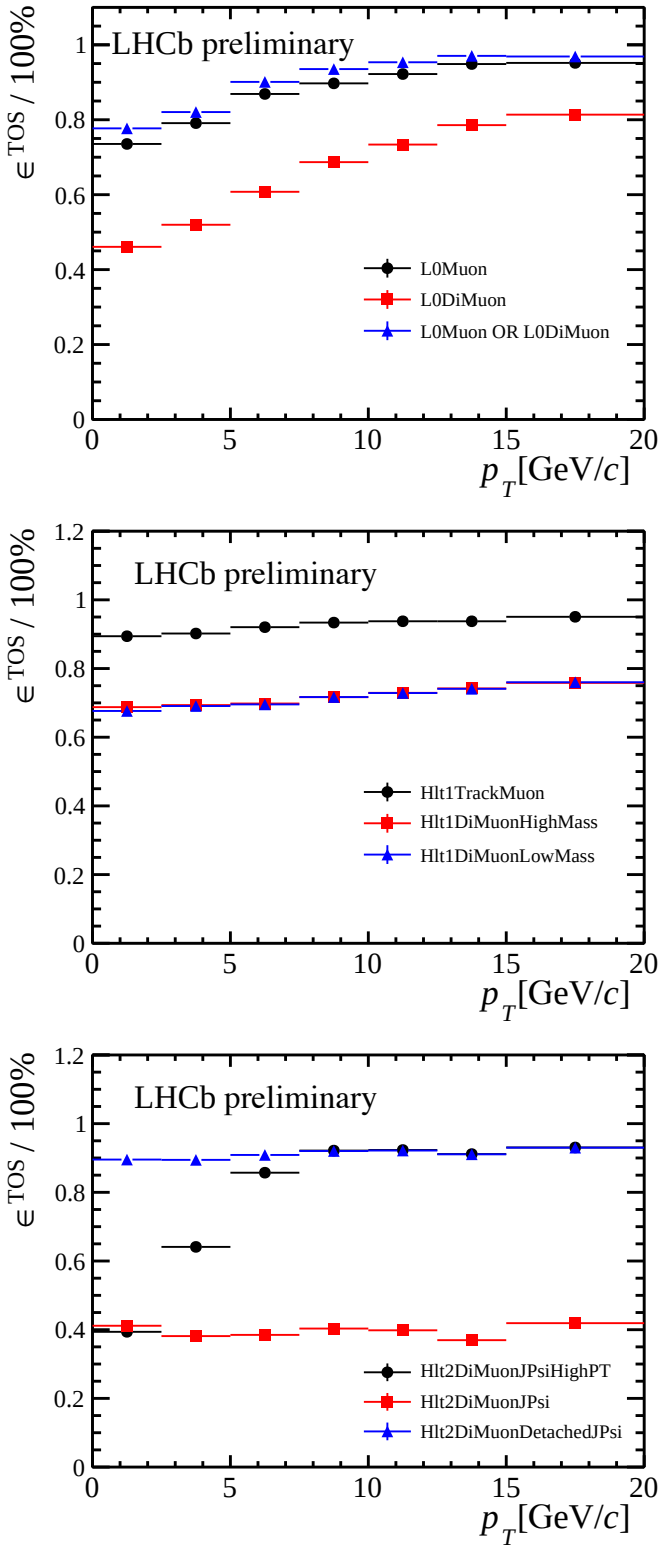

Figure 3.24: TOS efficiencies of L0 (top), HLT1 (middle) and HLT2 (bottom) muon trigger lines, calculated using $B^+ \to J/\psi K^+$ candidates, and as a function of the B^+ p_T [77].

3.2.7 Run I experimental conditions

The evolution of the LHCb operating conditions during LHC Run I is shown in Figure 3.25. Starting with luminosities of approximately $10^{28}\text{cm}^{-2}\text{s}^{-1}$ and almost no pile-up, the luminosity reached $10^{32}\text{cm}^{-2}\text{s}^{-1}$ [89], leading to world-best measurements published by the LHCb collaboration [97].

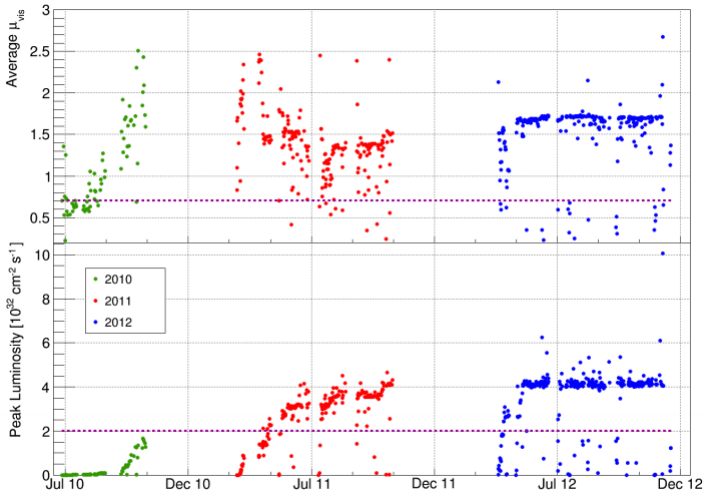

Figure 3.25: Average number of visible interactions per bunch crossing, "pile-up" (top) and instantaneous luminosity (bottom) at the LHCb interaction point during the Run I period. The dotted lines show the design values [89].

Despite the fact that the data taken during that year is not used for the analyses described in this thesis, it is worth to mention that LHCb recorded 38 pb^{-1} of data during 2010, under a constantly changing set of run conditions, being this small dataset the very first part of the data taken during the Run I period. During 2011, with a target luminosity of $\mathfrak{L} = 3.5 \times 10^{32}$ $\text{cm}^{-2}\text{s}^{-1}$ and a measured $b\bar{b}$ cross section of $\sigma(pp \to b\bar{b}X) = (284 \pm 20 \pm 49)$ μb at $\sqrt{s} = 7$ TeV [98], a total amount of the order of 10^{12} $b\bar{b}$ pairs was produced in 10^7 s, approximately corresponding to the canonical one year of data taking. That year, a luminosity levelling procedure was introduced at the LHCb interaction point. By adjusting the transverse overlap of the beams at LHCb, the instantaneous luminosity could be kept stable to within about 5% during a fill, as illustrated in Figure 3.26.

In 2012, the LHC beam energy was increased to 4 TeV. LHCb took data at a luminosity of 4×10^{32} $\text{cm}^{-2}\text{s}^{-1}$, twice the LHCb design luminosity. The LHC delivered stable beams for about 30% of the operational year. An effort was made in 2012 to use more efficiently the processing power available in the Event Filter Farm (EFF, see Chapter 3.2.4), which otherwise would have been idle during 70% of the time. The mechanism put in operation defers a fraction of the HLT processing to the inter-fill time, typically several hours, between the LHC collision periods. In this approach about 20% of the L0 accepted events during data-taking are temporarily saved on the local disks of the EFF nodes and

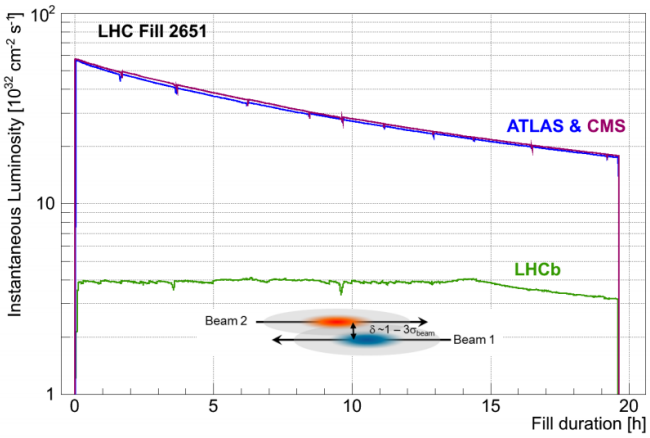

Figure 3.26: Development of the instantaneous luminosity for ATLAS, CMS and LHCb during LHC fill 2651. After ramping to the desired value of 4×10^{32} cm^{-2}s^{-1} for LHCb, the luminosity is kept stable in a range of 5% for about 15 hours by adjusting the transversal beam overlap [89].

are processed only after the end of stable beams. This deferred triggering method allowed LHCb to increase the data sample available for physics analysis.

The integrated luminosity recorded by LHCb was 1.11 fb^{-1} in 2011 and 2.08 fb^{-1} in 2012. The evolution of the integrated luminosity during Run I is shown in Figure 3.27 [89].

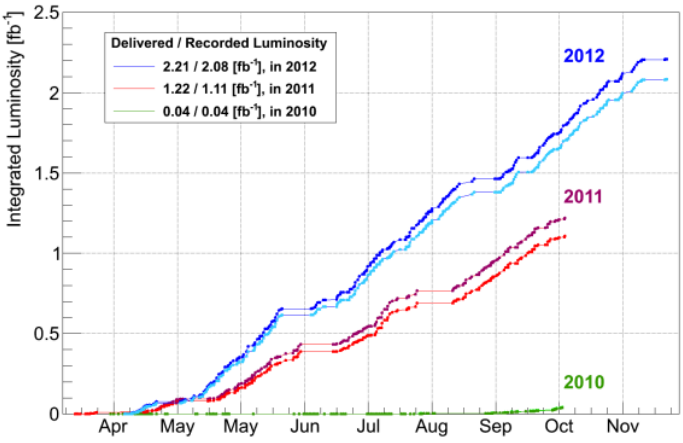

Figure 3.27: Integrated luminosity in LHCb during the LHC Run I period. The figure shows the curves for the delivered (dark coloured lines) and recorded (light coloured lines) integrated luminosities [89].

3.3 The LHCb Upgrade

The LHCb detector has already shown an excellent performance during Run I (see Chapter 3.2.7). However, the precision of many LHCb measurements is still limited by their statistical uncertainties: the LHCb Upgrade, with a prospected ten-years data acquisition of 50 fb^{-1} with a 40 MHz readout, is expected to bring a sensitivity improvement of about one order of magnitude for several key observables with respect to current measurements [97, 99, 100]. However, after the next Long Shutdown (LS), it is expected that LHCb will operate with a luminosity of $2 \times 10^{33}\text{cm}^{-2}\text{s}^{-1}$. In consequence, subdetectors must be upgraded as well [100].

3.3.1 Physical motivations

Predictions for most of the LHCb key measurements after the upgrade are presented in tables 3 and 4 of ref. [99]. The most relevant key measurements for this thesis are the branching fraction of $B_s^0 \to \mu^+\mu^-$ decays and the CP violation studies of the $B_s^0 \to J/\psi\phi$ analysis.

The decay mode $B_s^0 \to \mu^+\mu^-$ is highly suppressed in the SM: due to the absence of direct flavour neutral changing currents, these decays can only occur via higher order topologies. Possible NP particles may contribute in these topologies and thus enhance the branching fractions well beyond the SM predictions [28]. Also, in the Next-to-Minimal-Supersymmetric-SM [32], the main contribution of these decays are predicted to occur dominantly via the $A_1^0 \to \mu^+\mu^-$ decay mode (for more details, see Chapter 2.4), which is studied in Chapter 6.

The measurement of the CP violating ϕ_s phase in the golden mode $B_s^0 \to J/\psi\phi$ is also a relevant decay for this work as well. Pollution due to second order (penguin) topologies to this phase are studied in this work in Chapter 4. A significant improvement in sensitivity for the measurement of ϕ_s, of around an 80% of the statistical uncertainty w.r.t. Run I results [24], is expected after the upgrade of the LHCb detector [99].

3.3.2 The LHCb subsystems upgrade

Due to the challenging LHC Upgrade conditions, each LHCb subdetector must be redesigned considering the required precision, material budget, radiation hardness and occupancy rate. Tracking (see Chapter 3.3.2.1) and vertexing (see Chapter 3.3.3), particle identification (see Chapter 3.3.2.2), trigger (see Chapter 3.3.2.3) and online systems will be upgraded.

3.3.2.1 Tracking systems upgrade

The silicon sensors used in the construction of the ST are not radiation hard enough, the expected occupancy rate saturates the detectors and the readout electronics is not compatible with the 40 MHz readout. Therefore, the TT stations will be replaced by a

new generation of micro-strip silicon detectors, named Upstream Tracker (UT), with the same geometry as current TT but with higher granularity and eliminating gaps on the detection area. The OT and IT stations will be fully replaced by a Scintillating Fiber (SciFi) Tracker (SFT) with silicon photo-detectors, keeping the same current geometry and with the advantages of requiring less stringent temperature requirements, sufficient radiation hardness, and high granularity [101].

3.3.2.2 Particle identification systems upgrade

The overall structure of the RICH detectors will remain unchanged. The RICH1 detector, however, demands significant modifications due to its performance at high luminosities: the removal of the aerogel and a re-adjustment of the optical system will be performed. Photon detectors must also be replaced in both RICH detectors with a new generation of PMTs, the Multianode PMTs (MaPMTs), capable of operating at 40 MHz rate. A new subdetector, still in an early research and development stage, is being considered in order to recuperate the low momentum particle identification performance, the Time Of internally Reflected CHerenkov light (TORCH) detector. The key elements of the upgrade of the calorimeters are the re-design of the readout electronics, to be able to operate at a 40 MHz rate, the reduced gains in PMTs, to ensure longer lifetimes at high luminosity, and the removal of the SPD/PS systems, since their purpose is basically linked to the L0 trigger, which will be also removed (see Chapter 3.3.2.3). The ECAL and HCAL will not go through detection technology modifications. Finally, the main modification on the muon system for the upgrade is the removal of the M1 station, since with higher luminosities it would be extremely difficult to associate hits at M1 with muon tracks segments on the other stations, and its current function is mostly used in the L0 trigger, which as stated before, will be removed as well [102].

3.3.2.3 Trigger systems upgrade

As already mentioned, one of the most important features of the LHCb Upgrade is the removal of the L0 trigger level [100, 103]. The upgraded trigger goes to an all-software structure, providing flexibility to the selection strategies, in particular allowing more efficient triggering on low momentum tracks. Limits on processing power and bandwidth are the main challenges to overcome.

3.3.3 The LHCb VELO Upgrade

The upgraded VELO must maintain or improve its physics performance while delivering readout at 40 MHz in the operating conditions of the upgrade. This can only be achieved by a complete replacement of the silicon sensors and electronics. Following an externally refereed review, the LHCb Collaboration has chosen to install a subdetector based on hybrid pixel sensors. A new radiation hard ASIC, dubbed “VeloPix”, capable of coping with the data rates, is under development.

The module cooling design must be upgraded in order to protect the tip of the silicon from thermal runaway effects after significant irradiation, and to cope with the high speed pixel ASIC power dissipation. For this reason the upgrade cooling is integrated within the module, in contrast to the currently installed detector. The cooling is provided by evaporative CO_2 circulating within miniature channels etched into thin silicon substrates which form the backbone of the modules. The upgraded VELO reuses large parts of the current mechanical infrastructure, in particular the vacuum tank, and elements of the very successful mixed phase CO_2 cooling system.

The conceptual layout of the detector within the LHCb coordinate system is shown in Figure 3.28. It is very similar to the current VELO layout, however the z positions of the modules have been changed in order to reach similar acceptance given the smaller module size and smaller distance from the beam line to the first measured point. The positions of the modules in the closed (LHC stable beam operation) and open position are also shown. A more detailed module concept is shown in Figure 3.29. As for the current VELO it is important to optimise the material throughout the module, including the sensor, hybrid and base regions, since all elements fall at least partially within the detector acceptance, as illustrated in Figure 3.30 [104].

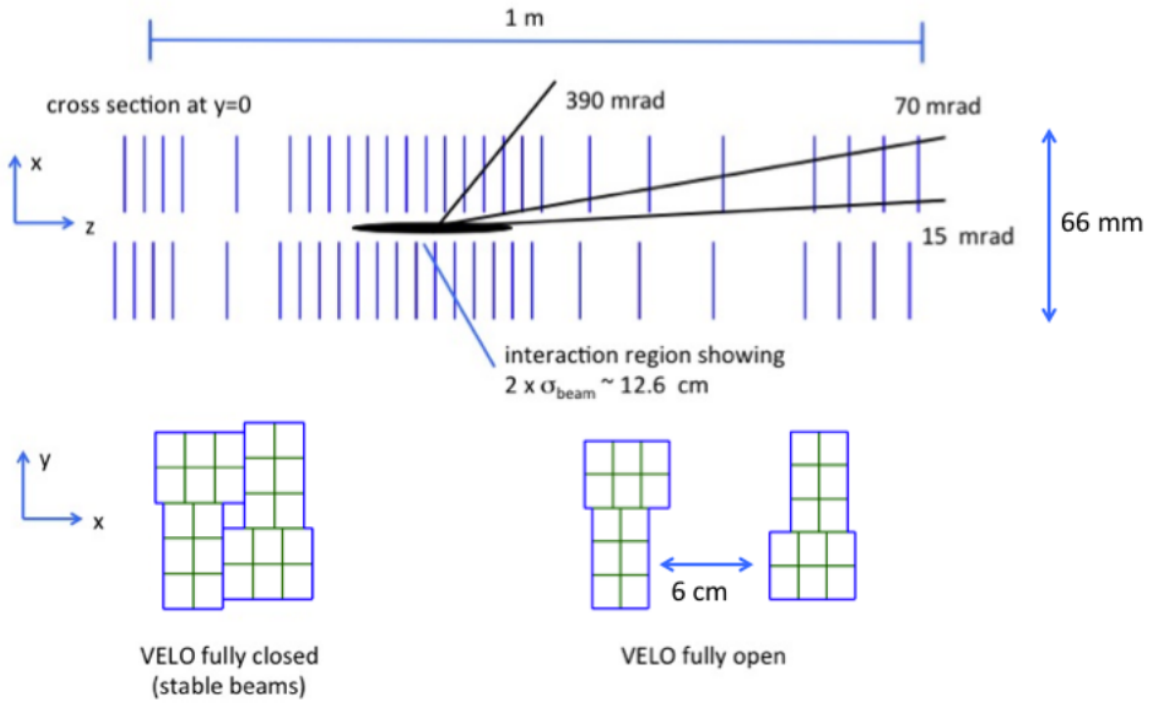

Figure 3.28: Schematic layout of the upgraded VELO [104].

One of the contributions to the research and development process which helped the collaboration to decide to install a subdetector based on hybrid pixel sensors, as stated at the beginning of this section, was the characterisation of Medipix3-based [105] silicon de-

tectors[14] using SPS test beams [106]. Since the corresponding publication is not authored by the LHCb Collaboration but by the LHCb VELO Upgrade team, the full LHCb public note is embedded, without any modification or typographic adaptation, in the following pages.

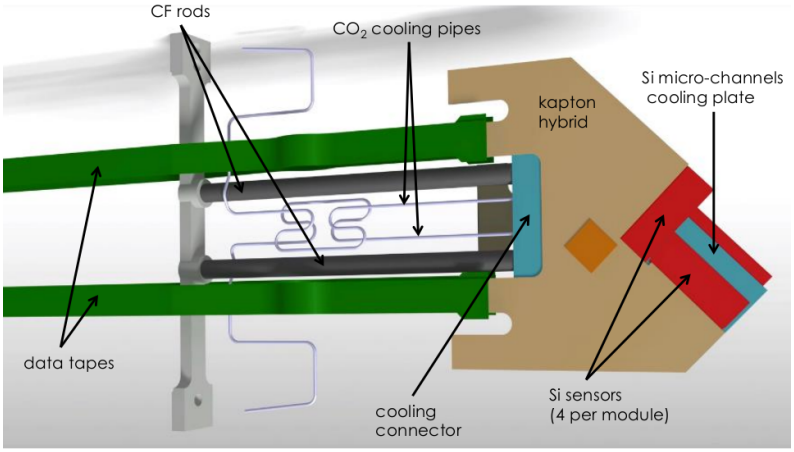

Figure 3.29: Detailed concept of a VELO Upgrade module [107].

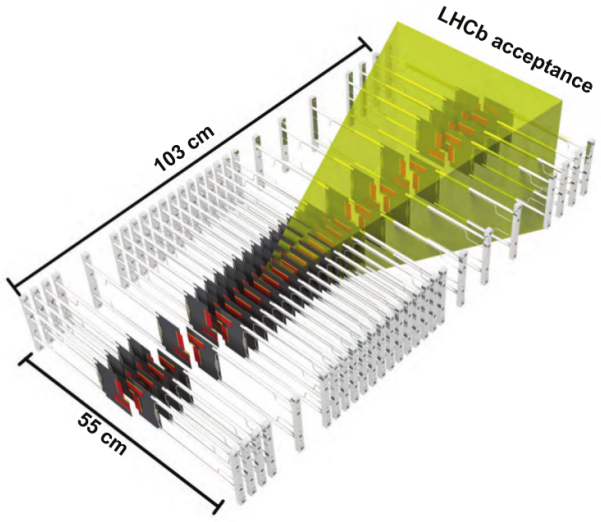

Figure 3.30: VELO Upgrade module layout, with the LHCb acceptance shaded [104].

[14]Henceforth simply referred to as "Medipix3 silicon detectors".

EUROPEAN ORGANIZATION FOR NUCLEAR RESEARCH (CERN)

LHCb-PUB-2016-002
January 12, 2016

Characterisation of Medipix3 Silicon Detectors in a Charged-Particle Beam

K. Akiba[1], J. Alozy[2], R. Aoude[3], M. van Beuzekom[4], J. Buytaert[2], P. Collins[2], A. Dosil Suárez[5], R. Dumps[2], A. Gallas[5], C. Hombach[6], D. Hynds[7], M. John[8], A. Leflat[9], Y. Li[10], E. Pérez Trigo[5], R. Plackett[11], M. M. Reid[12], P. Rodríguez Pérez[6], H. Schindler[2†], P. Tsopelas[4], C. Vázquez Sierra[5‡], J. J. Velthuis[13], M. Wysokiński[14]

[1] *Universidade Federal do Rio de Janeiro, Rio de Janeiro, Brazil*
[2] *European Organization for Nuclear Research (CERN), Geneva, Switzerland*
[3] *Pontifícia Universidade Católica do Rio de Janeiro, Rio de Janeiro, Brazil*
[4] *Nikhef National Institute for Subatomic Physics, Amsterdam, The Netherlands*
[5] *Universidade de Santiago de Compostela, Santiago de Compostela, Spain*
[6] *School of Physics and Astronomy, University of Manchester, Manchester, United Kingdom*
[7] *School of Physics and Astronomy, University of Glasgow, Glasgow, United Kingdom*
[8] *Department of Physics, University of Oxford, Oxford, United Kingdom*
[9] *Institute of Nuclear Physics, Moscow State University (SINP MSU), Moscow, Russia*
[10] *Center for High Energy Physics, Tsinghua University, Beijing, China*
[11] *Diamond Light Source Ltd., Didcot, United Kingdom*
[12] *Department of Physics, University of Warwick, Coventry, United Kingdom*
[13] *H.H. Wills Physics Laboratory, University of Bristol, Bristol, United Kingdom*
[14] *AGH - University of Science and Technology, Faculty of Computer Science, Electronics and Telecommunications, Kraków, Poland*

Abstract

While designed primarily for X-ray imaging applications, the Medipix3 ASIC can also be used for charged-particle tracking. In this work, results from a beam test at the CERN SPS with irradiated and non-irradiated sensors are presented and shown to be in agreement with simulation, demonstrating the suitability of the Medipix3 ASIC as a tool for characterising pixel sensors.

Published in JINST

†Corresponding author.
‡Corresponding author.

1 Introduction

As part of the upgrade of the LHCb experiment, scheduled for the second long shutdown of the LHC in 2018/19, the present microstrip-based Vertex Locator (VELO) is foreseen to be replaced by a silicon hybrid pixel detector [1] with an ASIC dubbed "VeloPix" which will be derived from the Medipix family of ASICs. Like its predecessors Medipix2, Timepix, Medipix3, and Timepix3, the VeloPix chip will feature a matrix of 256×256 square pixels with a pitch of 55 µm. Prior to the arrival of the Timepix3 ASIC, Timepix and Medipix3 were the most suitable devices for the qualification of prototype sensors for the VELO upgrade. Until the end of lifetime of the upgraded experiment, the pixels closest to the beam line ($r = 5.1\,\mathrm{mm}$) accumulate a fluence of up to $8 \times 10^{15}\,1\,\mathrm{MeV\,n_{eq}\,cm^{-2}}$. Qualifying silicon sensors in terms of radiation hardness is therefore a key element of the VELO upgrade R&D programme.

Timepix silicon detectors have been characterised extensively in terms of charged-particle tracking performance [2]. Since the ASIC has per-pixel information on the collected charge in terms of a time-over-threshold (ToT) value, a direct measurement of the charge deposition spectrum is possible.

Medipix3 [3, 4] on the other hand is a pure counting chip which was designed primarily for photon imaging applications. In order to measure the deposited charge in the sensor one therefore has to resort to indirect methods (Section 3). Among the large-scale ASICs in the high-energy physics community, Medipix3 has been the first to be based on IBM 130 nm CMOS technology. Compared to the Timepix (which was fabricated in 250 nm technology), it is expected to be more radiation tolerant [5] and thus lends itself for testing irradiated sensors.

In this work, we report on measurements with irradiated and non-irradiated Medipix3 assemblies carried out in 2012 at the H8 beamline of the CERN North Area facility, using positively charged hadrons with a momentum of 180 GeV/c. These measurements are intended to provide a validation of the chip functionality and performance complementary to characterisation measurements using photon sources. In addition, they also represent a first step towards a comprehensive evaluation of the radiation hardness of silicon pixel sensors with the "Medipix footprint" of 55×55 µm^2 pixels.

2 Setup

The Timepix telescope, described in Ref. [6], was used for reconstructing the tracks of particles crossing the Medipix3 device under test (DUT). In order to minimise the pointing error, the DUT was placed in the centre of the telescope. For reading out the Medipix3 chip, the "Merlin" data acquisition system [7] developed at the Diamond Light Source facility was used. The synchronisation of Timepix and Medipix3 is straightforward, as both ASICs work in a "camera-style" frame-based readout mode. An external circuit implemented using NIM modules was used for sending shutter opening and closing signals to the telescope and the device under test. The coincident firing of two scintillators located upstream and downstream of the telescope was used for counting the number of beam

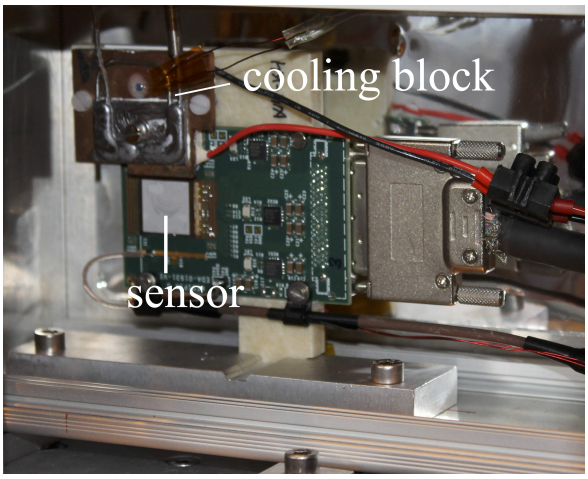

Figure 1: DUT mount and cooling setup. A Peltier cooler (not visible in the photograph) is clamped between the cooling block and the TPG sheet onto which the chip is glued.

particles traversing the telescope and the duration of a shutter was adjusted such that 50 scintillator triggers were accumulated in one frame. During one spill (9.6 s) typically about 500 frames were recorded.

The temperature of the irradiated samples was controlled using a combination of thermoelectric and CO_2 cooling, the latter being provided by a portable cooling plant [8]. As can be seen on the photograph in figure 1, the chip was glued onto a tape of Thermal Pyrolytic Graphite (TPG) the other end of which was attached to the cold side of a Peltier cooler. The hot side of the Peltier cooler was put in contact with an aluminium cooling block through which CO_2 was circulating. With the chip switched off, a temperature of approximately $-20°$ C was reached, rising to $-15°$ C with the chip in operation. The setup was placed in a light-tight aluminium case which was flushed with nitrogen. The non-irradiated assemblies were measured at room temperature.

In all measurements discussed below, the DUTs were n-on-p silicon sensors bump-bonded to Medipix3.1 ASICs. The ASICs were operated in single-pixel high-gain mode and only one threshold (DAC THL) was used. Before taking data, a threshold equalisation was performed using the front-end noise as reference. The equalisation procedure consists of optimising the DAC values of two global current sources (ThresholdN and DACpixel) and the threshold adjustment bits of each pixel, such that the THL value corresponding to the noise floor lies within a certain window for all pixels. For the non-irradiated assemblies a target window of $5 < \mathrm{THL} < 25$ was used.

Prior to the beam test, calibration measurements using testpulses were performed to determine the relation between THL DAC and injected charge. To verify the viability of the testpulse method, data were taken with a ^{241}Am source for the two non-irradiated assemblies discussed below, and – after applying the calibrations obtained from the testpulse scan – the signal peaks were found to match within 2% between the two assemblies. These measurements were however made with a different readout system [9] and equalisation

mask than used in the testbeam (at that time the testpulse functionality was not yet implemented in Merlin).

Where possible[1], calibration measurements using test pulses were later (after the beam test) made also using the Merlin system. These calibration curves are used in the following for a relative comparison of the signals measured with different sensors.

3 Measurements

For each track reconstructed in the telescope, the intercept with the DUT plane is calculated. In order to suppress fake tracks a requirement on the track quality is applied and the tracks are required to include hits on all telescope planes. If an unused cluster with a centre of gravity within a radius $r_w = 110$ µm around the track intercept is found, it is associated to the track and tagged as used. In case of multiple candidate clusters, the closest one is selected. The hit efficiency (or cluster finding efficiency) ε is then given by the fraction of tracks with an associated cluster on the DUT. The pointing resolution of the telescope (~ 1.5 µm in the present configuration) allows one to probe the hit efficiency as function of the track intercept within a pixel cell. In the analysis we divide the pixel cell in 9×9 bins and calculate separate efficiencies for each bin.

The most probable value (MPV) of the deposited charge can be estimated by scanning the hit efficiency as function of threshold. Assuming that the distribution of the collected charge can be described by a Landau distribution f_L convoluted with a Gaussian distribution f_G, the hit efficiency as a function of the threshold Q is given by

$$\varepsilon(Q) = \int_Q^\infty \mathrm{d}x f_L \otimes f_G(x). \tag{1}$$

By fitting the measured efficiency with Eq. (1), the MPV and width of the Landau distribution and the σ of the Gaussian can be determined (the mean of the Gaussian is fixed to zero). This method requires that the entire charge deposited by a track is collected by a single pixel. We therefore use the hit efficiency in the central bin of the 9×9 matrix for this measurement.

To determine the spatial resolution, the distributions of the residuals between the x, y coordinates of the track intercepts and the associated clusters are calculated. The standard deviation of the residual distribution is used as a resolution metric (the pointing error of the telescope represents only a small correction when subtracted in quadrature).

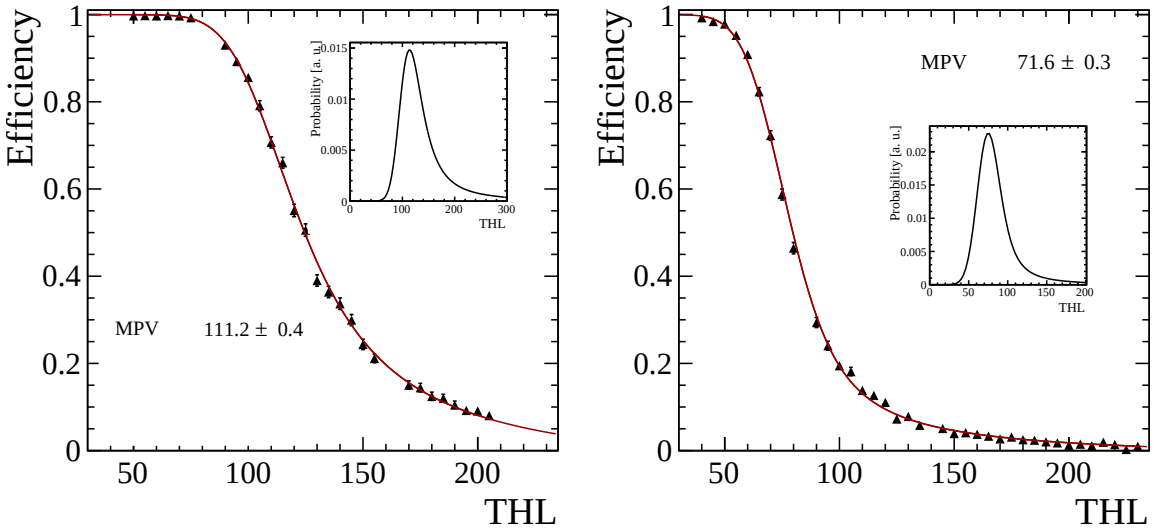

Figure 2: Hit efficiency (for tracks crossing the centre of a pixel cell) in non-irradiated Medipix3 assemblies with 100 µm thick n-on-p sensors as function of threshold, for (left) assembly W20_B6 and (right) assembly W20_J9. The insets show the distribution of the charge deposition in units of THL. The error bars represent the statistical uncertainty of the measurements. For several points the error bars are smaller than the symbols.

4 Results

4.1 Non-irradiated assemblies

The measurements before irradiation were carried out using n-on-p active-edge sensors with a nominal thickness of 100 µm manufactured by VTT[2]. The MPV of the charge deposition spectrum is thus expected to be around $7000 - 7500$ electrons.

Two assemblies, W20_B6 and W20_J9, were tested with beam. After the beam test, part of the backside metallisation was removed from the sensor on W20_B6, and by injecting laser pulses the depletion voltage V_{dep} was determined to be approximately -15 V. In the beam test, both sensors were operated at a bias voltage of -60 V, and were oriented perpendicularly to the beam. For each point in the threshold scan, a data set comprising typically $1 - 2 \times 10^5$ reconstructed telescope tracks was recorded.

From the hit efficiency in the centre of the pixel cell as function of threshold (figure 2), the most probable value of the charge deposition spectrum is determined to correspond to THL ~ 111.2 for assembly W20_B6 and THL ~ 71.6 for assembly W20_J9. The statistical errors of the fit values are given in figure 2. Uncertainties due to tracking cuts, alignment, non-linearity of the THL DAC give rise to a systematic error on the MPV of $\sim \pm 2.5\%$. The MPVs in terms of THL DAC values differ significantly between the two devices. This

[1]One of the assemblies (W20_B6) was accidentally damaged after the beam test.
[2]VTT Technical Research Centre of Finland, Espoo, Finland

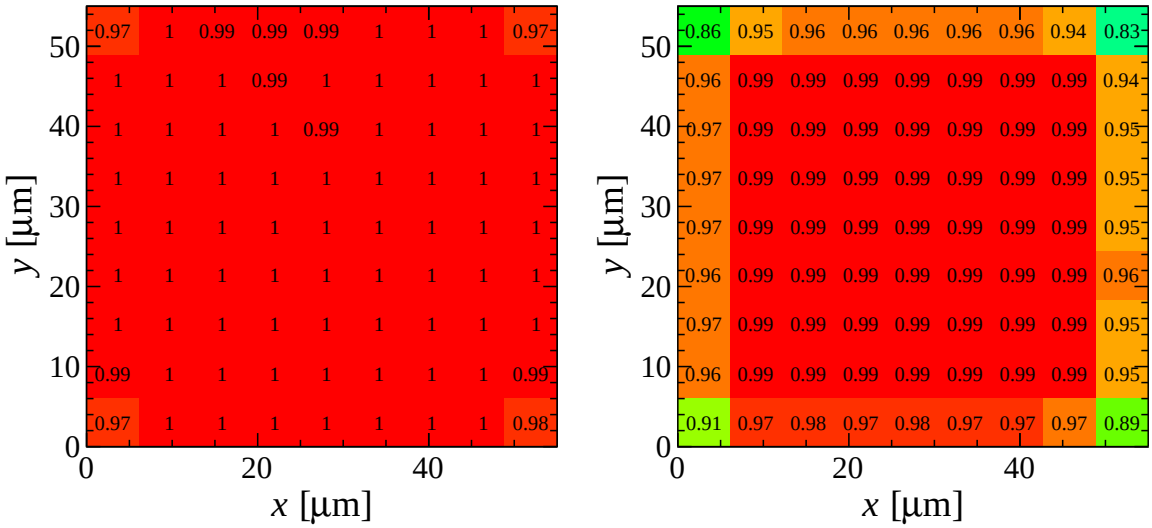

Figure 3: Hit efficiency in non-irradiated Medipix3 assemblies with 100 µm thick sensors as function of the track intercept within a pixel cell, for (left) assembly W20_B6 at THL/MPV$\sim$ 0.45 and (right) assembly W20_J9 at THL/MPV$\sim$ 0.56.

can be attributed to non-optimised settings of the DAC "Vcas" (for voltage cascode), which sets the reference voltage for some transistors in the pixel circuit and, if not tuned properly, can have an impact on the operating point of the circuit.

As discussed in section 2, testpulse calibration measurements using the Merlin readout system could only be made for assembly W20_J9. To facilitate the comparison between the devices, the results discussed below are therefore presented as function of the threshold-to-signal ratio, i. e. the applied THL DAC normalised to the respective MPV.

Figure 3 (left) shows the hit efficiency as function of the track intercept within a pixel cell for the lowest threshold-to-signal ratio (THL/MPV$\sim$ 0.45) covered by the threshold scan. At this threshold – which is high compared to a typical operational threshold of 1000 electrons – the detector can be seen to be fully efficient ($\varepsilon > 0.99$), except at the corners. With increasing threshold – as illustrated in figure 3 (right) – a drop in efficiency becomes noticeable at the borders of the pixel cell. This is a consequence of charge sharing due to diffusion, as can be seen from figure 4 which shows the average cluster size as function of the track intercept within the pixel cell.

Figure 5 (left) shows the average cluster size as function THL/MPV. At the lowest threshold, an average cluster size of 1.103 ± 0.001 is found, with single-pixel clusters constituting $\sim 91.3\%$ and two-pixel clusters $\sim 7.7\%$ of all associated clusters. The cluster size as function of threshold/signal follows the same shape for both sensors, exhibiting a minimum around THL/MPV$\sim$ 0.9 and a subsequent maximum around THL/MPV$\sim$ 1.6. With increasing threshold, an increasing fraction of the observed clusters is produced by primary particles which suffer collisions with large energy loss. These collisions give rise to energetic electrons which further ionise along their path and produce electron-hole pairs

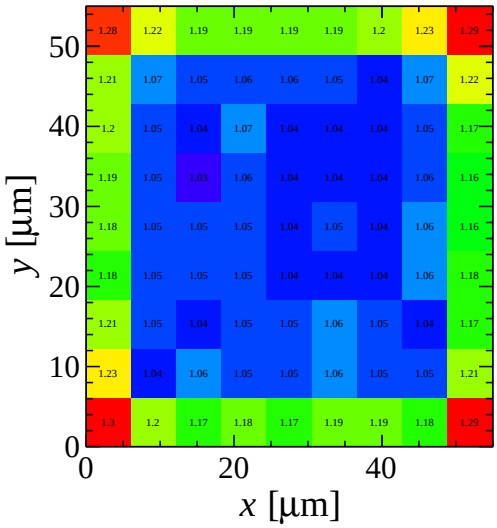

Figure 4: Average cluster size as function of the track intercept within a pixel cell for assembly W20_B6 (100 µm thick sensor) at THL/MPV$\sim$ 0.45. Multi-pixel clusters are found predominantly at the edges and corners of the pixel cell.

away from the trajectory of the primary particle.

The residual distributions (in the x direction) at low threshold for one-pixel and two-pixel clusters are shown in figure 6. Averaged over all cluster sizes, the standard deviation of the residual distribution is found to be $\sim$ 15.7 µm in both x and y. As expected from the dominance of one-pixel clusters, this value is close to the binary limit (55 µm/$\sqrt{12} \sim$ 15.9 µm). Figure 5 (right) shows the σ of the residual distribution in x as function of threshold/signal. The resolution can be seen to deteriorate significantly after the threshold crosses the MPV.

Figure 5 also includes results obtained with a Timepix ASIC bump-bonded to a 100 µm thick n-on-p sensor from the same batch. The Timepix assembly was measured in the same beam test campaign and was operated at a threshold of 1000 electrons and a bias voltage of -60 V. The data were taken in ToT mode, but the values shown in figure 5 were calculated with the ToT values set to one to mimic the Medipix3 behaviour. The results for the Timepix assembly are in agreement with the extrapolated results from the Medipix3 assemblies.

To understand better the observed shapes of resolution and cluster size as function of threshold, a simple simulation using the Garfield++ toolkit [10] was used. The primary ionisation process is calculated using the Heed program [11], which in addition to the energy loss by the traversing charged particle also simulates the ionisation cascade from high-energy ("delta") electrons produced in the interactions of the charged particle with the silicon medium as well as the spatial distribution of the resulting electron-hole pairs. Each electron is subsequently transported through the sensor, based on the drift velocity and diffusion coefficient as function of the electric field. A one-dimensional approximation

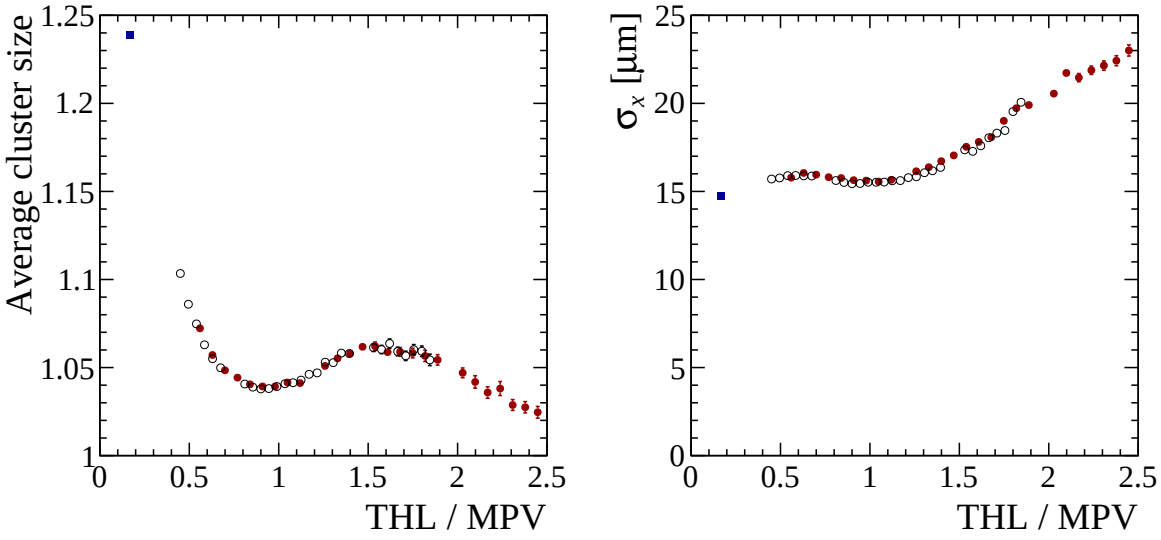

Figure 5: Average cluster size (left) and standard deviation of the x-residual distribution (right) at perpendicular track incidence as function of threshold-to-signal ratio for assemblies W20_B6 (empty circles) and W20_J9 (full circles). Results for a Timepix assembly with the same type of sensor are shown with full squares. The error bars represent the statistical uncertainty of the measurements. For most points the error bars are smaller than the symbols.

for the electric field is used[3].

As can be seen from figure 7, the features in the measured cluster size and resolution as function of threshold-to-signal ratio are reproduced by the simulation, provided that the spatial extent of the ionisation pattern is taken into account. This corroborates the conclusion that these features are due to "delta" electrons.

4.2 Irradiated assemblies

A set of Medipix3.1 assemblies, with VTT n-on-p active-edge sensors from the same batch as the non-irradiated sensors discussed above, were irradiated at the Ljubljana TRIGA reactor [12] to a 1 MeV neutron equivalent fluence of 5×10^{14} cm^{-2} and subsequently annealed for 80 minutes at 60° C. From lab measurements with a laser, the effective depletion voltage V_{dep} of these sensors after irradiation was measured to be between -85 and -105 V. One of the assemblies, W20_H5, was characterised in the beam test. The sensor, which has a pixel-to-edge distance of 100 μm, was operated at a bias voltage of -100 V as operation at higher bias was inhibited by the onset of electrical breakdown (figure 8).

In general, the irradiated assemblies exhibited a higher dark count rate compared to the non-irradiated ones, which was attributed to electrons from the β-decay of ^{182}Ta

[3]The electric field is assumed to vary linearly between $E = (V - V_{\text{dep}})/d$ at the sensor backside and $E = (V + V_{\text{dep}})/d$ at the implants, where d is the sensor thickness.

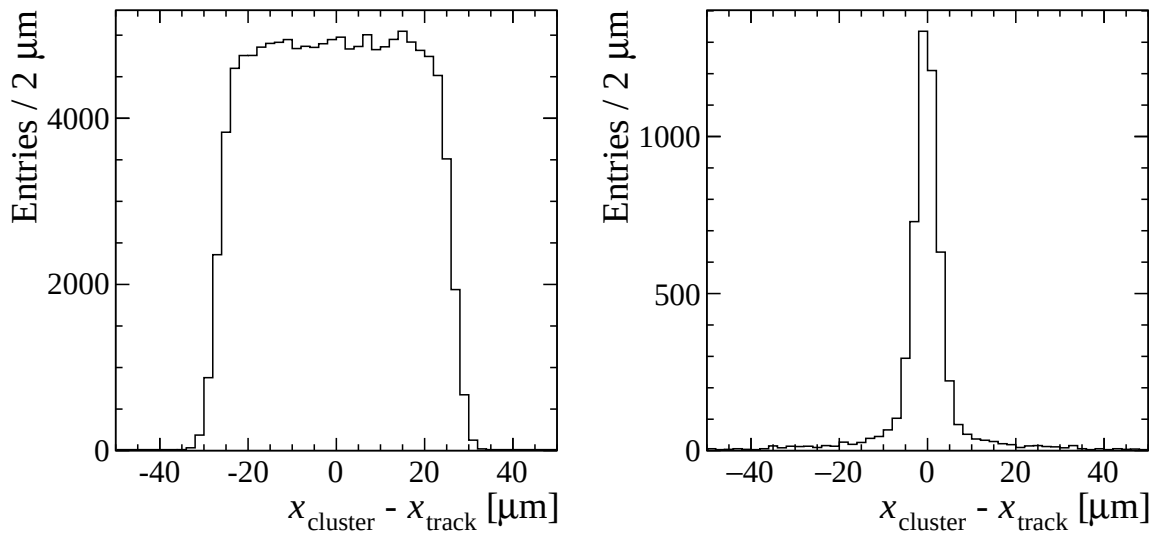

Figure 6: Residual distribution for (left) one-pixel and (right) two-pixel clusters extending over two columns in a non-irradiated 100 µm thick sensor (assembly W20_B6, at THL/MPV∼0.45).

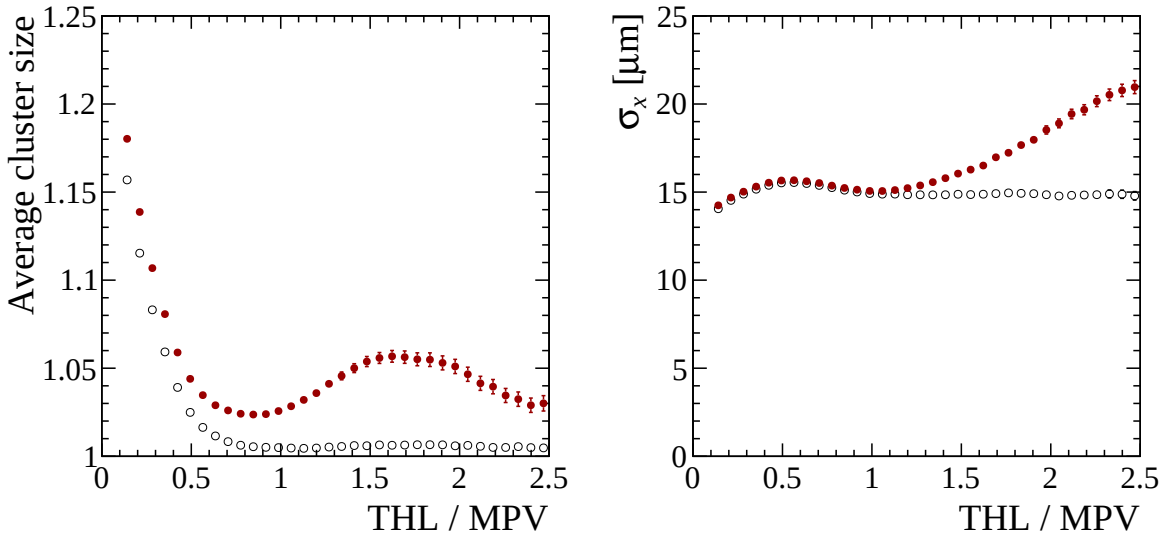

Figure 7: Simulated average cluster size (left) and standard deviation of the x-residual distribution (right) at perpendicular track incidence as function of threshold-to-signal ratio. Full (empty) symbols show the results with (without) the spatial extent of the ionisation pattern being included in the simulation.

produced by neutron activation during the irradiation of the ASIC[4]. This – presumably in combination with other radiation effects – resulted in problems during the equalisation

[4] The presence of ^{182}Ta in the irradiated assemblies was confirmed by gamma spectroscopy measurements performed by the CERN radioprotection group.

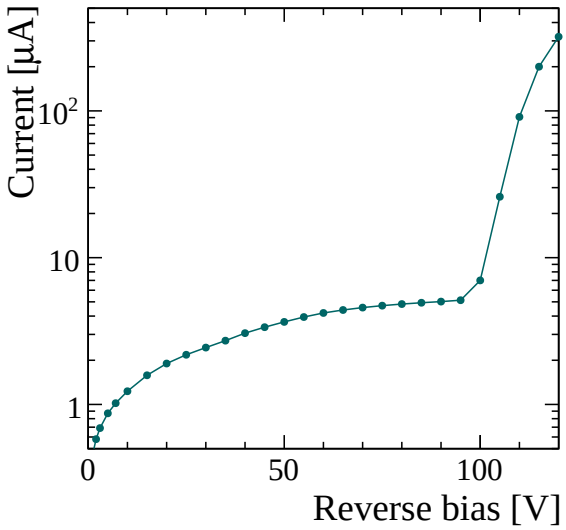

Figure 8: Leakage current as function of reverse bias voltage at $T = -13^\circ$ C after irradiation to 0.5×10^{15} 1 MeV n_{eq} cm^{-2} (100 µm thick n-on-p active-edge sensor with 100 µm pixel-to-edge distance).

procedure for some assemblies, as well as a larger threshold dispersion. The optimised values of the DACs which control the global currents (ThresholdN and DACpixel) were larger (by a factor 2 – 3) compared to the non-irradiated assemblies.

As can be seen from figure 9, the MPV of the charge deposition spectrum corresponds to a THL DAC of ~ 53.9. After correcting for the differences in gain and offset using testpulse calibration curves, this value is found to be approximately 8.5% lower than the MPV of the non-irradiated sensors.

As in the non-irradiated case, the cluster size spectrum is dominated by single-pixel clusters. Cluster size and σ of the x-residual distribution as function of threshold-to-signal ratio (figure 10) follow closely the corresponding curves for the non-irradiated assemblies (figure 5).

Figure 11 shows the hit efficiency as function of the track intercept within a pixel cell at the lowest measured threshold (THL = 40). In the centre of the pixel cell, an efficiency of 0.93 ± 0.01 is found, compared to 0.97 ± 0.01 for the non-irradiated assemblies at the same threshold-to-signal ratio (~ 0.74).

A further beam test measurement was performed with a Medipix3.1 ASIC bump-bonded to a 200 µm thick n-on-p sensor manufactured by CNM[5]. The sensor featured two guard rings and was diced at a distance of 400 µm from the border of the pixel matrix. The assembly (W20_D6) was also irradiated at Ljubljana, but to a higher fluence, 2.5×10^{15} 1 MeV n_{eq} cm^{-2}. During the equalisation procedure, a large threshold dispersion was observed, such that the upper limit of the equalisation target window needed to be increased to THL = 40. In addition, a significant fraction ($\sim 10\%$) of the pixels needed

[5]Centro Nacional de Microelectrónica, Barcelona, Spain

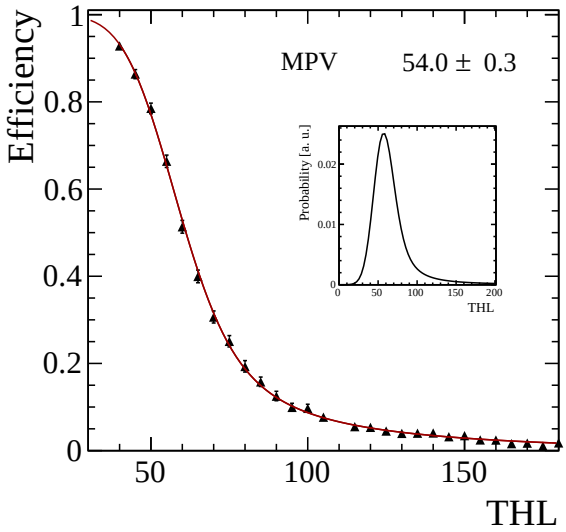

Figure 9: Hit efficiency in Medipix3 assembly W20_H5 with 100 µm thick n-on-p sensor as function of threshold, after irradiation to 0.5×10^{15} 1 MeV n_{eq} cm^{-2}. The inset shows the distribution of the charge deposition in units of THL (Landau distribution convoluted with a Gaussian).

to be masked. Tracks crossing a masked pixel were thus excluded from the efficiency measurements for this device.

Because of time constraints, data were taken only at three THL values with this device, such that determining the MPV of the charge deposit spectrum was not possible.

Figure 12 shows the efficiency as function of the track intercept. The dependency of the efficiency on the applied threshold and bias voltage is shown in figure 13.

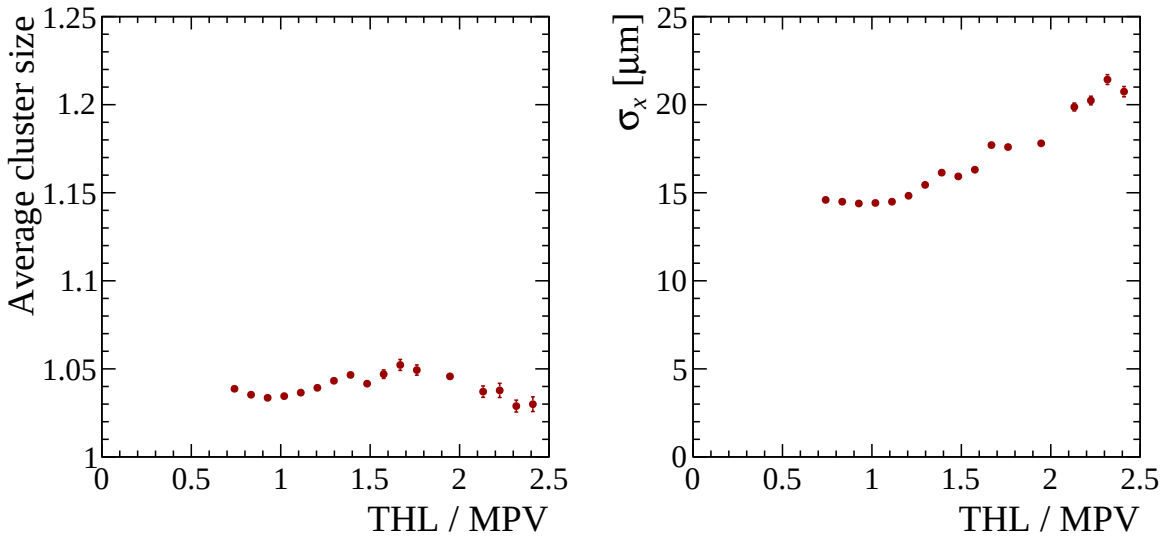

Figure 10: Average cluster size (left) and standard deviation of the x-residual distribution (right) at perpendicular track incidence as function of threshold-to-signal ratio for irradiated assembly W20_H5.

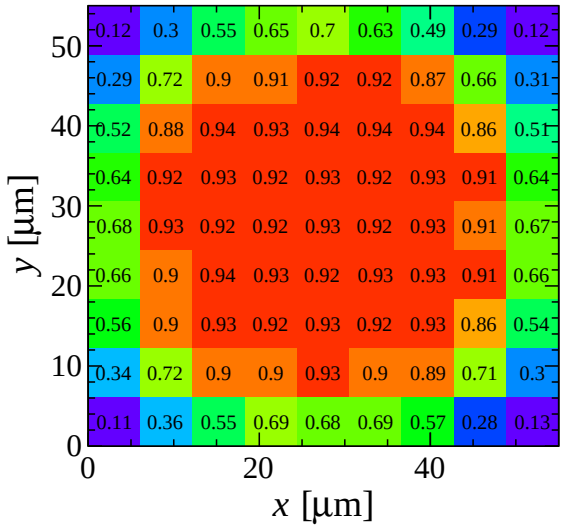

Figure 11: Hit efficiency in Medipix3 assembly W20_H5 with 100 µm thick n-on-p sensor as function of the track intercept within a pixel cell at THL = 40 (threshold/signal ~ 0.74), after irradiation to 0.5×10^{15} 1 MeV n_{eq} cm^{-2}. The drop in efficiency at the edges of the pixel cell is more pronounced than in figure 3 mainly because of the higher threshold-to-signal ratio.

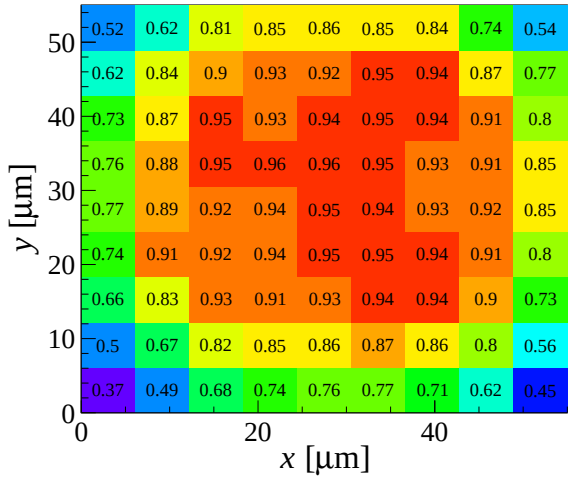

Figure 12: Hit efficiency in Medipix3 assembly W20_D6 with 200 µm thick n-on-p sensor (diced at 400 µm from the last pixel) as function of the track intercept within a pixel cell at THL = 50 and 300 V bias voltage, after irradiation to 2.5×10^{15} 1 MeV n_{eq} cm^{-2}. The asymmetry of the efficiency profile is attributed to a small inclination of the assembly with respect to the beam.

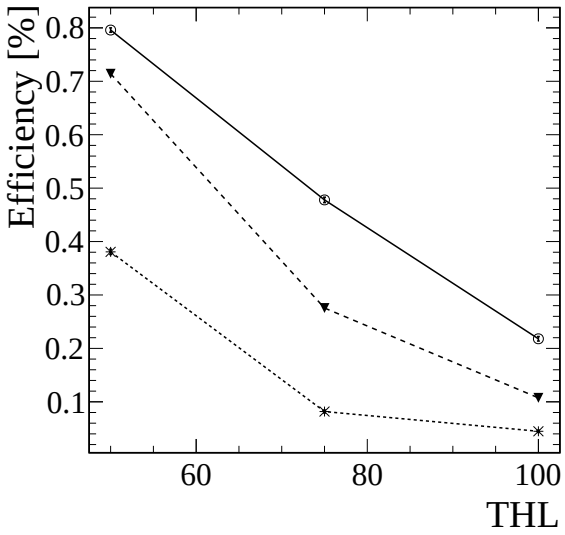

Figure 13: Overall hit efficiency in irradiated assembly W20_D6 with 200 µm thick n-on-p sensor as function of the THL value for different bias voltages (stars: −100 V, triangles: −200 V, circles: −300 V). The assembly was irradiated to a fluence of 2.5×10^{15} 1 MeV n_{eq} cm^{-2}. The lines are drawn to guide the eye.

5 Conclusions

First results on the performance of hadron-irradiated pixel detectors with the "footprint" of the upgraded LHCb VELO (55×55 μm^2 pixels) have been obtained from a beam test at the CERN SPS, using Medipix3.1 ASICs bump-bonded to thin n-on-p silicon sensors. As the Medipix3 ASICs do not provide a direct measurement of the collected charge, threshold scans were used for characterising the sensor.

Reference measurements with non-irradiated Medipix3.1 assemblies were made in the same testbeam campaign. The threshold DAC value (THL) corresponding to the most probable value of the charge deposition spectrum was determined from the hit efficiency as function of threshold. The measured cluster size and resolution as function of the THL/MPV ratio are consistent between the assemblies and in good agreement with simulations.

After irradiation with reactor neutrons to a fluence of $0.5 \times 10^{15}\,1\,\mathrm{MeV\,n_{eq}\ cm^{-2}}$, a larger threshold dispersion and an increased power consumption of the ASIC were observed. A direct comparison between the performance of irradiated and non-irradiated sensors is complicated due to the fact that the non-irradiated sensors were operated at overdepletion while the irradiated sensor (due to early electrical breakdown) needed to be operated close to depletion. The difference in operating conditions may explain the small drop in efficiency and MPV measured with the irradiated sensor. The shapes of average cluster size and resolution versus threshold are not changed significantly compared to the non-irradiated sensors.

The studies presented in this paper are being continued using the Timepix3 ASIC, which has recently become available.

Acknowledgements

We gratefully acknowledge strong support from the CERN Medipix Group. in particular Rafael Ballabriga. We would also like to thank Juha Kalliopuska and Sami Vähänen from VTT/Advacam and Giuglio Pellegrini from the IMB-CNM Radiation Detectors Group. The research leading to these results has received partial funding from the European Commission under the FP7 Research Infrastructures project AIDA, grant agreement no. 262025. We gratefully acknowledge the expert wire bonding support provided by Ian McGill of the CERN DSF bonding lab. We extend warm thanks to Igor Mandić and Vladimir Cindro for irradiating the Medipix3 assemblies.

References

[1] LHCb collaboration, R. Aaij et al., *LHCb VELO Upgrade Technical Design Report*, CERN-LHCC-2013-021. LHCB-TDR-013.

[2] K. Akiba et al., *Charged particle tracking with the Timepix ASIC*, *Nucl. Instr. Meth. A* **661** (2012), 31–49, [arXiv:1103.2739]

[3] R. Ballabriga, M. Campbell, E. Heijne, X. Llopart, L. Tlustos, and W. Wong, *Medipix3: A 64 k pixel detector readout chip working in single photon counting mode with improved spectrometric performance*, *Nucl. Instr. Meth. A* **633** (2011), S15 – S18

[4] R. Ballabriga et al., *Characterization of the Medipix3 pixel readout chip*, 2011 *JINST* **6** C01052

[5] R. Plackett, X. Llopart, R. Ballabriga, M. Campbell, L. Tlustos, and W. Wong, *Measurement of Radiation Damage to 130 nm Hybrid Pixel Detector Readout Chips*, Proceedings of Topical Workshop on Electronics for Particle Physics (TWEPP09), CERN-2009-006

[6] K. Akiba et al., *The Timepix Telescope for high performance particle tracking*, *Nucl. Instr. Meth. A* **723** (2013), 47–54, [arXiv:1304.5175]

[7] R. Plackett, I. Horswell, E. N. Gimenez, J. Marchal, D. Omar, and N. Tartoni, *Merlin: a fast versatile readout system for Medipix3*, 2013 *JINST* **8** C01038

[8] B. Verlaat, L. Zwalinski, R. Dumps, M. Ostrega, P. Petagna, and T. Szwarc, *TRACI, a multipurpose CO_2 cooling system for R&D*, 10^{th} IIR-Gustav Lorentzen Conference on Natural Working Fluids (2012), Refrigeration Science and Technology Proceedings 2012-1

[9] D. Tureček et al., *Pixelman: a multi-platform data acquisition and processing software package for Medipix2, Timepix and Medipix3 detectors*, 2011 *JINST* **6** C01046

[10] *Garfield++ – simulation of tracking detectors*, http://cern.ch/garfieldpp

[11] I. B. Smirnov, *Modeling of ionization produced by fast charged particles in gases*, *Nucl. Instr. Meth. A* **554** (2005), 474 – 493

[12] L. Snoj, G. Žerovnik, A. Trkov, *Computational analysis of irradiation facilities at the JSI TRIGA reactor*, *Applied Radiation and Isotopes* **70** (2012), 483–488

Chapter 4

Analysis of $B_s^0 \to J/\psi \overline{K}^{*0}$ decays

The CP-violating phase, ϕ_s, may be measured in processes that involve interference in the B_s^0 meson system, where the B_s^0 may decay directly to $J/\psi\phi$ or may do so after B_s^0-$\overline{B}_s^0$ oscillation. Within the Standard Model and ignoring penguin contributions, this phase is predicted to be $\phi_s^{\rm SM} = -2\beta_s$, with $\beta_s = \arg(-V_{cb}V_{cs}^*/V_{tb}V_{ts}^*)$. Since this parameter has a very small theoretical uncertainty and because NP can contribute to the B_s^0-$\overline{B}_s^0$ mixing box diagram, the measurement of ϕ_s is one of the highest priorities of LHCb since the beginning of the experiment. The above theoretical estimate changes when additional contributions to the leading $b \to \bar{c}cs$ tree Feynman diagram are taken into account. These contributions, called here "penguin pollution" are very difficult to compute, due to non-perturbative QCD estimates. However, it is mandatory to control this penguin pollution if one hopes to claim a NP discovery in the ϕ_s measurement. Various authors have proposed methods to tackle this problems [108–111]. For more details, see Chapter 2.1 and Chapter 2.2. LHCb has published an estimation of the penguin pollution using $B^0 \to J/\psi\rho^0$ events [112].

In this chapter, the experimental information from $B_s^0 \to J/\psi\overline{K}^{*0}$ needed to study penguin pollution in ϕ_s is presented [108]. The analysis is based on fitting for the angular parameters, defined in Chapter 4.4.1, in $m_{K\pi}$ bins around the $K^*(892)^0$ pole. This $m_{K\pi}$ binning, described in Chapter 4.3, is also used when calculating the ${}_s\mathcal{W}eights$ as defined in ref. [113], together with five bins of the cosine of the helicity angle θ_μ (defined in Figure 4.13). From the fit, polarisation fractions, CP asymmetries and $B_s^0 \to J/\psi\overline{K}^{*0}$ branching fraction are measured (see Chapter 4.7).

This chapter is organised as follows: in Chapter 4.1, the selection of $B_s^0 \to J/\psi\overline{K}^{*0}$ candidates is presented. In Chapter 4.2, the treatment of the peaking background is explained. In Chapter 4.3, the $\mu^+\mu^-K^-\pi^+$ mass model as well as the background subtraction method using ${}_s\mathcal{W}eights$ are described. The angular analysis is performed in Chapter 4.4 and the measurement of the branching ratio in Chapter 4.5. The systematic uncertainties are evaluated in Chapter 4.6 and the results presented in Chapter 4.7. This analysis, which has been already published in JHEP [114], supersedes that of [115], which was performed with $370\,{\rm pb}^{-1}$.

4.1 Event selection and data samples

Real data (Chapter 4.1.1) and simulated data (Chapter 4.1.2) samples used for this analysis are presented in this section, among with the requirements from the offline selection (Chapter 4.1.3) as well. The offline selection consists of two parts: a "cut-based" set of requirements to reduce the size of the real data sample to a manageable level, followed by the use of Boosted Decision Trees with Gradient boosting (BDTG) [116] to reject as much combinatorial background as possible while keeping a high signal efficiency. The J/ψ meson is reconstructed from $\mu^+\mu^-$ and the $\overline{K}^{*0}$ hadron from $K^-\pi^+$, as well as their charge conjugated decays. A very large $B^0 \to J/\psi K^{*0}$ component is present in the data and taken into account, also used as a control channel (see Chapter 4.5.3).

4.1.1 Real data samples

Real data events for this analysis are selected from two LHCb datasets with a total integrated luminosity of $3.0\,\text{fb}^{-1}$ of pp collision data:

- `Reco14-Stripping20r1`: corresponding to $1\,\text{fb}^{-1}$ of integrated luminosity, collected during 2011 at a centre-of-mass energy of $\sqrt{s} = 7\,\text{TeV}$, and analysed with DaVinci v32r2p3.
- `Reco14-Stripping20r0p1`: corresponding to $2\,\text{fb}^{-1}$ of integrated luminosity, collected during 2012 at a centre-of-mass energy of $\sqrt{s} = 8\,\text{TeV}$, and analysed with DaVinci v32r2p5.

Both datasets have been reconstructed using Brunel v43r2p6, Condition DataBase (CondDB) and Detector Description DataBase (DDDB) tags `cond-20130114` and `dddb-20130111`, respectively.[1]

4.1.2 Simulated samples

Three sets of simulated samples are used in this analysis, containing $B_s^0 \to J/\psi \overline{K}^{*0}$, $B^0 \to J/\psi K^{*0}$ and $B_s^0 \to J/\psi\phi$ simulated decays each one. Four samples per set, containing approximately the same number of simulated events all of them, are considered: one pair is representative of the data taken during 2011 (`Reco14a-Stripping20r1`, flagging mode, TCK `0x40760037`), whilst the other pair is representative of the data taken during 2012 (`Reco14a-Stripping20`, flagging mode, TCK `0x409f0045`). The only difference between members of a same pair is the polarity of the LHCb dipole magnet considered during the simulation. In summary, four samples (one per year and magnet polarity) per considered decay mode ($B_s^0 \to J/\psi \overline{K}^{*0}$, $B^0 \to J/\psi K^{*0}$ and $B_s^0 \to J/\psi\phi$) are used: 2 (polarity) $\times$ 2 (year) $\times$ 3 (decay mode). The total number of simulated events per mode are approximately 1 M, 2 M and 10 M, respectively. This information is summarized in

[1] LHCb database tags: CondDB (a) and DDDB (b).

Table 4.1: Simulated samples used in the analysis of $B_s^0 \to J/\psi \overline{K}^{*0}$ decays. Approximately half of the simulated events per each sample correspond to one of the two LHCb magnet polarities, while the other half corresponds to the opposite.

Decay mode	Simulated events	`Sim` pass	TCK (year)	Stripping version
$B_s^0 \to J/\psi \overline{K}^{*0}$	509 500	`Sim08c`	`0x40760037` (2011)	`Stripping20r1`
	531 498	`Sim08a`	`0x409f0045` (2012)	`Stripping20`
$B^0 \to J/\psi K^{*0}$	1 016 249	`Sim08b`	`0x40760037` (2011)	`Stripping20r1`
	1 019 996	`Sim08a`	`0x409f0045` (2012)	`Stripping20`
$B_s^0 \to J/\psi \phi$	5 028 485	`Sim08a`	`0x40760037` (2011)	`Stripping20r1`
	5 114 480	`Sim08a`	`0x409f0045` (2012)	`Stripping20`

Table 4.1. Information about the software packages used to simulate these samples can be found in Chapter 3.2.5, where Table 3.2 summarizes their corresponding versions.

4.1.3 "Cut-based" requirements

The "cut-based" set of requirements consists of two subsets: a first subset of cuts, applied once by the LHCb computing team to the triggered LHCb data immediately before the data sample is re-constructed, called "stripping line" (see Chapter 3.2.5); followed by a second subset of offline cuts tuned for the present analysis. The stripping line used for this analysis is named `StrippingBetaSBs2JpsiKstarWideLine`. The analysis is not restricted to any particular trigger line, i.e. an event should just pass at least one of the LHCb trigger lines.

Table 4.2 lists the final "cut-based" selection criteria (already taking into account both subsets of cuts). For $J/\psi \to \mu\mu$ candidates, a mass window of $150\,\mathrm{MeV}/c^2$ around the reconstructed J/ψ peak is imposed, along with good vertex and DOCA (or minimum distance between the two daughter muon tracks) reconstruction criteria ($\chi^2_{\mathrm{vtx}}/\mathrm{ndof} < 16$, $\chi^2_{\mathrm{DOCA}}/\mathrm{ndof} < 20$). For daughter muon tracks, a threshold cut in the p_T of $0.5\,\mathrm{GeV}/c$, good muon identification by the muon system and a cut in the χ^2 of the reconstructed impact parameter ($\Delta\mathrm{LL}\mu\pi > 0$, $\chi^2_{\mathrm{IP}} > 16$), are imposed. For $\overline{K}^{*0} \to K^-\pi^+$ candidates, a mass window in the $K^-\pi^+$ invariant mass of $70\,\mathrm{MeV}/c^2$ around the measured $\overline{K}^{*0}$ mass, along with good vertex and DOCA reconstruction criteria ($\chi^2_{\mathrm{vtx}}/\mathrm{ndof} < 25$, $\chi^2_{\mathrm{DOCA}}/\mathrm{ndof} < 30$), are required. For daughter hadron (h) candidates, threshold cuts in the p_T of $0.5\,\mathrm{GeV}/c$ and in the χ^2 of the reconstructed impact parameter are required as well. A requirement of the hadron candidates to not be a ghost (fake) track is also imposed ($\mathrm{Prob}_{\mathrm{ghost}}(\mathrm{track}) < 0.8$). Good pion ($\Delta\mathrm{LL}K\pi < 0$, $\mathrm{ProbNNK} < 0.01$) and kaon ($\Delta\mathrm{LL}K\pi > 0$, $\mathrm{ProbNNK} > 0.21$) identification by the RICH system, are also part of the requirements. Finally, for $B_s^0 \to J/\psi \overline{K}^{*0}$ candidates, a mass window in the four-body invariant mass, along with a good vertex reconstruction criterion and a threshold cut in the DIRA (angle between the direction of the momentum of the B_s^0 candidate and the direction defined by the difference between the secondary and the primary vertex) of the

B_s^0 meson ($M \in [5150, 5650]\,\mathrm{MeV}/c^2$, $\chi^2_{\mathrm{vtx}}/\mathrm{ndof} < 10$, DIRA > 0.999) are required. A threshold cut in the VS variable (separation between a vertex w.r.t. its associated primary vertex) of 1.5 mm is imposed as well. A final veto cut of $B^+ \to J/\psi K^+$ three-body decays, as the removal of the mass window defined $60\,\mathrm{MeV}/c^2$ around the B^+ measured mass in the $J/\psi K^+$ spectrum is also required.

Table 4.2: Selection criteria for $B_s^0 \to J/\psi \overline{K}^{*0}$ decays.

	Cut variable	Cut value
$J/\psi \to \mu\mu$	$\lvert M(\mu^+\mu^-) - M(J/\psi)\rvert$	$< 150\,\mathrm{MeV}/c^2$
	$\chi^2_{\mathrm{vtx}}/\mathrm{ndof}(J/\psi)$	< 16
	$\chi^2_{\mathrm{DOCA}}/\mathrm{ndof}(J/\psi)$	< 20
	$\Delta\mathrm{LL}\mu\pi(\mu)$	> 0
	$\chi^2_{\mathrm{IP}}(\mu)$	> 16
	$p_T\ (\mu)$	$> 0.5\,\mathrm{GeV}/c$
	$\mathrm{IsMuon}(\mu)$	true
$\overline{K}^{*0} \to K^-\pi^+$	$\lvert M(K^-\pi^+) - 896\rvert$	$< 70\,\mathrm{MeV}/c^2$
	$\chi^2_{\mathrm{vtx}}/\mathrm{ndof}(\overline{K}^{*0})$	< 25
	$\chi^2_{\mathrm{DOCA}}/\mathrm{ndof}(\overline{K}^{*0})$	< 30
	$p_T\ (h)$	$> 0.5\,\mathrm{GeV}/c$
	$\mathrm{Prob}_{\mathrm{ghost}}(\mathrm{track})(h)$	< 0.8
	$\chi^2_{\mathrm{IP}}(h)$	> 2
	$\Delta\mathrm{LL}K\pi(\pi)$	< 0
	$\mathrm{ProbNNK}(\pi)$	< 0.01
	$\Delta\mathrm{LL}K\pi(K)$	> 0
	$\mathrm{ProbNNK}(K)$	> 0.21
$B_s^0 \to J/\psi \overline{K}^{*0}$	$M(B_s^0)$	$\in [5150, 5650]\,\mathrm{MeV}/c^2$
	$\chi^2_{\mathrm{vtx}}/\mathrm{ndof}(B_s^0)$	< 10
	$\mathrm{DIRA}(B_s^0)$	> 0.999
	VS	$> 1.5\,\mathrm{mm}$
$B^+ \to J/\psi K^+$ veto	$\lvert M(J/\psi, K) - 5279\rvert$	$> 60\,\mathrm{MeV}/c^2$

4.1.4 BDTG requirements

As previously stated at the beginning of this section, most of the combinatorial background is rejected from data using a MultiVariate Analysis (MVA) method, consisting of Boosted Decision Trees with Gradient boosting. In order to obtain a cut value optimised separately for each data-taking year conditions, this BDTG is trained, tested and optimised separately for both 2011 and 2012 samples; but following a common procedure. Henceforth, the procedure described in the following paragraphs is assumed to be performed in parallel for 2011 and 2012 samples. Thus, for this purpose, a signal sample from $B_s^0 \to J/\psi \overline{K}^{*0}$ simulated decays and a background sample extracted from real data are

constructed. For both samples, a common selection, which consists of the same requirements as in Table 4.2 but excepting the ProbNN particle identification cuts for kaons and pions, is applied.

For the signal sample, true MC-*truth* for B_s^0 simulated candidates and a mass window constraint of 25 MeV/c^2 around the B_s^0 peak, are required. Here, MC-*truth* is a boolean variable associated to each simulated event which is true only when the corresponding event has a particle `TRUEID` equal to its corresponding ID defined in the PDG Monte Carlo numbering scheme [117]. Hereafter, referring to "true MC-*truth*" and simply "MC-*truth*" will be equivalent.

For the background sample, candidates from the high mass sideband with invariant masses between 5401.3 MeV/c^2 and 5700 MeV/c^2 are selected (this is the region 35 MeV/c^2 away from the B_s^0 peak in the high mass sideband, since $\sigma_{B_s^0}$ is estimated to be approximately 10 MeV/c^2 as shown in Chapter 4.3.2). A requirement on the RICH particle identification ProbNN variables of kaons and pions, complementary to those shown in Table 4.2 in order to use different real data samples during the MVA procedure and further steps of the analysis avoiding possible bias, is imposed too (ProbNNK(K) $<$ 0.21 $\|$ ProbNNK(π) $>$ 0.01). All these requirements which define signal and background samples, are summarised in Table 4.3.

Table 4.3: Signal and background sample definitions for samples used in MVA studies.

	Decay mode	Cut variable	Cut value
Signal sample	$B_s^0 \to J/\psi \overline{K}^{*0}$	$\lvert M(J/\psi K^-\pi^+) - 5366.3\rvert$	$< 25\,\text{MeV}/c^2$
		MC-*truth*	*true*
Background sample	$B_s^0 \to J/\psi \overline{K}^{*0}$	$M(J/\psi K^-\pi^+) - 5366.3$	$> 35\,\text{MeV}/c^2$
	$\overline{K}^{*0} \to K^-\pi^+$	ProbNNK(K) $\|$ ProbNNK(π)	$< 0.21 \,\|\, > 0.01$

TMVA toolkit [116] was used for this MVA procedure. After their preparation, each sample is split in two halves: 50% of the sample is used for training while the other 50% used for testing. A BDTG method is trained and tested over those samples using the following kinematic variables as discriminating variables for the MVA procedure (B_s^0 meson variables are named here as `B0`):

- `max_DOCA`: maximum of all distances between pairs of tracks from daughter particles.
- `B0_LOKI_DTF_CTAU`: time of flight ct of the B_s^0 meson candidate, where t is the decay time of the B_s^0 meson candidate measured in its proper reference frame.
- `lessIPS`: minimum of all significances on the impact parameter of a daughter particle (kaons, muons and pions) with respect to the B_s^0 meson candidate.
- `B0_PT`: transverse momentum of the B_s^0 meson candidate.
- `B0_IP_OWNPV`: impact parameter of the B_s^0 meson candidate with respect to its best own parent vertex.

- `B0_ENDVERTEX_CHI2`: reconstruction significance of a reconstructed decay vertex of the B_s^0 meson candidate.

Signal and background distributions for discriminating variables are presented in Figure 4.2 and Figure 4.3, among with the BDTG method response in Figure 4.1, for both 2011 and 2012 conditions separately. No overtraining is observed in Figure 4.1, showing a good discrimination power for the chosen BDTG method between both signal and background distributions.

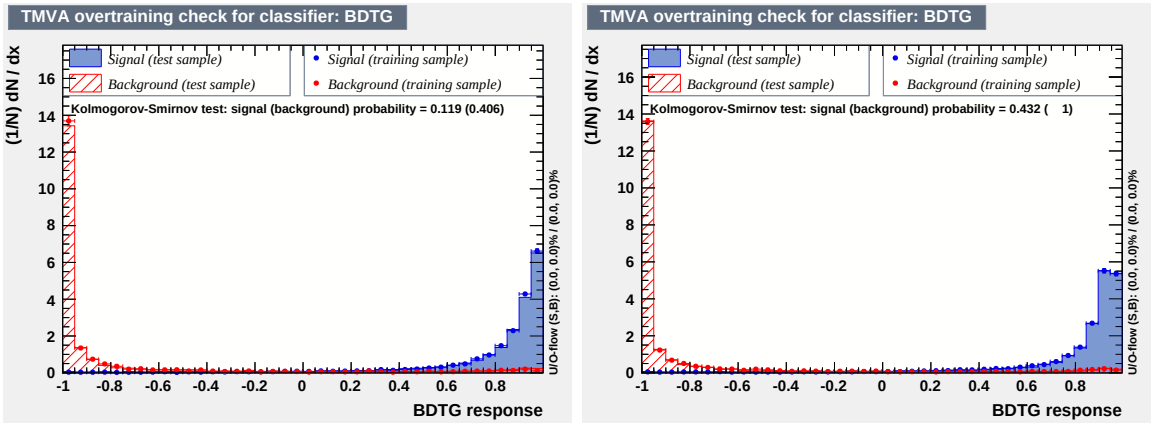

Figure 4.1: BDTG response to signal and background distributions for 2011 (left) and 2012 (right) conditions.

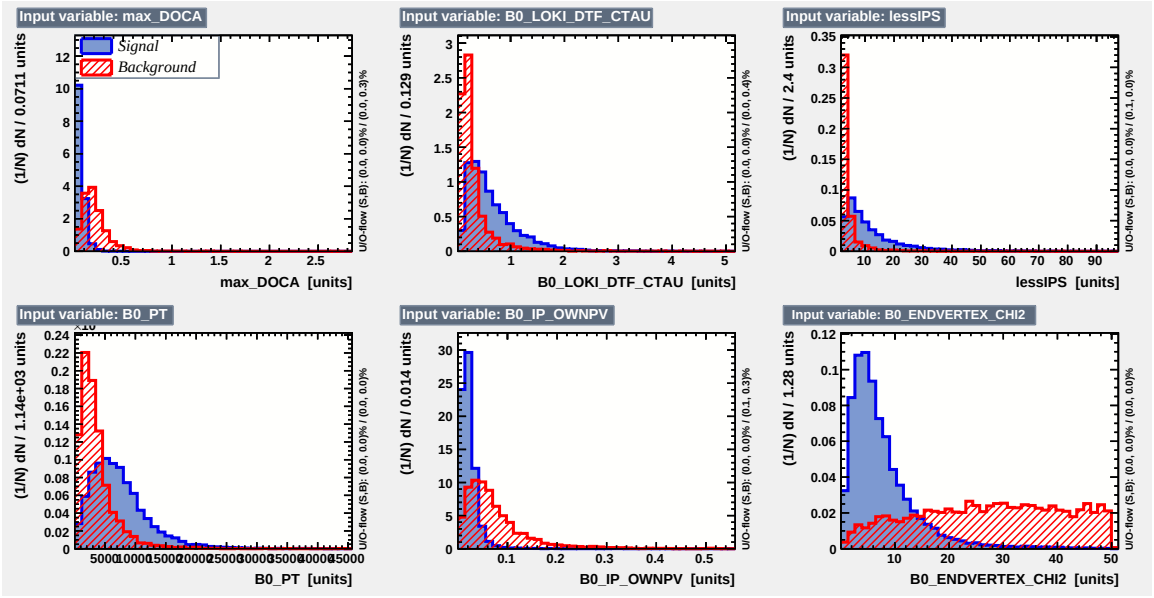

Figure 4.2: Distributions for MVA discriminating variables under 2011 conditions.

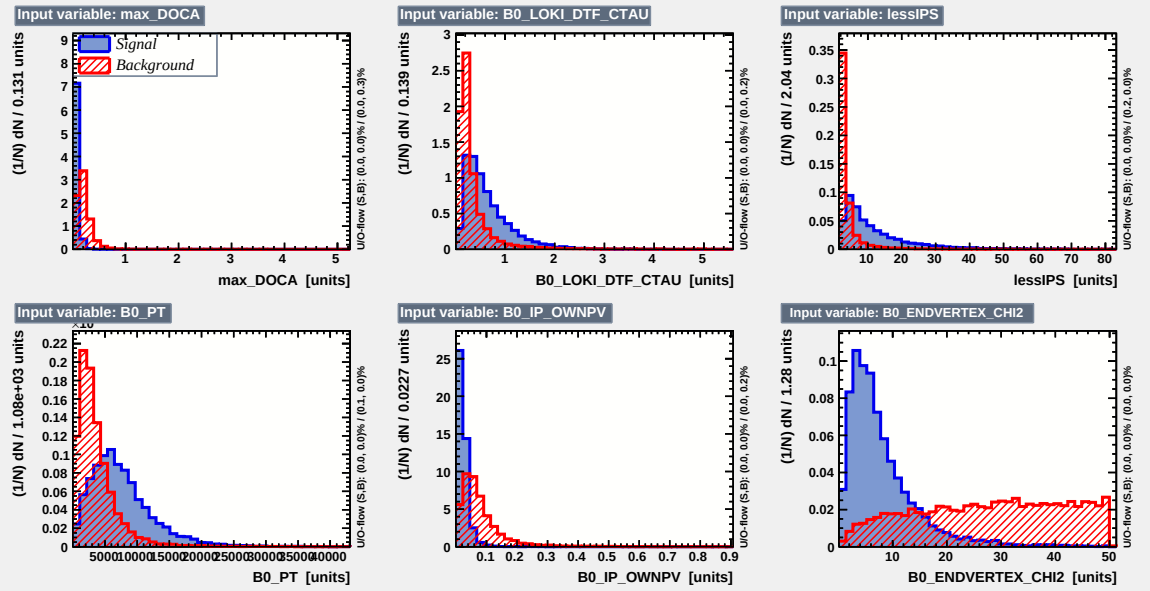

Figure 4.3: Distributions for MVA discriminating variables under 2012 conditions.

After training and testing it, a cut on the BDTG is applied: the purpose of this cut is to suppress as much combinatorial background contribution as possible from data. Since background and signal distributions are well discriminated (see Figure 4.1), it is possible to find an optimal cut value on the BDTG where most of the combinatorial background contribution on data with the same properties as the background sample used should be removed. The cut value, henceforth called also "optimal point", is chosen so that it maximises the figure of merit (FoM) [118]

$$F({}_s\mathcal{W}eights) = \frac{(\sum w_i)^2}{\sum w_i^2}, \tag{4.1}$$

where w_i are the ${}_s\mathcal{W}eights$ associated to each event, and calculated with the ${}_s\mathcal{P}lot$ technique [113], considering B_s^0 candidate events as signal yield. This FoM can be understood as an *effective signal value*, which is proportional to the number of events of a signal-only sample with the same statistical power as the sample used to compute $F({}_s\mathcal{W}eights)$. For these calculations, a mass model consisting of two Crystal-Ball [119] (signal parametrisation) and an exponential function (background parametrisation) is used. As previously noted, since the optimal point may be different for 2011 and for 2012 conditions, the optimisation as well is performed separately for 2011 and 2012 samples. After applying the requirements described in Table 4.2, these fits are performed in a single $M(J/\psi K\pi)$ bin. For a range of cut values applied on the BDTG, an ${}_s\mathcal{P}lot$ can be performed and a value for the FoM can be obtained. A pair of plots, one per data-taking year condition, containing the value of $F({}_s\mathcal{W}eights)$ versus the cut value applied on the BDTG, are shown in Figure 4.4. Optimal BDTG cut values are chosen as those that maximise

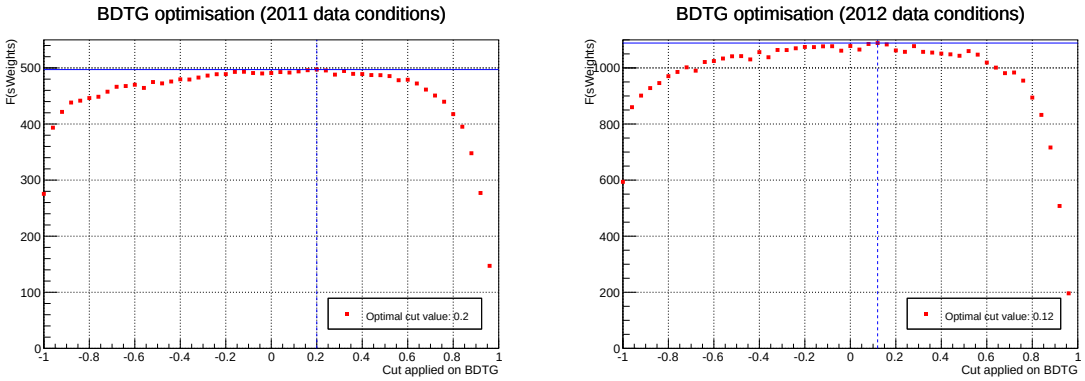

Figure 4.4: BDTG optimisation for 2011 (left) and 2012 (right) conditions.

$F({}_s\mathcal{W}eights)$. These values are BDTG > 0.2 for 2011 conditions and BDTG > 0.12 for 2012 conditions. For more details about the whole MVA procedure, see Appendix A.

4.1.5 Selection efficiencies

Signal efficiency and background rejection values are calculated separately for both 2012 and 2011 data samples. Signal and background samples used for these calculations are defined in Table 4.3, except the ProbNN particle identification cut for the background sample. Three different subsets of cuts are considered, resulting in three individual signal efficiencies (background rejections) values: a first set, corresponding to the requirements presented in Table 4.2, used to obtain ε_{sel} (r_{sel}). A second set, corresponding to the optimal BDT cut value obtained in Chapter 4.1.4, used to calculate ε_{MVA} (r_{MVA}). A third set, composed of RICH particle identification cuts for pions (ProbNNπ/ProbNNp > 21.9) and kaons (ProbNNK/ProbNNp > 0.99) to suppress Λ_b^0 peaking backgrounds (implemented a posteriori and described in Chapter 4.2.3), used to obtain $\varepsilon_{\Lambda_b^0}$ ($r_{\Lambda_b^0}$). Each one of these individual efficiencies (rejections) are calculated w.r.t. the corresponding previous set of cuts, in an inclusive way. Finally, a total efficiency (rejection) value is obtained, containing the information from all the efficiencies (rejections) computed in previous steps, ε_{tot} (r_{tot}). These efficiencies and rejections are shown in Table 4.4. Values related to cuts on RICH particle identification variables are corrected using the PIDCalib package [91,93,120]. This package is used in this analysis to correct ProbNN and ΔLL distributions for daughter hadrons in simulation using real data samples.

After applying the final selection cuts (which includes those cuts described in Table 4.2, the optimal BDTG cut value, and the cuts devoted to the Λ_b^0 backgrounds suppression), 147760 events are selected in the 2012 data sample and 68100 events are selected in the 2011 data sample.

From all the cuts in the RICH particle identification variables included in the previously defined final selection requirements, those used to suppress Λ_b^0 peaking backgrounds have a small effect on the other background components. As explained in Chapter 4.2.3,

Table 4.4: Signal efficiencies and background rejections for 2011 and 2012 conditions.

		ε_{sel} (r_{sel})	ε_{MVA} (r_{MVA})	$\varepsilon_{\Lambda_b^0}$ $(r_{\Lambda_b^0})$	ε_{tot} (r_{tot})
Signal efficiency,	2011	54.58 ± 0.23	92.73 ± 0.27	93.35 ± 0.20	47.25 ± 0.30
ε (%)	2012	54.56 ± 0.23	93.38 ± 0.28	93.41 ± 0.22	47.59 ± 0.31
Background rejection,	2011	99.12 ± 0.01	92.97 ± 0.35	21.22 ± 2.11	99.951 ± 0.003
r (%)	2012	99.30 ± 0.01	92.59 ± 0.23	23.69 ± 1.39	99.960 ± 0.002

the Λ_b^0 contributions are treated separately with respect to the rest of the peaking backgrounds present in the final data sample. In order to properly estimate the rejection level of $\Lambda_b^0 \to J/\psi p K^-$ ($\Lambda_b^0 \to J/\psi p \pi^-$) peaking backgrounds after the final selection, specific background samples where an MC-*truth* condition for protons and kaons (pions) is required, are used instead. After their calculation, the corresponding rejections are corrected using the PIDCalib package as done in the previous step. Table 4.5 gives the $\Lambda_b^0 \to J/\psi p K^-$ and $\Lambda_b^0 \to J/\psi p \pi^-$ background overall rejections as well as the ones from the specific cuts implemented to reduce the Λ_b^0 peaking backgrounds: equivalent percentages as in Table 4.4 are presented but using different background samples. These cuts result in a rejection of $\sim 7\%$ of signal events (see Table 4.4) while rejecting $\sim 90\%$ and $\sim 38\%$ of $\Lambda_b^0 \to J/\psi p K^-$ and $\Lambda_b^0 \to J/\psi p \pi^-$ backgrounds, respectively.

Table 4.5: Background rejections over specific Λ_b^0 samples, for 2011 and 2012 conditions.

		$r_{\text{sel \& MVA}}$ (%)	$r_{\Lambda_b^0}$ (%)	r_{tot} (%)
$\Lambda_b^0 \to J/\psi p K^-$ sample	2011	97.78 ± 0.032	91.89 ± 0.66	99.82 ± 0.0093
	2012	97.38 ± 0.036	87.80 ± 1.00	99.68 ± 0.013
$\Lambda_b^0 \to J/\psi p \pi^-$ sample	2011	97.98 ± 0.031	37.54 ± 2.06	98.74 ± 0.025
	2012	98.06 ± 0.031	38.02 ± 5.81	98.80 ± 0.024

4.2 Treatment of peaking backgrounds

In addition to the signal and combinatorial background, extensive studies of fully simulated samples show contributions from several specific backgrounds, such as $B_s^0 \to J/\psi K^+ K^-$, $B_s^0 \to J/\psi \pi^+ \pi^-$ and $B^0 \to J/\psi \pi^+ \pi^-$ decay modes. The invariant mass distribution of misidentified $B^0 \to J/\psi \pi^+ \pi^-$ and $B_s^0 \to J/\psi \pi^+ \pi^-$ decays peaks near the $B_s^0 \to J/\psi K \pi$ signal peak, as shown in Figure 4.5, whilst the misidentified $B_s^0 \to J/\psi K^+ K^-$ events are located almost under the $B^0 \to J/\psi K \pi$ signal peak, see Figure 4.6. This behaviour makes the invariant mass of the J/ψ $K\pi$ system not to be a discriminating variable, and hence those misidentified backgrounds cannot be added as extra species to the mass model used for the fit with the ${}_s\mathcal{P}lot$ technique [113], see Chapter 4.3.1. Instead, and in the same way as ${}_s\mathcal{W}eights$ are applied such that sideband events cancel out the likelihood contribution from background events underneath

the peak, simulated events with negative weights are used to cancel out the likelihood contribution from these peaking background events present in the real data.

In Chapter 4.2.1, raw yields of expected backgrounds using simulated samples are calculated. As a next step, in Chapter 4.2.2, a per-event weighting to correct those samples to look like real data is assigned. There are also contributions from misidentified $\Lambda_b^0 \to J/\psi p K^-$ and $\Lambda_b^0 \to J/\psi p \pi^-$ peaking backgrounds. Only the latter is treated separately, added as an extra specie to the mass model, as shown in Chapter 4.2.3.

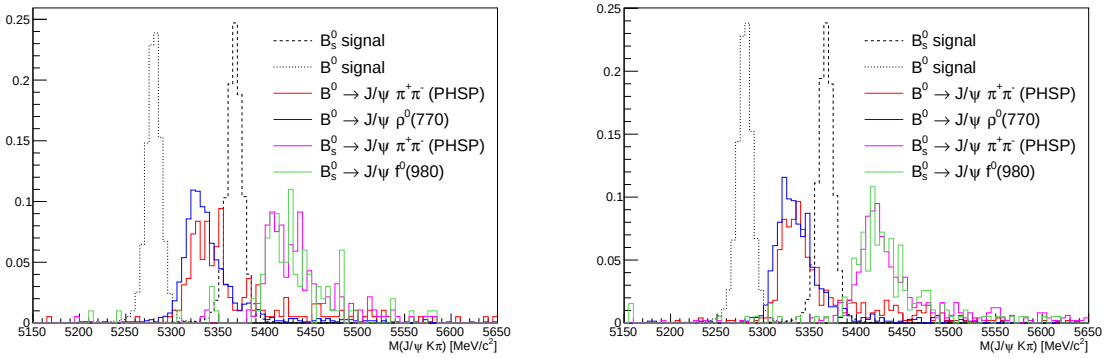

Figure 4.5: Invariant mass distributions from simulation of misidentified $B_s^0 \to J/\psi\pi^+\pi^-$ and $B^0 \to J/\psi\pi^+\pi^-$ peaking backgrounds, in comparison with invariant mass distributions from MC of $B_s^0 \to J/\psi K\pi$ and $B^0 \to J/\psi K\pi$ signal. MC-*truth* for kaons and pions is imposed, together with the offline requirements described in Chapter 4.1.3. Distributions are normalised to the same area. Left: Simulated data for 2011 conditions. Right: Simulated data for 2012 conditions.

4.2.1 Raw yields from simulated samples

The yields of the peaking backgrounds are estimated from simulated data as

$$N_{\text{exp}} = 2 \times \sigma_{b\bar{b}} \times P(b \to B_q) \times \mathcal{B}^{\text{vis}} \times \varepsilon \times \mathcal{L}, \tag{4.2}$$

being $P(b \to B_q)$ the hadronisation fraction (henceforth f_q), ε the total efficiency (reconstruction, offline selection and trigger), $\mathcal{L}$ the integrated luminosity of the real data, $\sigma_{b\bar{b}}$ the $b\bar{b}$ production cross section [121], and $\mathcal{B}^{\text{vis}}$ the visible branching fraction (taking into account not only the branching fraction of B_q but also the branching fractions of the daughter resonances) of the corresponding peaking background mode [117].

It is very convenient to just calculate the *effective luminosity* of the simulated samples and scale the yields to the luminosity of the data. The efficiencies of the particle identification (PID) requirements obtained in simulation are corrected using the PIDCalib package [91]. The angular and $m_{h^+h^-}$ properties of the $B^0_{(s)} \to J/\psi h^+h^-$ decays are also corrected using a weighting procedure (as described in Chapter 4.2.2). Hadronisation

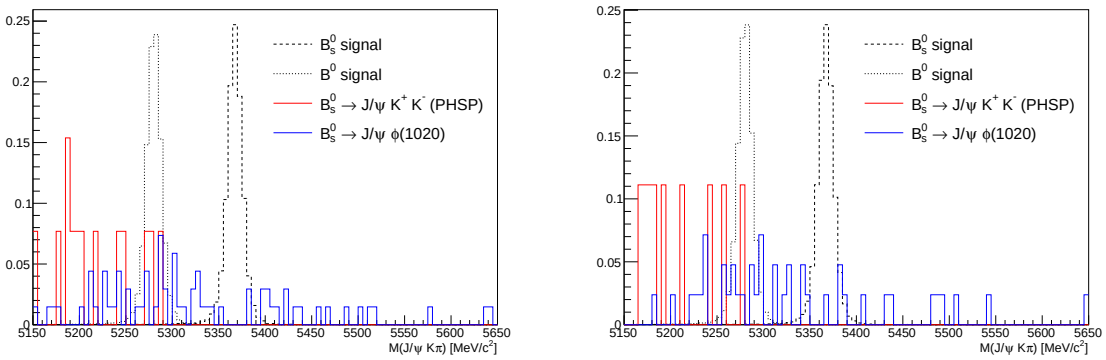

Figure 4.6: Invariant mass distributions from simulation of misidentified $B_s^0 \to J/\psi K^+K^-$ peaking background, in comparison with invariant mass distributions from MC of $B_s^0 \to J/\psi K\pi$ and $B^0 \to J/\psi K\pi$ signal. MC-*truth* for kaons and pions is imposed, together with the offline requirements described in Chapter 4.1.3. Distributions are normalised to the same area. Left: Simulated data for 2011 conditions. Right: Simulated data for 2012 conditions.

factors [122, 123] are obtained (see Appendix G) under the assumptions $f_d = f_u$ and $f_d + f_u + f_s + f_\Lambda = 1$, giving

$$f_d = f_u = 0.370 \pm 0.016, \qquad f_s = 0.0959 \pm 0.0068, \qquad f_{\Lambda_b^0} = 0.163 \pm 0.042. \tag{4.3}$$

The raw expectations found for the most relevant backgrounds are shown in Table 4.6. The predictions are shown for two assumptions of the decay model: only phase-space (PHSP), and that of the main resonance of the hh spectrum. In Chapter 4.2.2, events are weighted according to the latest measurements of their differential decay rates, in order to get more precise predictions.

4.2.2 Physical reweighting of simulated samples

The events from full simulation are generated in PHSP and hence do not contain the proper physical amplitudes. This can cause the yield estimations of Chapter 4.2.1 not to be accurate and cause the simulated events to be distributed in the decay angles and $K\pi$ mass space, $(\Omega, m_{K\pi})$, in a different way than the actual peaking background of the data.

The amplitude analysis of $B^0 \to J/\psi\pi^+\pi^-$, $B_s^0 \to J/\psi\pi^+\pi^-$, and $B_s^0 \to J/\psi K^+K^-$ decay modes has been performed in refs. [124], [125], and [126], respectively. Simulated events are weighted with

$$w_{\rm MC} = \frac{P_{DATA}(\Omega, m_{hh}|A_i)}{P_{\rm MC}(\Omega, m_{hh})}, \tag{4.4}$$

where the above PDFs are normalised to the phase space where $\cos\theta_K \in [-1, 1]$, $\cos\theta_\mu \in [-1, 1]$ and $\phi \in [-\pi, \pi]$, and where m_{hh} is inside the kinematical thresholds $[2 \times m_h, m_B -$

Table 4.6: Event yields predicted by MC simulation in the ± 70 MeV/c^2 $m_{K\pi}$ window and in the full $m_{K\pi}$ window, before any correction (other than PIDCalib). The predictions are shown for two assumptions of the decay model: PHSP, and that of the main resonance of the hh spectrum.

	hh model	Raw yield (2011)	Raw yield (2012)
$B^0 \to J/\psi\pi^+\pi^-$	PHSP	16.5 ± 3.8	37.4 ± 7.7
	$\rho^0(770)$	63 ± 13	134 ± 27
$B^0_s \to J/\psi\pi^+\pi^-$	PHSP	21.8 ± 5.1	45 ± 10
	$f^0(980)$	10.2 ± 2.5	22.8 ± 5.2
$B^0_s \to J/\psi K^+K^-$	PHSP	5.2 ± 1.3	9.6 ± 2.5
	$\phi(1020)$	7.3 ± 1.7	14.8 ± 3.2
$\Lambda^0_b \to J/\psi pK^-$	PHSP	4.6 ± 1.4	16.9 ± 5.0
$\Lambda^0_b \to J/\psi p\pi^-$	PHSP	13.1 ± 3.9	27.1 ± 6.3

$m_{J/\psi}$]. The functions P_{DATA} are constructed following ref. [127], and the mass dependency of the amplitudes is parameterised according to Table 4.7. Only the most significant resonances found in previous analyses (see refs. [124–126]) are considered.

Table 4.7: Resonances used to model $B^0_{(s)} \to J/\psi h^+h^-$ peaking backgrounds.

	Resonance	Shape
$B^0 \to J/\psi\pi^+\pi^-$	$\rho_0(770)$	relativistic Breit-Wigner
	$f_0(500)$	relativistic Breit-Wigner
	$f_2(1270)$	relativistic Breit-Wigner
$B^0_s \to J/\psi\pi^+\pi^-$	$f_0(980)$	Flatté
	$f_0(1500)$	relativistic Breit-Wigner
	$f_0(1790)$	relativistic Breit-Wigner
$B^0_s \to J/\psi K^+K^-$	$\phi(1020)$	relativistic Breit-Wigner
	$f_0(980)$	Flatté
	$f_2(1525)$	relativistic Breit-Wigner

Finally, for each peaking background, the corresponding weights are multiplied by overall normalisation constants,

$$W^{B^0_{(s)}\to J/\psi h^+h^-}_{\rm MC} = -\frac{N^{B^0_{(s)}\to J/\psi h^+h^-}_{exp}}{N^{B^0_{(s)}\to J/\psi h^+h^-}_{\rm MC\ entries}} \times w^{B^0_{(s)}\to J/\psi h^+h^-}_{\rm MC} . \tag{4.5}$$

As a side effect, this phase space weighting modifies the peaking background estimates, since events in different regions of the phase space are subject to different efficiencies. The updated effective yields are shown in Table 4.10.

Table 4.8: Approximated expected yields of each background after reweighting. It can be seen that the expectation for $B^0 \to J/\psi\pi^+\pi^-$ gets closer to that of $B^0 \to J/\psi\rho^0(\pi^+\pi^-)$ and $B_s^0 \to J/\psi\pi^+\pi^-$ gets closer to $B_s^0 \to J/\psi f_0(980)$ compared to those from PHSP. The mass binning used here is described in Chapter 4.3.

	Year	Total	Bin 1	Bin 2	Bin 3	Bin 4
$B^0 \to J/\psi\pi^+\pi^-$	2011	51.38	6.09	10.98	13.54	20.76
	2012	114.82	14.15	22.39	33.11	45.18
$B_s^0 \to J/\psi\pi^+\pi^-$	2011	9.34	1.62	2.23	2.85	2.64
	2012	24.97	3.88	4.68	7.00	9.40
$B_s^0 \to J/\psi K^+K^-$	2011	10.07	5.86	2.98	0.83	0.40
	2012	19.19	11.64	3.92	2.89	0.74
$\Lambda_b^0 \to J/\psi pK^-$	2011	36.11	7.30	8.38	10.51	9.91
	2012	90.06	18.9	21.7	23.94	25.53

4.2.3 The Λ_b^0 peaking backgrounds

The simulation studies of peaking background yields show contributions from the Λ_b^0 decay modes $\Lambda_b^0 \to J/\psi pK^-$ and $\Lambda_b^0 \to J/\psi p\pi^-$, which are treated differently in the mass fit model. On one hand, the $\Lambda_b^0 \to J/\psi pK^-$ channel is statistically subtracted by injecting simulated events from the model given in ref. [128], as done for backgrounds from B meson decays. On the other hand, since the full amplitude structure of $\Lambda_b^0 \to J/\psi p\pi^-$ decays was not yet known at the moment when this analysis was done, and because of the the fact that the peak of these decays in the $J/\psi\ K\pi$ mass spectrum is broad enough (see Figure 4.7) to make the ${}_s\mathcal{P}lot$ technique still effective; the $\Lambda_b^0 \to J/\psi p\pi^-$ channel is added as an extra specie to the mass fit model.

The $J/\psi\ K\pi$ mass line shape of the misidentified $\Lambda_b^0 \to J/\psi p\pi^-$ decays is parametrised using the Amoroso distribution [129], which provides a good description of the data (see Figure 4.7). The parameters of the distribution are obtained from simulation for each considered bin (see Chapter 4.3) of $m_{K\pi}$ and then fixed in the fit to real data. The two-dimensional Dalitz plane and projections of $\Lambda_b^0 \to J/\psi p\pi^-$ decays are measured in ref. [130], where some $p\pi^-$ resonances are identified. A conservative systematic (absolute difference between the original value and the re-estimated value) due to the effect of not taking into account these resonances (see Table 4.9) is estimated following the same weighting procedure as in Chapter 4.2.2, and then added in quadrature to the total uncertainty of $\Lambda_b^0 \to J/\psi p\pi^-$ yields from Table 4.6. The relative magnitude of this systematic uncertainty for the $\Lambda_b^0 \to J/\psi p\pi^-$ yield is approximately of 21.3% (21.7%) for 2011 (2012) conditions.

4.2.4 Summary of expected peaking backgrounds

The final estimates of peaking background yields are shown in Table 4.10.

Table 4.9: Resonances used to model $\Lambda_b^0 \to J/\psi p\pi^-$ peaking background for the estimation of a conservative systematic uncertainty.

	Resonance	Shape
$\Lambda_b^0 \to J/\psi p\pi^-$	$N(1440)$	relativistic Breit-Wigner
$\Lambda_b^0 \to J/\psi p\pi^-$	$N(1535)$	relativistic Breit-Wigner
$\Lambda_b^0 \to J/\psi p\pi^-$	$N(1650)$	relativistic Breit-Wigner

Table 4.10: Expected yields of each mode after reweighting, except for $\Lambda_b^0 \to J/\psi p\pi^-$ decays.

	Yield (2011)	Yield (2012)
$B^0 \to J/\psi\pi^+\pi^-$	51 ± 10	115 ± 23
$B_s^0 \to J/\psi\pi^+\pi^-$	9.3 ± 2.1	25.0 ± 5.4
$B_s^0 \to J/\psi K^+K^-$	10.1 ± 2.3	19.2 ± 4.0
$\Lambda_b^0 \to J/\psi pK^-$	36 ± 17	90 ± 43
$\Lambda_b^0 \to J/\psi p\pi^-$	13.8 ± 5.3	27.3 ± 9.0

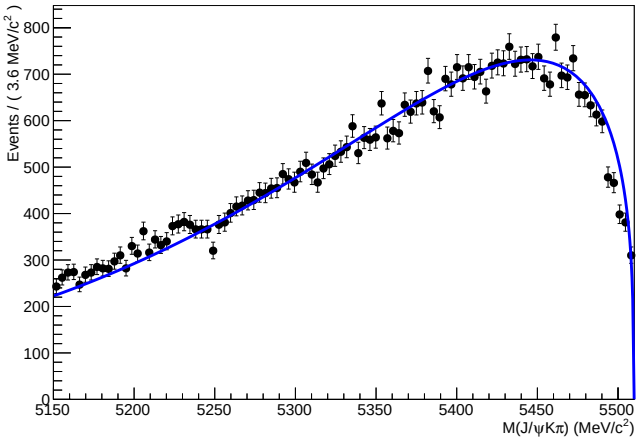

Figure 4.7: Fit of the Amoroso distribution (blue line) to $\Lambda_b^0 \to J/\psi p\pi^-$ simulated decays.

4.3 Mass model and invariant mass fit

After injecting $B^0 \to J/\psi\pi^+\pi^-$, $B_s^0 \to J/\psi\pi^+\pi^-$, $B_s^0 \to J/\psi K^+K^-$ and $\Lambda_b^0 \to J/\psi pK^-$ simulated events, the real data sample is left effectively with only $B^0 \to J/\psi K\pi$, $B_s^0 \to J/\psi K\pi$ and $\Lambda_b^0 \to J/\psi p\pi^-$ decays, along with combinatorial background (see Chapter 4.2). These four species are statistically disentangled through a mass fit using the ${}_s\mathcal{P}lot$ technique [113]. In the following paragraphs, a description of the mass model used for signal and background, along with the results from the invariant mass fit, are presented.

4.3.1 Mass model description

An exponential distribution is used to model the combinatorial background, while the $\Lambda_b^0 \to J/\psi p\pi^-$ decays are modelled using an Amoroso distribution (see Chapter 4.2.3). On the other hand, B_s^0 and B^0 signal decays are modeled using a double-sided Hypatia distribution [131]

$$
\begin{aligned}
&I(m,\mu,\sigma,\lambda,\zeta,\beta,a_1,a_2,n_1,n_2) \propto \\
&\begin{cases}
A/\left(B+m-\mu\right)^{n_1} & \text{if } m-\mu < -a_1\sigma\,, \\
C/\left(D+m-\mu\right)^{n_2} & \text{if } m-\mu > a_2\sigma\,, \\
\left((m-\mu)^2+\delta^2\right)^{\frac{1}{2}\lambda-\frac{1}{4}} e^{\beta(m-\mu)} K_{\lambda-\frac{1}{2}}\left(\alpha\sqrt{(m-\mu)^2+\delta^2}\right) & \text{otherwise}\,,
\end{cases}
\end{aligned}
\tag{4.6}
$$

where $K_\nu(z)$ is the modified Bessel function of the second kind, the parameter $\delta \equiv \sigma\sqrt{\zeta\, K_\lambda(\zeta)/K_{\lambda+1}(\zeta)}$, the parameter $\alpha \equiv \sqrt{\zeta\, K_{\lambda+1}(\zeta)/K_\lambda(\zeta)}/\sigma$, and A, B, C, D are obtained by imposing continuity and differentiability. This function is chosen because the event-by-event uncertainty on the mass has a dependence on the particle momenta.

The core of the Hypatia distribution models the resolution effects in which the per event variance is not constant, but rather an unknown quantity with certain prior probability. In addition, it allows to include extra (Crystal-Ball, CB [119]) tails in order to (phenomenologically) accommodate effects other than resolution. Those can be radiative tails, interplay of radiative tail with J/ψ mass constraint [131] or badly reconstructed events caused by decays of the final state hadrons (see Appendix B.2).

In the mass fit, the parameters ζ and β are fixed to zero, leaving free the mean and the resolution, μ and σ respectively. The other parameters, λ, a_1, and n_1 , a_2 and n_2, are determined from simulation. The parameters a_1 and n_1 describe the left-hand side radiative tail and are fixed given a known photon spectrum and resolution (which has been tuned in simulation to match that of the data). This means that the three parameters λ, a_2 and n_2 taken from MC do not rely on detector simulation, but only on the decay kinematics and in the knowledge of the mass resolution. A systematic associated to uncontrolled contributions to the mass tails is added by allowing a_2 to be finite using the value obtained from simulation. Setting a_2 "to infinity" effectively neglects

the contribution from events that are in the tails for reasons other than resolution. A fraction of $B^0 \to J/\psi K\pi$ events, whose estimation is extremely sensitive to the modelling of the tails of the B^0 peak, populates into the region of the B_s^0 peak (see Appendix B.1).

The ${}_s\mathcal{P}lot$ technique is used to subtract $\Lambda_b^0 \to J/\psi p\pi^-$ peaking background decays, and combinatorial background from the data sample. A fit to the discriminating variable, $M(J/\psi K\pi)$, assigns an sWeight, sW_i, to each event. Moreover, events that are likely to be background are assigned negative or very small weights. Thus, the so-called sFit can be performed to the weighted angular distribution, which reduces the computing time and the systematic uncertainties related to the background modelling. In order to have an accurate result, the discriminating variable, $M(J/\psi K\pi)$, should be independent from the variables used in the sFit. A correction factor $\alpha = \sum_i sW_i / \sum_i sW_i^2$ has to be applied to account for the effect of the ${}_s\mathcal{W}eights$ in the determination of the statistical uncertainties, that are usually underestimated by the sFit to the weighted data sample [113].

From simulation studies, some of the B_s^0 and B^0 Hypatia parameters appear to be significantly correlated with the $m_{K\pi}$ invariant mass. Since these parameters need to be fixed in the fit to the $J/\psi K\pi$ invariant mass, the latter is performed in four bins of the $m_{K\pi}$ mass spectrum. In addition, due to correlations between the invariant mass and the cosine of the helicity angle θ_μ (defined in Figure 4.13), which is a fit variable, the ${}_s\mathcal{P}lot$ formalism cannot be applied, unless taking explicitly the corresponding correlations into account while extracting the ${}_s\mathcal{W}eights$. Therefore, each bin of the $m_{K\pi}$ invariant mass is divided in five bins of $\cos(\theta_\mu)$, resulting in a total of 20 bins. The four $m_{K\pi}$ bins are defined as $[826, 861]$, $(861, 896]$, $(896, 931]$ and $(931, 966]$ MeV/c^2 (named as bins 1 to 4, respectively), while the five $\cos(\theta_\mu)$ bins are $[-1.0, -0.6)$, $[-0.6, -0.2)$, $[-0.2, 0.2)$, $[0.2, 0.6)$ and $[0.6, 1.0]$ (referred to as bins 1 to 5, respectively). The dependence with $m_{K\pi}$ and $\cos(\theta_\mu)$ of the $M(J/\psi, K\pi)$ lineshape for signal events is illustrated in Figure 4.8 using simulated events, where hereafter MC-*truth* is required over hadrons (kaons and pions).

The presence of eventual contamination from K/π swapped events from $B^0 \to J/\psi K^{*0}$ events under the B_s^0 peak is taken into account. Figure 4.9 shows the invariant mass distributions for MC-*truth* and K/π swaps simulated $B^0 \to J/\psi K^{*0}$ and $B_s^0 \to J/\psi \overline{K}^{*0}$ events, where the ProbNN requirements used in the final selection have been removed. In the limit of the simulated sample size, it appears that both the distributions from B^0 and B_s^0 K/π swapped events do not significantly leak under each other peaks. Without the ProbNN requirements, the K/π contamination is at the level of $\sim 5 \times 10^{-4}$. When putting back the ProbNN requirements, the level of K/π contamination goes down to $\sim 8 \times 10^{-6}$. It can be concluded that the K/π swaps are negligible in the present analysis.

4.3.2 Invariant mass fit results

The signal yield is extracted from 20 independent fits to the $m(\mu^+\mu^- K\pi)$ invariant mass spectrum using the mass fit model described in Chapter 4.3.1. For each fit, the dataset is split according to the $m_{K\pi}$ and $\cos(\theta_\mu)$ bins. The full results of each fit are given in Table 4.11 to Table 4.15. From a simultaneous fit split in the 20 categories, identical results as the ones obtained in the 20 independent fits are found. In addition, no correlation

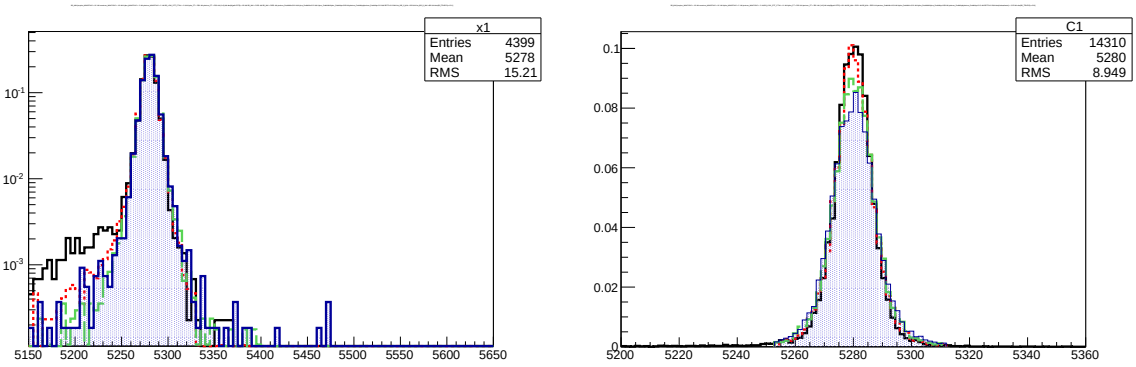

Figure 4.8: Invariant mass distribution for MC-*truth* simulated $B^0 \to J/\psi K^{*0}$ events in bins of $m_{K\pi}$ (left) and —cos(θ_μ) — (right). The color code is as follows. Left plot: bin 1 (solid black), bin 2 (red dotted), bin 3 (green dashed), bin 4 (blue filled). Right plot: $|\cos(\theta_\mu)| < 0.25$ (solid black), $0.25 < |\cos(\theta_\mu)| < 0.5$ (red dotted), $0.5 < |\cos(\theta_\mu)| < 0.75$ (green dashed), $|\cos(\theta_\mu)| > 0.75$ (blue filled).

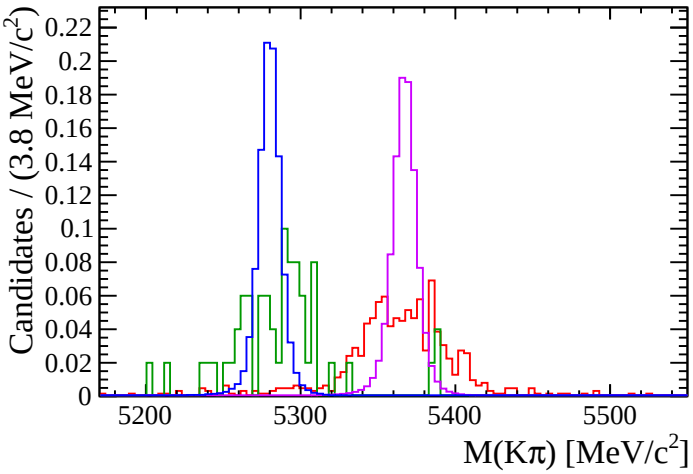

Figure 4.9: Comparison of the invariant mass distribution for MC-*truth* and K/π swaps simulated $B^0 \to J/\psi K^{*0}$ and $B_s^0 \to J/\psi \overline{K}^{*0}$ events without the ProbNN requirements in the final selection. All distributions are normalised to unit area. The color code is as follows: MC-*truth* B^0 (blue), K/π swap B^0 (green), MC-*truth* B_s^0 (red), K/π swap B_s^0 (violet).

among the parameters between the fitting categories are observed. Therefore, the overall B_s^0 and B^0 yields are obtained from the sum of yields over the 20 bins, giving

$$N_{B^0} = 208656 \pm 462^{+78}_{-76}\,, \tag{4.7}$$

$$N_{B_s^0} = \quad 1808 \pm 51^{+38}_{-33}\,, \tag{4.8}$$

where the first uncertainties are statistical and obtained from the quadratic sum of the ones in each fitting category, and the second uncertainties correspond to systematics. The correlations between the B^0 and B_s^0 yields in each fitting category are found to be smaller than 4%. Neglecting these correlations, the ratio

$$\frac{N_{B_s^0}}{N_{B^0}} = (8.66 \pm 0.24^{+0.18}_{-0.16}) \times 10^{-3} \tag{4.9}$$

obtained for the entire data sample is computed, where the first uncertainty is statistical and the second uncertainties correspond to systematics. Figure 4.11 shows the sum of the fit projections of each bin overlaid to the $m(J/\psi K^+\pi^-)$ mass spectrum for the entire data sample. Figure 4.12 shows the $\mu\mu$ spectrum and the $m_{K\pi}$ spectrum. While the B_s^0 or B^0 di-muon ${}_s\mathcal{P}lots$ have very similar shape, the $m_{K\pi}$ weighted spectrums exhibit different shapes. The B_s^0 $m_{K\pi}$ ${}_s\mathcal{P}lot$ seems to be slightly distorted. This could be due to the presence of interference between the $K\pi$ S-wave and the K^{*0}, which would appear to be stronger in the B_s^0 decays compared to the B^0.

In order to check the validity of this hypothesis, two additional studies are performed. First, it is checked if the peaking background treatment propagated to the ${}_s\mathcal{W}eights$ is responsible for this behavior. No significant difference between the B_s^0 $m_{K\pi}$ spectrum using ${}_s\mathcal{W}eights$ computed with and without MC data injection is found. An additional study looking at the $m_{K\pi}$ structure after correcting for efficiency effects using the normalisation weights coming from the angular acceptance study, is performed. The interference between the $K\pi$ S-wave and the K^{*0}P-wave vanishes, since an integration over the helicity angles is done. Figure 4.10 gives the efficiency corrected B_s^0 and B^0 $m_{K\pi}$ spectra using the nominal sets of ${}_s\mathcal{W}eights$. It is observed that the B_s^0 $m_{K\pi}$ distribution is closer to the one of the B^0 after applying the efficiency correction. This is a clear indication of the presence of stronger interference in the B_s^0 case compared to the B^0 one.

The effect of allowing the mean and sigma of the B_s^0 and B^0 Hypatia functions to share common values over the 20 bins from a simultaneous fit is checked. No significant gain was observed. The corresponding results are presented in Appendix B.3.

Table 4.11: Results of the fit to the invariant mass of each individual $m_{K\pi}$ bin category for $-1.0 \leq \cos(\theta_\mu) < -0.6$.

	$826 \leq m_{K\pi} \leq 861$ MeV/c^2	$861 < m_{K\pi} \leq 896$ MeV/c^2	$896 < m_{K\pi} \leq 931$ MeV/c^2	$931 < m_{K\pi} \leq 966$ MeV/c^2
k_{bkg}	$-0.0043 \pm 0.0014^{+0.0003}_{-0.0003}$	$-0.0007 \pm 0.0016^{+0.0008}_{-0.0007}$	$-0.0042 \pm 0.0011^{+0.0004}_{-0.0004}$	$-0.0043 \pm 0.0009^{+0.0004}_{-0.0004}$
μ_{B^0}	$5\ 280.95 \pm 0.15^{+0.00}_{-0.00}$	$5\ 281.00 \pm 0.07^{+0.03}_{-0.04}$	$5\ 281.44 \pm 0.08^{+0.02}_{-0.02}$	$5\ 281.72 \pm 0.14^{+0.01}_{-0.01}$
$\mu_{B_s^0}$	$5\ 370.17 \pm 2.48^{+0.33}_{-0.40}$	$5\ 369.05 \pm 0.87^{+0.55}_{-0.16}$	$5\ 368.38 \pm 1.17^{+0.50}_{-0.51}$	$5\ 367.68 \pm 1.72^{+0.19}_{-0.30}$
σ_{B^0}	$10.03 \pm 0.16^{+0.18}_{-0.14}$	$10.26 \pm 0.08^{+0.07}_{-0.06}$	$9.91 \pm 0.08^{+0.07}_{-0.07}$	$10.37 \pm 0.14^{+0.15}_{-0.12}$
$\sigma_{B_s^0}$	$12.23 \pm 3.15^{+0.36}_{-0.34}$	$9.07 \pm 0.95^{+0.38}_{-0.83}$	$12.67 \pm 1.51^{+1.48}_{-1.48}$	$9.02 \pm 2.06^{+0.84}_{-0.79}$
N_{B^0}	$4008.8 \pm 66.1^{+5.4}_{-5.0}$	$15964.8 \pm 127.4^{+12.6}_{-12.6}$	$14664.2 \pm 122.2^{+29.7}_{-29.6}$	$4842.2 \pm 70.9^{+15.7}_{-15.4}$
$N_{B_s^0}$	$31.9 \pm 7.7^{+1.1}_{-0.8}$	$132.2 \pm 13.2^{+3.6}_{-12.1}$	$138.0 \pm 14.4^{+16.9}_{-16.7}$	$42.0 \pm 8.8^{+4.3}_{-4.2}$
N_{Bkg}	$87.2 \pm 22.4^{+6.4}_{-7.3}$	$66.7 \pm 19.7^{+11.0}_{-11.7}$	$97.6 \pm 19.5^{+10.9}_{-11.2}$	$116.6 \pm 17.6^{+9.6}_{-9.7}$
$N_{\Lambda p\pi}$	$1.8 \pm 0.6^{+0.0}_{-0.0}$	$2.0 \pm 0.6^{+0.0}_{-0.0}$	$2.0 \pm 0.6^{+0.0}_{-0.0}$	$2.3 \pm 0.7^{+0.0}_{-0.0}$

Table 4.12: Results of the fit to the invariant mass of each individual $m_{K\pi}$ bin category for $-0.6 \leq \cos(\theta_\mu) < -0.2$.

	$826 \leq m_{K\pi} \leq 861$ MeV/c^2	$861 < m_{K\pi} \leq 896$ MeV/c^2	$896 < m_{K\pi} \leq 931$ MeV/c^2	$931 < m_{K\pi} \leq 966$ MeV/c^2
k_{bkg}	$-0.0028 \pm 0.0014^{+0.0002}_{-0.0002}$	$-0.0045 \pm 0.0008^{+0.0001}_{-0.0002}$	$-0.0030 \pm 0.0011^{+0.0002}_{-0.0002}$	$-0.0071 \pm 0.0014^{+0.0010}_{-0.0010}$
μ_{B^0}	$5\ 281.06 \pm 0.11^{+0.01}_{-0.01}$	$5\ 281.08 \pm 0.06^{+0.00}_{-0.00}$	$5\ 281.59 \pm 0.06^{+0.01}_{-0.01}$	$5\ 281.52 \pm 0.12^{+0.01}_{-0.01}$
$\mu_{B^0_s}$	$5\ 367.44 \pm 1.60^{+0.07}_{-0.05}$	$5\ 369.35 \pm 0.87^{+0.17}_{-0.09}$	$5\ 368.16 \pm 0.73^{+0.30}_{-0.32}$	$5\ 368.78 \pm 1.46^{+0.08}_{-0.11}$
σ_{B^0}	$8.42 \pm 0.12^{+0.15}_{-0.12}$	$8.69 \pm 0.06^{+0.05}_{-0.05}$	$8.58 \pm 0.07^{+0.06}_{-0.06}$	$9.04 \pm 0.12^{+0.12}_{-0.14}$
$\sigma_{B^0_s}$	$7.74 \pm 1.89^{+0.31}_{-0.25}$	$7.90 \pm 1.07^{+0.33}_{-0.28}$	$8.58 \pm 0.85^{+0.67}_{-0.65}$	$10.33 \pm 1.69^{+0.65}_{-0.46}$
N_{B^0}	$5012.9 \pm 72.8^{+7.9}_{-7.9}$	$17416.8 \pm 133.4^{+11.0}_{-10.9}$	$15481.1 \pm 125.6^{+26.4}_{-26.3}$	$5016.5 \pm 72.2^{+17.1}_{-15.8}$
$\text{N}_{B^0_s}$	$33.2 \pm 7.1^{+1.0}_{-0.8}$	$105.1 \pm 12.3^{+2.9}_{-2.8}$	$152.3 \pm 14.1^{+10.9}_{-10.7}$	$63.9 \pm 10.0^{+5.2}_{-4.0}$
N_{Bkg}	$78.4 \pm 19.8^{+10.1}_{-10.2}$	$169.9 \pm 24.0^{+12.3}_{-11.6}$	$95.9 \pm 19.6^{+13.9}_{-13.9}$	$95.6 \pm 16.5^{+12.3}_{-10.9}$
$\text{N}_{\Lambda p\pi}$	$1.8 \pm 0.6^{+0.0}_{-0.0}$	$2.0 \pm 0.6^{+0.0}_{-0.0}$	$2.0 \pm 0.6^{+0.0}_{-0.0}$	$2.3 \pm 0.7^{+0.0}_{-0.0}$

Table 4.13: Results of the fit to the invariant mass of each individual $m_{K\pi}$ bin category for $-0.2 \leq \cos(\theta_\mu) < 0.2$.

	$826 \leq m_{K\pi} \leq 861$ MeV/c^2	$861 < m_{K\pi} \leq 896$ MeV/c^2	$896 < m_{K\pi} \leq 931$ MeV/c^2	$931 < m_{K\pi} \leq 966$ MeV/c^2
k_{bkg}	$-0.0017 \pm 0.0011^{+0.0002}_{-0.0002}$	$-0.0040 \pm 0.0008^{+0.0002}_{-0.0002}$	$-0.0049 \pm 0.0008^{+0.0003}_{-0.0003}$	$-0.0040 \pm 0.0009^{+0.0003}_{-0.0003}$
μ_{B^0}	$5\ 281.11 \pm 0.10^{+0.01}_{-0.01}$	$5\ 281.00 \pm 0.05^{+0.16}_{-0.39}$	$5\ 281.67 \pm 0.06^{+0.01}_{-0.01}$	$5\ 281.45 \pm 0.11^{+0.02}_{-0.01}$
$\mu_{B^0_s}$	$5\ 370.94 \pm 2.72^{+0.27}_{-0.27}$	$5\ 369.72 \pm 0.82^{+0.45}_{-0.11}$	$5\ 368.59 \pm 0.76^{+0.11}_{-0.11}$	$5\ 370.61 \pm 1.12^{+0.10}_{-0.20}$
σ_{B^0}	$7.97 \pm 0.11^{+0.15}_{-0.11}$	$8.01 \pm 0.06^{+0.11}_{-0.11}$	$7.95 \pm 0.06^{+0.06}_{-0.05}$	$8.35 \pm 0.11^{+0.12}_{-0.09}$
$\sigma_{B^0_s}$	$14.59 \pm 4.91^{+1.11}_{-1.09}$	$7.53 \pm 0.89^{+0.50}_{-0.46}$	$8.88 \pm 0.92^{+0.50}_{-0.50}$	$8.08 \pm 1.20^{+0.49}_{-0.36}$
N_{B^0}	$5470.4 \pm 75.2^{+9.2}_{-8.7}$	$18252.7 \pm 136.3^{+12.2}_{-11.5}$	$15713.0 \pm 126.3^{+26.7}_{-26.2}$	$5102.4 \pm 72.8^{+15.5}_{-13.5}$
$\text{N}_{B^0_s}$	$38.1 \pm 9.0^{+1.8}_{-2.0}$	$110.1 \pm 12.1^{+3.6}_{-2.9}$	$144.9 \pm 13.8^{+8.8}_{-8.8}$	$67.2 \pm 9.8^{+3.4}_{-3.2}$
N_{Bkg}	$86.6 \pm 17.7^{+10.0}_{-9.9}$	$146.8 \pm 22.2^{+11.9}_{-11.3}$	$143.2 \pm 19.6^{+15.3}_{-14.9}$	$114.3 \pm 17.0^{+11.4}_{-9.8}$
$\text{N}_{\Lambda p\pi}$	$1.8 \pm 0.6^{+0.0}_{-0.0}$	$2.0 \pm 0.6^{+0.1}_{-1.1}$	$2.0 \pm 0.6^{+0.0}_{-0.0}$	$2.2 \pm 0.7^{+0.0}_{-0.0}$

Table 4.14: Results of the fit to the invariant mass of each individual $m_{K\pi}$ bin category for $0.2 \leq \cos(\theta_\mu) < 0.6$.

	$826 \leq m_{K\pi} \leq 861$ MeV/c^2	$861 < m_{K\pi} \leq 896$ MeV/c^2	$896 < m_{K\pi} \leq 931$ MeV/c^2	$931 < m_{K\pi} \leq 966$ MeV/c^2
k_{bkg}	$0.0000 \pm 0.0067^{+0.0001}_{-0.0003}$	$-0.0018 \pm 0.0011^{+0.0002}_{-0.0002}$	$-0.0054 \pm 0.0009^{+0.0004}_{-0.0004}$	$-0.0038 \pm 0.0008^{+0.0003}_{-0.0003}$
μ_{B^0}	$5\ 281.06 \pm 0.11^{+0.01}_{-0.01}$	$5\ 281.00 \pm 0.06^{+0.01}_{-0.01}$	$5\ 281.64 \pm 0.06^{+0.02}_{-0.02}$	$5\ 281.57 \pm 0.11^{+0.01}_{-0.01}$
$\mu_{B^0_s}$	$5\ 371.86 \pm 2.05^{+0.12}_{-0.12}$	$5\ 368.07 \pm 0.96^{+0.11}_{-0.12}$	$5\ 367.91 \pm 0.91^{+0.32}_{-0.32}$	$5\ 367.50 \pm 1.07^{+0.08}_{-0.18}$
σ_{B^0}	$8.37 \pm 0.12^{+0.15}_{-0.12}$	$8.70 \pm 0.06^{+0.06}_{-0.05}$	$8.50 \pm 0.06^{+0.06}_{-0.06}$	$8.80 \pm 0.12^{+0.12}_{-0.14}$
$\sigma_{B^0_s}$	$11.60 \pm 2.60^{+0.29}_{-0.28}$	$9.54 \pm 1.04^{+0.24}_{-0.23}$	$11.25 \pm 1.07^{+0.75}_{-0.75}$	$7.11 \pm 1.33^{+0.53}_{-0.32}$
N_{B^0}	$4904.6 \pm 70.6^{+5.4}_{-5.0}$	$17315.8 \pm 132.7^{+10.7}_{-10.7}$	$15528.2 \pm 125.6^{+26.4}_{-26.2}$	$4993.6 \pm 72.0^{+15.5}_{-14.9}$
$\text{N}_{B^0_s}$	$36.6 \pm 7.5^{+0.8}_{-0.8}$	$127.3 \pm 13.0^{+2.9}_{-2.8}$	$169.6 \pm 15.1^{+12.8}_{-12.7}$	$57.0 \pm 9.5^{+3.8}_{-3.2}$
N_{Bkg}	$53.2 \pm 11.0^{+7.2}_{-6.4}$	$103.9 \pm 20.2^{+11.3}_{-11.1}$	$135.8 \pm 19.8^{+11.6}_{-11.6}$	$129.4 \pm 17.7^{+10.9}_{-10.4}$
$\text{N}_{\Lambda p\pi}$	$1.8 \pm 0.6^{+0.0}_{-0.0}$	$2.0 \pm 0.6^{+0.0}_{-0.0}$	$2.0 \pm 0.6^{+0.0}_{-0.0}$	$2.3 \pm 0.7^{+0.0}_{-0.0}$

Table 4.15: Results of the fit to the invariant mass of each individual $m_{K\pi}$ bin category for $0.6 \leq \cos(\theta_\mu) \leq 1.0$.

	$826 \leq m_{K\pi} \leq 861$ MeV/c^2	$861 < m_{K\pi} \leq 896$ MeV/c^2	$896 < m_{K\pi} \leq 931$ MeV/c^2	$931 < m_{K\pi} \leq 966$ MeV/c^2
k_{bkg}	$-0.0057 \pm 0.0014^{+0.0005}_{-0.0006}$	$-0.0014 \pm 0.0015^{+0.0004}_{-0.0003}$	$-0.0017 \pm 0.0013^{+0.0002}_{-0.0003}$	$-0.0042 \pm 0.0012^{+0.0005}_{-0.0005}$
μ_{B^0}	$5\ 280.90 \pm^{+0.00}_{-0.00}$	$5\ 280.85 \pm 0.07^{+0.01}_{-0.01}$	$5\ 281.48 \pm 0.08^{+0.12}_{-0.11}$	$5\ 281.41 \pm 0.14^{+0.01}_{-0.01}$
$\mu_{B^0_s}$	$5\ 371.26 \pm 1.99^{+0.11}_{-0.20}$	$5\ 368.80 \pm 0.97^{+0.04}_{-0.08}$	$5\ 368.36 \pm 0.93^{+0.20}_{-0.20}$	$5\ 368.01 \pm 1.72^{+0.49}_{-0.26}$
σ_{B^0}	$10.05 \pm 0.16^{+0.18}_{-0.14}$	$10.23 \pm 0.08^{+0.06}_{-0.06}$	$9.80 \pm 0.08^{+0.08}_{-0.09}$	$10.28 \pm 0.15^{+0.15}_{-0.12}$
$\sigma_{B^0_s}$	$10.56 \pm 2.78^{+0.54}_{-0.52}$	$10.06 \pm 1.06^{+0.40}_{-0.38}$	$10.67 \pm 1.07^{+0.97}_{-0.97}$	$10.02 \pm 2.36^{+1.18}_{-1.04}$
N_{B^0}	$4046.6 \pm 65.3^{+6.5}_{-6.0}$	$15804.8 \pm 126.5^{+12.7}_{-11.1}$	$14422.5 \pm 120.9^{+30.3}_{-29.7}$	$4693.7 \pm 69.8^{+14.1}_{-14.1}$
$N_{B^0_s}$	$32.8 \pm 7.5^{+1.0}_{-0.9}$	$129.9 \pm 13.1^{+4.3}_{-3.5}$	$145.9 \pm 13.9^{+24.4}_{-14.0}$	$49.6 \pm 9.5^{+6.0}_{-5.2}$
N_{Bkg}	$71.7 \pm 17.9^{+8.9}_{-9.8}$	$63.1 \pm 17.2^{+9.8}_{-12.4}$	$62.0 \pm 15.5^{+13.2}_{-13.6}$	$80.2 \pm 16.5^{+7.8}_{-7.7}$
$N_{\Lambda p\pi}$	$1.8 \pm 0.6^{+0.0}_{-0.0}$	$2.0 \pm 0.6^{+0.0}_{-0.0}$	$2.0 \pm 0.6^{+0.1}_{-1.9}$	$2.3 \pm 0.7^{+0.0}_{-0.0}$

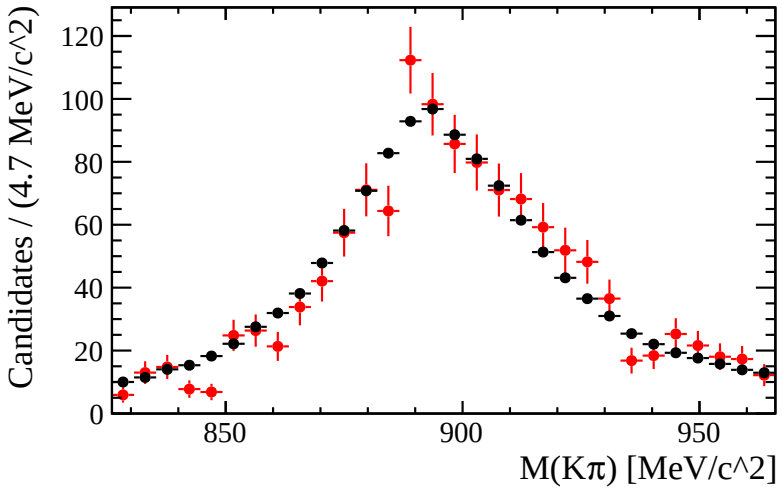

(b)

Figure 4.10: Efficiency corrected $K\pi$ invariant mass spectra using the B^0_s (red markers) and B^0 (black markers) ${}_s\mathcal{W}eights$ computed from the maximum likelihood fit to the $K\pi\mu^+\mu^-$ invariant mass spectrum.

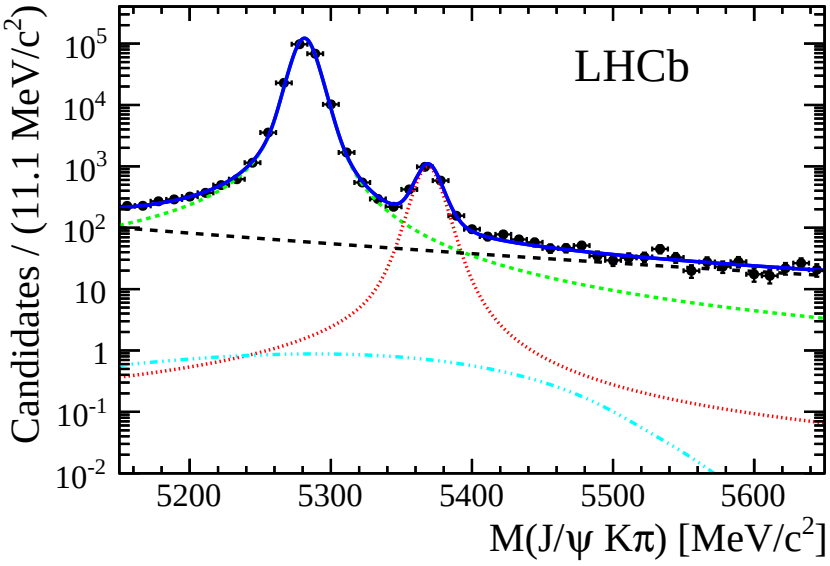

(a)

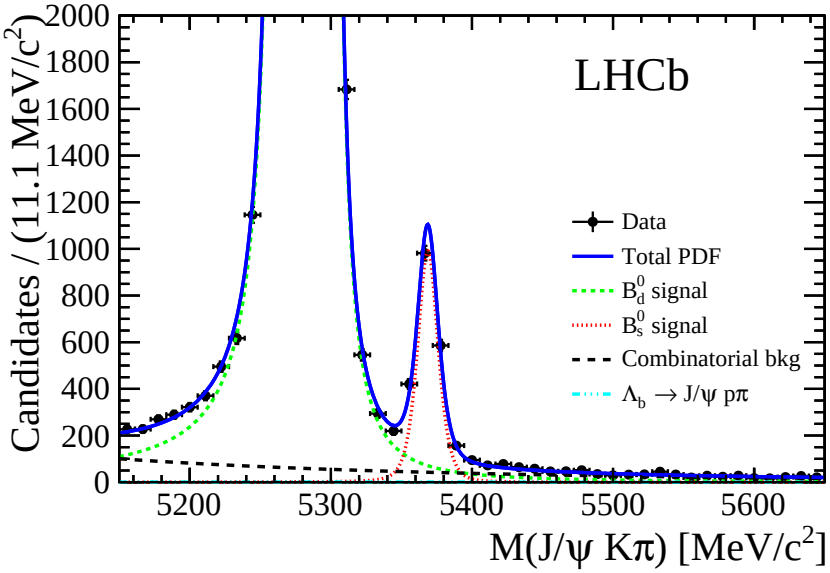

(b)

Figure 4.11: Sum of the fit projections in the 20 bins with a linear (a) and logarithmic scale (b) on the y-axis. The legend displayed in (b) also applies to (a).

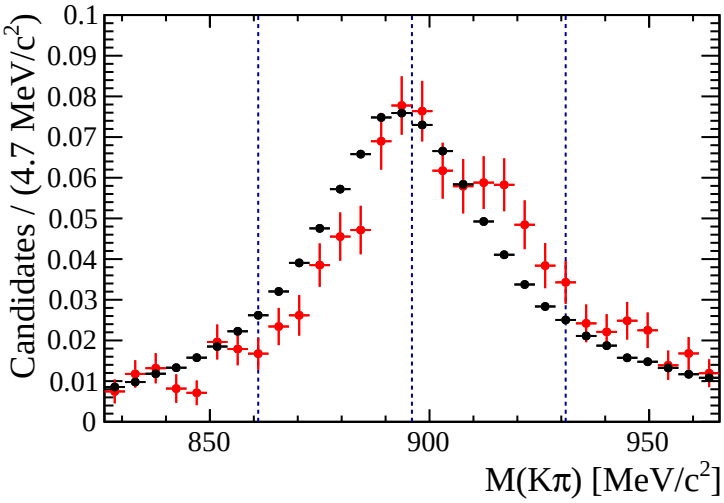

(a)

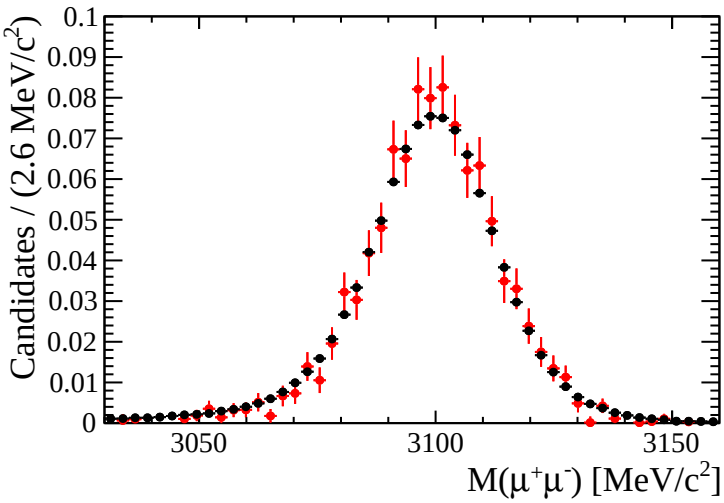

(b)

Figure 4.12: Weighted $K\pi$ (a) and $\mu^+\mu^-$ (b) invariant mass spectra using the B_s^0 (red markers) and B^0 (black markers) ${}_s\mathcal{W}eights$ computed from the maximum likelihood fit to the $K\pi\mu^+\mu^-$ invariant mass spectrum. The vertical dashed lines in (a) describe the four $m_{K\pi}$ bins.

4.3.3 Fit validation

In order to test the robustness of the fit model, before extracting the parameters of interest in the data, validation tests are performed by means of "toy MC" studies, using generated pseudoexperiments. These allow, using "pull" distributions, to estimate the potential biases that can arise from the model. In order to get a realistic estimation of these biases, each toy sample must be statistically equivalent to the real data sample. In other words, the different categories present in the fit model must have yields and characteristics corresponding to these expected in data. The pull of a free parameter a in the i-th pseudoexperiment is defined as

$$\text{pull}_i = \frac{a_i^f - a_i^t}{\sigma_i^f} \ , \tag{4.10}$$

where a_i^f and σ_i^f correspond to the fitted value of a parameter and its fit error, respectively, and a_i^t is the generated value. In case the parameter is unbiased, the corresponding pull distribution may be considered as a gaussian of zero mean and unity width. Otherwise, the pull distribution gives the bias in units of the statistical error. The pull definition in (4.10) is only valid in the case of symmetric fitted errors. In the case of asymmetric errors, the pull is now defined as

$$\text{pull}_i = \frac{\xi\left(a_i^f - a_i^t\right)}{\widetilde{\sigma}_i^f} \begin{cases} a_i^f < a_i^t \ \Rightarrow \ \xi = +1 \ ; \ \widetilde{\sigma}_i^f = \sigma_i^{f,+} \\ a_i^f \geq a_i^t \ \Rightarrow \ \xi = -1 \ ; \ \widetilde{\sigma}_i^f = \sigma_i^{f,-} \end{cases} \ , \tag{4.11}$$

where $\sigma_i^{f,+}$ and $\sigma_i^{f,-}$ correspond to the positive and negative errors returned by the fit, when using `MINOS`.

Two types of toy studies will be considered: *pure* and *embedded*. Pure toys consist in generating pseudoexperiments using the fit model itself. They allow to determine which PDF parameters can be varied in the fit, and are sensitive for instance to biases due to small number of events. Embedded toy studies use reconstructed simulation events for as many as possible event categories, which are embedded within generated samples for the other categories. They are sensitive to reconstruction effects, such as correlations between variables. It is ensured that for each embedded category, a simulation event does not appear twice, and thus the limitation of these studies is the number of statistically independent simulation samples that can be used to construct the pull distribution. Significant biases observed in these studies could then be corrected in the fit to data. Here the B_s^0, B^0 signals and combinatorial backgrounds are generated from their nominal PDFs, while the various peaking backgrounds are embedded from simulation samples. Since in the present analysis a fit to the invariant mass distribution is used in order to statistically disentangled the signal events (i.e. $B_s^0 \to J/\psi \overline{K}^{*0}$ decays) using the ${}_s\mathcal{P}lot$ technique [113], the toy MC studies must be performed in two steps.

First, a study using toy MC to check the presence of potential biases on the parameters entering the mass fit model is performed. The signal yield should not exhibit a large bias

in order to obtain an unbiased set of ${}_s\mathcal{W}eights$. The presence of significant biases on the other parameters should not affect the ${}_s\mathcal{W}eights$ corresponding to the signal. The results of this study are presented in Appendix F.1. In a second step, as described in Chapter 4.4, an angular analysis is performed using the sFit technique [132] in order to extract the parameters of interest. Therefore biases originating from two sources may occur here: intrinsic biases due to the fit model, and biases from the ${}_s\mathcal{W}eights$ applied to the data sample. These two potential sources of biases are studied using toy studies, as described in Appendix F.2. Note that the mass and the angular distributions are generated together to ensure that the ${}_s\mathcal{W}eights$ extracted from the fit to the mass are applied to the correct events when performing the toy studies of the angular fit model. Results from these studies are taken into account as systematic uncertainties for each corresponding parameter obtained from the final fit (see Chapter 4.6.5).

4.4 Angular analysis and *CP* asymmetries

This analysis uses the decay angles defined in the helicity basis. The helicity angles are denoted by $(\theta_K, \theta_\mu, \varphi_h)$ and their definition is shown in Fig. 4.13. The polar angle θ_K (θ_μ) is the angle between the kaon (μ^+) momentum and the direction opposite to the B_s^0 momentum in the $K\pi$ ($\mu^+\mu^-$) centre-of-mass system. The azimuthal angle between the $K\pi$ and $\mu^+\mu^-$ decay planes is φ_h. This angle is defined by a rotation from the pion side of the $K\pi$ plane to the μ^+ side of the $\mu^+\mu^-$ plane. The rotation is positive in the $\mu^+\mu^-$ direction in the B_s^0 rest frame. The definitions are the same whether a B_s^0 or a $\overline{B}_s^0$ decays. They are also the same for the $B^0 \to J/\psi K^{*0}$ decays.

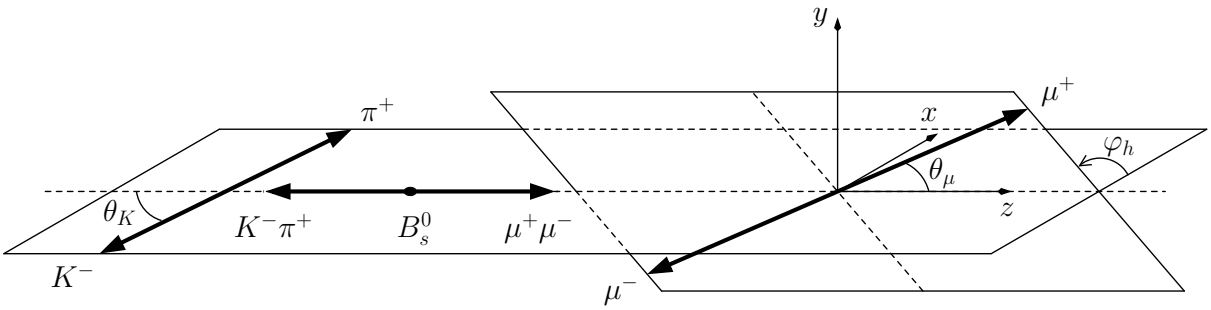

Figure 4.13: Definition of helicity angles.

4.4.1 Angular formalism

The angular distribution of $B_s^0 \to J/\psi \overline{K}^{*0}$ decays is obtained as [127]

$$\mathrm{PDF}(\theta_K, \theta_\mu, \varphi_h) = \sum_{\alpha_\mu = \pm 1} \left| \sum_{\lambda, J}^{|\lambda|<J} \sqrt{\frac{2J+1}{4\pi}} \mathcal{H}_\lambda^J e^{-i\lambda\varphi_h} d^1_{\lambda,\alpha_\mu}(\theta_\mu) d^1_{-\lambda,0}(\theta_K) \right|^2, \tag{4.12}$$

where $\lambda = 0, \pm 1$ is the J/ψ meson helicity, $\alpha_\mu = \pm 1$ is the helicity difference between the muons, J the spin of the $K\pi$ system, $\mathcal{H}$ are the helicity amplitudes, and d, the Wigner matrices. In order to determine the *CP* components, the helicity amplitudes are transformed into "transversity amplitudes",

$$A_S = \mathcal{H}_0^0, \tag{4.13}$$

$$A_{J0} = \mathcal{H}_0^J, \tag{4.14}$$

$$A_{J||} = \frac{1}{\sqrt{2}}(\mathcal{H}_+^J + \mathcal{H}_-^J), \tag{4.15}$$

$$A_{J\perp} = \frac{1}{\sqrt{2}}(\mathcal{H}_+^J - \mathcal{H}_-^J). \tag{4.16}$$

For simplicity, the transversity amplitudes associated with the P-wave ($K\pi$ system with spin $J = 1$) are simply written A_0, $A_{||}$ and $A_\perp$, while those associated with a D-wave ($K\pi$ system with spin $J = 2$) are written as A_{20}, $A_{2||}$ and $A_{2\perp}$. The modulus of

the transversity amplitude A_x is noted as $|A_x|$ while its CP-conserving phase is noted as δ_x. The convention $|A_0|^2 + |A_{||}|^2 + |A_\perp|^2 + |A_S|^2 = 1$ is adopted, and a S-wave fraction is defined as $F_S = |A_S|^2/(|A_0|^2 + |A_{||}|^2 + |A_\perp|^2 + |A_S|^2)$. The polarisation fractions are defined in the same way. The distribution of the CP conjugate decay is obtained by flipping the sign of the interference terms which contain $|A_\perp|$ or $|A_{2\perp}|$. The $K^+\pi^-$ and $K^-\pi^+$ samples are separated and fitted through a simultaneous fit. The full decay rate is shown in Appendix C.1. A check of this description by fitting MC-*truth* (required over kaons and pions) samples generated with several values for the amplitudes and phases, as well as by fitting the data used in a previous LHCb $B^0 \to J/\psi K^{*0}$ analysis [133], is also performed. In all cases, values in very good agreement with the expectations are obtained. For details, see Appendix C.2.

The $m_{K\pi}$ window around the K^{*0} peak has been increased to $\pm 70\,\text{MeV}/c^2$ with respect to the $\pm 40\,\text{MeV}/c^2$ window used in the previous publication [134]. In order to account for the variation of the amplitudes with $m_{K\pi}$ while keeping the framework of an angular-only fit, the mass range is subdivided into 4 bins of $35\,\text{MeV}/c^2$ in size, which are fitted simultaneously.

4.4.2 Partial wave correction factors

The parameters $|A_S|^2$ and δ_S are defined independently for each bin, in order to not include any $m_{K\pi}$ dependency in the fit. If the D-wave is included (for a systematics study, or for studies on $B_s^0 \to J/\psi \overline{K}_2^*(1430)^0$), one more fraction, $F_D = (|A_{20}|^2 + |A_{2\perp}|^2 + |A_{2||}|^2)/(|A_0|^2 + |A_\perp|^2 + |A_{||}|^2 + |A_{20}|^2 + |A_{2\perp}|^2 + |A_{2||}|^2)$, and one more phase, δ_{20}, are needed in order to absorb the variations along the $m_{K\pi}$ bins. After this re-definition, the PDF defined in (4.12) still contains some mass dependent terms, associated to the interference between waves [135]. For the case of the S-wave and P-wave alone, being s and p their respective propagators, such interference terms correspond to the complex integrals

$$\frac{\int_{m^L_{K\pi}}^{m^H_{K\pi}} p \times s^* \,\text{PHSP}\, \varepsilon_m(m_{K\pi})\; dm_{K\pi}}{\sqrt{\int_{m^L_{K\pi}}^{m^H_{K\pi}} |p|^2 \,\text{PHSP}\, \varepsilon_m(m_{K\pi})\; dm_{K\pi} \int_{m^L_{K\pi}}^{m^H_{K\pi}} |s|^2 \,\text{PHSP}\, \varepsilon_m(m_{K\pi})\; dm_{K\pi}}} = C_{SP} e^{-i\theta_{SP}}, \tag{4.17}$$

where ε_m is the $m_{K\pi}$ acceptance, and PHSP stands for the phase-space. The phase θ_{SP} can be absorbed in the definition of δ_S but the C_{SP} factors, corresponding to real numbers in the range $[0, 1]$, have to be computed and inserted in the angular fit as an input. If the D-wave is present, analogous C_{SD} and C_{PD} factors need to be included to account for the extra interference terms. The C_{ij} are calculated numerically from the integrals above, given a certain assumption for the mass lineshapes and m_{hh} resolution, and included as fixed parameters in the fit. A systematic (see Chapter 4.6.7) is further added to cover difference choices of the mass propagator models.

In order to calculate the factors defined in (4.17), a model for the S, P and D wave propagators is needed. Instead of choosing a given a priori model, a choice is made based

on a test on data. To check which model has a better description of data, a three-step procedure is followed:

1. The $m_{K\pi}$ range, from $826\,\mathrm{MeV}/c^2$ to $1631\,\mathrm{MeV}/c^2$, is subdivided into 23 bins of $35\,\mathrm{MeV}/c^2$ each one. For each bin, an angular fit is performed and the S-wave, P-wave, and D-wave amplitudes are extracted.

2. The obtained amplitudes in the previous step per bin are translated into three separated distributions on $m_{K\pi}$, representing the fitted contribution of each wave. In order to account for the errors associated to the normalisation weights due to the limited statistics of the simulated samples, a systematic uncertainty is addressed to the wave yields per bin by comparing their measured values with those obtained by using a real data sample of $B^0 \to J/\psi K^{*0}$ (with high statistics) to compute the normalisation weights.

3. The three distributions are fitted with different possible models, in order to choose the best propagator set.

This procedure is first performed using the $B^0 \to J/\psi(K\pi)$ data sample, in order to select one propagator per wave, given the high statistics of this channel in the sample and its similarity to $B_s^0 \to J/\psi(K\pi)$. In a second round, the study is repeated using the $B_s^0 \to J/\psi(K\pi)$ data sample, now only with the selected propagators, so as to account for the differences in physics between the two channels. In this sense, the free parameters of each propagator (if any) are floated during the $m_{K\pi}$ fits, and then used as the default values in the analysis. As the ${}_s\mathcal{W}eights$ presented some problems for the B_s^0 in the low statistic bins of the high $m_{K\pi}$ region, an alternative method is used to remove the background in this study. A $\pm 20\,\mathrm{MeV}/c^2$ mass window cut around the B_s^0 nominal mass is applied. Part of the offline selection requirements, namely the MVA cut, are re-optimised for the whole $m_{K\pi}$ range, both for 2011 and 2012 samples. The negative weights from Monte Carlo are kept in order to remove all peaking backgrounds but those coming from Λ_b decays, that are neglected here.

As candidate propagators for the S-wave component, the following models are used: an isobaric combination of $K_0^*(800)^0$, $K_0^*(1430)^0$ and a non-resonant (NR) term (M1), the LASS parametrisation [136] with $K_0^*(1430)^0$ and a NR term (M2), and a K-Matrix model with $K_0^*(800)^0$, $K_0^*(1430)^0$ and a NR term (M3). For the P-wave distribution, a model with the $K^*(892)^0$ alone (M1), one with an isobaric combination of $K^*(892)^0$ and $K_1^*(1410)^0$ (M2), and another one with an isobaric combination of $K^*(892)^0$, $K_1^*(1410)^0$ and $K_1^*(1680)^0$, are used. Finally, for the D-wave, only the $K_2^*(1430)^0$ is considered. For the resonances and the LASS propagator, the parametrisation explained in [137] is used. The nominal masses and widths of the resonances are taken from PDG [117]. The rest of the parameters are allowed to vary during the fit.

The three distributions obtained for $B^0 \to J/\psi(K\pi)$, accompanied by the fits performed using the different candidate propagators, can be found in the left plots of Figure 4.14. The corresponding χ^2 and p-values for each fit are written in Table 4.16. For the S-wave, the LASS parametrisation results to be the best model, having the highest

p-value and, at the same time, the minimum number of parameters. For the P-wave, the chosen model is the isobar combination of the $K^*(892)^0$ and $K_1^*(1410)^0$ resonances. It has the highest p-value, and the Fisher test for the change from M1 (with 23 degrees of freedom) to M2 (with 21 degrees of freedom) gives $F_\chi = 34.67$, justifying the model election with a probability $p_F > 99\%$.

The fits of the propagators to the $B_s^0 \to J/\psi(K\pi)$ distributions return the values for the parameters that appear in Table 4.17. The quantities a_{LASS} and r_{LASS} correspond to the ones in the formula for the LASS parametrisation that is used in [137]. The complex number δ corresponds to the relative amplitude between the $K_1^*(1410)^0$ and the $K^*(892)^0$ in the P-wave model. In the right part of Figure 4.14, the propagator fits for this channel can be found. Concerning the D-wave distribution for B_s^0, the difference between model and data (no fit is performed here since all parameters of the Breit-Wigner model are fixed) suggests that the $K_2^*(1430)^0$ contribution is very small, compared to the one for B^0. A similar behaviour was seen in ref. [138], where not enough evidence was found for this resonance in the B_s^0 decay.

Table 4.16: Quality of the fits to the S, P and D wave line-shapes of $B^0 \to J/\psi(K\pi)$ with the different propagators.

Model	χ^2/ndof	p-value
		S-wave
M1: Isobar, 2 Res. + NR	49.9/19	$1.4 \cdot 10^{-4}$
M2: LASS	50.5/21	$3.2 \cdot 10^{-4}$
M3: K-Matrix, 2 Res. + NR	52.2/21	$1.8 \cdot 10^{-4}$
		P-wave
M1: $K^*(892)^0$	621.5/23	$1.4 \cdot 10^{-116}$
M2: Isobar, 2 Res.	144.5/21	$2.0 \cdot 10^{-20}$
M3: Isobar, 3 Res.	218.9/19	$5.6 \cdot 10^{-36}$
		D-wave
M1: $K_2^*(1430)^0$	11.3/23	0.98

Table 4.17: Values of the S and P wave propagators measured for $B_s^0 \to J/\psi(K\pi)$.

Parameter	Value
a_{LASS} (GeV^{-1})	2.88 ± 0.39
r_{LASS} (GeV^{-1})	$(1.152 \pm 0.072) \cdot 10^{-2}$
$\lvert\delta\rvert$	1.359 ± 0.031
$\arg(\delta)$	-3.098 ± 0.081

The C_{SP}, C_{SD} and C_{PD} factors used in the analysis are presented in Table 4.21. The central values use a LASS parametrisation for the S-wave, an isobar combination of $K^*(892)^0$ and $K_1^*(1410)^0$ for the P-wave and a relativistic Breit-Wigner distribution, corresponding to the $K_2^*(1430)^0$, for the D-wave. The $m_{K\pi}$ acceptance is obtained from

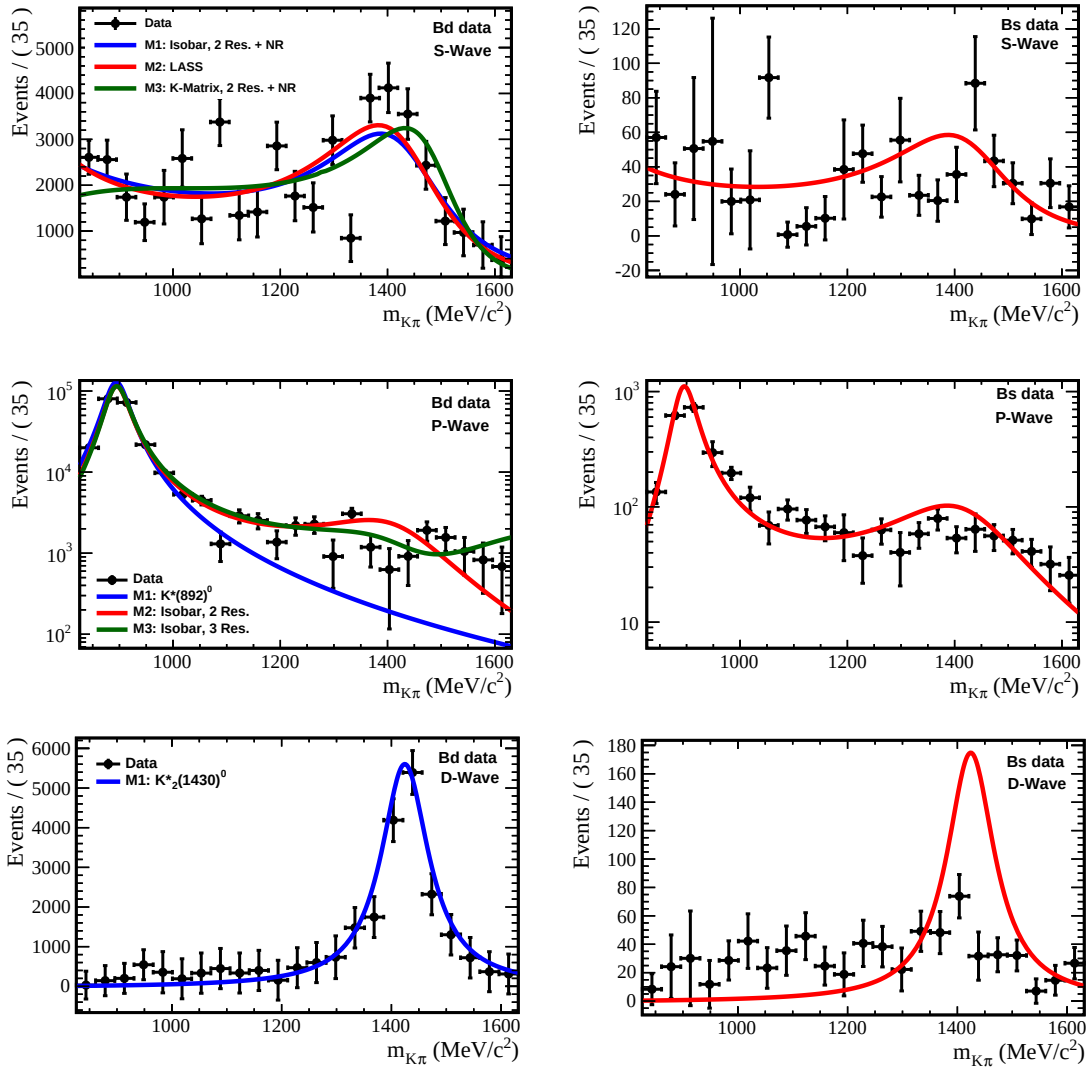

Figure 4.14: Data-like distributions for the three wave components, resulting from the amplitudes measured in the 23 independent angular fits along the $m_{K\pi}$ bins. Also the resulting fits to these distributions are shown, with the different propagator models.

the simulated sample of $B_s^0 \to J/\psi \bar{K}^{*0}$. For comparison, the C_{SP}, C_{SD} and C_{PD} factors computed using any combination of the considered models are written in Table 4.18, Table 4.19 and Table 4.20, respectively. As an additional check, a pure phase space S-wave, here denoted by M4, is also considered. It can be seen that the variations are very small, and numbers are very close to unity. This is a feature of the $m_{K\pi}$ binning scheme chosen.

Table 4.18: C_{SP} factors obtained using the different combinations of the considered propagator models, for $B_s^0 \to J/\psi K\pi$.

S-wave	P-wave	Bin 1	Bin 2	Bin 3	Bin 4
M1	M1	0.97527	0.93659	0.94801	0.98411
M1	M2	0.96806	0.92979	0.95155	0.98861
M1	M3	0.96363	0.92713	0.95333	0.98989
M2	M1	0.97536	0.93793	0.94816	0.98329
M2	M2	0.96810	0.93117	0.95185	0.98803
M2	M3	0.96363	0.92851	0.95368	0.98938
M3	M1	0.97922	0.93770	0.94276	0.98047
M3	M2	0.97277	0.93156	0.94693	0.98561
M3	M3	0.96882	0.92923	0.94896	0.98709
M4	M1	0.98468	0.94278	0.94004	0.97718
M4	M2	0.97920	0.93745	0.94502	0.98312
M4	M3	0.97580	0.93548	0.94734	0.98482

Table 4.19: C_{SD} factors obtained using the different combinations of the considered propagator models, for $B_s^0 \to J/\psi K\pi$.

S-wave	D-wave	Bin 1	Bin 2	Bin 3	Bin 4
M1	M1	0.99698	0.99770	0.99803	0.99828
M2	M1	0.99678	0.99776	0.99828	0.99864
M3	M1	0.99863	0.99895	0.99909	0.99918
M4	M1	0.99978	0.99982	0.99983	0.99983

4.4.3 Angular acceptance

Effects of angular acceptance are modelled with "normalisation weights" [139]. Due to limitations with the size of the simulated samples, the normalisation weights are obtained from fully simulated $B^0 \to J/\psi K^{*0}$ signal events. These weights are further refined in Chapter 4.3.2, where the simulated sample is first weighted to match the distributions of final-state kinematics in the real data in order to correct for imperfections in the detector simulation. The normalisation weights are calculated separately for each of the 8 data category combinations, coming from the 4 $K\pi$ mass bins and the 2 kaon signs. As an example, Table 4.22 shows the normalisation weights for one of data categories. Table 4.23 shows the correlations between the weights for the same category. No re-weighting of final-state kinematics is applied to determine these numbers yet. In Table 4.24 the weights are split by data-taking year conditions. As no overall significant difference is observed (see Appendix C.3), the 2011 and 2012 simulated samples are merged and a single acceptance is calculated.

The angular acceptance normalisation weights determined with simulated samples need to be corrected for potential differences with data. The differences in the kinematic distributions of the reconstructed particles may reflect a different acceptance in data com-

Table 4.20: C_{PD} factors obtained using the different combinations of the considered propagator models, for $B_s^0 \to J/\psi K\pi$.

P-wave	D-wave	Bin 1	Bin 2	Bin 3	Bin 4
M1	M1	0.98751	0.94493	0.93654	0.97362
M2	M1	0.98268	0.94016	0.94211	0.98022
M3	M1	0.97965	0.93846	0.94465	0.98210

Table 4.21: C_{SP}, C_{SD} and C_{PD} factors calculated for the 4 $m_{K\pi}$ bins around the K^{*0} peak, using the nominal set of propagators for $B_s^0 \to J/\psi K\pi$. Uncertainties are computed as the maximum differences found when comparing with the values obtained using the alternative models.

	Bin 1	Bin 2	Bin 3	Bin 4
C_{SP}	0.968 ± 0.017	0.931 ± 0.012	0.952 ± 0.012	0.988 ± 0.011
C_{SD}	0.9968 ± 0.0030	0.9978 ± 0.0021	0.9983 ± 0.0016	0.9986 ± 0.0012
C_{PD}	0.9827 ± 0.0048	0.9402 ± 0.0048	0.9421 ± 0.0056	0.9802 ± 0.0066

pared to simulation. On the other hand, the differences can partially be due to differences in the underlying physics of the simulation with respect to data. For example, the presence of S-wave in the real data can cause a difference in the observed kaon momentum spectrum even though the angular acceptance may be perfectly simulated. In order to overcome this dependency, simulated samples are re-weighted using an iterative procedure in order to match the best estimate of the underlying physics. The data-simulation agreement improves after each step in the iteration. A detailed discussion of this issue can be found in ref. [140].

Table 4.22: Uncorrected angular acceptance weights for the imulated samples. $3^{\text{rd}} K\pi$ bin, negative kaons. The normalisation weights are normalised with respect to the ξ_{00} weight.

k		ξ_k/ξ_1
1	(00)	$+1.00000$
2	($\parallel\parallel$)	$+1.4478 \pm 0.01716$
3	($\perp\perp$)	$+1.4631 \pm 0.01901$
4	($\parallel\perp$)	$+0.0134 \pm 0.01506$
5	(0$\parallel$)	-0.0123 ± 0.00787
6	(0$\perp$)	$+0.0019 \pm 0.00691$
7	(SS)	$+1.2535 \pm 0.01195$
8	(S$\parallel$)	-0.0383 ± 0.01216
9	(S$\perp$)	$+0.0060 \pm 0.01044$
10	(S0)	-0.7992 ± 0.02151

Table 4.23: Correlations between the uncorrected angular acceptance weights for the simulated samples. $3^{\text{rd}}K\pi$ bin, negative kaons. Correlations $< 10\%$ are not shown.

k	1 (00)	2 ($\|\|\|\|$)	3 ($\perp\perp$)	4 ($\|\|\perp$)	5 (0 $\|\|$)	6 (0 $\perp$)	7 (SS)	8 (S$\|\|$)	9 (S$\perp$)	10 (S0)
1	1.0	-	-	-	-	-	-	-	-	-
2	-	1.0	-	-	-	-	-	-	-	-
3	-	0.798	1.0	-	-	-	-	-	-	-
4	-	-	-	1.0	-	-	-	-	-	-
5	-	-	-	-	1.0	-	-	-	-	-
6	-	-	-	-	-	1.0	-	-	-	-
7	-	0.761	0.789	0.136	-	-	1.0	-	-	-
8	-	-	-	-	-	-	-	1.0	-	-
9	-	-	-	-	-	0.229	-	-	1.0	-
10	-	-	-	-	-	-	-	0.119	-	1.0

Table 4.24: Uncorrected angular acceptance weights determined with 2011 and 2012 simulated samples $3^{\text{rd}}K\pi$ bin, negative kaons. The weights are normalised to the ξ_{00} weight.

k		2011	2012	difference (σ)
1	(00)	+1.0000	+1.0000	-
2	($\|\|\|\|$)	+1.4321 $\pm$ 0.0210	+1.4655 $\pm$ 0.0226	+0.0334 $\pm$ 0.0308 (+1.1 σ)
3	($\perp\perp$)	+1.4364 $\pm$ 0.0215	+1.4932 $\pm$ 0.0236	+0.0567 $\pm$ 0.0319 (+1.8 σ)
4	($\|\|\perp$)	-0.0268 $\pm$ 0.0137	+0.0015 $\pm$ 0.0149	+0.0283 $\pm$ 0.0203 (+1.4 σ)
5	(0$\|\|$)	-0.0075 $\pm$ 0.0083	-0.0178 $\pm$ 0.0088	-0.0102 $\pm$ 0.0121 (-0.8 σ)
6	(0$\perp$)	-0.0027 $\pm$ 0.0076	-0.0011 $\pm$ 0.0082	+0.0016 $\pm$ 0.0112 (+0.1 σ)
7	(SS)	+1.2416 $\pm$ 0.0131	+1.2668 $\pm$ 0.0143	+0.0252 $\pm$ 0.0194 (+1.3 σ)
8	(S$\|\|$)	-0.0496 $\pm$ 0.0125	-0.0257 $\pm$ 0.0134	+0.0238 $\pm$ 0.0183 (+1.3 σ)
9	(S$\perp$)	+0.0109 $\pm$ 0.0116	+0.0005 $\pm$ 0.0124	-0.0104 $\pm$ 0.0170 (-0.6 σ)
10	(S0)	-0.8101 $\pm$ 0.0185	-0.7869 $\pm$ 0.0200	+0.0233 $\pm$ 0.0272 (+0.9 σ)

At each re-weighting step the simulated sample is corrected for the current estimate of the physics parameters and the two dimensional $(p_{K^\pm}, p_{\pi^\mp})$ momenta distribution. The normalisation weights are re-evaluated with the corrected simulated sample and then the fit is repeated. This changes the best estimate of the physics parameters. This last step is repeated until the normalisation weights converge. An example of the different values obtained during the full procedure for one of the bins and for positive kaons, is shown in Table 4.25. For more details, see Appendix C.4. The full procedure by steps can be summarized as:

1. Calculate the angular normalisation weights using uncorrected $B^0 \to J/\psi K^{*0}$ simulated samples.

2. Perform an sFit on the $B_s^0 \to J/\psi \overline{K}^{*0}$ data using the uncorrected normalisation weights, and obtain the first estimate of the physics parameters.

3. Re-weight each simulated event for the difference between the obtained from the sFit

angular PDF and the angular PDF used to generate the simulated sample. This essentially means that the underlying physics of the reweighted simulated sample corresponds to the physics obtained in the previous step.

4. Compare the $(p_{K^\pm}, p_{\pi^\mp})$ momenta distribution of the re-weighted simulated sample of the previous step with the background-subtracted $B_s^0 \to J/\psi \overline{K}^{*0}$ real data, and re-weight simulated events to account for the difference.

5. Re-estimate the angular normalisation weights using the physics plus momentum corrected $B^0 \to J/\psi K^{*0}$ simulated sample, and repeat the sFit on the $B_s^0 \to J/\psi \overline{K}^{*0}$ data.

6. Go back to step 4 and repeat until the change in the physics parameters is negligible ($< 0.01\sigma$).

Table 4.25: Corrected angular acceptance weights for the simulated samples after each iteration. $1^{\text{st}} K\pi$ bin, positive kaons. The upper half of the table shows the value of each normalisation weight after each iteration. The iteration number is denoted by the column on the right. The two middle rows show the statistical uncertainty on each normalisation weight and the significance of its change defined as $(\xi_k^{\text{uncorr}} - \xi_k^{\text{final}})/\sigma_k^{\text{final}}$, respectively. The lower half of the table shows the change on the value of each normalisation weight after each iteration divided by its statistical error. This essentially shows the convergence of each weight. The normalisation weights converge when the changes gradually tend to zero. All the normalisation weights are normalised with respect to ξ_{00}.

	2 ($\parallel\parallel$)	3 ($\perp\perp$)	4 ($\parallel\perp$)	5 (0 $\parallel$)	6 (0 $\perp$)	7 (SS)	8 (S$\parallel$)	9 (S$\perp$)	10 (S0)
0	+1.3666	+1.3759	+0.0329	-0.0012	+0.0110	+1.1822	-0.0380	-0.0295	-0.8761
1	+1.3842	+1.3934	+0.0350	+0.0028	+0.0092	+1.1929	-0.0418	-0.0293	-0.9053
2	+1.3812	+1.3901	+0.0347	+0.0030	+0.0095	+1.1911	-0.0420	-0.0291	-0.9222
3	+1.3803	+1.3891	+0.0346	+0.0030	+0.0096	+1.1905	-0.0420	-0.0291	-0.9262
4	+1.3797	+1.3885	+0.0345	+0.0030	+0.0096	+1.1902	-0.0420	-0.0291	-0.9280
5	+1.3794	+1.3882	+0.0345	+0.0030	+0.0096	+1.1900	-0.0420	-0.0291	-0.9287
σ	+0.0290	+0.0299	+0.0190	+0.0116	+0.0107	+0.0180	+0.0173	+0.0160	+0.0241
diff/σ	+0.45	+0.42	+0.09	+0.37	-0.13	+0.44	-0.24	+0.03	-2.14
1	+0.623	+0.599	+0.113	+0.345	-0.167	+0.614	-0.225	+0.011	-1.187
2	-0.105	-0.110	-0.015	+0.016	+0.024	-0.103	-0.009	+0.011	-0.682
3	-0.031	-0.033	-0.005	+0.004	+0.006	-0.031	-0.002	+0.003	-0.168
4	-0.020	-0.021	-0.002	+0.002	+0.002	-0.020	-0.000	+0.001	-0.072
5	-0.010	-0.011	-0.001	+0.001	+0.001	-0.010	-0.000	+0.000	-0.031

The re-weighting of the simulated sample is done using two-dimensional histograms, with a binning scheme that is shown in Table 4.26. At least 4 iterations are necessary for convergence. Detailed evolution of the normalisation weights and the physics result after each iteration can be found in Table 4.25. The final set of weights for all categories is summarized in Appendix C.5. Two dimensional projections of the efficiency functions are shown in Appendix C.6.

Table 4.26: Binning scheme for each of the re-weighted variables. Bins have equal width.

variables	range	#bins
$p_{K^\pm}$	$[0, 140]$ GeV/c^2	10
$p_{\pi^\pm}$	$[0, 60]$ GeV/c^2	10

In the nominal fit to $B_s^0 \to J/\psi \overline{K}^{*0}$ data, the normalisation weights calculated with $B^0 \to J/\psi K^{*0}$ simulated events are used. To validate this choice, fits performed using weights extracted from $B_s^0 \to J/\psi \overline{K}^{*0}$ and $B^0 \to J/\psi K^{*0}$ simulated samples before the iterative procedure are compared. The fits are performed simultaneously in 4 bins of $m_{K\pi}$ around the K^{*0} nominal mass, i.e $m_{K\pi} \in [826, 966]\,\text{MeV}/c^2$. The results of both fits are compatible, as reported in Table 4.27.

Table 4.27: Parameters resulting from the angular fit performed simultaneously in 4 $m_{K\pi}$ bins around the $K^*(892)^0$ nominal mass, using simulated samples. The values of the polarisation-dependent *CP* asymmetries are blinded. The last column is the difference between the fitted value of each parameter in both fits.

Parameter	$B^0 \to J/\psi K^{*0}$	$B_s^0 \to J/\psi \overline{K}^{*0}$	Abs. diff.
A_0^{CP}	blind $\pm$ 0.061	blind$^{+0.061}_{-0.060}$	0.015
A_S^{CP}	blind$^{+0.114}_{-0.112}$	blind$^{+0.115}_{-0.112}$	0.023
$A_\parallel^{CP}$	blind $\pm$ 0.164	blind $\pm$ 0.164	0.035
$A_\perp^{CP}$	blind$^{+0.101}_{-0.100}$	blind$^{+0.101}_{-0.100}$	0.023
f_0	0.502 ± 0.026	0.507 ± 0.026	0.005
$f_\parallel$	$0.177^{+0.029}_{-0.027}$	$0.173^{+0.028}_{-0.027}$	0.003
$\delta_\parallel$	$-2.570^{+0.169}_{-0.174}$	$-2.524^{+0.168}_{-0.173}$	0.046
$\delta_\perp$	$0.033^{+0.121}_{-0.122}$	$0.056^{+0.119}_{-0.120}$	0.023
F_S_826_861	$0.445^{+0.117}_{-0.119}$	$0.433^{+0.117}_{-0.116}$	0.012
δ_S_826_861	$0.482^{+0.170}_{-0.173}$	$0.513^{+0.170}_{-0.175}$	0.032
F_S_861_896	$0.075^{+0.030}_{-0.024}$	$0.077^{+0.030}_{-0.024}$	0.002
δ_S_861_896	$-0.497^{+0.265}_{-0.224}$	$-0.522^{+0.250}_{-0.212}$	0.025
F_S_896_931	$0.065^{+0.054}_{-0.039}$	$0.060^{+0.052}_{-0.037}$	0.005
δ_S_896_931	$-1.744^{+0.175}_{-0.224}$	$-1.763^{+0.182}_{-0.240}$	0.019
F_S_931_966	$0.589^{+0.105}_{-0.114}$	$0.584^{+0.105}_{-0.113}$	0.005
δ_S_931_966	$-1.841^{+0.146}_{-0.161}$	$-1.826^{+0.144}_{-0.158}$	0.015

4.4.4 CP asymmetries

In this analysis, the following *CP* asymmetry can be built

$$A^{CP}(B^0_{(s)} \to f_{(s)}) = \frac{\int_0^\infty \left[\Gamma(B^0_{(s)} \to f^-_{(s)}) + \Gamma(\overline{B}^0_s \to f^-_{(s)})\right] \mathrm{d}t \; - \; \int_0^\infty \left[\Gamma(B^0_{(s)} \to f_{(s)}) + \Gamma(\overline{B}^0_s \to f_{(s)})\right] \mathrm{d}t}{\int_0^\infty \left[\Gamma(B^0_{(s)} \to f^-_{(s)}) + \Gamma(\overline{B}^0_s \to f^-_{(s)})\right] \mathrm{d}t \; + \; \int_0^\infty \left[\Gamma(B^0_{(s)} \to f_{(s)}) + \Gamma(\overline{B}^0_s \to f_{(s)})\right] \mathrm{d}t}, \quad (4.18)$$

being $f_{(s)} = J/\psi K^{*0}(\overline{K}^{*0})$ and $\bar{f}_{(s)} = J/\psi \overline{K}^{*0}(K^{*0})$, where B^0_s decays into a $\overline{K}^{*0}$ meson ($\to K^-\pi^+$) and B^0 decays into a K^{*0} meson ($\to K^+\pi^-$). The angular distribution as a function of the amplitudes for B^0_s and $\overline{B}^0_s$ is given in Appendix C.1. If $|p/q| = 1$ is assumed, it is clear from (4.18) that the time-dependence factorizes and can be cancelled out to get, in a simplified notation (here and throughout this section),

$$A^{CP} = \frac{\Gamma(\overline{B}^0_s \to \bar{f}_{(s)}) - \Gamma(B^0_{(s)} \to f_{(s)})}{\Gamma(\overline{B}^0_s \to \bar{f}_{(s)}) + \Gamma(B^0_{(s)} \to f_{(s)})}. \quad (4.19)$$

For the three polarisation states $(0, \|, \perp)$, it is measured

$$A^{\mathrm{raw}}_{CP}(B^0_{(s)} \to f_{(s)}) = \frac{N^{\mathrm{obs}}(\bar{f}_{(s)}) - N^{\mathrm{obs}}(f_{(s)})}{N^{\mathrm{obs}}(\bar{f}_{(s)}) + N^{\mathrm{obs}}(f_{(s)})}, \quad (4.20)$$

then, calling N^+ (N^-) the number of events with a positive (negative) final state kaon, one can write

$$|A_i|^2 = \frac{N^+|A_i^+|^2 + N^-|A_i^-|^2}{N^+ + N^-}, \quad (4.21)$$

where i denotes a given polarisation state ($i = S, 0, \|, \perp$) and $A_i^\pm$ the corresponding amplitude measured in the sample with a positive (negative) kaon. Explicitly imposing the normalisation $\sum_i |A_i|^2 = 1$ and introducing untagged polarisation fractions for the P-wave, f_0, $f_\|$ and $f_\perp$, it can be written

$$|A_k|^2 = (1 - |A_s|^2) f_k \qquad (k = 0, \|, \perp), \quad (4.22)$$

with the normalisation condition $\sum_k f_k = 1$. The *CP* asymmetry for the given polarisation is

$$A_i^{CP} = \frac{N^+|A_i^+|^2 - N^-|A_i^-|^2}{N^+|A_i^+|^2 + N^-|A_i^-|^2}, \quad (4.23)$$

so given the *CP* asymmetries, the untagged polarisation fractions and the overall signal yields, one can easily compute the polarisation fractions to be used in each sample, where

$\xi = N^+ + N^-/2N^+$, as

$$
\begin{aligned}
|A_S^+|^2 &= \xi(1 + A_S^{CP})|A_S|^2, && (4.24)\\
|A_k^+|^2 &= \xi(1 + A_k^{CP})(1 - |A_S|^2)f_k, && (4.25)\\
|A_S^-|^2 &= \frac{\xi}{2\xi - 1}(1 - A_S^{CP})|A_S|^2, && (4.26)\\
|A_k^-|^2 &= \frac{\xi}{2\xi - 1}(1 - A_k^{CP})(1 - |A_S|^2)f_k. && (4.27)\\
& && (4.28)
\end{aligned}
$$

However, the raw asymmetry is corrected as follows

$$A_{CP}(B^0_{(s)} \to f_{(s)}) = A^{\rm raw}_{CP}(B^0_{(s)} \to f_{(s)}) - \zeta_{(s)}A_{\rm D}(f) - \kappa_{(s)}A_P(B^0_{(s)}), \tag{4.29}$$

where $A_{\rm D}(f)$ is the detection asymmetry, $A_P(B^0_{(s)})$ the production asymmetry, $\zeta_{(s)} = +1(-1)$ and $\kappa_{(s)}$ account for the dilution due to $B^0_{(s)} - \overline{B}^0_{(s)}$ oscillations [141]. $\kappa_{(s)}$ can be written as

$$\kappa_{(s)} = \frac{\int_0^\infty e^{-\Gamma_{(s)}t}\cos\left(\Delta {\rm M}_{(s)}t\right)\varepsilon(B^0_{(s)} \to K\pi;\, t){\rm d}t}{\int_0^\infty e^{-\Gamma_{(s)}t}\cosh\left(\frac{\Delta\Gamma_{(s)}}{2}t\right)\varepsilon(B^0_{(s)} \to K\pi;\, t){\rm d}t}, \tag{4.30}$$

where $\varepsilon(t)$ is the time-dependent acceptance function. Now, the extended PDFs used in the fit cannot be normalised to $N^\pm$ because the overall yields are affected by previously defined asymmetries. Therefore, the chosen definition for the normalisation factors of the PDFs is

$$\tilde{N}^\pm = (1 \pm A_I^{CP})N^\pm, \tag{4.31}$$

where A_I^{CP} contains the induced CP asymmetries.

The presence of a $B^0_{(s)} - \overline{B}^0_{(s)}$ production asymmetry must be considered. The effective B production asymmetries for this analysis are obtained from reweighting the results reported in Tables 3 and 4 of ref. [142] for the different bins in B transverse momentum and pseudorapidity. The production asymmetry is defined as

$$A_{\rm prod}(B) \equiv \frac{\sigma(\overline{B}) - \sigma(B)}{\sigma(\overline{B}) + \sigma(B)}\,, \tag{4.32}$$

where σ represents the production cross-section. The production asymmetries $A_{\rm P}(B)$ reported in Tables 3 and 4 are reweighted as

$$A^{\rm eff}_{\rm prod}(B) \equiv \sum_{\rm Bins\ i} f_i A_{{\rm P},i}(B)\,, \qquad f_i \equiv \frac{\#B \in \text{Bin i}}{N_B}\,, \tag{4.33}$$

where f_i is the fraction of $B^0_{(s)}$ events in bin i, obtained by summing over the ${}_s\mathcal{W}eights$ obtained from a fit to the mass distribution of the nominal data sample. Using the weights

Table 4.28: B^0 production asymmetries in bins of B transverse momentum p_T and pseudo-rapidity η, and the event weights obtained from sWeighted $B^0 \to J/\psi K^{*0}$ candidates. For $A_{\mathrm{P},i}(B^0)$ the first uncertainty is statistical, whereas the second is systematic.

Bin	p_T (GeV/c)	η	Weight f_i	$A_{\mathrm{P},i}(B)$
1	(1.0, 4.0)	(4.5,5.2)	0.0350 ± 0.0004	0.0016 ± 0.0253 ± 0.0016
2	(1.0, 4.0)	(3.7,4.5)	0.1037 ± 0.0007	−0.0158 ± 0.0162 ± 0.0015
3	(2.0, 4.0)	(3.0,3.7)	0.0552 ± 0.0005	0.0055 ± 0.0254 ± 0.0016
4	(4.0,12.0)	(4.5,4.7)	0.0031 ± 0.0001	0.0160 ± 0.0736 ± 0.0067
5	(4.0, 7.0)	(3.7,4.5)	0.0957 ± 0.0007	−0.0189 ± 0.0158 ± 0.0032
6	(4.0, 7.0)	(3.0,3.7)	0.1671 ± 0.0010	−0.0311 ± 0.0132 ± 0.0014
7	(4.0, 7.0)	(2.5,3.0)	0.0513 ± 0.0005	0.0556 ± 0.0254 ± 0.0020
8	(7.0,12.0)	(3.7,4.5)	0.0432 ± 0.0005	−0.0145 ± 0.0205 ± 0.0027
9	(7.0,12.0)	(3.0,3.7)	0.1558 ± 0.0009	−0.0142 ± 0.0111 ± 0.0015
10	(7.0,12.0)	(2.5,3.0)	0.1035 ± 0.0007	−0.0236 ± 0.0138 ± 0.0014
11	(7.0,12.0)	(2.2,2.5)	0.0172 ± 0.0003	−0.0190 ± 0.0348 ± 0.0034
12	(12.0,30.0)	(3.7,4.5)	0.0080 ± 0.0002	−0.0550 ± 0.0473 ± 0.0020
13	(12.0,30.0)	(3.0,3.7)	0.0508 ± 0.0005	0.0067 ± 0.0180 ± 0.0021
14	(12.0,30.0)	(2.5,3.0)	0.0557 ± 0.0005	0.0177 ± 0.0162 ± 0.0023
15	(12.0,30.0)	(2.0,2.5)	0.0276 ± 0.0004	−0.0018 ± 0.0236 ± 0.0020
A	(0.2, 1.0)	(4.5,6.0)	0.0098 ± 0.0002	−0.0391 ± 0.0501 ± 0.0016
B	(1.0, 2.2)	(5.2,6.0)	0.0034 ± 0.0001	0.0523 ± 0.0684 ± 0.0025

and production asymmetries listed in Table 4.28 and Table 4.29 for the B^0 and B_s^0 system, respectively, the obtained effective production asymmetries are

$$A_{\mathrm{prod}}^{\mathrm{eff}}(B^0) = (\ -1.04 \pm 0.48\ (\mathrm{stat}) \pm 0.14\ (\mathrm{syst}))\%\ , \tag{4.34}$$

$$A_{\mathrm{prod}}^{\mathrm{eff}}(B_s^0) = (\ -1.64 \pm 2.28\ (\mathrm{stat}) \pm 0.55\ (\mathrm{syst}))\%. \tag{4.35}$$

In order to calculate the $\kappa_{(s)}$ factor (4.30), the decay time acceptance is determined on the nominal data sample after applying the B^0 ${}_s\mathcal{W}eights$ (see Figure 4.15). As in [143],

$$\varepsilon(t) = \frac{[1+\beta(t-t_0)][a(t-t0)]^n}{1+[a(t-t_0)]^n}, \tag{4.36}$$

where $a = 1.814$, $n = 1.552$, $t_0 = 0.219$ and $\beta = 0.020$. The dilution factor in (4.30) is equal to 0.06% for B_s^0 decays, and 41% for B^0 decays. This reduces the effect of the production asymmetry to the level of 10^{-5} for $B_s^0 \to J/\psi \overline{K}^{*0}$ and 10^{-3} for $B^0 \to J/\psi K^{*0}$ decays. At the level of 0.4%, the production asymmetry can still significantly contribute to the overall direct CP violation in the $B^0 \to J/\psi K^{*0}$ decay channel.

Another asymmetry arises from the detector acceptance, event reconstruction and the difference in the interaction cross-section between particles and antiparticles in the final

Table 4.29: B_s^0 production asymmetries in bins of B transverse momentum p_T and pseudo-rapidity η, and the event weights obtained from sWeighted $B_s^0 \to J/\psi \overline{K}^{*0}$ candidates. For $A_{\mathrm{P},i}(B_s^0)$ the first uncertainty is statistical, whereas the second is systematic.

Bin	p_T (GeV/c)	η	Weight f_i	$A_{\mathrm{P},i}(B)$
1	(2, 4)	(3.0,5.0)	0.1670 ± 0.0104	−0.1475 ± 0.0895 ± 0.0192
2	(4, 8)	(3.5,4.5)	0.1811 ± 0.0109	−0.0471 ± 0.0513 ± 0.0112
3	(4, 9)	(2.5,3.5)	0.2819 ± 0.0142	0.0376 ± 0.0467 ± 0.0083
4	(8,12)	(3.5,4.5)	0.0523 ± 0.0055	0.0582 ± 0.0537 ± 0.0053
5	(8,12)	(2.5,3.5)	0.1820 ± 0.0110	0.0370 ± 0.0332 ± 0.0051
6	(12,30)	(3.5,4.5)	0.0123 ± 0.0026	−0.0339 ± 0.0750 ± 0.0095
7	(12,30)	(2.5,3.5)	0.0786 ± 0.0069	−0.0333 ± 0.0309 ± 0.0040
8	(8,30)	(2.2,2.5)	0.0281 ± 0.0040	−0.0351 ± 0.0485 ± 0.0059

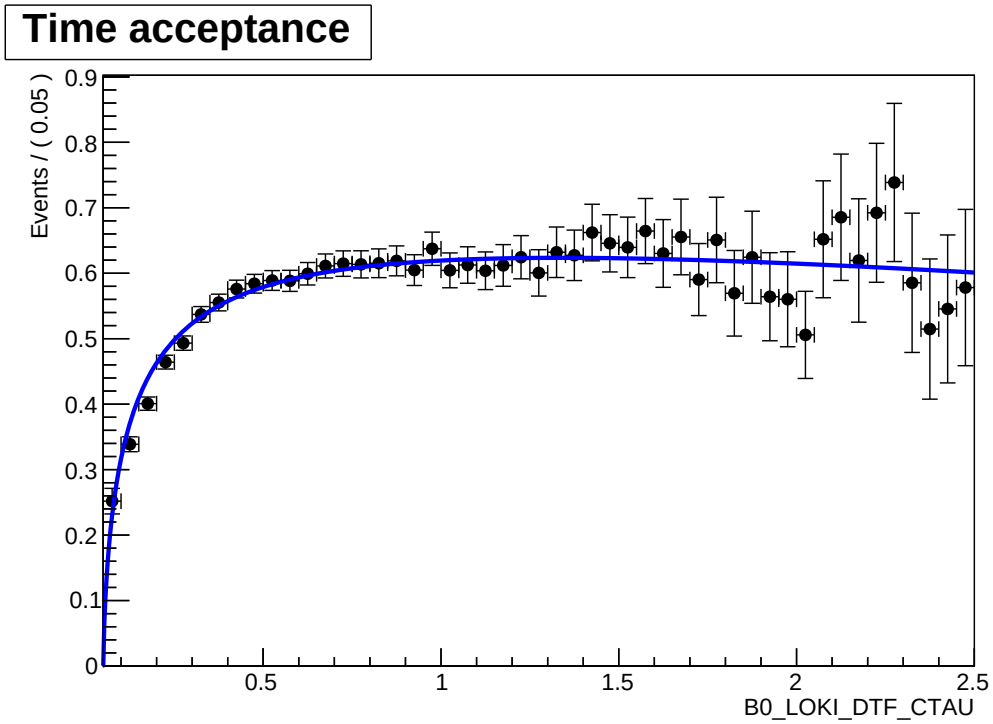

Figure 4.15: Decay time acceptance fit on data.

state and the detector. $A_{\mathrm{D}}(f)$ is the detection asymmetry of the final state f, defined in terms of the detection efficiencies as

$$A_{\mathrm{D}}(f) \equiv \frac{\epsilon(\bar{f}) - \epsilon(f)}{\epsilon(\bar{f}) + \epsilon(f)}\,, \tag{4.37}$$

where $A_{\mathrm{D},i}(K\pi)$ is measured in bins of the K^+ momentum is used, assuming a negligible contribution from the pion to this asymmetry [144], and then weighting this with the

Table 4.30: $(K^-\ \pi^+)$ detection asymmetries in bins of kaon momentum, and the event weights obtained from sWeighted $B^0 \to J/\psi K^{*0}$ candidates. The uncertainty is statistical [144].

Bin	$p\,(\,\mathrm{GeV}/c)$	Weight f_i	$A_{\mathrm{D},i}(K^-)$
1	(02.0,10.0)	0.1838 ± 0.0010	-1.37 ± 0.11
2	(10.0,17.5)	0.2957 ± 0.0013	-1.21 ± 0.10
3	(17.5,22.5)	0.1458 ± 0.0009	-1.15 ± 0.11
4	(22.5,30.0)	0.1445 ± 0.0009	-1.10 ± 0.12
5	(30.0,50.0)	0.1580 ± 0.0009	-0.89 ± 0.16
6	(50.0,70.0)	0.0471 ± 0.0005	-0.72 ± 0.29
7	(70.0,100)	0.0191 ± 0.0003	-0.33 ± 0.30
8	(100 ,150)	0.0054 ± 0.0002	0.18 ± 0.45

Table 4.31: $(K^-\ \pi^+)$ detection asymmetries in bins of kaon momentum, and the event weights obtained from sWeighted $B_s^0 \to J/\psi \overline{K}^{*0}$ candidates. The uncertainty is statistical [144].

Bin	$p\,(\,\mathrm{GeV}/c)$	Weight f_i	$A_{\mathrm{D},i}(K^-)$
1	(02.0,10.0)	0.1655 ± 0.0104	-1.37 ± 0.11
2	(10.0,17.5)	0.2782 ± 0.0141	-1.21 ± 0.10
3	(17.5,22.5)	0.1349 ± 0.0092	-1.15 ± 0.11
4	(22.5,30.0)	0.1424 ± 0.0095	-1.10 ± 0.12
5	(30.0,50.0)	0.1842 ± 0.0110	-0.89 ± 0.16
6	(50.0,70.0)	0.0664 ± 0.0063	-0.72 ± 0.29
7	(70.0,100)	0.0210 ± 0.0034	-0.33 ± 0.30
8	(100 ,150)	0.0066 ± 0.0019	0.18 ± 0.45

momentum distribution of the kaon resulting from $B^0_{(s)} \to J/\psi K^{*0}(\overline{K}^{*0})$ decay.

$$A_{\mathrm{D}}^{\mathrm{eff}}(B) \equiv \sum_{\text{Bins i}} f_i A_{\mathrm{D},i}(B)\,, \qquad f_i \equiv \frac{\#B \in \text{Bin i}}{N_B} \tag{4.38}$$

For simplicity, a correlation of 100% between the bins is assumed. Using the kaon detection asymmetries reported in Table 4.30, the following detection asymmetries for B^0 and B_s^0 are obtained, respectively

$$A_{\mathrm{D}}^{\mathrm{eff}}(B^0) = (1.115 \pm 0.547\ (\mathrm{stat}))\%, \tag{4.39}$$

$$A_{\mathrm{D}}^{\mathrm{eff}}(B_s^0) = (-1.086 \pm 0.531\ (\mathrm{stat}))\%. \tag{4.40}$$

As a reminder, B_s^0 decays to a $\overline{K}^{*0}$, while the B^0 gives K^{*0}, hence the above opposite signs are expected, following the definition in (4.29).

4.5 Measurement of $\mathcal{B}(B_s^0 \to J/\psi \overline{K}^{*0})$

Two normalised branching fractions are obtained: one with respect to the $B_s^0 \to J/\psi\phi$ decay channel (ideal for the study of penguin pollution), and the other one with respect to the $B^0 \to J/\psi K^{*0}$ mode (ideal for the cancellation of systematic uncertainties in the efficiency evaluation). Then, a weighted average taking into account both results is calculated, leading to a final value of the $B_s^0 \to J/\psi \overline{K}^{*0}$ branching fraction.

For the first step, the following expression to calculate the normalised $B_s^0 \to J/\psi \overline{K}^{*0}$ branching fraction to a given decay $B_q \to J/\psi X$ is used,

$$\frac{\mathcal{B}(B_s^0 \to J/\psi \overline{K}^{*0}) \times \mathcal{B}(J/\psi \to \mu^+\mu^-) \times \mathcal{B}(K^{*0} \to K^+\pi^-)}{\mathcal{B}(B_q \to J/\psi X)} = \frac{N_{B_s^0 \to J/\psi \overline{K}^{*0}}}{N_{B_q \to J/\psi X}} \times \frac{\varepsilon_{B_q \to J/\psi X}}{\varepsilon_{B_s^0 \to J/\psi \overline{K}^{*0}}} \times \frac{P(b \to B_q)}{P(b \to B_s^0)}, \quad (4.41)$$

where N refers to the number of events of that given decay, ε corresponds to the total (reconstruction, trigger and selection) efficiency (see 4.5.1), and P are the hadronisation probabilities of the b quark to a given B meson. For the second step, the procedure to obtain the weighted average is described in detail in Appendix D.1.

4.5.1 Efficiency ratios obtained from simulation

The ratios of efficiencies are taken from simulation, separately for 2011 and 2012 conditions. Simulated samples used are described in Chapter 4.1.2, where an MC-*truth* condition is imposed for daughter hadrons. A total efficiency using simulated samples (reconstruction, trigger and selection), ε_{TOT}, is computed separately for each data-taking year conditions. The requirements of the offline selection used for the $B_s^0 \to J/\psi\phi$ normalisation mode are listed in Table 4.32, where the same BDTG constructed and optimised for $B_s^0 \to J/\psi \overline{K}^{*0}$ signal decays (see Chapter 4.1.4) is used. For the $B^0 \to J/\psi K^{*0}$ channel, the same final selection requirements as for $B_s^0 \to J/\psi \overline{K}^{*0}$ decays are used, described in Chapter 4.1. The values of these total efficiencies are shown in Table 4.33, where their ratios are, for 2011 (2012) conditions,

$$\frac{\varepsilon^{\text{MC}}_{B^0 \to J/\psi K^{*0}}}{\varepsilon^{\text{MC}}_{B_s^0 \to J/\psi \overline{K}^{*0}}} = 0.929 \pm 0.012 \ (0.927 \pm 0.012), \quad (4.42)$$

$$\frac{\varepsilon^{\text{MC}}_{B_s^0 \to J/\psi\phi}}{\varepsilon^{\text{MC}}_{B_s^0 \to J/\psi \overline{K}^{*0}}} = 1.991 \pm 0.025 \ (1.986 \pm 0.027). \quad (4.43)$$

A detailed discussion can be found in Appendix D.2. Due to the similarity of the final state between signal and normalisation channel in the case of the normalisation to the $B^0 \to J/\psi K^{*0}$ decay mode, the systematics associated to discrepancies between data and simulation are assumed to cancel out. However, as the efficiency depends on the

angular distribution of the decay products, a correction due to the difference between the angular amplitudes used in simulation and those measured on data has to be done. This is discussed in Chapter 4.5.2, for both normalisations to $B^0 \to J/\psi K^{*0}$ and $B_s^0 \to J/\psi\phi$ decay channels.

Table 4.32: Final selection criteria for $B_s^0 \to J/\psi\phi$ candidates.

	Cut variable	Cut value
$J/\psi \to \mu\mu$	$\lvert M(\mu^+\mu^-) - M(J/\psi)\rvert$	$< 150\,\mathrm{MeV}/c^2$
	$\chi^2_{\mathrm{vtx}}/\mathrm{ndof}(J/\psi)$	< 16
	$\chi^2_{\mathrm{DOCA}}/\mathrm{ndof}(J/\psi)$	< 20
	$\Delta\mathrm{LL}\mu\pi(\mu)$	> 0
	$\chi^2_{\mathrm{IP}}(\mu)$	> 16
	$p_T\ (\mu)$	$> 0.5\,\mathrm{GeV}/c$
	$\mathrm{IsMuon}(\mu)$	true
$\phi \to K^-K^+$	$\lvert M(K^-K^+) - 1019.46\rvert$	$< 20\,\mathrm{MeV}/c^2$
	$p_T\ (\phi)$	$> 1.0\,\mathrm{GeV}/c$
	$\chi^2_{\mathrm{vtx}}/\mathrm{ndof}(\phi)$	< 25
	$\chi^2_{\mathrm{DOCA}}/\mathrm{ndof}(\phi)$	< 30
	$p_T\ (K)$	$> 0.5\,\mathrm{GeV}/c$
	$\chi^2_{\mathrm{IP}}(K)$	> 2
	$\Delta\mathrm{LL}K\pi(K)$	> 0
	$\chi^2_{\mathrm{track}}/\mathrm{ndof}(K)$	< 5
	$\mathrm{ProbNNK}(K)$	> 0.21
	$\mathrm{ProbNNK}(K)/\mathrm{ProbNNp}(K)$	> 0.99
$B_s^0 \to J/\psi\phi$	$M(B_s^0)$	$\in [5150,\ 5650]\,\mathrm{MeV}/c^2$
	$\chi^2_{\mathrm{vtx}}/\mathrm{ndof}(B_s^0)$	< 10
	$\mathrm{DIRA}(B_s^0)$	> 0.999
	VS	$> 1.5\,\mathrm{mm}$
	BDTG (2011/2012)	$> 0.2/> 0.12$
$B^+ \to J/\psi K^+$ veto	$\lvert M(J/\psi, K) - 5279\rvert$	$> 60\,\mathrm{MeV}/c^2$

Table 4.33: Total efficiencies obtained from simulation.

	$\varepsilon^{\mathrm{MC}}$ (2011) (%)	$\varepsilon^{\mathrm{MC}}$ (2012) (%)
$B^0 \to J/\psi K^{*0}$	0.5482 ± 0.0046	0.5052 ± 0.0040
$B_s^0 \to J/\psi\phi$	1.1742 ± 0.0099	1.0823 ± 0.0098
$B_s^0 \to J/\psi \overline{K}^{*0}$	0.5898 ± 0.0054	0.5451 ± 0.0054

4.5.2 Physical corrections due to angular distributions

The number of events ($N_{B_s^0\to J/\psi\overline{K}^{*0}}$, $N_{B^0\to J/\psi K^{*0}}$, $N_{B_s^0\to J/\psi\phi}$) can be approximately obtained from a fit to the mass distribution of B candidates selected around the pole of the corresponding hh resonance. The number of events $N_{B_s^0\to J/\psi\phi}$ is obtained from a fit to the $M(J/\psi, KK)$ distribution of events selected with the final selection cuts described in Chapter 4.1 (see Figure 4.16). However, some correction is needed, since the peak is polluted with S-wave as well as S-wave/P-wave interference. Thus,

$$N_{\rm fit} = N^{\rm P-wave} + N^{\rm S-wave} + N^{\rm interference}, \tag{4.44}$$

where the last term, $N^{\rm interference}$ vanishes in the case of a flat angular acceptance, but not otherwise. Thus, the relative contribution that is not pure P-wave needs to be calculated. This can be done by means of an angular analysis,

$$\frac{N^{\rm P-wave}}{N_{\rm fit}} = \frac{\int_{4\pi}\int_0^{+\infty}\int_{m_{hh}\rm bin}|A(\Omega,t,m_{hh}|A_S=0)|^2\varepsilon(\Omega,t,m_{hh})\,d\Omega\,dt\,dm_{hh}}{\int_{4\pi}\int_0^{+\infty}\int_{m_{hh}\rm bin}|A(\Omega,t,m_{hh})|^2\varepsilon(\Omega,t,m_{hh})\,d\Omega\,dt\,dm_{hh}}, \tag{4.45}$$

where the integral is folded over m_{hh} in the C_{SP} factors, and the integral over the angles in the normalisation weights. The decay time acceptance is irrelevant for $B^0_{(s)}\to J/\psi K^{*0}(\overline{K}^{*0})$, but not for $B_s^0\to J/\psi\phi$ since the angular distribution is time dependent. Hence, the fraction of the P-wave resonance in a given decay is

$$F^{\rm Res}_{\rm decay} := \frac{N^{P-wave}}{N_{\rm massFit}} = \frac{\int_0^{+\infty}\sum_{ij}^{i,j!=S}\xi_{ij}\times A_i^*A_j(t)\varepsilon(t)dt}{\int_0^{+\infty}\sum_{ij}\xi_{ij}\times C_{ij}\times A_i^*A_j(t)\varepsilon(t)dt}, \tag{4.46}$$

where ξ_{ij} are the normalisation weights, shown in Table 4.34. In the case of the $B_s^0\to J/\psi\overline{K}^{*0}$ one can ignore the lifetime dependence of the PDF, since it factorizes out from the angular PDF and hence cancels out in the ratio.

In addition to the correction of the observed yield in which the subtraction of the contribution from sub-dominant waves is done, it would be also needed to correct the efficiencies obtained in the simulation because the generator values of the decay parameters differ slightly from the measured ones. For this purpose, it is defined

$$c_{\rm decay} := \frac{\varepsilon^{\rm data}_{\rm decay}}{\varepsilon^{\rm MC}_{\rm decay}} = \frac{\int_0^{+\infty}\sum_{ij}^{i,j!=S}\xi_{ij}\times a_i^*a_j(t)\varepsilon(t)dt\|_{data}}{\int_0^{+\infty}\sum_{ij}^{i,j!=S}\xi_{ij}\times a_i^*a_j(t)\varepsilon(t)dt\|_{MC}}, \tag{4.47}$$

where in this case the P-wave amplitudes a are re-normalised so that $|a_{||}|^2+|a_0|^2+|a_\perp|^2=1$. For $B_s^0\to J/\psi\phi$ decays, it can be assumed $c_{B_s^0\to J/\psi\phi}=1$ to a very good precision, since the simulated samples were generated with latest measurements from data [145]. Defining

$$\kappa_{\rm decay} = \frac{c_{\rm decay}}{F^{\rm Res}_{\rm decay}}, \tag{4.48}$$

Table 4.34: Uncorrected angular acceptance weights computed on $B_s^0 \to J/\psi\phi$ simulated samples. The normalisation weights are normalised with respect to the ξ_{00} weight.

	k	ξ_k/ξ_1
1	(00)	+1.00000
2	($\parallel\parallel$)	+1.19377
3	($\perp\perp$)	+1.05515
4	($\parallel\perp$)	−0.03926
5	(0$\parallel$)	+0.24583
6	(0$\perp$)	−0.02961
7	(SS)	+1.10256
8	(S$\parallel$)	−0.06505
9	(S$\perp$)	+0.09569
10	(S0)	−0.12612

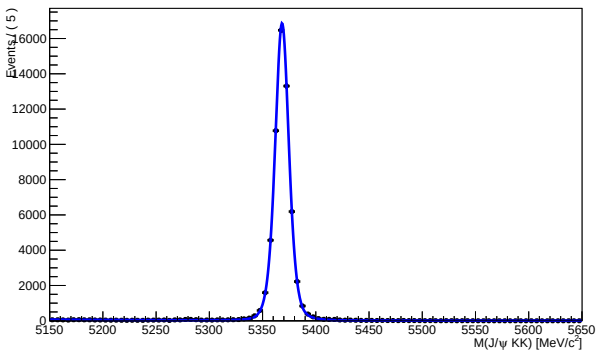

Figure 4.16: Simultaneous fit (2011 + 2012 conditions) to M($J/\psi, KK$) using Hypatia distribution to model $B_s^0 \to J/\psi K^+K^-$ and an exponential distribution to model the combinatorial background (resulting in 58091 ± 243 (stat) ± 319 (syst) candidate events).

which is convenient since F and c share common parameters, one can rewrite the normalisation expression as

$$\frac{\mathcal{B}(B_s^0 \to J/\psi \overline{K}^{*0})}{\mathcal{B}(B_q \to J/\psi X)} = \frac{N^{\text{massFit}}_{B_s^0 \to J/\psi K\pi}}{N^{\text{massFit}}_{B_q \to J/\psi X}} \times \frac{\varepsilon^{\text{MC}}_{B_q \to J/\psi X}}{\varepsilon^{\text{MC}}_{B_s^0 \to J/\psi \overline{K}^{*0}}} \times \frac{\kappa_{B_q \to J/\psi X}}{\kappa_{B_s^0 \to J/\psi \overline{K}^{*0}}}. \tag{4.49}$$

To calculate $\kappa_{B_s^0 \to J/\psi\phi}$, the time-dependent efficiency $\varepsilon_2(t)$ of the $B_s^0 \to J/\psi\phi$ events is needed. It is obtained from simulation and parametrised as (see Figure 4.17)

$$\varepsilon_2(t) \propto \frac{p_2}{1 + p_1 \times t^{p_0}}. \tag{4.50}$$

The parameter values are shown in Table 4.36.

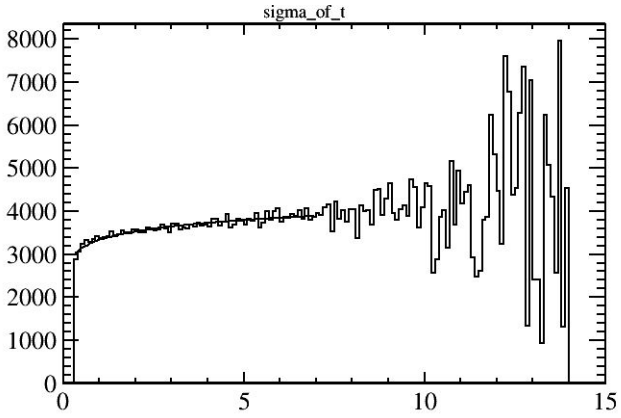

Figure 4.17: Fit of (4.50) to the decay time acceptance observed in $B_s^0 \to J/\psi\phi$ simulation.

Table 4.35: Obtained values for $F^{\phi}_{B_s^0\to J/\psi K^+K^-}$ using the values of $F_S^{B_s^0\to J/\psi K^+K^-}$ at the two central bins of [146]. The result obtained using a value of $F_S^{B_s^0\to J/\psi K^+K^-}$ from a custom $B_s^0 \to J/\psi\phi$ untagged fit is also shown.

	$F_S^{B_s^0\to J/\psi K^+K^-}$	N^{P-wave}	$N^{massFit}_{B_s^0\to J/\psi K^+K^-}$	$F^{\phi}_{B_s^0\to J/\psi K^+K^-}$
Custom fit	0.0001 ± 0.0017	70867.5387	70879.4227	0.9998 ± 0.0020
Bin(2) [146]	0.008	56391.9193	57139.1610	0.98692242
Bin(3) [146]	0.016	56391.9193	57743.9938	0.97658501

The results of $F^{\phi}_{B_s^0\to J/\psi K^+K^-}$ are shown in Table 4.35. The second line in the table is calculated using the amplitudes got from $B_s^0 \to J/\psi K^+K^-$ data. The third line and fourth line use amplitudes from [146]. Adopting a conservative systematic uncertainty to cover all three values, the following result is obtained,

$$F^{\phi}_{B_s^0\to J/\psi K^+K^-} = 0.9817 \pm 0.0020(\text{stat}) \pm 0.0073(\text{syst}). \tag{4.51}$$

The systematic is also big enough to cover the limited knowledge of the $B_s^0 \to J/\psi\phi$ acceptance. The values obtained for the κ factors are

$$\kappa_{B_s^0\to J/\psi \overline{K}^{*0}} = 1.149 \pm 0.044(\text{stat}) \pm 0.018(\text{syst}), \tag{4.52}$$
$$\kappa_{B^0\to J/\psi K^{*0}} = 1.107 \pm 0.0028(\text{stat}) \pm 0.038(\text{syst}), \tag{4.53}$$
$$\kappa_{B_s^0\to J/\psi\phi} = 1.013 \pm 0.0020(\text{stat}) \pm 0.0074(\text{syst}), \tag{4.54}$$

where the systematic is due to the acceptance. Henceforth, $N^{\text{massFit}}_{B_q\to J/\psi X}$ will be simply written as $N_{B_q\to J/\psi X}$.

Table 4.36: Values of the parameters obtained from a fit of (4.50) to the $B_s^0 \to J/\psi\phi$ proper time acceptance observed in simulation.

	Value	Error
p_0	0.142	0.096
p_1	0.7	1.0
p_2	5600	3400

4.5.3 Normalisation to the $B^0 \to J/\psi K^{*0}$ decay mode

The normalisation to the $B^0 \to J/\psi K^{*0}$ mode is performed using the formula

$$\frac{\mathcal{B}(B_s^0 \to J/\psi \overline{K}^{*0})}{\mathcal{B}(B^0 \to J/\psi K^{*0})} = \frac{N_{B_s^0 \to J/\psi K\pi}}{N_{B^0 \to J/\psi K\pi}} \times \frac{f_d}{f_s} \times \frac{\varepsilon^{MC}_{B^0 \to J/\psi K^{*0}}}{\varepsilon^{MC}_{B_s^0 \to J/\psi \overline{K}^{*0}}} \times \frac{\kappa_{B^0 \to J/\psi K^{*0}}}{\kappa_{B_s^0 \to J/\psi \overline{K}^{*0}}}, \tag{4.55}$$

where $\kappa_{B_s^0 \to J/\psi \overline{K}^{*0}}$ and $\kappa_{B^0 \to J/\psi K^{*0}}$ are taken from Chapter 4.5.2. Taking into account the correlation of the systematic uncertainties, one gets

$$\frac{\kappa_{B^0 \to J/\psi K^{*0}}}{\kappa_{B_s^0 \to J/\psi \overline{K}^{*0}}} = 0.963 \pm 0.036(\text{stat}) \pm 0.031(\text{syst}). \tag{4.56}$$

Thus,

$$\frac{\mathcal{B}(B_s^0 \to J/\psi \overline{K}^{*0})}{\mathcal{B}(B^0 \to J/\psi K^{*0})} = (2.99 \pm 0.14(\text{stat}) \pm 0.12(\text{syst}) \pm 0.17(\frac{f_d}{f_s}))\%. \tag{4.57}$$

Multiplying (4.57) by the branching fraction of $B^0 \to J/\psi K^{*0}$ decays measured at Belle [147],

$$\mathcal{B}(B^0 \to J/\psi K^{*0}) = (1.29 \pm 0.05(\text{stat}) \pm 0.13(\text{syst})) \times 10^{-3}, \tag{4.58}$$

and taking into account the difference in production rates for the B^+B^- and $B^0\overline{B}^0$ pairs at the $\Upsilon(4S)$ resonance, i.e. $\Gamma(B^+B^-)/\Gamma(B^0\overline{B}^0) = 1.058 \pm 0.024$ [148], the value

$$\mathcal{B}(B_s^0 \to J/\psi \overline{K}^{*0})_d = (3.95 \pm 0.18(\text{stat}) \pm 0.16(\text{syst}) \pm 0.23(\frac{f_d}{f_s}) \pm 0.43(\mathcal{B}(B^0 \to J/\psi K^{*0}))) \times 10^{-5} \tag{4.59}$$

is obtained.

4.5.4 Normalisation to the $B_s^0 \to J/\psi\phi$ decay mode

The study of the "penguin pollution" requires the calculation of ratios of absolute amplitudes between $B_s^0 \to J/\psi \overline{K}^{*0}$ and $B_s^0 \to J/\psi\phi$ decay modes. Thus, normalising the

$\mathcal{B}(B_s^0 \to J/\psi \overline{K}^{*0})$ to $\mathcal{B}(B_s^0 \to J/\psi\phi)$ becomes very useful in this context. The normalisation to $B_s^0 \to J/\psi\phi$ is performed using the formula

$$\frac{\mathcal{B}(B_s^0 \to J/\psi \overline{K}^{*0})}{\mathcal{B}(B_s^0 \to J/\psi\phi)} = \frac{N_{B_s^0 \to J/\psi K\pi}}{N_{B_s^0 \to J/\psi K^+K^-}} \times \frac{\varepsilon^{MC}_{B_s^0 \to J/\psi\phi}}{\varepsilon^{MC}_{B_s^0 \to J/\psi \overline{K}^{*0}}} \times \frac{\kappa_{B_s^0 \to J/\psi\phi}}{\kappa_{B_s^0 \to J/\psi \overline{K}^{*0}}} \times \frac{\mathcal{B}(\phi \to K^+K^-)}{\mathcal{B}(\overline{K}^{*0} \to K^-\pi^+)}, \tag{4.60}$$

where $\mathcal{B}(\overline{K}^{*0} \to K^-\pi^+) = 2/3$[2] and $\mathcal{B}(\phi \to K^+K^-) = (49.5 \pm 0.5)\%$ [117]. Using $\kappa_{B_s^0 \to J/\psi \overline{K}^{*0}}$ and $\kappa_{B_s^0 \to J/\psi\phi}$ from Chapter 4.5.2, the ratio

$$\frac{\mathcal{B}(B_s^0 \to J/\psi \overline{K}^{*0})}{\mathcal{B}(B_s^0 \to J/\psi\phi)} = (4.05 \pm 0.19(\text{stat}) \pm 0.13(\text{syst}))\%. \tag{4.61}$$

is obtained. Taking the value of $\mathcal{B}(B_s^0 \to J/\psi\phi)$ from [126] after updating it with the latest $\frac{f_d}{f_s} = 0.259 \pm 0.015$ [149],

$$\mathcal{B}(B_s^0 \to J/\psi\phi) = (1.038 \pm 0.013 \pm 0.063 \pm 0.060) \times 10^{-3}, \tag{4.62}$$

the following value for $\mathcal{B}(B_s^0 \to J/\psi \overline{K}^{*0})$,

$$\mathcal{B}(B_s^0 \to J/\psi \overline{K}^{*0})_\phi = (4.20 \pm 0.20(\text{stat}) \pm 0.13(\text{syst}) \pm 0.36(\mathcal{B}(B_s^0 \to J/\psi\phi))) \times 10^{-5}, \tag{4.63}$$

is obtained. Both time-averaged values for $\mathcal{B}(B_s^0 \to J/\psi \overline{K}^{*0})$ are compatible within uncorrelated systematics ($\mathcal{B}(B_s^0 \to J/\psi\phi)$ also depends on $\frac{f_d}{f_s}$).

4.5.5 Weighted average of $B_s^0 \to J/\psi \overline{K}^{*0}$ branching fraction

Both values for $\mathcal{B}(B_s^0 \to J/\psi \overline{K}^{*0})$, calculated in Chapter 4.5.4 and in Chapter 4.5.3, are finally combined into a correlated weighted average (see Appendix D.1),

$$\mathcal{B}(B_s^0 \to J/\psi \overline{K}^{*0}) = (4.14 \pm 0.18(\text{stat}) \pm 0.26(\text{syst}) \pm 0.24(\frac{f_d}{f_s})) \times 10^{-5}, \tag{4.64}$$

which is in good agreement with previous LHCb publication [115] as well as with SM expectations.

[2] Assuming $SU(2)$ flavour symmetry.

4.6 Systematic uncertainties

In the following paragraphs, the different sources of systematic uncertainties considered in the present analysis on the B_s^0 angular parameters, as well as on the branching fraction, are detailed.

4.6.1 Angular acceptance

There are two types of systematic uncertainties relevant to the angular acceptance. The first one is due to limited simulation statistics. These uncertainties are evaluated by varying the normalisation weights by a gaussian variation of ± 5 times their statistical uncertainty taking into account their correlations and repeating the angular fit 200 times. For each fitted parameter the root mean square (rms) from those fits is taken as a systematic for that parameter. Normalisation weights are varied independently in each $m_{K\pi}$ category.

The second is due to the data–simulation corrections in the angular acceptance. This kind of systematic uncertainties have been evaluated taking the difference between two angular fit results. The first fit uses the default set of normalisation weights (meaning the ones extracted from corrected $B^0 \to J/\psi K^{*0}$ simulation as described in Chapter 4.4.3). The second fit uses a set of normalisation weights extracted from $B^0 \to J/\psi K^{*0}$ background-subtracted real data. The amplitudes measured by LHCb for $B^0 \to J/\psi K^{*0}$ [133] are used in that fit as the the best estimate of their true values. The difference between the two fit results is assigned as a systematic.

4.6.2 $m(J/\psi K^+\pi^-)$ mass model

Not all the PDFs parameters are free to vary in the fit to data. Namely, the fixed parameters are λ, a_1, n_1, a_2 and n_2 of the B_s^0 and B^0 Hypatia functions, as well as all the parameters of the Amoroso functions describing the two Λ_b peaking backgrounds. These parameters are fixed to values taken from simulated events. In order to account for systematic uncertainties due to these fixed parameters, the mass fit is repeated 1000 times where the value of each fixed parameter is randomly taken from a Gaussian distribution of mean and width corresponding to the nominal value extracted from a fit to simulated events and the corresponding uncertainty, respectively. Note that correlations among the parameters extracted from simulation are taken into account in this procedure. Then using the new sets of ${}_s\mathcal{W}eights$ 1000 fits to the weighted angular distributions are performed. The plus (minus) one σ systematic uncertainties are taken as the values at $\pm 34.1\%$ of the considered parameter distribution integral around the nominal parameter value. In addition, the systematic uncertainties due to the fixed value of a_2 are evaluated by fixing a_2 "to infinity" and letting it free to vary in the fit (see Chapter 4.3.1).

4.6.3 Resonant backgrounds

Since some components in the mass fit are directly accounted for in the mass model, but subtracted using negative weights, another strategy than the one adopted in Chapter 4.6.2 needs to be considered in order to estimate the systematic uncertainties related to the knowledge on these subtracted peaking backgrounds. In order to evaluate the systematic uncertainties due to the fixed yields of the $B_s^0 \to J/\psi K^+K^-$, $B_s^0 \to J/\psi\pi^+\pi^-$, $B^0 \to J/\psi\pi^+\pi^-$, and $\Lambda_b^0 \to J/\psi pK^-$ peaking backgrounds[3] the fit to the invariant mass is repeated moving the normalisation injected simulated sample by $\pm 1\sigma$ according to the yields estimated in Table 4.6. For each of the new mass fit using the two different sets of injected weights, the angular fit is repeated using the corresponding new sets of ${}_s\mathcal{W}eights$. The deviations on each of the angular parameters are then added in quadrature.

4.6.4 Correlations between mass and angles in the ${}_s\mathcal{P}lot$ context

Correlations between the $J/\psi K^+\pi^-$ invariant mass and the cosine of the helicity angle θ_μ while extracting the ${}_s\mathcal{W}eights$ are taken into account in the nominal fit model (see Chapter 4.3.1). In order to evaluate systematic uncertainties due to these correlations, the mass fit is repeated with 6 and 4 $\cos(\theta_\mu)$ bins.[4] For both of the new mass fit, the angular fit is repeated using the corresponding set of ${}_s\mathcal{W}eights$. The deviations on each of the angular parameters are then added in quadrature. Since only two new fits are performed, the corresponding uncertainty is symmetrised when both deviations are either positive or negative.

4.6.5 Fit bias

From the results of the toy simulation studies (see Chapter 4.3.3), the biases corresponding to each parameter are symmetrised and add them into the systematics.

4.6.6 C_{SP} factors

The uncertainties due to the choice of the propagator models for the C_{SP} factors have been evaluated as the maximum difference observed in the measured parameters when computing the C_{SP} factors with all of the considered alternative models.

4.6.7 D-wave contribution

The uncertainties due to neglecting the D-wave contribution in the fit are computed as the differences in the measured parameters when comparing the fit with and without a

[3] The yields of the subtracted background can be considered as fixed, since the sum of negative weights used to subtract them is constant in the nominal fit.

[4] In both cases, the bin size is constant and corresponds to the allowed range (i.e. $-1 \leq \cos(\theta_\mu) \leq 1$) divided by the number of bins.

D-wave component. The D-wave parameters are fixed to their values measured in the $K_2^*(1430)^0$ region (with the correct extrapolation to low $m_{K\pi}$ bins).

4.6.8 Nuisance *CP* asymmetries

The uncertainties from detection and production asymmetries are evaluated by varying the detection and production asymmetries by $\pm 1\sigma$ in the fit.

4.6.9 Branching fraction calculations

The uncertainties from the external parameters $\frac{f_d}{f_s}$, $\mathcal{B}(B^0 \to J/\psi K^{*0})$, $\mathcal{B}(B_s^0 \to J/\psi\phi)$, and $\mathcal{B}(\phi \to K^+K^-)$ are taken as systematic sources for this analysis. They are added in quadrature to the estimation of $\mathcal{B}(B_s^0 \to J/\psi \overline{K}^{*0})$. The κ factors used in the normalisation are sensitive (to some degree) to all the systematics affecting the angular parameters. Those have been calculated in Chapter 4.5.2.

4.6.10 Summary

The full list of systematic uncertainties related to the angular parameters is given in Table 4.38 and Table 4.39 for the P-wave and S-wave parameters, respectively. Two sources of systematics are found to be dominant: the size of the simulation sample used to estimate the normalisation weights of the angular acceptance; the correlation between the $J/\psi K^+\pi^-$ invariant mass and the cosine of the helicity angle θ_μ. The total uncertainties on the angular parameters remain largely dominated by the statistical uncertainties. Furthermore, the list of systematic uncertainties related to the branching fraction measurement is Table 4.37.

Table 4.37: Summary of the statistical and systematic uncertainties for the branching fraction measurements. Numbers are in units of 10^{-2}.

	$\frac{\mathcal{B}(B_s^0 \to J/\psi \overline{K}^{*0})}{\mathcal{B}(B^0 \to J/\psi K^{*0})}$	$\frac{\mathcal{B}(B_s^0 \to J/\psi \overline{K}^{*0})}{\mathcal{B}(B_s^0 \to J/\psi \phi)}$
Statistical	0.14	0.19
$\frac{f_d}{f_s}$	0.17	0
Efficiency ratio	0.039	0.054
Peaking backgrounds effect on the yield	0.018	0.025
Angular corrections	0.092	0.070
Mass fit model	0.057	0.078
Fit bias	0.0050	0.0068
$\mathcal{B}(\phi \to K^+K^-)$	0	0.041
Quadratic sum	0.18 (0.25 w/ $\frac{f_d}{f_s}$)	0.23

Table 4.38: Summary of the measured $B_s^0 \to J/\psi \overline{K}^{*0}$ P-wave properties and their statistical and systematic uncertainties. When no value is given, it means an uncertainty below 5×10^{-4}, except for the two phases, $\delta_\parallel$ and $\delta_\perp$, where the uncertainty is below 5×10^{-3}.

	f_0	$f_\parallel$	$\delta_\parallel$	$\delta_\perp$	A_0^{CP}	$A_\parallel^{CP}$	$A_\perp^{CP}$
Nominal value	0.497	0.179	-2.70	0.01	-0.048	0.171	-0.049
Statistical uncertainties	$^{+0.024}_{-0.025}$	$^{+0.027}_{-0.026}$	$^{+0.15}_{-0.16}$	0.11	0.057	0.152	$^{+0.095}_{-0.096}$
Angular acceptance (sim. stat)	0.018	0.008	0.02	0.01	0.009	0.017	0.008
Angular acceptance (data-sim. corrections)	0.015	0.007	0.17	0.10	0.007	—	0.015
C_{SP} factors	—	0.001	—	—	0.001	0.002	0.002
D-wave contribution	0.004	0.003	—	—	0.002	0.015	0.002
Background angular model	$^{+0.004}_{-0.003}$	0.002	0.02	0.01	$^{+0.003}_{-0.004}$	$^{+0.012}_{-0.004}$	0.002
Mass parameters and B^0 contamination	—	—	—	—	0.001	0.001	—
Mass–cos(θ_μ) correlations	0.007	0.006	0.07	$^{+0.02}_{-0.04}$	0.014	$^{+0.009}_{-0.012}$	0.016
Fit bias	—	0.001	0.01	0.07	0.003	0.002	0.005
Detection asymmetry	—	—	—	—	0.005	0.005	$^{+0.005}_{-0.006}$
Production asymmetry	—	—	—	—	—	—	—
Quadratic sum of systematics	0.025	0.013	0.19	$^{+0.012}_{-0.013}$	$^{+0.019}_{-0.020}$	$^{+0.028}_{-0.027}$	0.025
Total uncertainties	0.035	$^{+0.030}_{-0.029}$	$^{+0.24}_{-0.25}$	$^{+0.016}_{-0.017}$	0.060	0.154	$^{+0.098}_{-0.099}$

Table 4.39: Summary of the measured $B_s^0 \to J/\psi \overline{K}^{*0}$ S-wave properties and their statistical and systematic uncertainties. When no value is given, it means an uncertainty below 5×10^{-4}, except for the four strong phases related to the S-wave component, δ_S, where the uncertainty is below 5×10^{-3}.

	A_S^{CP}	$m_{K\pi}^{\text{bin1}}$		$m_{K\pi}^{\text{bin2}}$		$m_{K\pi}^{\text{bin3}}$		$m_{K\pi}^{\text{bin4}}$	
		F_S	δ_S	F_S	δ_S	F_S	δ_S	F_S	δ_S
Nominal value	0.167	0.475	0.54	0.080	−0.53	0.044	−1.46	0.523	−1.76
Statistical uncertainties	$^{+0.113}_{-0.114}$	$^{+0.108}_{-0.112}$	0.16	$^{+0.031}_{-0.025}$	$^{+0.25}_{-0.21}$	$^{+0.042}_{-0.029}$	$^{+0.22}_{-0.19}$	$^{+0.109}_{-0.112}$	$^{+0.13}_{-0.14}$
Angular acceptance (sim. stat)	0.028	0.039	0.03	0.012	0.065	0.015	0.10	0.065	0.06
Angular acceptance (data–sim. corrections)	0.015	0.058	0.08	0.019	0.18	0.027	0.27	0.006	0.04
C_{SP} factors	—	0.002	0.01	0.001	—	0.002	—	0.001	0.01
D-wave contribution	0.008	0.010	0.02	0.005	0.03	0.008	0.08	0.002	0.04
Background angular model	0.001	0.002	0.01	$^{+0.000}_{-0.001}$	0.01	—	$^{+0.03}_{-0.02}$	$^{+0.002}_{-0.000}$	$^{+0.07}_{-0.04}$
Mass parameters and B^0 contamination	0.001	0.001	$^{+0.00}_{-0.01}$	—	—	—	—	—	—
Mass–$\cos(\theta_\mu)$ correlations	$^{+0.023}_{-0.029}$	$^{+0.040}_{-0.028}$	0.05	0.003	0.04	$^{+0.006}_{-0.016}$	0.02	$^{+0.009}_{-0.011}$	$^{+0.02}_{-0.03}$
Fit bias	0.004	0.005	0.01	0.003	0.02	0.007	0.032	0.015	0.01
Detection asymmetry	0.005	—	—	—	—	—	—	—	—
Production asymmetry	—	—	—	—	—	—	—	—	—
Quadratic sum of systematics	$^{+0.041}_{-0.044}$	$^{+0.081}_{-0.076}$	0.10	0.023	0.20	$^{+0.033}_{-0.036}$	0.30	0.068	$^{+0.11}_{-0.09}$
Total uncertainties	$^{+0.120}_{-0.122}$	0.135	0.19	$^{+0.039}_{-0.034}$	$^{+0.32}_{-0.29}$	$^{+0.054}_{-0.047}$	$^{+0.37}_{-0.35}$	$^{+0.128}_{-0.131}$	0.17

4.7 Results

The main results from this analysis are summarized in this section. A further discussion on penguin pollution in the ϕ_s phase, using these results, is presented in next Chapter 5.

4.7.1 Angular analysis and mass fit

Using 3 fb^{-1} of real data, a simultaneous fit is carried out in 4 bins of $m_{K\pi}$ around the K^{*0} nominal mass, i.e $m_{K\pi} \in [826, 966]\,\text{MeV}/c^2$. All the steps of the fit model construction are described in Chapter 4.4.1. The parameters of interest are the polarisation fractions and polarisation-dependent *CP* asymmetries. The angular parameters obtained from the fit are summarized in Table 4.40 with their statistical uncertainties. The P-wave amplitudes and strong phases are common among the 4 bins of $m_{K\pi}$, while the S-wave parameters are split in the different bins. The previous analysis of $B_s^0 \to J/\psi \overline{K}^{*0}$ polarisation amplitudes and phases was based on fits with a single bin in $m_{K\pi}$ and did not account for possible *CP* asymmetries. Using 0.37 fb^{-1}, LHCb has measured [134]

$$f_0 = 0.50 \pm 0.08 \pm 0.02, \tag{4.65}$$
$$f_\parallel = 0.19^{+0.10}_{-0.08} \pm 0.02, \tag{4.66}$$
$$\delta_\parallel = -2.78 \pm 0.54, \tag{4.67}$$

where f_0 and $f_\parallel$ are the longitudinal and parallel polarisation fractions, respectively, defined as $f_i = |A_i|^2 / \sum_i |A_i|^2$, $i = 0, \parallel, \perp$. The first uncertainty is statistical, the second is systematic. The results with 3 fb^{-1} are compatible with (4.65), (4.66) and (4.67), and more accurate by a factor of 3.

The signal angular distribution and the projections of the fitted PDF are shown in Figure 4.18. Slices of the same plots in bins of $m_{K\pi}$ are shown in Appendix E. Additionally, the correlations between the fitted parameters are presented in Table 4.41.

An additional compatibility check of the polarisation amplitudes between $B_s^0 \to J/\psi \overline{K}^{*0}$ and $B^0 \to J/\psi K^{*0}$ decay modes is performed in view of the fitted parameters of Table 4.40. Namely the P-wave, S-wave fractions and the S-wave phases in bins of $m_{K\pi}$. The checks emphasize on the compatibility of P-wave and S-wave fractions trends between $B_s^0 \to J/\psi \overline{K}^{*0}$ and $B^0 \to J/\psi K^{*0}$. This is why the absolute scale is ignored and both curves are normalised to one. The fraction central values in each $m_{K\pi}$ bin are estimated using (4.45) of Chapter 4.5.2, whereas the errors using

$$\begin{aligned} \sigma(\mathrm{N}^{\text{S-wave}}_{B_s^0,B^0}) &= \sigma(\mathrm{N}_{B_s^0,B^0} \cdot F_S), \\ \sigma(\mathrm{N}^{\text{P-wave}}_{B_s^0,B^0}) &= \sigma(\mathrm{N}_{B_s^0,B^0} \cdot (1 - F_S)). \end{aligned} \tag{4.68}$$

The plots include only statistical uncertainties coming from $\mathrm{N}_{B_s^0,B^0}$ and F_S. As a reminder, $\mathrm{N}_{B_s^0,B^0}$ is the B_s^0, B^0 fitted signal yield that comes from the fit B_s^0 mass of Chapter 4.3.2. An additional systematic is added due to the assumption of $A^{CP} = 0$. The dominant source of uncertainty is statistical.

Table 4.40: Parameters resulting from the angular fit performed simultaneously in four $m_{K\pi}$ bins around the $K^*(892)^0$ nominal mass.

	Measured value
A_0^{CP}	-0.048 ± 0.057
$A_\parallel^{CP}$	0.171 ± 0.152
$A_\perp^{CP}$	$-0.049^{+0.095}_{-0.096}$
A_S^{CP}	$0.167^{+0.113}_{-0.114}$
f_0	$0.497^{+0.024}_{-0.025}$
$f_\parallel$	$0.179^{+0.027}_{-0.026}$
$\delta_\parallel$	$-2.70^{+0.15}_{-0.16}$
$\delta_\perp$	-0.01 ± 0.11
F_S_826_861	$0.475^{+0.108}_{-0.112}$
δ_S_826_861	0.54 ± 0.16
F_S_861_896	$0.080^{+0.031}_{-0.025}$
δ_S_861_896	$-0.53^{+0.25}_{-0.21}$
F_S_896_931	$0.044^{+0.042}_{-0.029}$
δ_S_896_931	$-1.46^{+0.22}_{-0.19}$
F_S_931_966	$0.523^{+0.109}_{-0.112}$
δ_S_931_966	$-1.76^{+0.13}_{-0.14}$

4.7.2 Comparison with results from $B^0 \to J/\psi\rho^0$ analysis

The polarisation fractions and *CP* asymmetries obtained here for $B_s^0 \to J/\psi\overline{K}^{*0}$ are also compared with those from a previous LHCb $B^0 \to J/\psi\rho^0$ analysis [112] in Table 4.42. In the $SU(3)$-limit and ignoring contributions from additional decay topologies, these results should agree. However, because the $B^0 \to J/\psi\rho^0$ mode also has contributions from exchange and penguin-annihilation diagrams which do not have a counterpart in $B_s^0 \to J/\psi\overline{K}^{*0}$ decays, differences can arise. The direct *CP* asymmetries are in good agreement with one another. The difference is not significant enough to deduce any information on $SU(3)$-breaking.

4.7.3 Branching fraction measurement

A correlated weighted average for $\mathcal{B}(B_s^0 \to J/\psi\overline{K}^{*0})$ is also obtained (see Chapter 4.5.5),

$$\mathcal{B}(B_s^0 \to J/\psi\overline{K}^{*0}) = (4.14 \pm 0.18(\text{stat}) \pm 0.26(\text{syst}) \pm 0.24(\frac{f_d}{f_s})) \times 10^{-5}, \qquad (4.69)$$

which is in good agreement with previous LHCb publication [115] as well as with SM expectations [22].

Table 4.41: Statistical correlation matrix for the parameters from the angular fit.

	A_0^{CP}	A_S^{CP}	$A_\parallel^{CP}$	$A_\perp^{CP}$	F_S^0	F_S^1	F_S^2	F_S^3	$\delta_\parallel$	$\delta_\perp$	δ_S^0	δ_S^1	δ_S^2	δ_S^3	f_0	$f_\parallel$
A_0^{CP}	+1.00	−0.12	−0.11	−0.17	−0.13	−0.02	−0.06	−0.01	+0.03	+0.02	+0.10	−0.00	+0.07	+0.01	+0.06	−0.05
A_S^{CP}		+1.00	−0.14	−0.12	+0.16	−0.12	+0.03	−0.10	+0.00	−0.06	+0.02	+0.07	+0.05	+0.07	+0.01	+0.03
$A_\parallel^{CP}$			+1.00	−0.49	+0.02	+0.09	−0.02	+0.08	+0.09	+0.06	−0.06	−0.04	−0.05	−0.12	−0.04	−0.07
$A_\perp^{CP}$				+1.00	−0.00	−0.01	−0.06	−0.07	−0.09	−0.03	−0.03	+0.01	−0.02	+0.07	+0.01	−0.06
F_S^0					+1.00	+0.01	−0.01	−0.03	−0.10	−0.24	−0.77	+0.01	+0.04	−0.00	+0.10	−0.09
F_S^1						+1.00	−0.01	−0.00	−0.02	−0.05	−0.01	−0.25	+0.03	−0.01	+0.15	−0.10
F_S^2							+1.00	+0.01	−0.04	+0.07	+0.01	−0.00	−0.22	+0.00	−0.02	+0.04
F_S^3								+1.00	+0.08	+0.08	+0.00	−0.01	−0.03	−0.29	−0.09	+0.04
$\delta_\parallel$									+1.00	+0.62	+0.10	+0.14	+0.03	+0.11	+0.04	−0.03
$\delta_\perp$										+1.00	+0.17	+0.13	−0.02	+0.13	+0.05	−0.04
δ_S^0											+1.00	+0.04	+0.03	+0.04	+0.08	+0.04
δ_S^1												+1.00	+0.04	+0.04	+0.13	−0.05
δ_S^2													+1.00	+0.04	+0.27	−0.08
δ_S^3														+1.00	+0.11	+0.00
f_0															+1.00	−0.34
$f_\parallel$																+1.00

Figure 4.18: Angular PDF plots on top of the fitted sWeighted data for $B_s^0 \to J/\psi \overline{K}^{*0}$. Blue solid: total. Blue dashed: P-wave + P-P interference. Green dotted: S-wave. Red dotted-dashed: S-P interference.

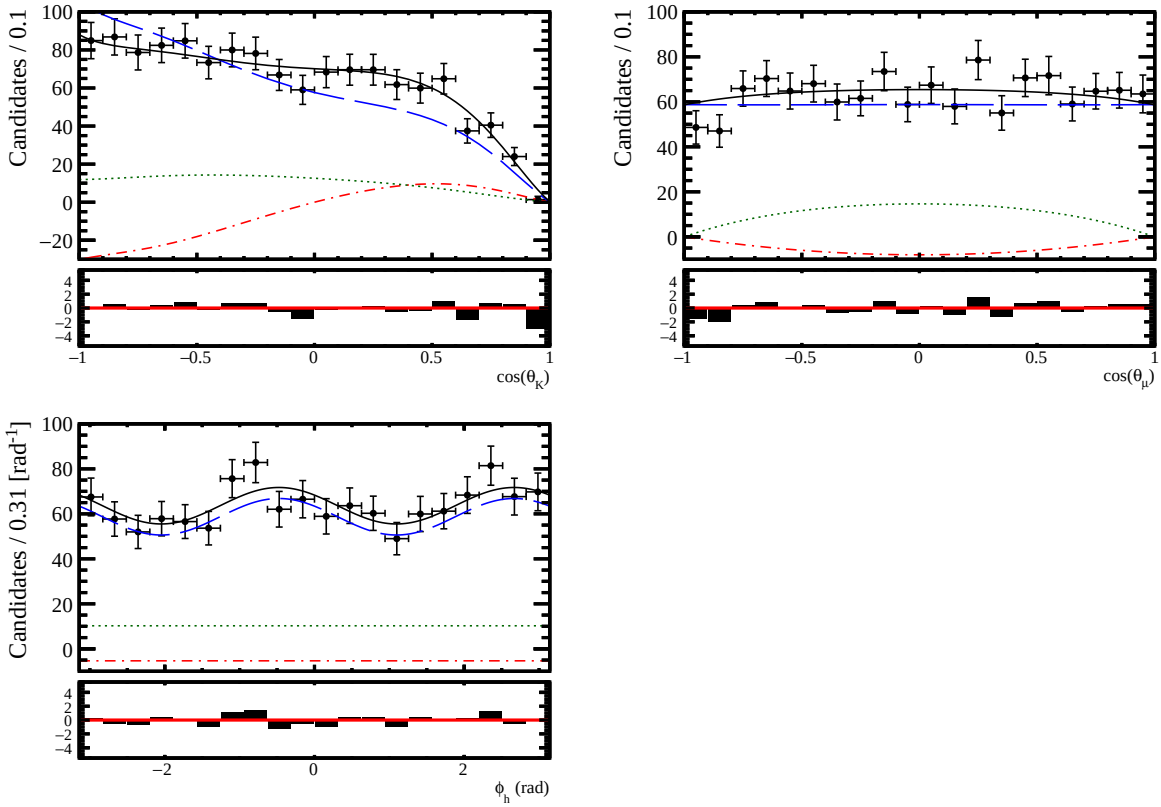

Table 4.42: Comparison between the results from $B_s^0 \to J/\psi \overline{K}^{*0}$ decays presented in this work and those from $B^0 \to J/\psi \rho^0$ analysis [112]. The systematic uncertainties are included.

	$B^0 \to J/\psi \rho^0$	$B_s^0 \to J/\psi \overline{K}^{*0}$	Difference	Sig.
A_0^{CP}	0.094 ± 0.071	-0.048 ± 0.060	-0.142 ± 0.093	-1.5σ
$A_\parallel^{CP}$	0.122 ± 0.120	0.171 ± 0.155	0.049 ± 0.196	0.3σ
$A_\perp^{CP}$	-0.034 ± 0.222	-0.049 ± 0.099	-0.015 ± 0.243	-0.1σ
f_0	0.574 ± 0.037	0.497 ± 0.035	0.077 ± 0.051	1.5σ
$f_\parallel$	0.234 ± 0.021	0.179 ± 0.030	0.055 ± 0.037	1.5σ
$f_\perp$	0.192 ± 0.042	0.324 ± 0.033	-0.132 ± 0.053	-2.5σ

Chapter 5

Penguin pollution in the ϕ_s phase

The penguin pollution as given by (2.33) in Chapter 2.3, $\Delta\phi_{s,i}$, is parameterised [110, 150] by the relative size a_i of the penguin to tree amplitudes, which has an associated strong phase difference θ_i and weak phase difference is given by the UT angle γ. Alternatively, the penguin effects can also be parametrised in cartesian coordinates as $\Re[a_i] = a_i \cos\theta_i$ and $\Im[a_i] = a_i \sin\theta_i$. The penguin parameters a_i and θ_i can be extracted from two times three parameters (two for each polarisation i) [108, 110, 150]:

- H_i, related to the branching fraction ratios and polarisation fractions,

$$\begin{aligned} H_i &\equiv \frac{1}{\epsilon}\left|\frac{\mathcal{A}'_i}{\mathcal{A}_i}\right|^2 \frac{\mathrm{PHSP}\,(B_s^0 \to J/\psi\phi)}{\mathrm{PHSP}(B_s^0 \to J/\psi\overline{K}^{*0})} \frac{\mathcal{B}(B_s^0 \to J/\psi\overline{K}^{*0})_{\mathrm{theo}}}{\mathcal{B}(B_s^0 \to J/\psi\phi)_{\mathrm{theo}}} \frac{f_i}{f'_i} \\ &= \frac{1 - 2a_i\cos\theta_i\cos\gamma + a_i^2}{1 + 2\epsilon a'_i\cos\theta'_i\cos\gamma + \epsilon^2 a_i'^2}\,, \end{aligned} \tag{5.1}$$

- A_i^{CP}, the direct CP violation asymmetries, [1]

$$A_i^{CP} = -\frac{2a_i\sin\theta_i\sin\gamma}{1 - 2a_i\cos\theta_i\cos\gamma + a_i^2}\,. \tag{5.2}$$

In the above equations, the prime ($'$) refers to the $B_s^0 \to J/\psi\phi$ channel while the non-primed quantities refers to the $B_s^0 \to J/\psi\overline{K}^{*0}$ channel. $\mathcal{A}'_i/\mathcal{A}_i$ are hadronic quantities discussed in the Chapter 5.1. Here,

$$\mathrm{PHSP}(B \to V_1V_2) \equiv \frac{1}{16\pi m_B}\Phi\left(\frac{m_{V_1}}{m_B}, \frac{m_{V_2}}{m_B}\right)\,, \tag{5.3}$$

is a phase-space factor, where m_B is the mass of the B meson, and Φ is the standard two-body phase-space factor. Contrary to $B \to VP$ and $B \to PP$ decays and due to the complexity of the expressions for the hadronic amplitudes of $B \to VV$ decays, all

[1] Conventions: $A_i^{CP} = -\mathcal{A}_{\mathrm{dir}}^{CP}$ used in ref. [110].

other mass-dependent terms are absorbed into the ratio $\mathcal{A}'_i/\mathcal{A}_i$. Note that the conversion factors [151]

$$\frac{\mathcal{B}(B_s \to f)_{\text{theo}}}{\mathcal{B}(B_s \to f)_{\text{exp}}} = \left[\frac{1 - y_s^2}{1 + \mathcal{A}_{\Delta\Gamma}\, y_s}\right], \qquad y_s \equiv \frac{\Delta\Gamma_s}{2\Gamma_s}, \tag{5.4}$$

between the "theoretical" branching ratio concept and the experimentally measured time-integrated branching fraction depend on the CP observable $\mathcal{A}_{\Delta\Gamma}$[2] and are therefore polarisation dependent. As $B_s^0 \to J/\psi \overline{K}^{*0}$ is a flavour specific decay, $\mathcal{A}_{\Delta\Gamma}(B_s^0 \to J/\psi \overline{K}^{*0}) = 0$, thus the conversion factor is equal to 0.9963 ± 0.0006. For $B_s^0 \to J/\psi\phi$, $\mathcal{A}_{\Delta\Gamma}$ depends on the penguin parameters again. For simplicity, $a = \theta = 0$ is assumed when calculating the correction factor in (5.4), obtaining 1.0608 ± 0.0045 (0.9392 ± 0.0045) for the CP even (odd) states.

Assuming

$$a_i = a'_i\,, \qquad \theta_i = \theta'_i\,, \tag{5.5}$$

each pair of observables (5.1) and (5.2) can be used to determine the penguin parameters a_i and θ_i. In turn, the penguin parameters quantify the penguin shift

$$\tan(\Delta\,\phi_{s,i}) = \frac{2\epsilon a'_i \cos\theta'_i \sin\gamma + \epsilon^2 a'^2_i \sin 2\gamma}{1 + 2\epsilon a'_i \cos\theta'_i \cos\gamma + \epsilon^2 a'^2_i \cos 2\gamma}. \tag{5.6}$$

affecting the determination of ϕ_s from $B_s^0 \to J/\psi\phi$ decays.

5.1 External inputs

The hadronic amplitudes $|\mathcal{A}'_i/\mathcal{A}_i|$ are calculated following the method described in ref. [153], using the latest results on form factors from Light Cone QCD Sum Rules (LCSR) [154]. Further details on the calculation can be found in Section 5.5.1 of ref. [152]. The results are

$$\left|\frac{\mathcal{A}'_0(B_s^0 \to J/\psi\phi)}{\mathcal{A}_0(B_s^0 \to J/\psi \overline{K}^{*0})}\right| = 1.23 \pm 0.16\,, \tag{5.7}$$

$$\left|\frac{\mathcal{A}'_\parallel(B_s^0 \to J/\psi\phi)}{\mathcal{A}_\parallel(B_s^0 \to J/\psi \overline{K}^{*0})}\right| = 1.28 \pm 0.15\,, \tag{5.8}$$

$$\left|\frac{\mathcal{A}'_\perp(B_s^0 \to J/\psi\phi)}{\mathcal{A}_\perp(B_s^0 \to J/\psi \overline{K}^{*0})}\right| = 1.20 \pm 0.12\,, \tag{5.9}$$

and lead to

$$H_0 = 0.98 \pm 0.07\,(\text{stat}) \pm 0.06\,(\text{syst}) \pm 0.26\,(|\mathcal{A}'_i/\mathcal{A}_i|) = 0.98 \pm 0.28\,, \tag{5.10}$$

$$H_\parallel = 0.90 \pm 0.14\,(\text{stat}) \pm 0.08\,(\text{syst}) \pm 0.21\,(|\mathcal{A}'_i/\mathcal{A}_i|) = 0.90 \pm 0.26\,, \tag{5.11}$$

$$H_\perp = 1.46 \pm 0.14\,(\text{stat}) \pm 0.11\,(\text{syst}) \pm 0.28\,(|\mathcal{A}'_i/\mathcal{A}_i|) = 1.46 \pm 0.33\,. \tag{5.12}$$

[2] Defined e.g. in Eq. 4.47 of [152].

5.2 Fit results

For each of the three polarisation states individually, a modified least squares fit is performed. This means that correlations between the experimental inputs are ignored. It has three degrees of freedom: $\Re[a]$, $\Im[a]$ and γ, with the latter parameter being Gaussian constrained to [155]

$$\gamma = \left(73.2^{+6.3}_{-7.0}\right)^\circ \,. \tag{5.13}$$

The χ^2 functions reach their minimum value at

$$\Re[a_0] = 0.03^{+0.97}_{-0.32}\,, \qquad \Im[a_0] = 0.025^{+0.034}_{-0.031}\,, \qquad \chi^2_{\rm min} = 1.3\times10^{-7}\,, \tag{5.14}$$

$$\Re[a_\parallel] = 0.31^{+0.57}_{-0.50}\,, \qquad \Im[a_\parallel] = -0.082^{+0.074}_{-0.085}\,, \qquad \chi^2_{\rm min} = 4.5\times10^{-3}\,, \tag{5.15}$$

$$\Re[a_\perp] = -0.43^{+0.27}_{-0.21}\,, \qquad \Im[a_\perp] = 0.037^{+0.078}_{-0.075}\,, \qquad \chi^2_{\rm min} = 1.2\times10^{-6}\,, \tag{5.16}$$

which translates to

$$a_0 = 0.04^{+0.95}_{-0.04}\,, \qquad \theta_0 = \left(40^{+140}_{-220}\right)^\circ\,, \tag{5.17}$$

$$a_\parallel = 0.32^{+0.57}_{-0.32}\,, \qquad \theta_\parallel = -\left(15^{+148}_{-14}\right)^\circ\,, \tag{5.18}$$

$$a_\perp = 0.44^{+0.21}_{-0.27}\,, \qquad \theta_\perp = \left(175^{+11}_{-10}\right)^\circ\,. \tag{5.19}$$

For the longitudinal polarisation state, the strong phase θ is unconstrained. The constraints on the penguin parameters derived from the individual observables entering the χ^2 fit are illustrated as different light-coloured bands in Figure 5.1 and Figure 5.2 for the parametrisations in terms of $(\Re[a], \Im[a])$ and (θ, a), respectively. Assuming perfect $SU(3)$ symmetry, the penguin parameters from (5.14) to (5.16) result in a penguin phase shift on $\phi_s(B^0_s \to J/\psi\phi)$,

$$\Delta\phi^{J/\psi\phi}_{s,0} = 0.003^{+0.084}_{-0.011}\,(\text{stat})^{+0.014}_{-0.009}\,(\text{syst})^{+0.047}_{-0.030}\,(|\mathcal{A}'_i/\mathcal{A}_i|) = 0.003^{+0.097}_{-0.033}\,, \tag{5.20}$$

$$\Delta\phi^{J/\psi\phi}_{s,\parallel} = 0.031^{+0.047}_{-0.037}\,(\text{stat})^{+0.010}_{-0.013}\,(\text{syst})^{+0.032}_{-0.032}\,(|\mathcal{A}'_i/\mathcal{A}_i|) = 0.031^{+0.058}_{-0.051}\,, \tag{5.21}$$

$$\Delta\phi^{J/\psi\phi}_{s,\perp} = -0.045^{+0.012}_{-0.012}\,(\text{stat})^{+0.007}_{-0.008}\,(\text{syst})^{+0.017}_{-0.024}\,(|\mathcal{A}'_i/\mathcal{A}_i|) = -0.045^{+0.022}_{-0.028}\,, \tag{5.22}$$

or in degrees

$$\Delta\phi^{J/\psi\phi}_{s,0} = \left(0.2^{+4.8}_{-0.6}\,(\text{stat})^{+0.8}_{-0.5}\,(\text{syst})^{+2.7}_{-1.7}\,(|\mathcal{A}'_i/\mathcal{A}_i|)\right)^\circ = \left(0.2^{+5.6}_{-1.9}\right)^\circ\,, \tag{5.23}$$

$$\Delta\phi^{J/\psi\phi}_{s,\parallel} = \left(1.8^{+2.7}_{-2.1}\,(\text{stat})^{+0.6}_{-0.8}\,(\text{syst})^{+1.8}_{-1.9}\,(|\mathcal{A}'_i/\mathcal{A}_i|)\right)^\circ = \left(1.8^{+3.3}_{-2.9}\right)^\circ\,, \tag{5.24}$$

$$\Delta\phi^{J/\psi\phi}_{s,\perp} = -\left(2.6^{+0.7}_{-0.7}\,(\text{stat})^{+0.5}_{-0.4}\,(\text{syst})^{+1.4}_{-1.0}\,(|\mathcal{A}'_i/\mathcal{A}_i|)\right)^\circ = -\left(2.6^{+1.6}_{-1.3}\right)^\circ\,. \tag{5.25}$$

5.3 $SU(3)$-breaking

$SU(3)$-breaking effects are parametrised by including the $SU(3)$-breaking parameters ξ and δ in the relation (5.5)

$$a'_i = \xi \times a_i\,, \qquad \theta'_i = \theta_i + \delta\,. \tag{5.26}$$

Because $a_i^{(\prime)}$ are ratios of amplitudes, the leading order factorisable $SU(3)$-breaking corrections cancel. The $a_i^{(\prime)}$ are therefore only affected by non-factorisable $SU(3)$-breaking corrections, which are suppressed compared to their factorisable counterparts. As there are no dedicated studies quantifying ξ and/or δ, it is assumed here by default perfect $SU(3)$ symmetry, i.e. $\xi = 1$ and $\delta = 0$, but include uncertainties on these parameters as Gaussian constraints to the χ^2 fit. The dependence of $\Delta\phi_{s,i}^{J/\psi\phi}$ on the assumed uncertainty on ξ is shown in Figure 5.3. No dependence of $\Delta\phi_{s,i}^{J/\psi\phi}$ on the assumed uncertainty on δ could be observed. This is due to the algebraic structure of $\Delta\phi_{s,i}^{J/\psi\phi}$ in (5.6) and the specific solution where $\Im[a] \approx 0$, which makes the effect of δ on $\Delta\phi_{s,i}^{J/\psi\phi}$ negligible compared to the other contributing factors.

5.4 Further cross-checks

As a cross-check, a second fit strategy is explored: a (single) χ^2 that takes into account the correlations between the *CP* asymmetries and the polarisation fractions is also implemented. The results of this fit are

$$\Re[a_0] = 0.03^{+0.95}_{-0.33}\,, \qquad \Im[a_0] = 0.025^{+0.035}_{-0.032}\,, \tag{5.27}$$

$$\Re[a_\parallel] = 0.31^{+0.60}_{-0.54}\,, \qquad \Im[a_\parallel] = -0.082^{+0.085}_{-0.099}\,, \tag{5.28}$$

$$\Re[a_\perp] = -0.43^{+0.26}_{-0.22}\,, \qquad \Im[a_\perp] = 0.037^{+0.091}_{-0.087}\,, \tag{5.29}$$

which gives slightly larger uncertainties for some of the parameters. In addition, the results on the constraint parameters are:

Obs.	Init.	Fit
$f_0^{J/\psi\phi}$	0.5241 ± 0.0075	0.5241 ± 0.0093
$f_\perp^{J/\psi\phi}$	0.2504 ± 0.0080	0.2504 ± 0.0099
$f_0^{J/\psi\overline{K}^{*0}}$	0.4970 ± 0.0354	0.4962 ± 0.0391
$f_\parallel^{J/\psi\overline{K}^{*0}}$	0.1790 ± 0.0300	0.1803 ± 0.0276
$\mathcal{B}(\overline{K}^{*0})/\mathcal{B}(\phi)$	0.0405 ± 0.0023	0.0405 ± 0.0023

Beyond the results given here, this strategy is not further pursued.

5.5 Extended fit including the $B^0 \to J/\psi\rho^0$ decay mode

The information on the penguin parameters provided by the *CP* and branching ratio information in $B_s^0 \to J/\psi\overline{K}^{*0}$ can be combined with that from the $SU(3)$-related mode $B^0 \to J/\psi\rho^0$. There are three ways to make this combination:

1. Use only "theoretically clean" observables. Perform the fit using only information on $C_i(B^0 \to J/\psi\rho^0)$, $S_i(B^0 \to J/\psi\rho^0)$ and $A_i^{CP}(B_s^0 \to J/\psi\overline{K}^{*0})$, and ignore the two H observables.

2. Use all available observables and include external information for $|\mathcal{A}_i'/\mathcal{A}_i|$.

3. Following the suggestion in ref. [110], use all available observables and fit $|\mathcal{A}_i'/\mathcal{A}_i|$ under the assumption

$$\left|\frac{\mathcal{A}_i'(B_s^0 \to J/\psi\phi)}{\mathcal{A}_i(B_s^0 \to J/\psi\overline{K}^{*0})}\right| = \left|\frac{\mathcal{A}_i'(B_s^0 \to J/\psi\phi)}{\mathcal{A}_i(B^0 \to J/\psi\rho^0)}\right| . \tag{5.30}$$

   This allows to confront the theoretical calculations of $|\mathcal{A}_i'/\mathcal{A}_i|$ with experimental data.

The second option is disfavoured because the use of the H observables introduces additional theoretical uncertainties which might be larger than the improvement in the fit compared to the first option. Given the limited precision on the H observables, first and third options will essentially lead to the same solution for the penguin parameters and penguin shifts, while the third option provides additional insights. Therefore the third option is pursued below.

For each of the three polarisation states individually, a modified least squares fit is performed. This means that correlations between the experimental inputs are ignored (for further details on the formalism, see refs. [110, 152]). It has five degrees of freedom, $\Re[a]$, $\Im[a]$, $|\mathcal{A}_i'/\mathcal{A}_i|$, γ and ϕ_d, with the latter two parameters being Gaussian constrained. For γ, (5.13) is used, while for ϕ_d the value [152]

$$\phi_d = 0.767 \pm 0.029 \tag{5.31}$$

is used. Assuming $SU(3)$ flavour symmetry and neglecting contributions from additional decay topologies, the χ^2 functions reach their minimum value at

$$\Re[a_0] = 0.00^{+0.11}_{-0.13}\,, \quad \Im[a_0] = -0.006 \pm 0.024\,, \quad \left|\frac{\mathcal{A}_0'}{\mathcal{A}_0}\right| = 1.195^{+0.074}_{-0.056}\,, \tag{5.32}$$

$$\Re[a_\parallel] = 0.01^{+0.11}_{-0.16}\,, \quad \Im[a_\parallel] = -0.073^{+0.050}_{-0.052}\,, \quad \left|\frac{\mathcal{A}_\parallel'}{\mathcal{A}_\parallel}\right| = 1.238^{+0.104}_{-0.080}\,, \tag{5.33}$$

$$\Re[a_\perp] = 0.03^{+0.12}_{-0.16}\,, \quad \Im[a_\perp] = 0.024 \pm 0.047\,, \quad \left|\frac{\mathcal{A}_\perp'}{\mathcal{A}_\perp}\right| = 1.042^{+0.081}_{-0.063}\,, \tag{5.34}$$

which translates to

$$a_0 = 0.01^{+0.10}_{-0.01}\,, \qquad \theta_0 = -\left(83^{+97}_{-263}\right)^\circ\,, \tag{5.35}$$

$$a_\parallel = 0.07^{+0.11}_{-0.05}\,, \qquad \theta_\parallel = -\left(85^{+72}_{-63}\right)^\circ\,, \tag{5.36}$$

$$a_\perp = 0.04^{+0.12}_{-0.04}\,, \qquad \theta_\perp = \left(38^{+142}_{-218}\right)^\circ\,. \tag{5.37}$$

For longitudinal and perpendicular polarisation states, the strong phase θ is unconstrained. The combined fit leads to a penguin phase shift on $\phi_s(B_s^0 \to J/\psi\phi)$,

$$\Delta\phi_{s,0}^{J/\psi\phi} = 0.000^{+0.009}_{-0.011}\,(\text{stat})^{+0.004}_{-0.009}\,(\text{syst}) = 0.000^{+0.010}_{-0.014}\,, \tag{5.38}$$

$$\Delta\phi_{s,\parallel}^{J/\psi\phi} = 0.001^{+0.010}_{-0.014}\,(\text{stat})^{+0.007}_{-0.008}\,(\text{syst}) = 0.001^{+0.012}_{-0.016}\,, \tag{5.39}$$

$$\Delta\phi_{s,\perp}^{J/\psi\phi} = 0.003^{+0.010}_{-0.014}\,(\text{stat})^{+0.007}_{-0.008}\,(\text{syst}) = 0.003^{+0.012}_{-0.016}\,, \tag{5.40}$$

or in degrees,

$$\Delta\phi_{s,0}^{J/\psi\phi} = \left(0.01^{+0.50}_{-0.63}\,(\text{stat})^{+0.32}_{-0.47}\,(\text{syst})\right)^\circ = \left(0.01^{+0.59}_{-0.79}\right)^\circ\,, \tag{5.41}$$

$$\Delta\phi_{s,\parallel}^{J/\psi\phi} = \left(0.04^{+0.59}_{-0.78}\,(\text{stat})^{+0.32}_{-0.53}\,(\text{syst})\right)^\circ = \left(0.04^{+0.67}_{-0.94}\right)^\circ\,, \tag{5.42}$$

$$\Delta\phi_{s,\perp}^{J/\psi\phi} = \left(0.18^{+0.60}_{-0.78}\,(\text{stat})^{+0.32}_{-0.51}\,(\text{syst})\right)^\circ = \left(0.18^{+0.68}_{-0.93}\right)^\circ\,. \tag{5.43}$$

The constraints on the penguin parameters derived from the individual observables entering the χ^2 fit are illustrated as different light-coloured bands in Figure 5.4 and Figure 5.5 for the parametrisations in terms of $(\Re[a], \Im[a])$ and (θ, a), respectively.The current results indicate a slight tension between the H observables constructed with $B_s^0 \to J/\psi\overline{K}^{*0}$ and $B^0 \to J/\psi\rho^0$. Assuming for the sake of argument that this tension is genuine, i.e. not merely due to statistical fluctuations in the input data, then the picture emerging from Figure 5.5 suggests that the source of this tension lies with factorisable $SU(3)$-breaking effects and thus a violation of the assumption (5.30).

Figure 5.1: Determination of the penguin parameters a_i and θ_i through intersecting contours derived from the *CP* asymmetries and branching ratio information in $B_s^0 \to J/\psi \overline{K}^{*0}$. The inner dark-coloured line represents the contour associated with the central value of the input quantity. Superimposed are the confidence level contours obtained from a χ^2 fit to the data. Shown are the longitudinal (left), parallel (right) and perpendicular (bottom) polarisation.

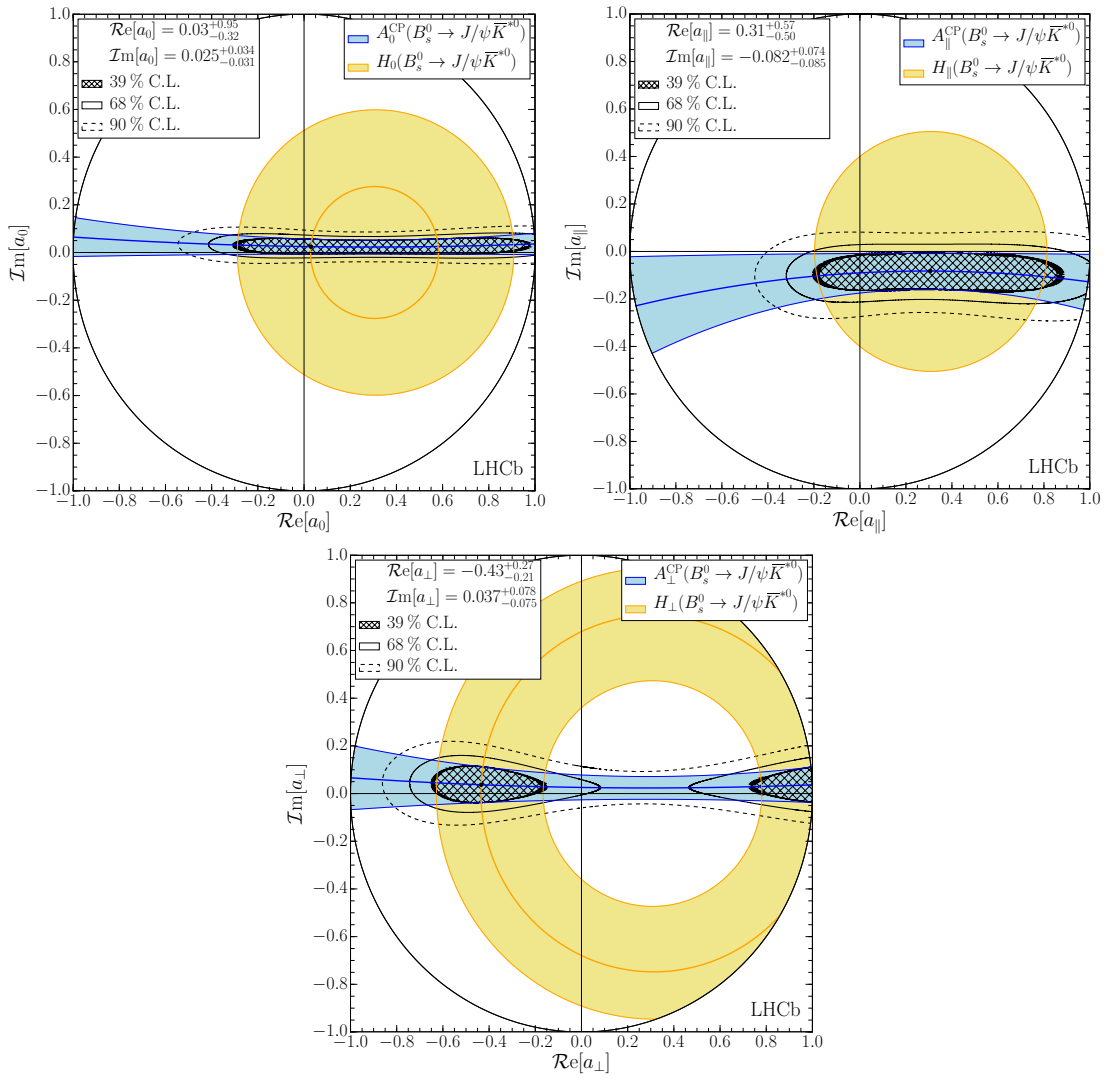

Figure 5.2: Determination of the penguin parameters a_i and θ_i through intersecting contours derived from the *CP* asymmetries and branching ratio information in $B_s^0 \to J/\psi \overline{K}^{*0}$. Superimposed are the confidence level contours obtained from a χ^2 fit to the data. Shown are the longitudinal (top), parallel (middle) and perpendicular (bottom) polarisation.

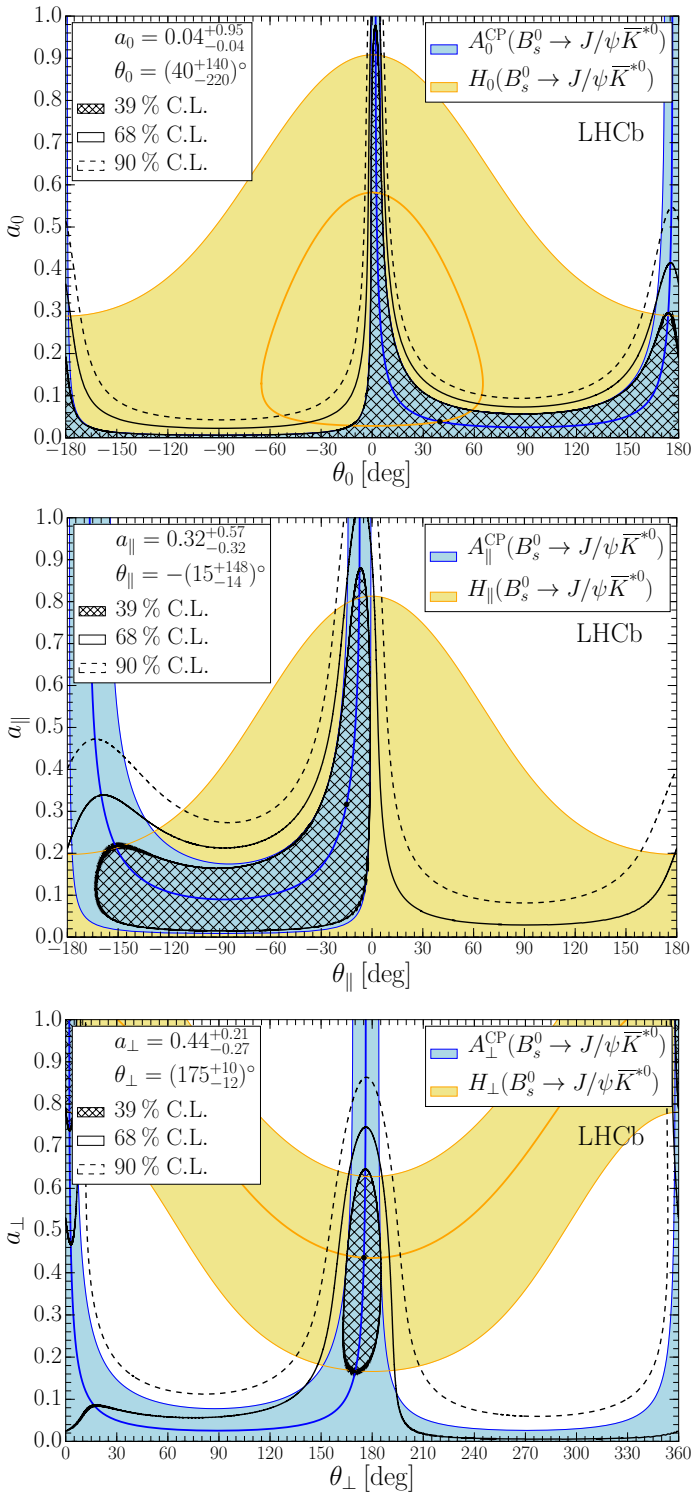

Figure 5.3: Dependence of the penguin shift $\Delta\phi_{s,i}^{J/\psi\phi}$ on the uncertainty on ξ. The bands correspond to the 68% C.L.

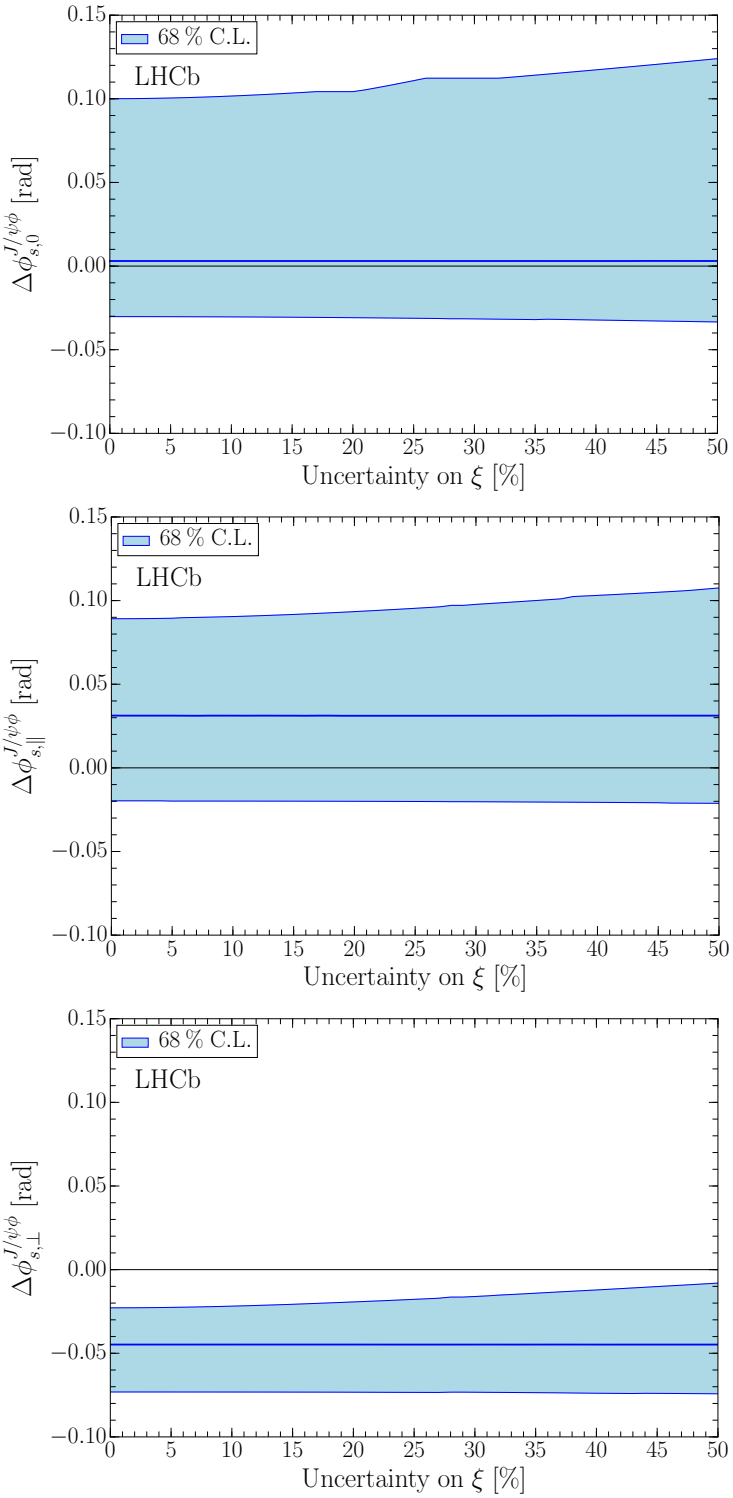

Figure 5.4: Determination of the penguin parameters $\Re[a_i]$ and $\Im[a_i]$ through intersecting contours derived from the *CP* observables and branching ratio information in $B_s^0 \to J/\psi\overline{K}^{*0}$ and $B^0 \to J/\psi\rho^0$. The inner dark-coloured line represents the contour associated with the central value of the input quantity.Superimposed are the confidence level contours obtained from a χ^2 fit to the data. Shown are the longitudinal (left), parallel (right) and perpendicular (bottom) polarisation.

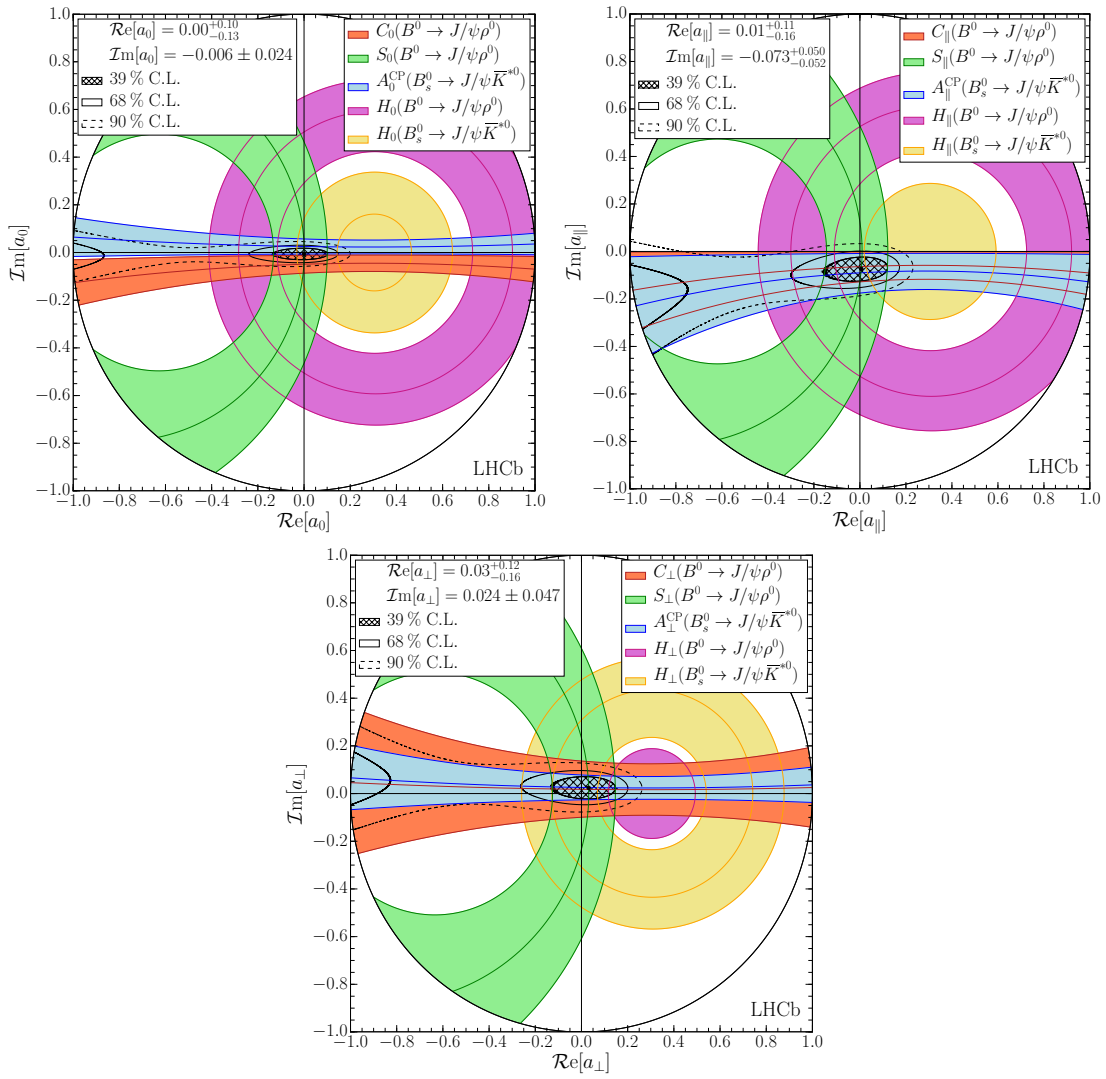

Figure 5.5: Determination of the penguin parameters a_i and θ_i through intersecting contours derived from the *CP* asymmetries and branching ratio information in $B_s^0 \to J/\psi \overline{K}^{*0}$ and $B^0 \to J/\psi\rho^0$. The inner dark-coloured line represents the contour associated with the central value of the input quantity. Superimposed are the confidence level contours obtained from a χ^2 fit to the data. Shown are the longitudinal (top), parallel (middle) and perpendicular (bottom) polarisation.

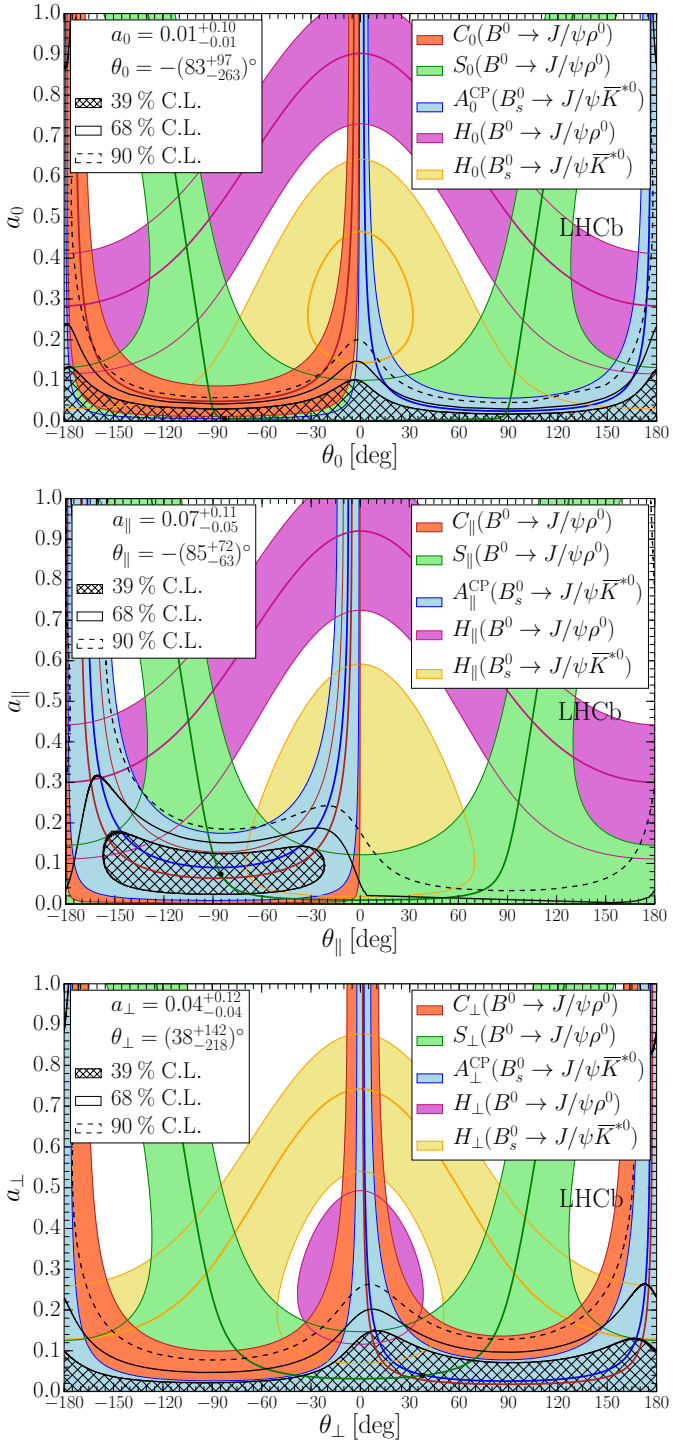

Chapter 6

Analysis of $A_1^0 \to \mu^+\mu^-$ decays

First steps of a model-independent search for $A_1^0 \to \mu^+\mu^-$ decays, where A_1^0 corresponds to the light *CP*-odd Higgs boson in an extension of the Standard Model, the Next-To-Minimal Supersymmetric Standard Model (NMSSM) [31, 32], are performed, using $2.97\,\text{fb}^{-1}$ of data from pp collisions recorded by the LHCb experiment at a centre-of-mass energy of $\sqrt{s} = 7\ (8)\,\text{GeV}$ during 2011 (2012). Upper limits in $\mathcal{B}(A_1^0 \to \mu^+\mu^-)$ are prospected to be calculated using the CLs technique [156]. A possible model-dependent search, considering certain NMSSM production modes, may be taken into account. However, at the moment of writing this document, only selection and mass model studies were performed.

In Chapter 6.1, the selection of $A_1^0 \to \mu^+\mu^-$ candidates, consisting in a simple "cut-based" selection together with more complex multivariate requirements using Uniform Boosted Decision Trees (UBDT), is presented. In Chapter 6.2, studies of the mass model used to fit the two-muon mass spectrum are explained. A summary of these early studies and future prospects for this analysis are presented in Chapter 6.3. **Recent updates to this analysis can be found in the internal LHCb analysis note numbered LHCb-ANA-2017-004.**

6.1 Event selection and data samples

Real data (Chapter 6.1.1) and simulated data (Chapter 6.1.2) samples used for this analysis are presented in this section, with the requirements from the offline selection (Chapter 6.1.3) as well. The offline selection consists of two parts: a "cut-based" set of requirements to reduce the size of the real data sample to a manageable level, followed by the use of Uniform Boosted Decision Trees [116, 157] to reject background as much as possible, keeping a high signal efficiency.

6.1.1 Real data samples

Real data events for this analysis are selected from two LHCb datasets with a total integrated luminosity of $2.97\,\text{fb}^{-1}$ of pp collision data:

- `Reco14-Stripping21r1`: corresponding to $0.98\,\text{fb}^{-1}$ of integrated luminosity, collected during 2011 at a centre-of-mass energy of $\sqrt{s} = 7\,\text{TeV}$.
- `Reco14-Stripping21`: corresponding to $1.99\,\text{fb}^{-1}$ of integrated luminosity, collected during 2012 at a centre-of-mass energy of $\sqrt{s} = 8\,\text{TeV}$.

Both datasets have been analysed with DaVinci v36r1 and Bender v28r2p1 (Erasmus v11r2), and reconstructed using Brunel v43r2p6, CondDB tag `cond-20141107`. For 2011 (2012) conditions, the DDDB tag was `dddb-20130929` (`dddb-20130929-1`).

6.1.2 Simulated samples

Simulated samples used in this analysis can be classified in three different groups:

- A first group of three sets of samples containing each one simulated decays of different spectroscopic excited states of the Υ meson, $\Upsilon(1S) \to \mu^+\mu^-$ decays, $\Upsilon(2S) \to \mu^+\mu^-$ decays and $\Upsilon(3S) \to \mu^+\mu^-$ decays, respectively.
- A second group of two sets of samples, containing each one simulated decays of the $A_1^0 \to \mu^+\mu^-$ mode, but under different mass hypotheses for the A_1^0 boson, $M(A_1^0) = 10\,\text{GeV}/c^2$ and $M(A_1^0) = 12\,\text{GeV}/c^2$, respectively.
- A third group of a single set of samples, containing simulated Drell-Yan (DY) processes with a mass threshold of $5\,\text{GeV}/c^2$ and where the virtual neutral boson decays to a pair of muons, namely $Z/\gamma^* \to \mu^+\mu^-$ decays.

Two pair of samples per set, containing each pair approximately the same number of simulated events, are used: one pair is representative of the data taken during 2011 (`Reco14a/Reco14c-Stripping20r1`, flagging mode, TCK `0x40760037`), whilst the other pair is representative of the data taken during 2012 (`Reco14a/Reco14c-Stripping20`, flagging mode, TCK `0x409f0045`). The only difference between members of a same pair is the polarity of the LHCb dipole magnet in the simulation. In summary, four samples (one per year and magnet polarity) per decay mode (three Υ meson decays, two A_1^0 boson modes and one Drell-Yan channel) are used: 2 (polarity) $\times$ 2 (year) $\times$ 6 (decay mode). The total number of simulated events per simulated mode are approximately 6 M per each Υ decay mode, 0.2 M per each A_1^0 decay channel, and 2 M of Drell-Yan events. This information is summarized in Table 6.1. Information about the software packages used to simulate these samples can be found in Chapter 3.2.5, where Table 3.2 summarizes their corresponding versions.

6.1.3 "Cut-based" requirements

The "cut-based" set of requirements consists of two subsets: a first subset of cuts, applied once by the LHCb computing team to the triggered LHCb data immediately before the data sample is constructed, called "stripping line" (see Chapter 3.2.5); followed by a second subset of offline cuts tuned for the present analysis. To select

Table 6.1: Simulated samples used in the analysis of $A_1^0 \to \mu^+\mu^-$ decays. Approximately half of the events are simulated with the LHCb magnet polarity up, while the other half with polarity down.

Decay mode	Simulated events	`Sim` pass	TCK (year)	Stripping version
$\Upsilon(1S) \to \mu^+\mu^-$	2 024 999	`Sim08c`	`0x40760037` (2011)	`Stripping20r1`
	4 019 988	`Sim08c`	`0x409f0045` (2012)	`Stripping20`
$\Upsilon(2S) \to \mu^+\mu^-$	2 019 995	`Sim08c`	`0x40760037` (2011)	`Stripping20r1`
	4 036 985	`Sim08c`	`0x409f0045` (2012)	`Stripping20`
$\Upsilon(3S) \to \mu^+\mu^-$	2 019 995	`Sim08c`	`0x40760037` (2011)	`Stripping20r1`
	4 033 488	`Sim08c`	`0x409f0045` (2012)	`Stripping20`
$A_1^0 \to \mu^+\mu^-$	124 069	`Sim08h`	`0x40760037` (2011)	`Stripping20r1`
$M(A_1^0) = 10\,\text{GeV}/c^2$	115 416	`Sim08h`	`0x409f0045` (2012)	`Stripping20`
$A_1^0 \to \mu^+\mu^-$	112 945	`Sim08h`	`0x40760037` (2011)	`Stripping20r1`
$M(A_1^0) = 12\,\text{GeV}/c^2$	115 464	`Sim08h`	`0x409f0045` (2012)	`Stripping20`
Drell-Yan	1 089 769	`Sim08h`	`0x40760037` (2011)	`Stripping20r1`
$M(\mu^+\mu^-) > 5\,\text{GeV}/c^2$	1 200 892	`Sim08h`	`0x409f0045` (2012)	`Stripping20`

$A_1^0 \to \mu^+\mu^-$ signal decays in real (simulated) data samples, the stripping line used is named `Stripping(A1MuMu)A1MuMuLine`. Table 6.2 lists the final "cut-based" selection criteria (already taking into account both subsets of cuts). However, the background sample used to construct the UBDT (see Chapter 6.1.4) consists of $\mu^\pm\mu^\pm$ events, where both muons have the same sign (SS) in terms of electrical charge. To select these events in real data, a different stripping line, `StrippingA1MuMuA1MuMuSameSignLine`, is used. Since the only difference between both stripping lines is how the candidate muons are chosen, and both consists of the same kinematic and hadronic PID cuts, no distinction is made in Table 6.2. The analysis is not restricted to any particular trigger line, i.e. an event should just pass at least one of the LHCb trigger lines.

For daughter μ candidates, a threshold cut in the p_T of $2.5\,\text{GeV}/c$ is imposed, along with good track, vertex and DOCA reconstruction criteria ($\chi^2_{\text{track}}/\text{ndof} < 10$, $\chi^2_{\text{vtx}} < 25$, $\chi^2_{\text{DOCA}} < 30$). Also, good muon identification by the muon system, a cut in the RICH particle identification variables to avoid mis-identification of muons as kaons, and a cut in the χ^2 of the reconstructed impact parameter ($\Delta\text{LL}\mu\pi > 0$, $\Delta\text{LL}K\pi < 10$, $\chi^2_{\text{IP}} > 4$), are imposed. Alternative possible particle identification cuts would be studied in further steps on the analysis (see Chapter 6.3). For parent di-muon resonances (A_1^0 candidates), a mass constraint in the two-body mass is required ($M \in [5.5,\, 15]\,\text{GeV}/c^2$), where the lower limit of the mass range is set above the mass of the B_s^0 meson, in order to avoid possible contamination from $B_s^0 \to \mu^+\mu^-$ decays. A threshold cut in the p_T of $7.5\,\text{GeV}/c$ and good vertex reconstruction criterion, $\chi^2_{\text{vtx}}/\text{ndof} < 12$, are imposed. Finally, since a possible A_1^0 boson is assumed to decay promptly, a very restrictive cut in the lifetime of A_1^0 candidates ($\tau < 0.1\,\text{ps}$) is imposed.

A first estimation of the signal efficiency (background rejection) of this selection is

Table 6.2: Selection criteria for $A_1^0 \to \mu^+\mu^-$ decays.

	Cut variable	Cut value
μ candidates	$p_T\ (\mu)$	$> 2.5\,\mathrm{GeV}/c$
	$\chi^2_{\mathrm{track}}/\mathrm{ndof}(\mu)$	< 10
	$\chi^2_{\mathrm{vtx}}(\mu)$	< 25
	$\chi^2_{\mathrm{DOCA}}(\mu)$	< 30
	$\Delta\mathrm{LL}\mu\pi(\mu)$	> 0
	$\Delta\mathrm{LL}K\pi(\mu)$	< 10
	$\chi^2_{\mathrm{IP}}(\mu)$	> 4
A_1^0 candidates	$M(\mu\mu)$	$\in [5.5,\ 15]\,\mathrm{GeV}/c^2$
	$p_T\ (\mu\mu)$	$> 7.5\,\mathrm{GeV}/c$
	$\chi^2_{\mathrm{vtx}}/\mathrm{ndof}(\mu\mu)$	< 12
	$\tau(\mu\mu)$	$< 0.1\,\mathrm{ps}$

computed using a simulated sample of $A_1^0 \to \mu^+\mu^-$ decays where the mass hypothesis of the A_1^0 boson is set to $10\,\mathrm{GeV}/c^2$ (real data sample of SS muon candidates), leading to an efficiency (rejection) above than 95% (75%). An example of the discriminant behaviour of two of the selected variables, namely $\tau(\mu\mu)$ and $\Delta\mathrm{LL}\mu\pi(\mu)$, is presented in Figure 6.1, where the distribution of those variables is compared among different simulated samples and the SS muon real data sample.

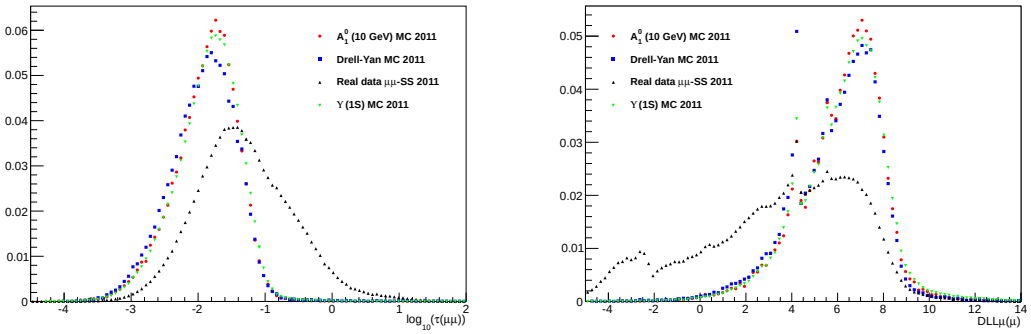

Figure 6.1: Comparison between the distributions for $\tau(\mu\mu)$ in $\log_{10}$ scale (top) and $\Delta\mathrm{LL}\mu\pi(\mu)$ (bottom) variables for different simulated and SS muon real data samples, normalised to the same area.

6.1.4 UBDT requirements

In order to leave the data samples with prompt di-muon signal and reject any other component to the background (heavy flavour, combinatorial...) as much as possible, a MVA method consisting of boosted decision trees is used. However, since this analysis aims for a model independent search in a certain di-muon mass range from $5.5\,\mathrm{GeV}/c^2$ to $15\,\mathrm{GeV}/c^2$, it is necessary to avoid possible induced bias (false peaks) because of the mass structure of the chosen training sample. For this reason, the uBoost method [157] is used, where the boosted decision trees are trained such the response efficiency is kept flat in mass. These kind of boosted decision trees are known as Uniform Boosted Decision Trees. This MVA method has been successfully used in previous LHCb analyses [158].

This UBDT is trained and tested separately for both 2011 and 2012 samples, but following a common procedure. Henceforth, the procedure described in the following paragraphs is assumed to be performed in parallel for 2011 and 2012 samples. For this purpose, a signal sample from Drell-Yan simulated decays and a background sample extracted from real data SS muon are constructed. Extensive studies in order to decide which is the optimal simulated sample to be used as signal sample were performed: despite of the fact that there is no resonant di-muon structure, the Drell-Yan sample shows similar behaviour of the most relevant kinematic and particle identification discriminating variables, along with the fact that there is signal available in the whole mass range considered. On the other hand, a simple decision was taken for the background sample: due to its own structure, real data SS muon sample is the only one where it is 100% assured that there is no trace of $A_1^0 \to \mu^+\mu^-$ signal. For both samples, a common selection, which consists of the same requirements as in Table 6.2, is applied.

For the signal sample, true MC-*truth* for both muons is imposed. For the background sample, validation studies show that no same sign replica is present for some of the trigger lines, thus a requirement on a certain set of HLT (see Chapter 3.2.3) lines was imposed. The only consequence of this cut is a minor reduction of the size of the background sample.

TMVA toolkit [116] was used for this MVA procedure. After their preparation, each sample is split in two halves: 50% of the sample is used for training while the other 50% used for testing. An UBDT method consisting of 100 efficiency steps is trained and tested over those samples using the following discriminating variables for the MVA procedure:

- `mu12iso5`: sum of the two track isolation [159] variables, "iso5", each one computed per candidate muon.
- `logmu1(2)ip`: decimal logarithm of the impact parameter of one of the candidate muons (labelled as 1 or 2) of the pair.
- `logmu1(2)pt`: decimal logarithm of the tranverse momentum of one of the candidate muons (labelled as 1 or 2) of the pair.
- `logmu1(2)ptot`: decimal logarithm of the total momentum of one of the candidate muons (labelled as 1 or 2) of the pair.

- `logBip`: decimal logarithm of the impact parameter of the dimuon (A_1^0 candidate) pair.
- `mu1(2)_track_Chi2Dof`: track reconstruction significance of one of the candidate muons (labelled as 1 or 2) of the pair.
- `lessIPSmu`: minimum of all significances on the impact parameter of muon candidates.
- `C_angle`: angle between the two candidate muons in the centre-of-mass reference frame.

A better agreement in track isolation variables is achieved using information from real data of the number of hits in the VELO and in the SPD, for this purpose simulated samples are re-weighted using Yandex software.[1] Signal and background distributions for discriminating variables are presented in Figure 6.3 and Figure 6.4, together with the UBDT method response in Figure 6.2, for both 2011 and 2012 conditions separately. No overtraining is observed in Figure 4.1, showing a smooth background response and thus no false peaks. For 2011 (2012) conditions, approximately 22 600 (24 300) signal and 51 100 (44 700) background events were used to train the UBDT discriminant. As shown in the signal and background correlation matrices of the discriminating variables, Figure 6.5 and Figure 6.6 respectively, some of those variables are correlated. In a further step of these MVA studies, a clean-up of the discriminating variables may be considered.

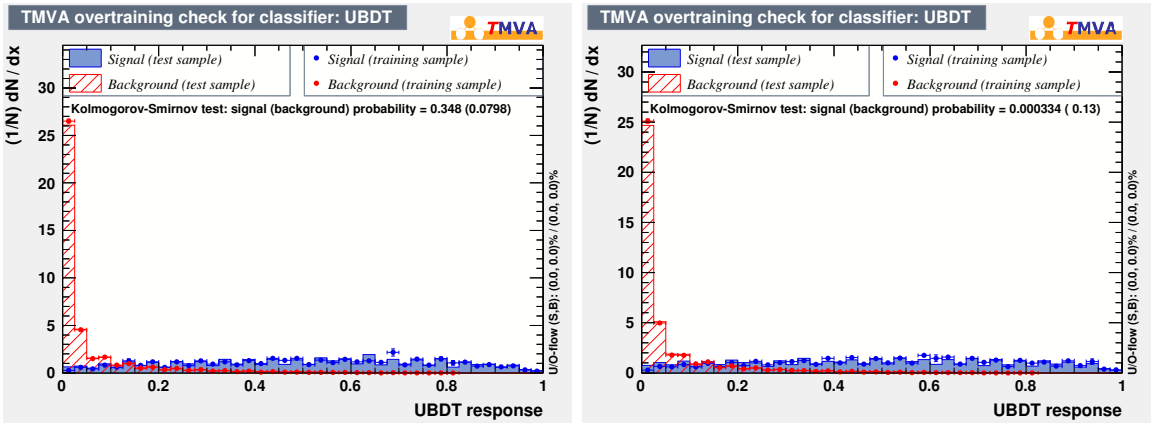

Figure 6.2: UBDT response to signal and background distributions for 2011 (left) and 2012 (right) conditions.

Validation studies of the flatness of the previously constructed UBDT response efficiency are performed as well: for different random UBDT threshold cuts, its efficiency is calculated in bins of the di-muon invariant mass. These studies are performed separately on SS muon real data and DY simulated events, for both 2011 and 2012 conditions. On

[1] For more information, see (a).

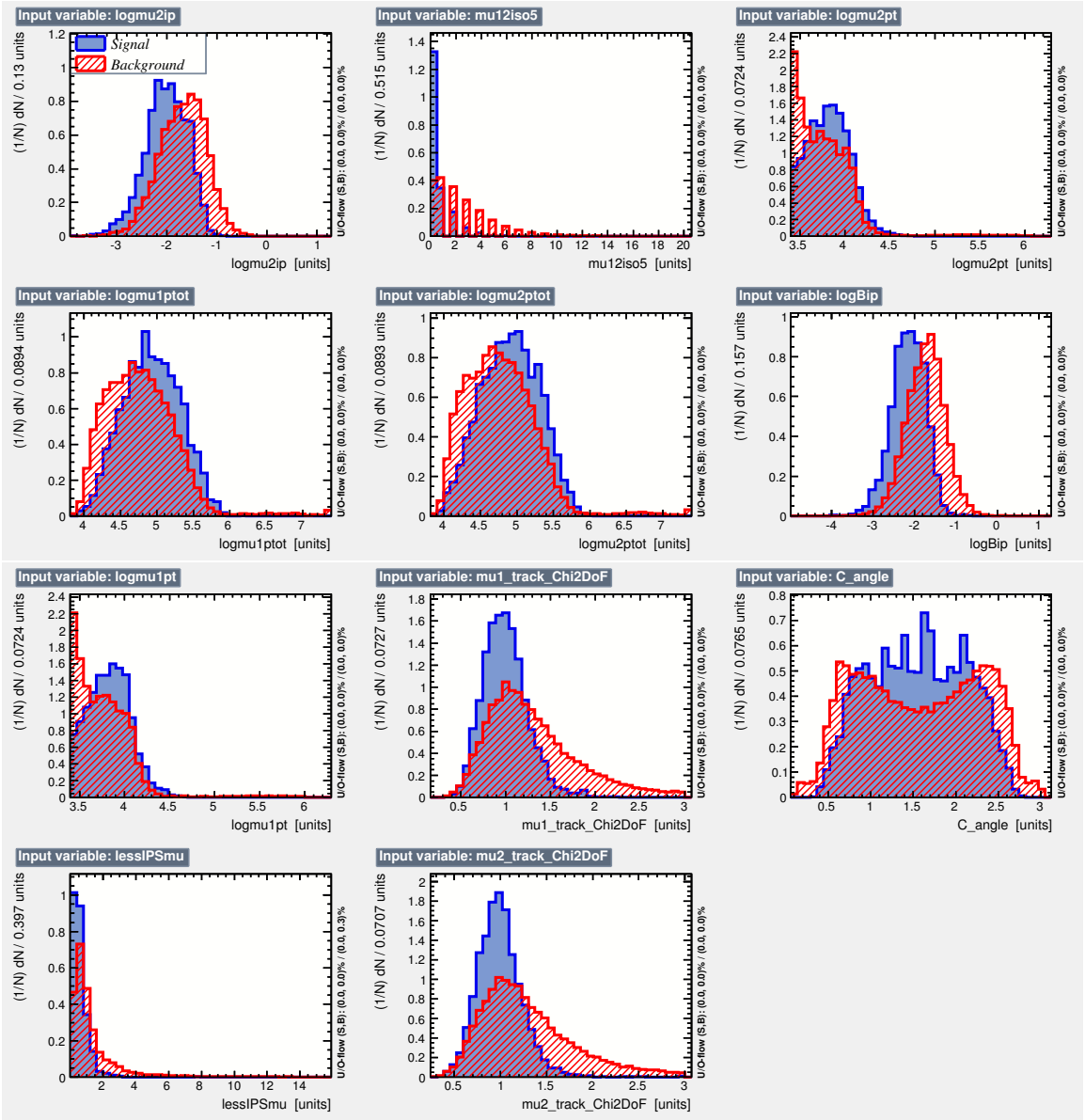

Figure 6.3: Distributions for MVA discriminating variables under 2011 conditions.

simulated signal (DY) events, one can expect a flat efficiency, not necessarily the same on background (SS muon real data) events. As shown in Figure 6.7, a flattish efficiency for signal events is found, while as presented in Figure 6.8, low efficiency (or high rejection) response for background events is found as well. A quantitative non-flatness measurement per UBDT threshold cut using Standard Deviation of Efficiency on bins (SDE^2) [160], where values closer to zero mean a flatter response, is also done: if comparing this response with that obtained from a simple (where uniformity is not assured) BDT discriminant constructed under the same conditions, the SDE^2 value is 10 times smaller

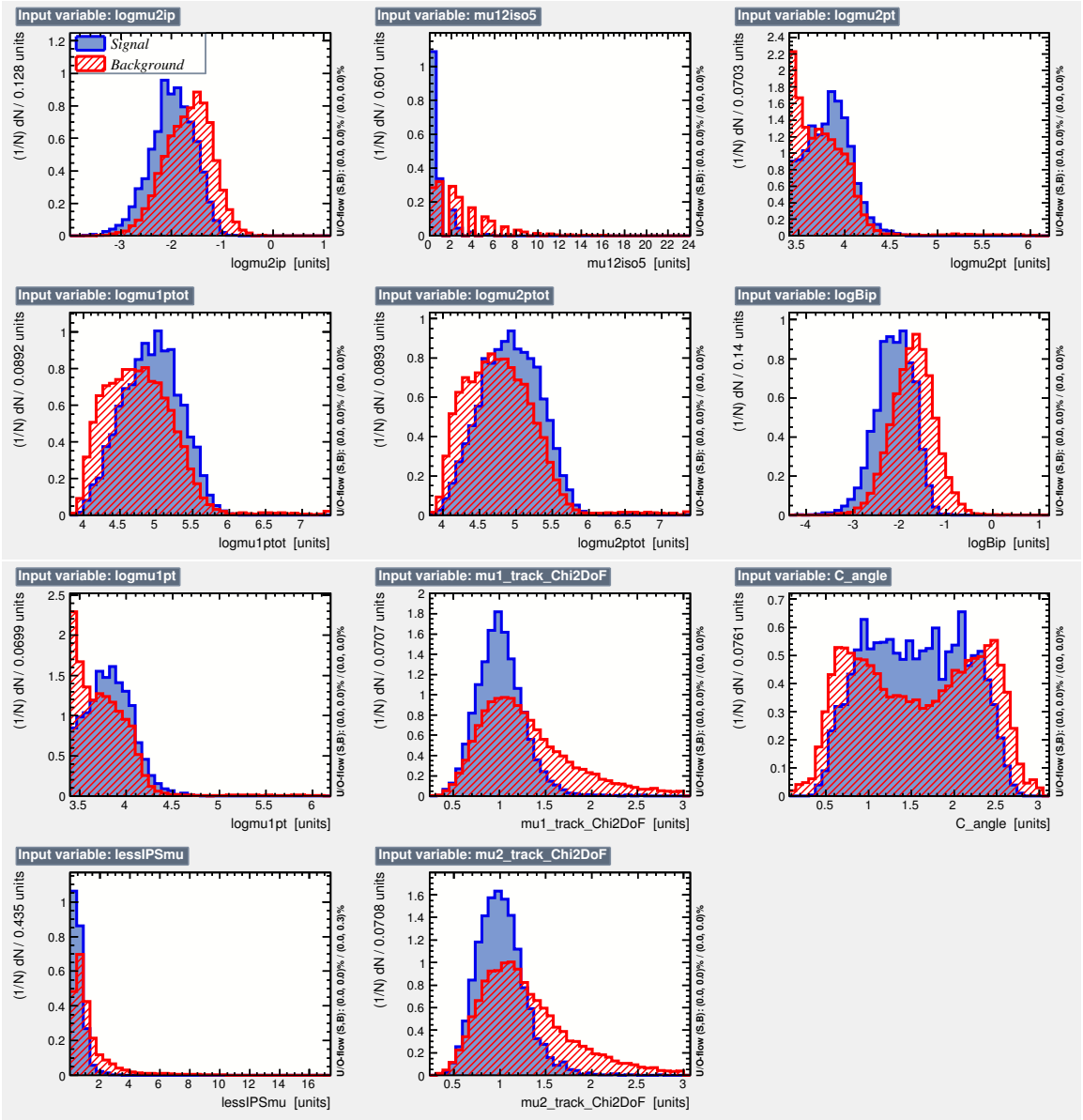

Figure 6.4: Distributions for MVA discriminating variables under 2012 conditions.

for the UBDT than for the BDT discriminant.

As summarized in Chapter 6.3, further studies to improve current MVA procedure are not yet discarded, such as a possible new signal sample for the procedure. Since the signal response seems easy to model, as shown in Figure 6.2, it needs to be decided if it is worth or not to optimise a possible UBDT threshold cut, or just perform the invariant di-muon mass fit (see Chapter 6.2) in bins of the UBDT response.

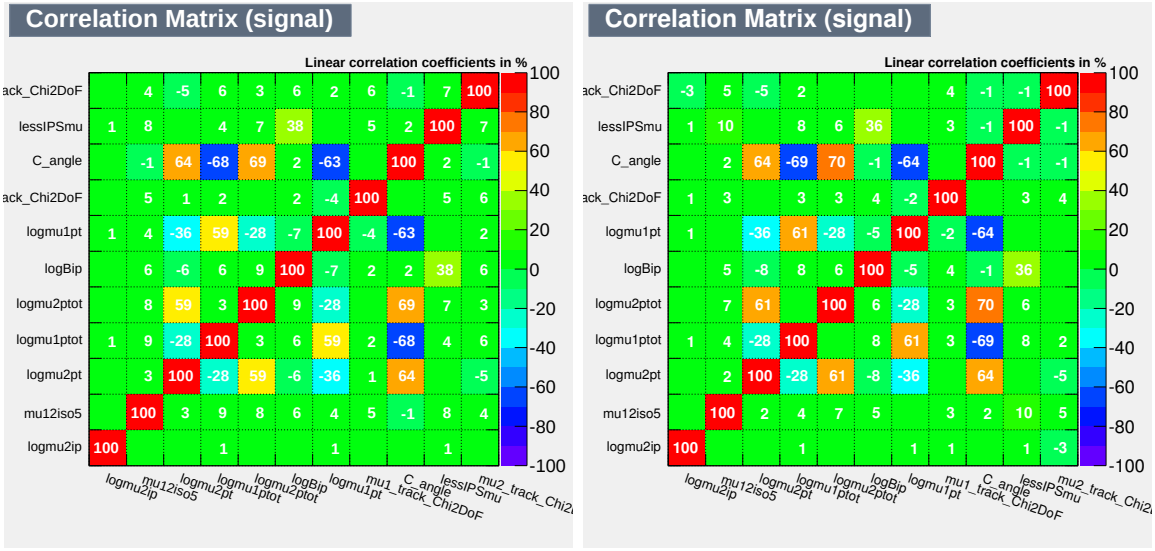

Figure 6.5: Correlation matrices evaluated in the signal sample for the discriminating variables for 2011 (left) and 2012 (right) conditions.

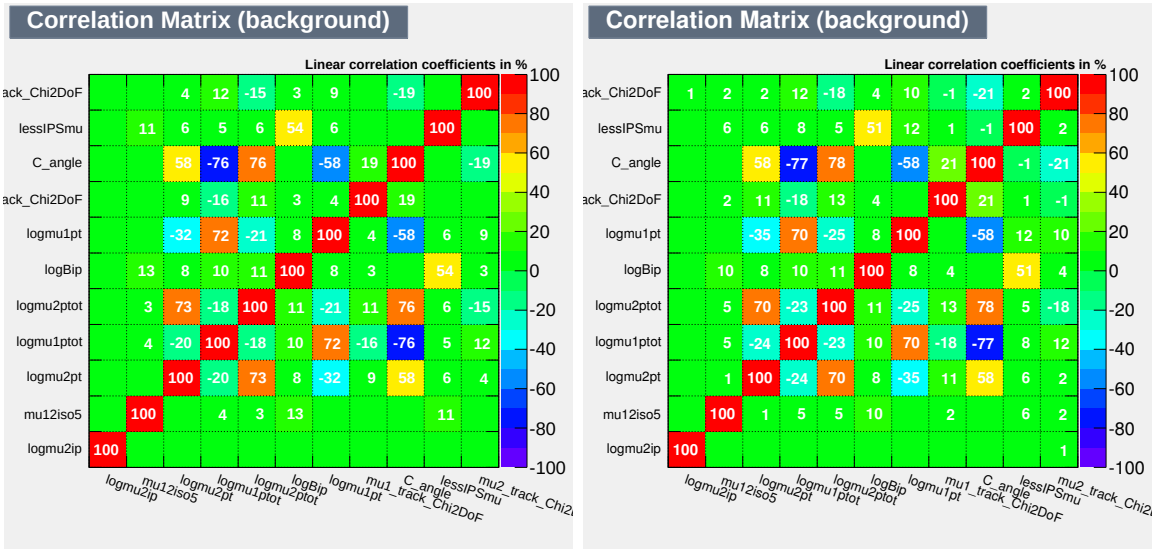

Figure 6.6: Correlation matrices evaluated in the background sample for the discriminating variables for 2011 (left) and 2012 (right) conditions.

6.2 Mass model studies

The di-muon mass shape is modelled using the full Hypatia distribution (referred to as Υ in ref. [131]), which has an accurate formulation with Gaussian smearing and allows to separate Multiple Scattering (MS) and spatial resolution terms. A validation test fit to

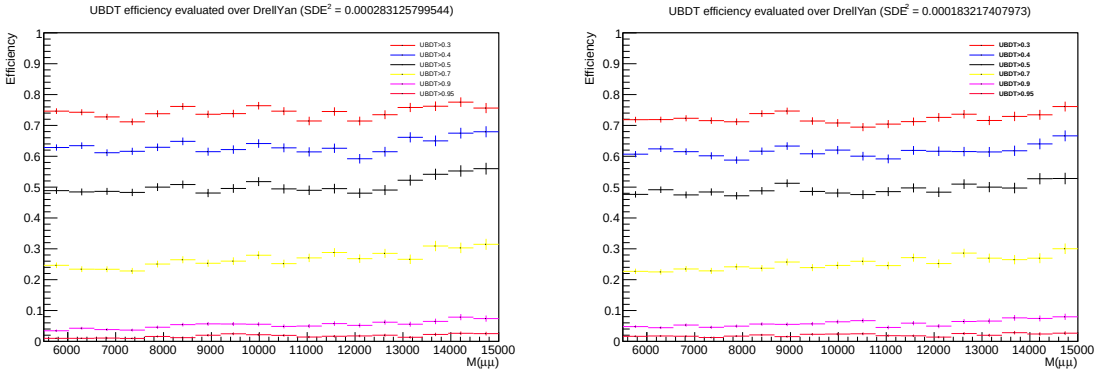

Figure 6.7: UBDT response signal efficiency, for a random set of UBDT threshold cuts and in bins of di-muon invariant mass, for 2011 (left) and 2012 (right) conditions.

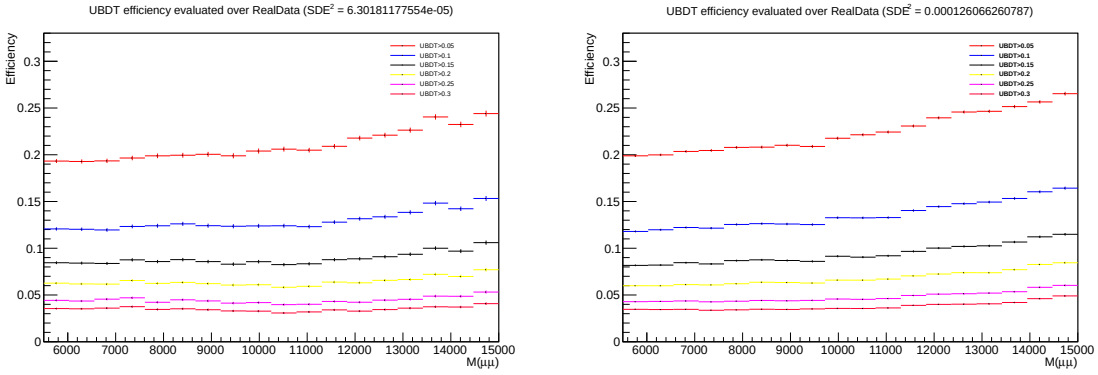

Figure 6.8: UBDT response background efficiency, for a random set of UBDT threshold cuts and in bins of di-muon invariant mass, for 2011 (left) and 2012 (right) conditions.

the di-muon invariant mass of simulated $\Upsilon(1S) \to \mu^+\mu^-$ decays is shown in Figure 6.9, where the fit significance is very close to unity: 0.99 (1.02) for 2011 (2012) conditions. At the moment of writing this thesis, it has been performed an initial test to a model of a more complex di-muon mass spectrum, containing the following components:

- Three simulated Υ resonances (1S, 2S and 3S), modelling each peak using a full Hypatia distribution where the relevant (mainly related to the p_T distribution) parameters for this test are the MS term σ_0, λ and μ. However, instead of fitting 9 parameters (3 peaks $\times$ 3 relevant parameters), two new parameters, taking into account information from the different λ and μ, are constructed. These two parameters, defined as $\kappa = \mu/M(\Upsilon)$ and $\rho = \lambda/\mu$, reduce significantly the complexity of the Υ mass model without any loss of fit convergence. Thus, the fit is performed with 5 instead of 9 parameters: three σ_0, κ and ρ.

- Simulated $A_1^0 \to \mu^+\mu^-$ decays, with a A_1^0 mass hypothesis of $12\,\mathrm{GeV}/c^2$, also mod-

elled using a full Hypatia distribution, and where the relevant parameters are also σ_0, λ and μ.

- Simulated exponential background.

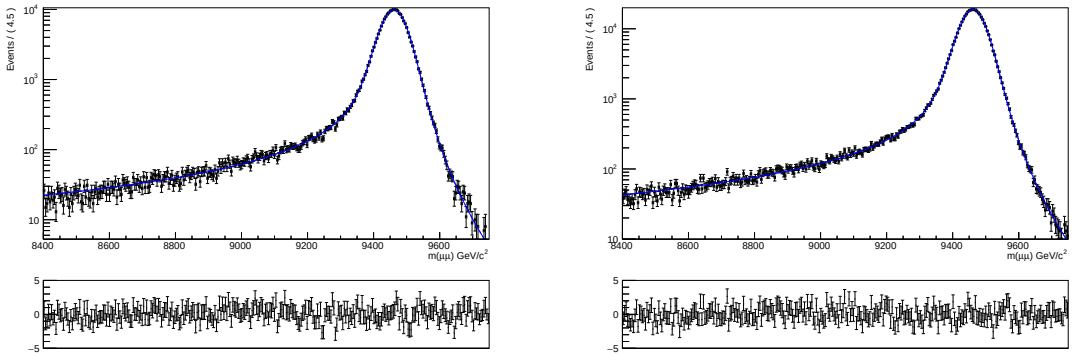

Figure 6.9: Validation test fit to the di-muon invariant mass of simulated $\Upsilon(1S) \to \mu^+\mu^-$ decays for 2011 (left) and 2012 (right) conditions.

For this initial study, only samples under 2011 conditions are considered. Due to the correlations between mass and transverse momentum, the fit is performed in bins of the p_T of the A_1^0 candidates. In further steps of the analysis, a fit also in bins of the pseudorapidity of the A_1^0 candidates will be considered as well. The procedure of this initial test is summarized in four steps in the following four paragraphs.

First, the different MS term σ_0 are obtained from simulation separately for each mode: this terms corresponds to the ramp-up (quantitatively defined for this test as the value corresponding to the 1% of the distribution) of the per-event mass error distribution. Per-event mass error distributions for the different Υ simulated samples are shown in Figure 6.10. The validity of this statement is also tested using Drell-Yan simulated events: as shown in Figure 6.11, ramp-up values from real data and from Drell-Yan simulated data in bins of the di-muon invariant mass are practically the same. An overall comparison between previous ramp-up values and those σ_0 values obtained from fits to Υ and A_1^0 candidates is presented in Figure 6.12, showing good agreement between them. For the final analysis stage, these MS parameters will be obtained from real data instead of simulation.

Second, with the previously obtained MS terms, a simultaneous fit to the three Υ resonances is performed, in order to get the shared shape parameters κ and ρ of the Hypatia distributions, the latter is assumed (as a first rough assumption) to be linear in mass. The rest of the parameters, non-relevant for this test, are shared among the three resonances.

Third, the parameters obtained in the previous two steps are used to get the shape of the A_1^0 peak, using previous κ and ρ to extrapolate here $\mu = \kappa M(A_1^0)$ and $\lambda = \rho\mu = \rho\kappa M(A_1^0)$, taking the MS term σ_0 from the first step.

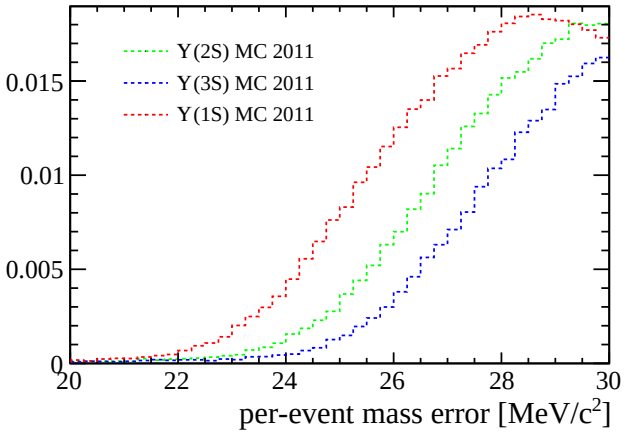

Figure 6.10: Per-event mass error distributions of Υ simulated samples (2011 conditions).

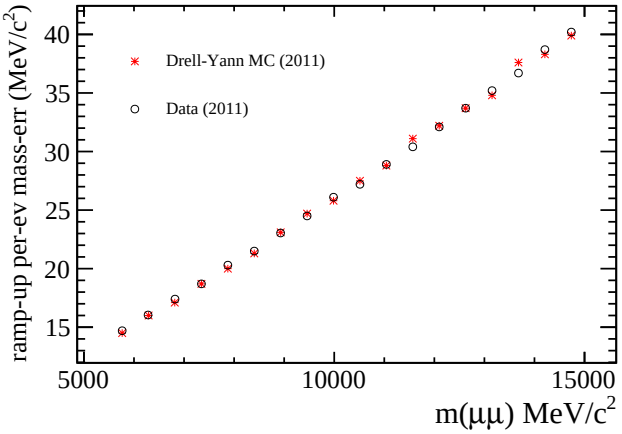

Figure 6.11: Comparison of the ramp-up of the per-event mass error distributions of simulated Drell-Yan and real data samples (2011 conditions).

Fourth and finally, a comparison between the fitted A_1^0 yields and the injected number of A_1^0 events in simulation is performed, looking for model dependencies as well. A cross-check of the procedure is also done using the Υ yields instead.

Mass projection from this simultaneous fit in one of the p_T bins is shown in Figure 6.13, where simulated events are well-described by the proposed mass model. No model dependence has been found from the comparison between fitted yields and injected number of events for Υ simulated decays, showing very good fit consistency. Unfortunately, for $A_1^0 \to \mu^+\mu^-$ simulated decays a little discrepancy up to approximately a 5% has been found, showing a clear dependency of the model with the di-muon invariant mass distribution. One possible explanation for this behaviour is that, for A_1^0 simulated decays, the λ parameter of the Hypatia distribution was assumed linear in mass, which is a very

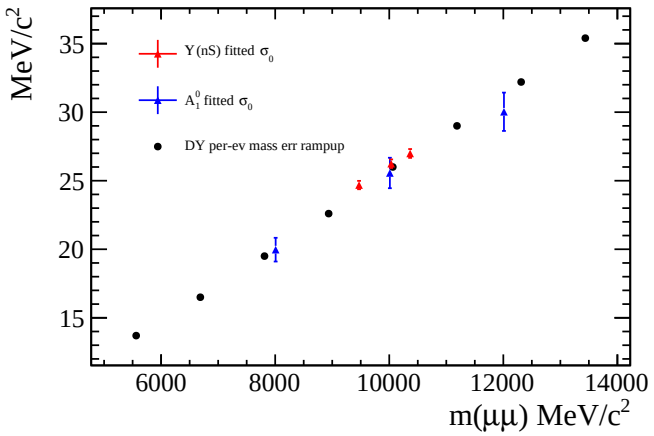

Figure 6.12: Comparison of the ramp-up of the per-event mass error distribution of a simulated Drell-Yan sample and fitted σ_0 values from simulated Υ and A_1^0 samples (2011 conditions).

rough assumption and needs to be studied in more detail. Further steps of the analysis will include more precise dependencies of sensitive parameters of the mass model.

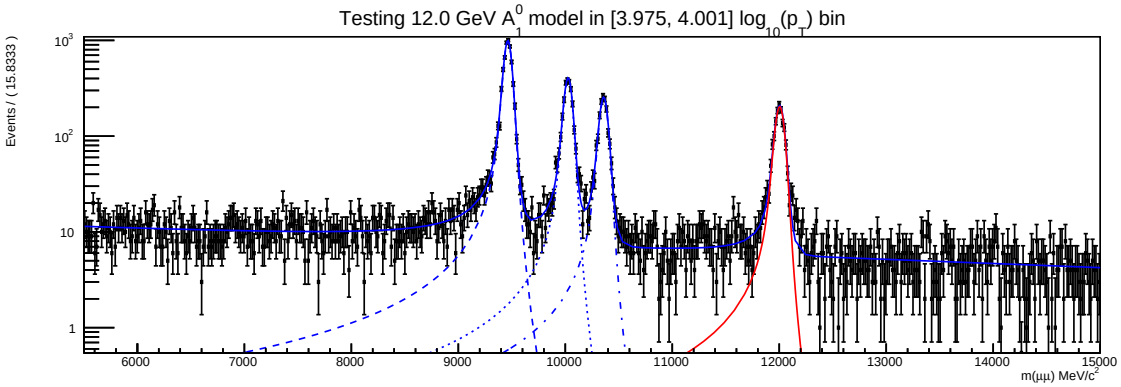

Figure 6.13: Mass fit to the di-muon invariant mass in one of the bins of p_T of the A_1^0 candidate, for 2011 conditions.

6.3 Summary and prospects

First steps of a model-independent search of $A_1^0 \to \mu^+\mu^-$ decays, using three times more integrated luminosity than in previous studies published by CMS [36], were performed.

At the moment of writing this work, a selection consisting of "cut-based" requirements and a UBDT discriminant has been constructed (see Chapter 6.1). In further steps of this analysis, a possible improvement of the "cut-based" requirements using other particle identification variables, an improvement of the set of discriminating variables used to constructed the UBDT and the use of a different signal sample (cocktail of $A_1^0 \to \mu^+\mu^-$ simulated decays under different A_1^0 mass hypothesis), may be considered.

Also, in Chapter 6.2, first steps of the validation studies of the proposed mass model for the di-muon invariant mass fit were performed. However, further studies are needed in order to understand discrepancies and method dependencies with the di-muon mass distribution. A fit in bins of the UBDT discriminant instead of a threshold cut optimisation is also a considered option for the future.

Once the selection and mass studies are completed, upper limits in $\mathcal{B}(A_1^0 \to \mu^+\mu^-)$ will be calculated, using the CLs technique [156]. Simulation efficiencies will need to be calculated as well. Studies of possible systematic uncertainty sources will be also performed at the end. An additional step on this analysis, repeating the calculation of these upper limits but in certain NMSSM production modes instead of a model-independent search, may be considered. However, sensitivity studies will be needed before, in order to check if it is worth or not to perform such a model-dependent search.

Chapter 7

Conclusions

This thesis presents the analysis of $B_s^0 \to J/\psi \overline{K}^{*0}$ decays, using 3 fb^{-1} of data collected by LHCb during 2011 and 2012, from LHC pp collisions at centre-of-mass energies of 7 TeV and 8 TeV, respectively. First steps of the analysis of the $A_1^0 \to \mu^+\mu^-$ decay mode, using 2.97 fb^{-1} of Run I LHCb pp data, have been also reported, along with the characterisation of silicon pixel detectors using SPS test beams consisting of charged hadrons with a momentum of 180 GeV/c, in the context of the upgraded LHCb VELO R&D programme.

The excellent performance of the LHCb detector during 2011 and 2012, especially the muon and trigger systems, crucial for the reconstruction of muon tracks, has been also reported. Some details about the on-going upgrade of LHCb subsystems have been reviewed as well. In the context of development studies of the upgraded LHCb VELO, results on the performance of hadron-irradiated pixel detectors have been obtained from test beams at the CERN SPS, using Medipix3.1 Application-Specific Integrated Circuits (ASICs) bump-bonded to thin n-on-p silicon sensors. After irradiation with reactor neutrons to a fluence of 0.5×10^{15} 1 MeV $\mathrm{n_{eq}}$ cm^{-2}, a larger threshold dispersion and an increased power consumption of the ASIC have been observed. However, the shapes of average cluster size and resolution versus threshold are not changed significantly compared to the non-irradiated sensors: consistent results between assemblies and agreement with simulation have been shown. These studies have been continued using the Timepix3 ASIC as well.

On the other hand, the phenomenon of CP violation in the neutral B_s^0 meson system, focused in the measurement of the mixing-induced CP-violating phase ϕ_s in $B_s^0 \to J/\psi\phi$ decays, has been reviewed. In particular, the importance of disentangling contributions due to second order (penguin) topologies to this phase, which may be confused with signals of possible NP. These contributions could be seized with the help of information from $B_s^0 \to J/\psi \overline{K}^{*0}$ and $B^0 \to J/\psi\rho^0$ decays. Branching fraction, polarisation fractions and direct CP violation parameters in $B_s^0 \to J/\psi \overline{K}^{*0}$ decays have been measured, obtaining the following results,

$$\mathcal{B}(B_s^0 \to J/\psi \overline{K}^{*0}) = (4.14 \pm 0.18(\mathrm{stat}) \pm 0.26(\mathrm{syst}) \pm 0.24(f_d/f_s)) \times 10^{-5},$$

$$
\begin{aligned}
f_0 &= 0.497 \quad {}^{+0.024}_{-0.025}\ (\text{stat}) \pm 0.025\ (\text{syst}),\\
f_\parallel &= 0.179 \quad {}^{+0.027}_{-0.026}\ (\text{stat}) \pm 0.013\ (\text{syst}),\\
A^0_{CP}(B^0_s \to J/\psi \overline{K}^{*0}) &= -0.048 \pm 0.057\ (\text{stat}) \quad {}^{+0.019}_{-0.020}\ (\text{syst}),\\
A^\parallel_{CP}(B^0_s \to J/\psi \overline{K}^{*0}) &= 0.171 \pm 0.152\ (\text{stat}) \quad {}^{+0.028}_{-0.027}\ (\text{syst}),\\
A^\perp_{CP}(B^0_s \to J/\psi \overline{K}^{*0}) &= -0.049 \quad {}^{+0.095}_{-0.096}\ (\text{stat}) \pm 0.025\ (\text{syst}).
\end{aligned}
$$

Neglecting the difference between the ϕ and the $\overline{K}^{*0}$ mesons, the penguin annihilation and exchanges topologies, the following constraints on the penguin pollution parameters affecting the *CP*-violating phase ϕ_s measured in $B^0_s \to J/\psi\phi$ decays have been found,

$$
\begin{aligned}
\Delta\phi^{J/\psi\phi}_{s,0} &= 0.001^{+0.087}_{-0.011}\,(\text{stat})^{+0.013}_{-0.008}\,(\text{syst})^{+0.048}_{-0.030}\,(|\mathcal{A}'_f/\mathcal{A}_f|)\,,\\
\Delta\phi^{J/\psi\phi}_{s,\parallel} &= 0.031^{+0.049}_{-0.038}\,(\text{stat})^{+0.013}_{-0.013}\,(\text{syst})^{+0.031}_{-0.033}\,(|\mathcal{A}'_f/\mathcal{A}_f|)\,,\\
\Delta\phi^{J/\psi\phi}_{s,\perp} &= -0.046^{+0.012}_{-0.012}\,(\text{stat})^{+0.007}_{-0.008}\,(\text{syst})^{+0.017}_{-0.024}\,(|\mathcal{A}'_f/\mathcal{A}_f|)\,.
\end{aligned}
$$

Combining previous results with those obtained from the analysis of the $B^0 \to J/\psi\rho^0$ decay mode, with the assumption of identical $(|\mathcal{A}'_f/\mathcal{A}_f|)$ terms and neglecting $SU(3)$-breaking effects, the penguin phase shifts on the phase ϕ_s measured in $B^0_s \to J/\psi\phi$ decays are

$$
\begin{aligned}
\Delta\phi^{J/\psi\phi}_{s,0} &= 0.000^{+0.010}_{-0.014},\\
\Delta\phi^{J/\psi\phi}_{s,\parallel} &= 0.001^{+0.012}_{-0.016},\\
\Delta\phi^{J/\psi\phi}_{s,\perp} &= 0.003^{+0.012}_{-0.016},
\end{aligned}
$$

where the quoted uncertainty is the total corresponding to the quadratic sum of statistical and systematic uncertainties.

Finally, implications on NP searches, focused in the NMSSM, have been also discussed. First steps of a model-independent search of $A^0_1 \to \mu^+\mu^-$ decays have been performed. At present moment, a selection and a multivariate UBDT discriminant have been constructed, along with the first steps of validation studies of the proposed mass model for the di-muon invariant mass fit. However, improvements still need to be done, as well as the calculation of upper limits in $\mathcal{B}(A^0_1 \to \mu^+\mu^-)$ using the CLs technique, the computation of simulation efficiencies and the study of sources of systematic uncertainties.

Chapter 8

Summary

The Standard Model (SM) of Particle Physics, based on strong, weak and electromagnetic (electroweak) interactions, is a very powerful and self-consistent model which has led to many successes in providing accurate descriptions of experimental measurements. As of today this theory is considered the benchmark model to classify subatomic particles and explain their interactions, except gravitation, which is not incorporated in the SM. However, as the scientific community knows very well, being successful is still far from being perfect: some tensions between results from several experiments and SM predictions have arisen in the previous years, such as the inability to find a proper SM candidate for dark matter in the Universe, the existence of neutrino masses, or the necessary imbalance between matter and antimatter in the Universe, among others. The SM is not able to explain these phenomena, which are intensively investigated in several High Energy Physics (HEP) experiments. Searching for both direct or indirect evidence of possible New Physics (NP), which may lead to the establishment of a new benchmark model able to explain all these tensions, can be considered as the *avant-garde* of HEP.

8.1 Basic theoretical aspects

Regarding indirect searches of possible NP, the violation of a certain discrete symmetry, the CP violation, is one of the ingredients necessary to explain the imbalance between matter and antimatter in the Universe, also known as the problem of the baryogenesis. However, experimental results have shown that the amount of CP violation predicted by the SM is not enough to satisfy the conditions needed to solve that baryogenesis puzzle: a search for new NP sources of CP violation is mandatory. The study of CP violation in the neutral B_s^0 meson system offers an excellent opportunity to detect possible deviations from SM predictions. A study of second order (penguin) contributions to the mixing-induced CP-violating phase ϕ_s in $b \to c\bar{c}s$ processes, which may be confused as a signal of NP, has been done using $B_s^0 \to J/\psi \overline{K}^{*0}$ decays.

As for direct searches of possible NP, one way to complement the SM are its supersymmetric extensions. Direct searches of possible new particles predicted by those extensions, such as in the Next-to-Minimal-Supersymmetric-SM (NMSSM), constitute a direct way

to test the robustness of the SM, where the observation of possible NP particles predicted by alternative candidate models, might be achieved. First steps of a model-independent search of the $A_1^0 \to \mu^+\mu^-$ decay mode, where A_1^0 is the light CP-odd Higgs boson in the NMSSM, have been performed as well.

8.2 The LHCb experiment

The LHCb (Large Hadron Collider beauty) experiment is dedicated to Heavy Flavor (HF) physics at the Large Hadron Collider (LHC) located at CERN. As of June 2016, the experiment is driven by a collaboration of 1199 members, from 69 institutes in 16 countries around the world. The primary goal of the experiment is to look for indirect evidence of NP in CP violation and rare decays of beauty and charm hadrons.

8.2.1 The LHC machine

The Large Hadron Collider, operating at CERN since September 2008, is the most powerful hadron accelerator and collider ever built by humankind. Installed in the 27 km circular tunnel built to house the Large Electron Positron (LEP) collider, it is located between 45 m and 170 m underneath surface at the French-Swiss border. The LHC machine was designed to accelerate proton beams up to an energy of 7 TeV per beam and to collide them with a centre-of-mass energy of 14 TeV. Data used for the studies described in this thesis were taken during 2011 and 2012, as part of the first LHC run period, named Run I.

8.2.2 The LHCb detector

The LHCb detector is a single-arm spectrometer with a forward angular coverage, focused on the high rapidity region on one side of the Interaction Point (IP). It approximately covers an angular range from 10 to 300 mrad in the bending plane. The angular coverage is smaller in the non-bending plane, from 10 to 250 mrad. The polar distribution of the $b\bar{b}$ pair production at the LHC justifies this design, because at high energies these pairs are predominantly produced in the same forward or backward cone. The layout of the LHCb spectrometer is shown in Figure 8.1. The right-handed coordinate system adopted has the z axis along the beam, and the y axis along the vertical. With an overall dimension of approximately 6 m $\times$ 5 m $\times$ 20 m, the detector is composed by the following main parts: the beam pipe, the magnet, the tracking and vertexing systems: VErtex LOcator (VELO), Silicon Tracker and Outer Tracker; and the particle identification systems: Ring Imaging CHerenkov (RICH) detectors, the calorimeter system, and the muon system. Also, because of the high interaction rate and the low branching ratio of those rare decays of interest, an efficient rejection of data needs to take place. For this purpose a trigger system is built, consisting of a hardware based system (Level 0 or L0) and a pure software based trigger (High Level Trigger or HLT).

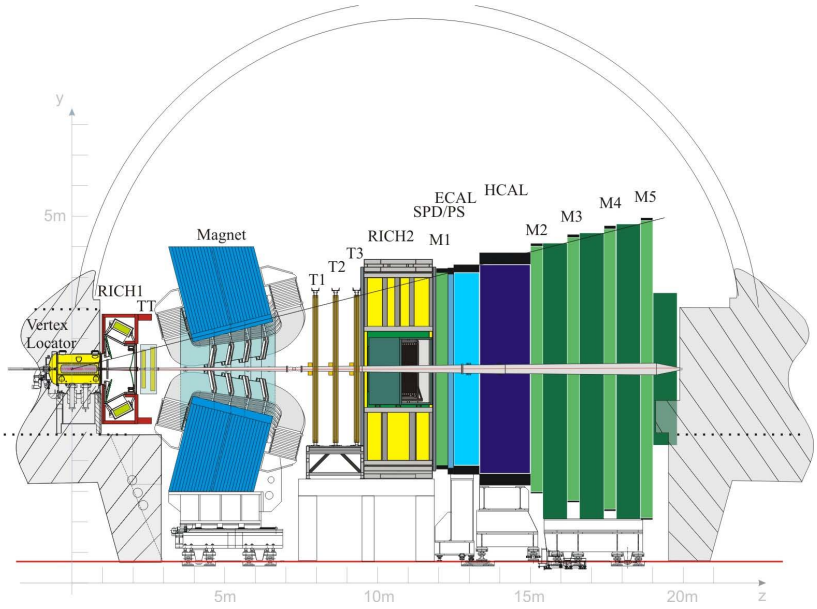

Figure 8.1: Schematic two-dimensional view of the LHCb detector.

Data taken by LHCb from collisions at the LHC, at a rate of several million events per second, need to be selected, prepared and distributed in the most possible efficient way for its subsequent analysis. The different steps leading the raw detected data to the physics results can be summarised as follows:

1. An initial and fast selection which allows to discard most of the events that are not interesting for the physics analysis, that is, the LHCb trigger, which is ran over the data taken by the detector.

2. Data selected by the trigger is transformed by different mathematical algorithms in an ensemble of tracks and vertices. This is done by the tracking and vertexing system. Then, information from the particle identification system is added to identify the nature of the tracks.

3. Once all the triggered events have been reconstructed, it becomes mandatory to separate them according to their physics content. This is done by selecting the different decays using their particular features, with a procedure called "stripping" in the framework of LHCb.

4. The triggered, reconstructed and stripped dataset has to be then distributed to a series of computing centers spread worldwide, using the DIRAC framework to the distributed system called Grid.

8.2.3 The LHCb Upgrade

The LHCb detector has already shown an excellent performance during Run I. However, the precision of many LHCb measurements is still limited by their statistical uncertainties: the LHCb Upgrade, with a prospected ten-years data acquisition of 50 fb^{-1} with a 40 MHz readout, is expected to bring a sensitivity improvement of about one order of magnitude for several key observables with respect to current measurements. After the next Long Shutdown (LS), it is expected that LHCb will operate with a luminosity of $2\times10^{33}\text{cm}^{-2}\text{s}^{-1}$.

8.2.3.1 The LHCb VELO Upgrade

The upgraded VELO must maintain or improve its physics performance while delivering readout at 40 MHz in the operating conditions of the upgrade. This can only be achieved by a complete replacement of the silicon sensors and electronics. Following an externally refereed review, the LHCb Collaboration has chosen to install a subdetector based on hybrid pixel sensors, where research and development studies have been done, among others, using silicon pixel detectors, such as the characterisation of Medipix3 detectors using SPS test beams. Hence, a new radiation hard ASIC, dubbed "VeloPix", capable of coping with the data rates, is under development.

As previously mentioned, results on the performance of hadron-irradiated pixel detectors have been obtained from test beams at the CERN SPS, using Medipix3.1 Application-Specific Integrated Circuits (ASICs) bump-bonded to thin n-on-p silicon sensors. After irradiation with reactor neutrons to a fluence of 0.5×10^{15} 1 MeV n_{eq} cm^{-2}, a larger threshold dispersion and an increased power consumption of the ASIC have been observed. However, the shapes of average cluster size and resolution versus threshold are not changed significantly compared to the non-irradiated sensors: consistent results between assemblies and agreement with simulation have been shown. These studies have been continued using the Timepix3 ASIC as well.

8.3 The $B_s^0 \to J/\psi \overline{K}^{*0}$ decay mode

Experimental information from $B_s^0 \to J/\psi \overline{K}^{*0}$ decays needed to study penguin pollution in ϕ_s is presented in the following paragraphs. The analysis is based on fitting for the angular parameters in bins of $M(K\pi)$ and $\cos(\theta_\mu)$ around the $\overline{K}^*(892)^0$ mass pole. The J/ψ meson is reconstructed from $\mu^+\mu^-$ and the $\overline{K}^{*0}$ hadron from $K^-\pi^+$, as well as their charge conjugated decays. A very large $B^0 \to J/\psi K^{*0}$ component is present in the data and taken into account, used as a normalisation channel.

Real data events are selected from two LHCb datasets with a total integrated luminosity of 3.0 fb^{-1} of pp collision data, corresponding to 1 (2) fb^{-1} of data taken during 2011 (2012) at a centre-of-mass energy of 7 (8) TeV. Three sets of simulated samples are also used in this analysis, containing $B_s^0 \to J/\psi \overline{K}^{*0}$, $B^0 \to J/\psi K^{*0}$ and $B_s^0 \to J/\psi\phi$ simulated decays each one. Each set consists of a pair of samples, representative of data

taken during 2011 (2012). The total number of simulated events per decay mode are approximately 1 M, 2 M and 10 M, respectively.

8.3.1 Event selection

The event selection consists of two parts: a "cut-based" set of requirements to reduce the size of the real data sample to a manageable level, followed by the use of Boosted Decision Trees with Gradient Boosting (BDTG) to reject as much combinatorial background as possible while keeping a high signal efficiency. The analysis is not restricted to any particular trigger line, an event should just pass at least one of the LHCb trigger lines.

The "cut-based" set of requirements consists of mass constraints, kinematic cuts and particle identification requirements of kaons, pions and muons. A veto cut of $B^+ \to J/\psi K^+$ three-body decays is also required. However, as already stated, most of the combinatorial background is rejected using a BDTG, constructed separately for each data-taking year conditions. A signal sample of $B_s^0 \to J/\psi \overline{K}^{*0}$ simulated decays and a background sample of real data B_s^0 candidates from the high mass sideband are used. Both samples are selected with a common set of requirements consisting of the same cuts as those of the "cut-based" set, except for the particle identification requirements: complementary cuts are imposed to kaons and pions of the background sample in order to avoid possible bias in further steps of the analysis.

The BDTG discriminant is then trained and tested over those samples using purely kinematic variables as discriminant variables. After its construction, a threshold cut is optimised using a figure of merit based on ${}_s\mathcal{W}eights$, calculated with the ${}_s\mathcal{P}lot$ technique in a single $M(K\pi)$ bin, and considering B_s^0 candidates as signal yield. A simple mass model consisting of two Crystal-Ball (signal) and an exponential function (background) is used for the fit.

Signal efficiency and background rejection values are calculated separately for both 2011 and 2012 data samples. Values related to cuts on hadronic particle identification variables are corrected using the PIDCalib package. A final signal efficiency (background rejection) of $\sim 47\%$ ($\sim 99.9\%$) is achieved. After applying this final event selection, 68 100 (147 760) events are selected in the 2011 (2012) real data sample.

8.3.2 Peaking backgrounds

Extensive studies of simulated samples have shown contributions from several specific backgrounds, such as misidentified $B_s^0 \to J/\psi K^+K^-$, $B_s^0 \to J/\psi \pi^+\pi^-$ (peaking near $B_s^0 \to J/\psi K\pi$) and $B^0 \to J/\psi \pi^+\pi^-$ (peaking near $B^0 \to J/\psi K\pi$) decays. In the same way as ${}_s\mathcal{W}eights$ are applied such that sideband events cancel out the likelihood contribution from background events underneath the peak, simulated events with negative weights are used to cancel out the likelihood contribution from these peaking backgrounds present in the real data. Raw yields of those backgrounds are estimated from simulated data. However, events from simulation are generated in phase-space which does not contain the proper physical amplitudes. Hence, a physical reweighting of simulated samples

is performed to obtain the final expected yields.

Apart from the previous $B_q \to J/\psi X$ contributions, simulation studies have shown contamination from the Λ_b^0 decay modes $\Lambda_b^0 \to J/\psi p K^-$ and $\Lambda_b^0 \to J/\psi p \pi^-$, although at a somewhat reduced level due to the particle identification requirements during the event selection step. These misidentified baryonic modes are treated differently in the mass fit model: the $\Lambda_b^0 \to J/\psi p K^-$ decay mode is statistically substracted by injecting simulated events as done for $B_q \to J/\psi X$ contributions, while the $\Lambda_b^0 \to J/\psi p \pi^-$ decay channel is added as an extra specie to the mass fit model, parametrised using the Amoroso distribution.

Final expected yields for each mode, except for the $\Lambda_b^0 \to J/\psi p \pi^-$ decay channel, are not smaller than 10 (19) and not greater than 51 (115) events for 2011 (2012) conditions.

8.3.3 Mass model and fit

The mass model consists of an exponential distribution for the combinatorial background, an Amoroso distribution for $\Lambda_b^0 \to J/\psi p \pi^-$ decays, and a double-sided Hypatia for the B_s^0 and B^0 signal decays. The Hypatia distribution is chosen because the event-by-event uncertainty on the mass has a dependence on the particle momenta. The Hypatia model parameters ζ and β are fixed to zero, while the mean and the resolution are left free in the fit. The rest of the parameters are determined from simulation.

However, from simulation studies it is known that some of the Hypatia parameters appear to be significantly correlated with the $K\pi$ invariant mass. Since these parameters need to be fixed in the invariant mass fit, the latter is performed in four bins of the $M(K\pi)$ spectrum. In addition, due to correlations between the invariant mass and the cosine of the helicity angle θ_μ, an additional splitting in five bins of $\cos(\theta_\mu)$ is done. Hence, the invariant mass fit is performed in a total of 20 bins. Eventual contamination of K/π swapped events from $B^0 \to J/\psi K^{*0}$ decays under the B_s^0 peak is taken into account: it has been concluded that those swaps were negligible.

The ${}_s\mathcal{P}lot$ technique is used to substract $\Lambda_b^0 \to J/\psi p \pi^-$ peaking background decays and combinatorial background from the data sample. The signal yield is extracted from 20 independent fits to the four-body invariant mass spectrum using the mass fit model previously described. Overall B_s^0 and B^0 yields are obtained from the sum of yields over the 20 bins, giving $N_{B^0} = 208\,656 \pm 462^{+78}_{-76}$ and $N_{B_s^0} = 1\,808 \pm 51^{+38}_{-33}$, where the first uncertainties are statistical and obtained from the quadratic sum of those in each fitting category, and the second uncertainties are systematic. Fit projections are shown in Figure 8.2. The correlations between the B^0 and B_s^0 yields in each fitting category are found to be smaller than 4%. Additional cross-check studies are performed, in order to assess the validity of the hypotheses adopted. Final validation tests, performed to test the robustness of the fit model, are done by means of "toy Monte Carlo", using generated pseudoexperiments and obtaining satisfactory results.

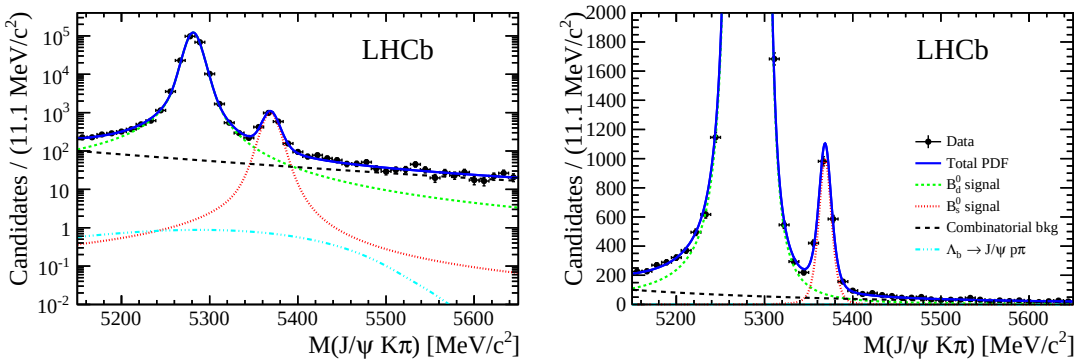

Figure 8.2: Sum of the fit projections in the 20 bins with a logarithmic (left) and linear scale (right) on the y-axis. The legend displayed in the right plot also applies to the left one.

8.3.4 Angular analysis and CP asymmetries

The decay angles used for the angular analysis are defined in the helicity basis, denoted by θ_K, θ_μ and φ_h. The polar angle θ_K (θ_μ) is the angle between the kaon (μ^+) momentum and the direction opposite to the B_s^0 momentum in the $K\pi$ ($\mu^+\mu^-$) centre-of-mass system. The azimuthal angle between the $K\pi$ and the $\mu^+\mu^-$ decay planes is φ_h, defined by a rotation from the pion side of the $K\pi$ plane to the μ^+ side of the $\mu^+\mu^-$ plane. The rotation is positive in the $\mu^+\mu^-$ direction in the B_s^0 rest frame. These definitions are the same whether a B_s^0 or a $\overline{B}_s^0$ decays, and for $B^0 \to J/\psi K^{*0}$ decays as well.

In order to determine the CP components, the helicity amplitudes calculated in the helicity basis are transformed into "transversity amplitudes", where those associated with the P-wave ($K\pi$ system with spin $J = 1$) are written as A_0, $A_\parallel$ and $A_\perp$, and those associated with the D-wave ($K\pi$ system with spin $J = 2$) are written as A_{20}, $A_{2\parallel}$ and $A_{2\perp}$. The modulus of the transversity amplitude A_x is noted as $|A_x|$ while its strong phase is written as δ_x, and the convention $|A_0|^2 + |A_\parallel|^2 + |A_\perp|^2 + |A_S|^2 = 1$ is adopted. The $K^+\pi^-$ and $K^-\pi^+$ samples are separated and fitted through a simultaneous fit.

The S-wave parameters $|A_S|^2$ and δ_S are defined independently for each bin, in order to not include any $K\pi$ mass dependence in the fit. If the D-wave is included (only for the evaluation of systematic uncertainties but not meant to be included in the final fit), some more parameters as those defined for the S-wave are needed in order to absorb variations along the $K\pi$ mass bins. However, some mass dependent terms, associated to the interference between waves, are present. Such interference terms arise from a certain set of complex integrals, used to compute numerically the so-called C_{ij} factors, given a certain assumption for the mass lineshapes, and included as fixed parameters in the fit in order to take into account those interferences. Mass lineshape models are chosen based on a data-driven test: a LASS parametrisation is used for the S-wave, an isobar combination of $K^*(892)^0$ and $K_1^*(1410)^0$ for the P-wave and a relativistic Breit-Wigner distribution, corresponding to the $K_2^*(1430)^0$, for the D-wave.

Effects of angular acceptance are modelled with sets of "normalisation weights", obtained from simulated $B^0 \to J/\psi K^{*0}$ events. These weights are further refined, where the simulated sample is weighted to match the distributions of final-state kinematics in real data, to correct for imperfections in the detector simulation. An iterative procedure is used to (re-)weight these simulated samples.

For the three final polarisation states (0, $\parallel$, $\perp$) of the $J/\psi K\pi$ system, a raw CP asymmetry is measured. However, this asymmetry needs to be corrected to take into account the detector acceptance and the differences in the interaction between particles in the final state and the detector (detection asymmetry), and also the $B_s^0 - \overline{B}_s^0$ production asymmetry, and the dilution because of $B_s^0 - \overline{B}_s^0$ oscillations (dilution factor).

Finally, a simultaneous fit is carried out in the four mass bins of $M(K\pi)$ around the $\overline{K}^{*0}$ nominal mass, where the P-wave amplitudes and strong phases are common among those bins, while the S-wave parameters are split. Angular projections of the fit are shown in Figure 8.3. The results obtained for the polarisation fractions and CP asymmetries are

$$\begin{aligned}
f_0 &= 0.497 \;{}^{+0.024}_{-0.025}\;(\text{stat}) \pm 0.025\;(\text{syst}),\\
f_\parallel &= 0.179 \;{}^{+0.027}_{-0.026}\;(\text{stat}) \pm 0.013\;(\text{syst}),\\
A_{CP}^0(B_s^0 \to J/\psi \overline{K}^{*0}) &= -0.048 \pm 0.057\;(\text{stat}) \;{}^{+0.019}_{-0.020}\;(\text{syst}),\\
A_{CP}^{\parallel}(B_s^0 \to J/\psi \overline{K}^{*0}) &= 0.171 \pm 0.152\;(\text{stat}) \;{}^{+0.028}_{-0.027}\;(\text{syst}),\\
A_{CP}^{\perp}(B_s^0 \to J/\psi \overline{K}^{*0}) &= -0.049 \;{}^{+0.095}_{-0.096}\;(\text{stat}) \pm 0.025\;(\text{syst}).
\end{aligned}$$

These results are compared with those from a previous LHCb $B^0 \to J/\psi\rho^0$ analysis: direct CP asymmetries are in good agreement and the small differences found are not significant enough to deduce any information on $SU(3)$-breaking.

8.3.5 Branching fractions

Two normalised branching fractions are obtained: one with respect to the $B_s^0 \to J/\psi\phi$ decay mode (ideal for the study of penguin pollution), and another one with respect to the $B^0 \to J/\psi K^{*0}$ decay channel (ideal for the cancellation of systematic uncertainties during the efficiency evaluation). Finally, a weighted average taking into account both results is calculated.

The efficiency ratios are obtained from simulation, separately for each data-taking year conditions. The requirements used to select the $B_s^0 \to J/\psi\phi$ normalisation mode are very similar but not identical to those used to select $B_s^0 \to J/\psi \overline{K}^{*0}$ signal decays. Nevertheless, both $B^0 \to J/\psi K^{*0}$ and $B_s^0 \to J/\psi \overline{K}^{*0}$ modes are selected using identical requirements. Hence, due to the similarity of the final state between both modes in the latter case, systematics associated to discrepancies between data and simulation are assumed to cancel out. However, as the efficiency depends on the angular distribution of the decay products, corrections due to the difference between angular amplitudes in simulation and real data are taken into account.

The normalisation to the $B^0 \to J/\psi K^{*0}$ mode is performed, where the ratio is multiplied by the branching fraction of the $B^0 \to J/\psi K^{*0}$ decay mode, measured at Belle. The difference in the production rates of B^+B^- and $B^0\overline{B}^0$ pairs at the $\Upsilon(4S)$ resonance is

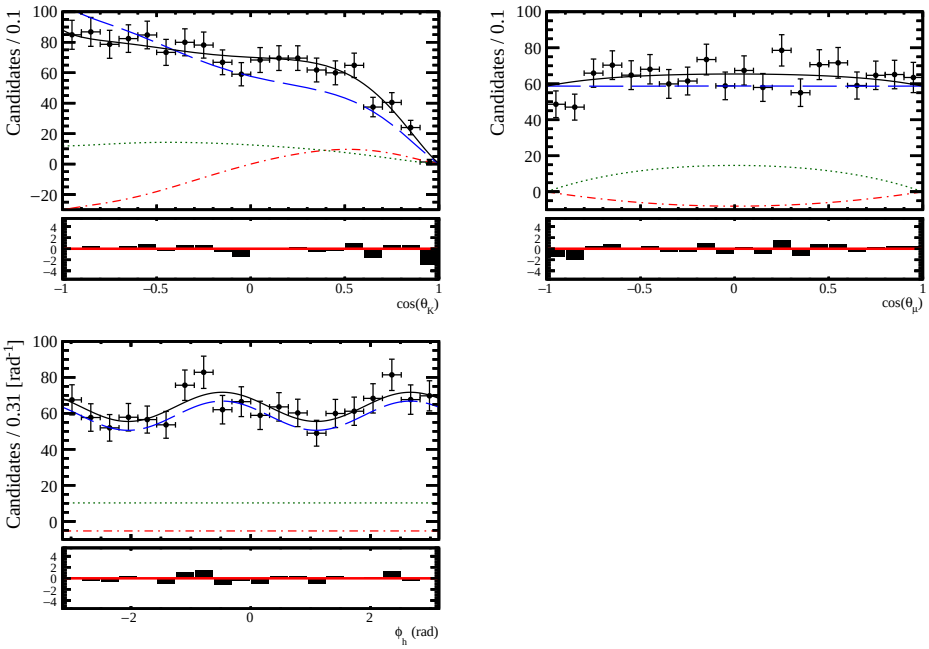

Figure 8.3: Angular plots on top of the fitted sWeighted data for $B_s^0 \to J/\psi \overline{K}^{*0}$ decays. Blue solid: total. Blue dashed: P-wave + P-P interference. Green dotted: S-wave. Red dotted-dashed: S-P interference.

also taken into account. The normalisation to the $B_s^0 \to J/\psi\phi$ mode is performed as well, using the value of $\mathcal{B}(B_s^0 \to J/\psi\phi)$ previously obtained by LHCb but updating it with the latest f_d/f_s measurement. Both estimations are finally combined into a correlated weighted average,

$$\mathcal{B}(B_s^0 \to J/\psi \overline{K}^{*0}) = (4.14 \pm 0.18(\text{stat}) \pm 0.26(\text{syst}) \pm 0.24(f_d/f_s)) \times 10^{-5},$$

which is in good agreement with previous $B_s^0 \to J/\psi \overline{K}^{*0}$ LHCb publication as well as with SM expectations.

8.3.6 Systematic uncertainties

The most relevant sources of systematic uncertainties studied in this analysis are:

- Peaking backgrounds: limited model knowledge of the considered decays.
- ${}_s\mathcal{P}lot$ technique: correlations between $M(J/\psi K\pi)$ and $\cos(\theta_\mu)$.
- C_{ij} factors: choice of a certain mass lineshape model for each wave.
- D-wave contribution: neglecting of the D-wave contribution in the fit.
- Mass model: fixing some parameter values from MC.

- Fit biases, obtained from the results of the toy MC studies.
- Angular acceptance: limited MC statistics and data-simulation corrections.
- CP asymmetries: detection and production asymmetries.
- Branching fractions: inclusion of external parameters in the calculations.

From the previous list, two sources of systematic uncertainties are found to be dominant: the size of the simulation samples used to estimate the normalisation weights of the angular acceptance, and the correlation between the four-body invariant mass and the cosine of the helicity angle θ_μ.

8.4 Penguin pollution in the ϕ_s phase

The penguin pollution to the ϕ_s phase measured in $B_s^0 \to J/\psi\phi$ decays, $\Delta\phi_{s,i}$, is parametrised by the relative size a_i of the penguin to tree amplitudes, which has an associated strong phase difference θ_i and where the weak phase difference is given by the Unitary Triangle angle γ. Thus, the penguin parameters a_i and θ_i can be extracted from two times three parameters (two for each polarisation i), H_i, related to the branching fraction ratios and polarisation fractions, and to the direct CP violation asymmetries A_i^{CP}.

For each of the three polarisation states individually, a modified least squares fit is performed. This means that the correlations between the experimental inputs are ignored. The parameters a_i are only affected by non-factorisable $SU(3)$-breaking corrections, which are suppressed compared to their factorisable counterparts. Due to lack of dedicated studies, it is assumed here by default perfect $SU(3)$ symmetry. Hence, the penguin parameters result in a penguin phase shift on $\phi_s(B_s^0 \to J/\psi\phi)$,

$$\begin{aligned}
\Delta\phi_{s,0}^{J/\psi\phi} &= 0.003^{+0.084}_{-0.011}\,(\text{stat})^{+0.014}_{-0.009}\,(\text{syst})^{+0.047}_{-0.030}\,(|\mathcal{A}_i'/\mathcal{A}_i|) = 0.003^{+0.097}_{-0.033}\,,\\
\Delta\phi_{s,\parallel}^{J/\psi\phi} &= 0.031^{+0.047}_{-0.037}\,(\text{stat})^{+0.010}_{-0.013}\,(\text{syst})^{+0.032}_{-0.032}\,(|\mathcal{A}_i'/\mathcal{A}_i|) = 0.031^{+0.058}_{-0.051}\,,\\
\Delta\phi_{s,\perp}^{J/\psi\phi} &= -0.045^{+0.012}_{-0.012}\,(\text{stat})^{+0.007}_{-0.008}\,(\text{syst})^{+0.017}_{-0.024}\,(|\mathcal{A}_i'/\mathcal{A}_i|) = -0.045^{+0.022}_{-0.028}\,.
\end{aligned}$$

The information on the penguin parameters provided by the CP and branching ratio information in $B_s^0 \to J/\psi\overline{K}^{*0}$ decays can be combined with that from the $SU(3)$-related mode $B^0 \to J/\psi\rho^0$, previously studied by LHCb. Assuming $SU(3)$ flavour symmetry and neglecting contributions from additional decay topologies, the combined fit (as shown in Figure 8.4) leads to a penguin phase shift on $\phi_s(B_s^0 \to J/\psi\phi)$ of

$$\begin{aligned}
\Delta\phi_{s,0}^{J/\psi\phi} &= 0.000^{+0.009}_{-0.011}\,(\text{stat})^{+0.004}_{-0.009}\,(\text{syst}) = 0.000^{+0.010}_{-0.014}\,,\\
\Delta\phi_{s,\parallel}^{J/\psi\phi} &= 0.001^{+0.010}_{-0.014}\,(\text{stat})^{+0.007}_{-0.008}\,(\text{syst}) = 0.001^{+0.012}_{-0.016}\,,\\
\Delta\phi_{s,\perp}^{J/\psi\phi} &= 0.003^{+0.010}_{-0.014}\,(\text{stat})^{+0.007}_{-0.008}\,(\text{syst}) = 0.003^{+0.012}_{-0.016}\,.
\end{aligned}$$

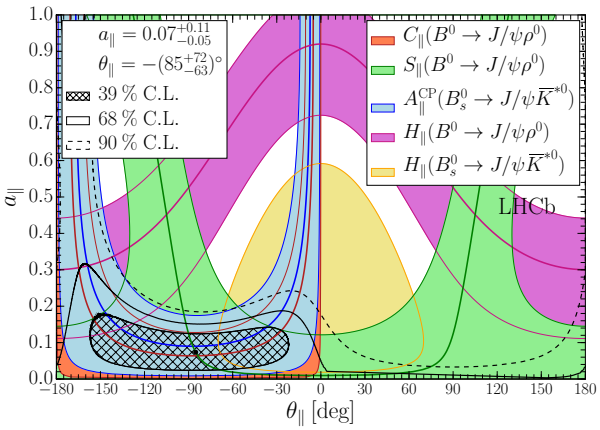

Figure 8.4: Determination of the penguin parameters a_i and θ_i through intersecting contours derived from the *CP* asymmetries and branching ratio information in $B_s^0 \to J/\psi\overline{K}^{*0}$ and $B^0 \to J/\psi\rho^0$ decay modes. The inner dark-coloured line represents the contour associated with the central value of the input quantity. Superimposed are the confidence level contours obtained from a χ^2 fit to the data. Shown is only the parallel polarisation.

8.5 The $A_1^0 \to \mu^+\mu^-$ decay mode

First steps of a model-independent search for $A_1^0 \to \mu^+\mu^-$ decays in a certain di-muon mass range, where A_1^0 corresponds to the light *CP*-odd Higgs boson in an extension of the SM, the NMSSM, were performed. Upper limits in $\mathcal{B}(A_1^0 \to \mu^+\mu^-)$ will be calculated using the CLs technique. However, at the present moment only selection and mass model studies were done: computation of simulation efficiencies and studies of possible systematic uncertainty sources will be performed as well.

Real data events are selected from two LHCb datasets with a total integrated luminosity of 2.97 fb^{-1} of pp collision data, corresponding to 0.98 (1.99) fb^{-1} of data taken during 2011 (2012) at a centre-of-mass energy of 7 (8) TeV. Three groups of sets of simulated samples are also used in this analysis: a first group contains three sets of simulated Υ decays ($\Upsilon(1S) \to \mu^+\mu^-$, $\Upsilon(2S) \to \mu^+\mu^-$ and $\Upsilon(3S) \to \mu^+\mu^-$), a second group contains two sets of simulated $A_1^0 \to \mu^+\mu^-$ decays under two different mass hypotheses for the A_1^0 boson (10 GeV/c^2 and 12 GeV/c^2), and the third group consists of a single set of simulated Drell-Yan (DY) processes with a mass threshold of 5 GeV/c^2. Each set consists of a pair of samples, representative of data taken during 2011 (2012). The total number of simulated events are approximately 6 M per each Υ decay mode, 0.2 M per each A_1^0 decay channel and 2 M of DY events.

8.5.1 Event selection

Since this analysis aims for a model independent search in a certain di-muon mass range, as previously stated, it would be desirable to avoid possible induced bias (false peaks) because

of the mass structure of the chosen training sample when constructing a multivariate discriminant. For this reason, the uBoost method is considered, where boosted decision trees are trained such the response efficiency is kept flat in mass. These kind of boosted decision trees are known as Uniform Boosted Decision Trees (UBDT). Thus, the event selection consists of two parts: a "cut-based" set of requirements to reduce the size of the real data sample to a manageable level, followed by the use of an UBDT discriminant to reject as much background as possible, keeping a high signal efficiency. The analysis is not restricted to any particular trigger line, an event should just pass at least one of the LHCb trigger lines.

The "cut-based" set of requirements consists of mass constraints, kinematic cuts and particle identification requirements of muons. The di-muon mass range from $5.5\,\mathrm{GeV}/c^2$ to $15\,\mathrm{GeV}/c^2$ is studied. A first estimation of the signal efficiency (background rejection) of these requirements is computed using a simulated sample of $A_1^0 \to \mu^+\mu^-$ decays with a mass hypothesis for the A_1^0 boson of 10 GeV/c^2 (real data sample of $\mu^\pm\mu^\pm$ candidates, henceforth referred to as same sign, SS, muon sample), leading to an efficiency (rejection) of 95% (75%).

Then, an UBDT discriminant is constructed separately for each data-taking year conditions. A signal sample of simulated DY decays and a background sample of real data SS muon are used. The choice of previous samples is not arbitrary, but driven by extensive studies on several options. Both samples are selected with a common set of requirements consisting of the same cuts as those of the "cut-based" set. The UBDT discriminant is then trained and tested over those samples using kinematic and cone isolation muon variables as discriminant variables. As shown in Figure 8.5, a smooth background response is obtained, where no overtraining or false peaks are observed. Flatness studies of the UBDT response are performed as well: flattish efficiency for signal events and high rejection for background events are found. However, it has still to be decided if it is worth or not to optimise a possible UBDT threshold cut, or just perform the di-muon mass fit in bins of the UBDT response.

8.5.2 Mass model

Di-muon resonances are modelled using the full Hypatia distribution, which has an accurate formulation with Gaussian smearing and allows to separate Multiple Scattering (MS) and spatial resolution terms. An initial mass fit test in bins of p_T to a fully simulated di-muon mass spectrum under 2011 conditions has been performed. The mass spectrum consisted of three Υ resonances (1S, 2S and 3S), one A_1^0 peak under a mass hypothesis of 12 GeV/c^2, and a exponential background component. In further steps, a fit also in bins of pseudorapidity will be considered. It has been found that the MS term corresponds to the "ramp-up" point (quantitatively defined for this test as the value corresponding to the 1% of the distribution), of the per-event mass error distribution.

After the test fit (see Figure 8.6), a comparison between the fitted A_1^0 yields and the injected number of A_1^0 events in simulation is done, looking for model dependencies. A clear dependency of the model with the di-muon invariant mass distribution has been

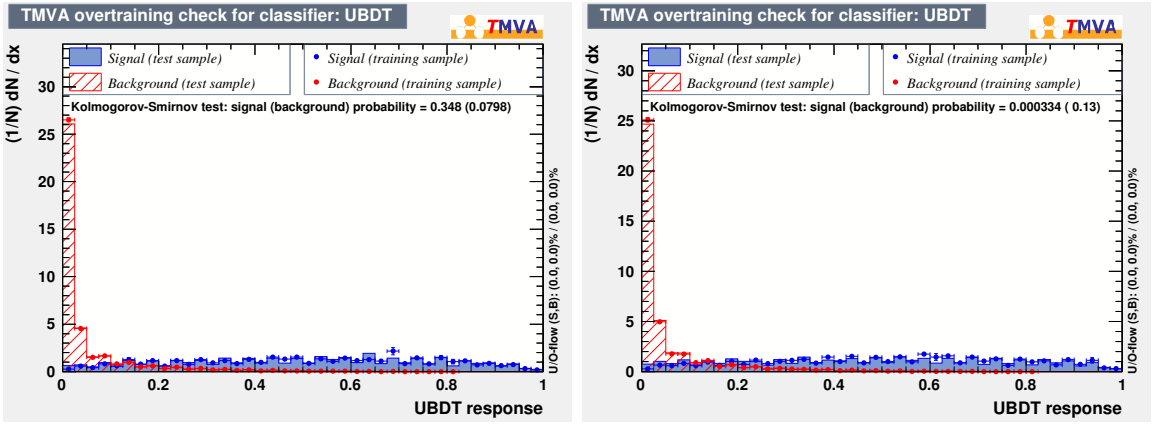

Figure 8.5: UBDT response to signal and background distributions for 2011 (left) and 2012 (right) conditions.

found, probably due to the rough modelling of certain Hypatia parameters. Studies to find more precise dependencies of these sensitive parameters of the mass model will be performed.

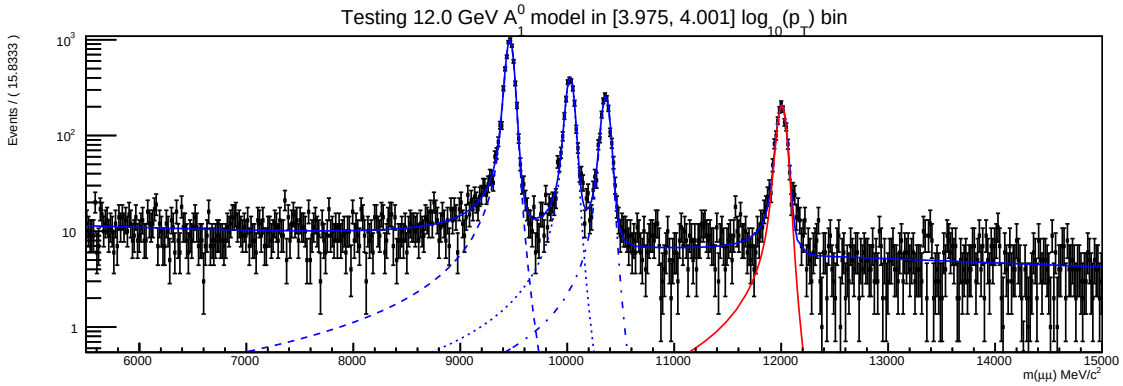

Figure 8.6: Fit to the di-muon invariant mass (2011 conditions) in one of the bins of p_T.

Chapter 9

Resumo

O modelo estándar (SM) da física de partículas, baseado nas interaccións forte, feble e electromagnética (electrofeble), é unha ferramenta moi potente e autoconsistente que levou, de forma exitosa, a numerosas predicións teóricas de resultados experimentais. A día de hoxe, esta teoría é considerada como o modelo de referencia á hora de clasificar as partículas subatómicas e explicar as súas interaccións, exceptuando a gravitación, a cal non está incorporada no SM. Sen embargo, tensións entre os resultados experimentais e certas predicións do SM surxiron nos anos previos, como a incapacidade de atopar un candidato para materia escura no universo, a existencia da masa dos neutrinos, ou o desequilibrio entre materia e antimateria presente no universo, entre outros. O SM non é capaz de explicar estes fenómenos, os cales son investigados por numerosos experimentos de física de altas enerxías (HEP). Buscas tanto directas como indirectas de posíbel evidencia de nova física (NP), as cales poden levar á consolidación dun novo modelo de referencia capaz de explicar todas estas tensións, poden ser consideradas como a vangarda da HEP.

9.1 Aspectos teóricos básicos

En relación ás buscas indirectas de posíbel NP, a violación dunha certa simetría discreta, a violación CP, é un dos ingredientes necesarios para explicar o desequilibrio entre materia e antimateria no universo, tamén coñecido como o problema da barioxénese. Sen embargo, certos resultados experimentais concluíron que a cantidade de violación CP predita polo SM non é suficiente para satisfacer as condicións necesarias para resolver o problema da barioxénese: a busca de novas fontes de violación CP alén do SM é necesaria. O estudo de violación CP no contexto do sistema de mesóns neutros B_s^0 ofrece unha excelente oportunidade de detectar posíbeis desviacións das predicións do SM. Un estudo das contribucións de segunda orde (contaminación por pingüíns) á fase ϕ_s de violación CP, debida á mestura entre oscilación e decaemento en procesos $b \to c\bar{c}s$, é parte do traballo presentado nesta tese. O estudo de ditas contribucións é importante xa que poden ser confundidas cunha posíbel sinal de NP. Dito estudo realizouse usando os decaementos da canle $B_s^0 \to J/\psi \overline{K}^{*0}$.

Con respecto ás buscas directas de posíbel NP, unha das formas propostas para complementar o SM son as súas extensións supersimétricas. Buscas directas de posíbeis novas partículas preditas por algunha destas extensións, como por exemplo a extensión supersimétrica do SM a segunda orde (NMSSM), constitúen unha forma directa de probar a robustez do SM, onde a observación de posíbeis partículas no senso de NP e preditas por ditos modelos podería ter lugar. Os primeiros pasos da busca dos decaementos da canle $A_1^0 \to \mu^+\mu^-$, onde A_1^0 é o bosón de Higgs lixeiro e CP impar predito no NMSSM, forman parte deste traballo.

9.2 O experimento LHCb

O LHCb é un experimento dedicado á física de sabor pesado (HF) no gran colisionador de hadróns (LHC), situado no CERN. A xuño de 2016, o experimento está dirixido por unha colaboración científica de 1199 membros, procedentes de 69 institucións en 16 países diferentes. O obxectivo principal de LHCb é a busca de evidencias indirectas de NP no senso da violación CP en decaementos raros de hadróns con beleza e encanto.

9.2.1 O gran colisionador de hadróns

O gran colisionador de hadróns, operando no CERN dende setembro de 2008, é o acelerador e colisionador de hadróns máis poderoso xamáis construído. Está instalado no tunel circular de 27 kilómetros que fóra construído para aloxar o gran colisionador de electróns e positróns (LEP), entre 45 m e 170 m baixo a superficie e na fronteira franco-suíza. O LHC foi deseñado para acelerar feixes de protóns a unha enerxía de 7 TeV por feixe, e para colisionalos a un enerxía de centro de masas de 14 TeV. Os datos empregados para os estudos descritos nesta tese foron tomados durante 2011 e 2012, parte do primeiro período de traballo do LHC, nomeado "Run I".

9.2.2 O detector LHCb

O detector LHCb é un espectrómetro de brazo único con cobertura angular na zona dianteira, entre 10 e 300 (250) mrad no plano perpendicular ó campo magnético (paralelo ó campo magnético). A distribución no ángulo polar da producción de pares $b\bar{b}$ no LHC xustifica este deseño, xa que a altas enerxías ditos pares son producidos predominantemente no mesmo cono hacia adiante ou hacia atrás. A vista esquemática do espectrómetro LHCb pode atoparse na Figura 9.1. O sistema de coordenadas á dereitas empregado é tal que o feixe atoparíase na dirección do eixo z, mentres que o eixo y corresponderíase co plano vertical. Cunhas dimensións globais de aproximadamente 6 m $\times$ 5 m $\times$ 20 m, o detector está composto polas seguintes partes principais: a tubería pola que circulan os feixes ou *beam pipe*, o imán de dipolo, os sistemas de trazado e localización de vértices, compostos á súa vez polo localizador de vértice (VELO), o sistema de trazado de silício (Silicon Tracker) e de trazado exterior (Outer Tracker); e o sistema de identificación de partículas,

composto polos detectores de aneis Cherenkov (RICH), o sistema de calorímetros e os sistema de detección de muóns. Además, debido á alta tasa de interacción e ás baixas fraccións de ramificación dos decaementos raros de interese, é necesario un rexeitamento eficiente daqueles datos que non son relevantes para as análises pertinentes. Isto levou á necesidade de construir un sistema de *trigger*, composto por un sistema de *hardware*, o nivel 0 (L0), e por un sistema de *software*, o trigger de alto nivel (HLT).

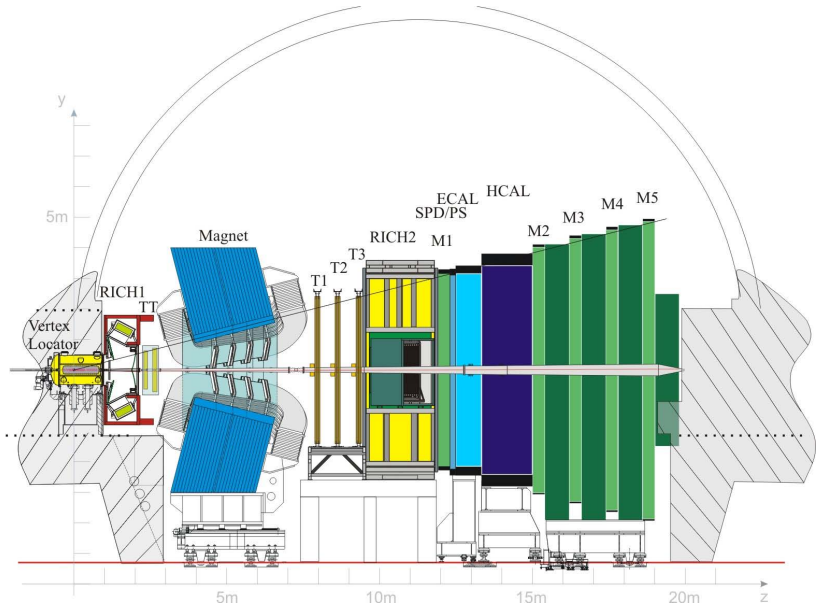

Figura 9.1: Vista esquemática en dúas dimensións do detector LHCb.

Os datos tomados polo LHCb de colisións no LHC, a unha tasa de varios millóns de sucesos por segundo, precisan ser seleccionados, preparados e distribuídos na forma máis eficiente posíbel para a súa análise. Os diferentes pasos que teñen lugar neste proceso pódense resumir da seguinte forma:

1. Nunha primeira etapa inicial, unha selección rápida ten lugar para descartar moitos daqueles sucesos que non son de interese para as análises físicas, isto é, o trigger de LHCb, o cal aplícase sobre todos os datos tomados polo detector.

2. Os datos seleccionados polo trigger son transformados, mediante o emprego de diferentes algoritmos matemáticos, nun conxunto de trazas e de vértices. Esta tarefa é realizada polo sistema de trazado e localización de vértices. Tras isto, e para poder identificar a natureza das trazas reconstruídas, a información do sistema de identificación de partículas é engadida ó conxunto.

3. Unha vez os sucesos seleccionados polo trigger son reconstruídos, é imprescindíbel a súa separación acorde ó seu contido físico. Dita tarefa é realizada mediante a selección dos diferentes decaementos tendo as súas características propias de cada

un deles, mediante un procedemento coñecido como "stripping" no marco de traballo de LHCb.

4. Finalmente, os datos xa preparados para a súa análise no paso anterior precisan ser distribuídos a diversos centros de computación arredor do mundo, a través da plataforma DIRAC e mediante o sistema de distribución coñecido como *Grid*.

9.2.3 Mellora do detector LHCb

O detector LHCb mostrou un excelente funcionamiento durante o Run I. Sen embargo, a precisión de moitas das medidas feitas polo experimento están aínda limitadas polas súas incertidumes estadísticas: coa mellora do LHCb, programada para unha toma de datos de 50 fb^{-1} durante dez anos a unha frecuencia de lectura de 40 MHz, espérase obter unha mellora na sensitividade de aproximadamente unha orde de magnitude para algúns dos observábeis clave, con respecto ás medidas actuais. Sen embargo, tralo próximo longo apagado (LS) do LHC, espérase que LHCb opere a unha luminosidade de $2 \times 10^{33} \text{cm}^{-2}\text{s}^{-1}$. Polo tanto, unha mellora dos subdetectores faise tamén necesaria.

9.2.4 Mellora do VELO do detector LHCb

O VELO mellorado debe manter ou mellorar a súa capacidade de reconstrucción de vértices baixo unhas condicións de lectura de 40 MHz e operando baixo as condicións da mellora do detector LHCb. Isto soamente é posíbel se se leva a cabo una substitución completa dos sensores de silício e da electrónica. Segundo estudos levados a cabo baixo revisión externa, a colaboración LHCb acordou a instalación dun subdetector baseado en sensores híbridos de pixeles. Estudos de investigación e desenvolvemento neste senso, además de outros, foron realizados usando detector de píxeles de silicio, como a caracterización de detectores Medipix3 usando feixes de proba do SPS. Polo tanto, un novo circuíto integrado (ASIC) resistente á radiación, denominado "VeloPix", capaz de traballar baixo unha alta tasa de toma de datos, está a seres desenvolvido.

Como xa foi mencionado previamente, realizáronse estudos, usando feixes de proba do SPS no CERN, de detectores de píxeles irradiados con hadróns, compostos por circuítos integrados Medipix3.1 e conectados a sensores de silicio n sobre p. Trala irradiación con neutróns dun reactor nuclear a unha fluencia de $0.5 \times 10^{15}\,1\,\text{MeV}\,\text{n}_{\text{eq}}\,\text{cm}^{-2}$, un aumento na dispersión do umbral de carga e un maior consumo enerxético foron observados nos ASIC previamente descritos. Sen embargo, o tamaño promedio dos *cluster* de carga colectada e a resolución como función do umbral de carga non sufriron cambios significativos en comparación cos sensores non irradiados: os resultados obtidos foron consistentes entre mostras irradiadas e non-irradiadas, e tamén coas predicións feitas pola simulación. Estes estudos foron continuados posteriormente usando os circuítos integrados Timepix3.

9.3 O modo de decaemento $B_s^0 \to J/\psi \overline{K}^{*0}$

A información experimental dos decaementos $B_s^0 \to J/\psi \overline{K}^{*0}$ necesaria para estudar a contaminación por pingüíns á fase ϕ_s é presentada nos seguintes parágrafos. Esta análise consiste no axuste dos parámetros angulares en *bins* de $M(K\pi)$ e $\cos(\theta_\mu)$ arredor do polo de masa do mesón $\overline{K}^*(892)^0$. O mesón J/ψ é reconstruído en $\mu^+\mu^-$, e o hadrón $\overline{K}^{*0}$ en $K^-\pi^+$, así coma os seus decaementos conxugados en carga. Unha moi grande contribución da compoñente $B^0 \to J/\psi K^{*0}$ está presente nos datos e tomada en conta, usada como canle de normalización.

Os sucesos de datos reais son seleccionados de dous conxuntos de datos de LHCb, obtidos a partires de colisións *pp* e cunha luminosidade total integrada de 3.0 fb^{-1}. Ditos conxuntos correspóndense con 1 (2) fb^{-1} de datos obtidos durante 2011 (2012) a unha enerxía de centro de masas de 7 (8) TeV. Tres conxuntos de mostras simuladas son tamén usadas nesta análise, contendo decaementos simulados de $B_s^0 \to J/\psi \overline{K}^{*0}$, $B^0 \to J/\psi K^{*0}$ e $B_s^0 \to J/\psi\phi$ cada un deles. Cada conxunto está composto por un par de mostras, representativas dos datos tomados durante 2011 (2012). O número total de sucesos simulados por modo de decaemento son aproximadamente 1 M, 2 M e 10 M, respectivamente.

9.3.1 Selección de sucesos

A selección de sucesos consiste en dúas partes: un conxunto de requerimentos baseado en cortes para reducir o tamaño da mostra de datos reais a unha escala manexable, seguido do emprego dun discriminante multi-variábel BDTG, co obxectivo de rexeitar a maior cantidade de fondo combinatorio posíbel, mantendo sempre unha alta eficiencia de sinal. Esta análise non está restrinxida a ningunha liña particular de trigger, é dicir, con que un suceso pase unha das liñas de trigger de LHCb é suficiente.

O conxunto de requirementos baseado en cortes está composto por cortes en ventá de masa, cortes cinemáticos e requerimentos nas variábeis de identificación de kaóns, pións e muóns. Un veto de masa dos decaementos $B^+ \to J/\psi K^+$ é tamén imposto. Sen embargo, como xa se mencionou con anterioridade, unha gran parte do fondo combinatorio é rexeitado mediante o emprego dunha BDTG, construída separadamente para as mostras de 2011 e 2012. Para o adestramento da BDTG, empregouse como mostra de sinal unha mostra simulada de decaementos $B_s^0 \to J/\psi \overline{K}^{*0}$, e como mostra de fondo, unha mostra de datos reais que contiña sucesos na *sideband* da rexión de alta masa. Ámbalas mostras foron seleccionadas usando un conxunto de requerimentos case idéntico ao conxunto baseado en cortes previamente descrito, exceptuando os requerimentos en identificación de hadróns: no seu lugar foron impostos requerimentos complementarios na identificación de kaóns e pións para evitar unha posíbel contaminación dos resultados en etapas posteriores da análise.

Usando ditas mostras, o discriminante BDTG foi adestrado empregando únicamente variábeis cinemáticas como variábeis discriminatorias. Trala súa construcción, un corte no mesmo foi optimizado usando unha figura de mérito baseada nos chamados ${}_s\mathcal{W}eights$, calculados mediante un axuste de masa no contexto da técnica do ${}_s\mathcal{P}lot$. Para o devandito

axuste, considerando un único bin de masa, foi empregado un modelo moi simple composto por dúas Crystal-Ball para a sinal e un función exponencial para o fondo.

Obtívose un valor final de eficiencia de sinal (rexeitamento de fondo) do ($\sim$ 47%) ($\sim$ 99.9%). As eficiencias relacionadas cos requerimentos na identificación de hadróns foros correxidas mediante o emprego do paquete PIDCalib. Coa selección de sucesos descrita previamente, un total de 68 100 (147 760) sucesos foron seleccionados na mostra de datos reais de 2011 (2012).

9.3.2 Fondos específicos

Como resultado de estudos extensivos en mostras simuladas, atopáronse contribucións de diversos fondos específicos debido á reconstrucción de hadróns mal identificados, como os decaementos $B_s^0 \to J/\psi K^+K^-$, $B_s^0 \to J/\psi\pi^+\pi^-$ (resonando preto dos sucesos da canle $B_s^0 \to J/\psi\overline{K}^{*0}$) e $B^0 \to J/\psi\pi^+\pi^-$ (resonando preto dos sucesos da canle $B^0 \to J/\psi K^{*0}$). Do mesmo modo que o uso de ${}_s\mathcal{W}eights$ permite eliminar a contribución de sucesos debaixos dos picos de sinal, ditos fondos específicos son suprimidos nos datos reais mediante o emprego de sucesos simulados con pesos negativos. Unha primeira estimación do número de sucesos de cada un dos decaementos previamente citados é obtida a partires de mostras simuladas. Sen embargo, xa que as mostras obtidas mediante simulación (empregando un modelo simple de espacio fase sen resonancias) non conteñen as distribucións físicas apropiadas, certas correccións son necesarias a *posteriori* para obter estimacións de sucesos máis realistas.

Dous modos bariónicos de decaemento adicionais, da familia do hadrón Λ_b^0, tamén contribúen á colección de fondos específicos a teres en conta nesta análise, os decaementos $\Lambda_b^0 \to J/\psi pK^-$ e $\Lambda_b^0 \to J/\psi p\pi^-$. O primeiro é estatísticamente cancelado mediante o emprego de pesos negativos, da mesma forma que os decaementos citados no parágrafo anterior. Sen embargo, o canle $\Lambda_b^0 \to J/\psi p\pi^-$ é engadido como unha contribución adicional ó modelo de masa, e parametrizado mediante unha distribución de Amoroso.

O número de sucesos predito para cada canle, a excepción do decaemento $\Lambda_b^0 \to J/\psi p\pi^-$, non é menor que 10 (19) e non supera en ningún caso os 51 (115) sucesos, para mostras de 2011 (2012).

9.3.3 Modelo de masa e axuste

O modelo de masa empregado consiste nunha distribución exponencial para o fondo combinatorio, unha distribución de Amoroso para os decaementos $\Lambda_b^0 \to J/\psi p\pi^-$, e unha distribución de *Hipatia* dobre empregada para modelar os decaementos de sinal de B_s^0 e B^0. A distribución de Hipatia é elexida xa que a incertidume evento a evento na masa é dependente do momento das partículas. Os parámetros ζ e β fíxanse a cero, mentres que a media e a resolución déixanse libres no axuste.

Sen embargo, como resultado de estudos con mostras simuladas, determinouse que certos parámetros da distribución Hipatia están fortemente correlacionados coa masa invariante do par $K\pi$. A consecuencia disto, o axuste de masa é realizado en catro bins

do espectro de masa $K\pi$. Ademáis, debido ás correlacións entre a masa e o coseno do ángulo de helicidade θ_μ, realízase unha separación adicional en cinco bins do $\cos(\theta_\mu)$. En consecuencia, o axuste de masa invariante realízase nun total 20 bins. Tamén tense en conta unha posíbel contaminación debida ó intercambio entre kaons e pións procedentes de decaementos $B_s^0 \to J/\psi \overline{K}^{*0}$, se enmbargo, concluíse que a contribución debida a este efecto é prácticamente nula.

A técnica do ${}_s\mathcal{P}lot$ é empregada para eliminar dos datos reais as contribucións do fondo específico $\Lambda_b^0 \to J/\psi p\pi^-$ e máis do fondo combinatorio. A cantidade de sinal é obtida mediante 20 axustes independientes á masa invariante de catro corpos empregando a o modelo masa anteriormente descrito. As cantidades de sinal obtidas para os decaementos $B_s^0 \to J/\psi \overline{K}^{*0}$ e $B^0 \to J/\psi K^{*0}$, mediante a suma de cada un dos valores resultantes de cada un dos vinte axustes, son $N_{B^0} = 208\,656 \pm 462^{+78}_{-76}$ e $N_{B_s^0} = 1\,808 \pm 51^{+38}_{-33}$, onde a primeira incertidume é estatística e obtida a partires da suma cuadrática das incertidumes en cada un dos bins considerados, e a segunda incertidume é sistemática. As proxeccións do fit global móstranse na Figura 9.2. As correlacións entre as cantidades de sinal obtidas para ámbolos dous decaementos son menores do 4%. Finalmente, realizouse un conxunto de estudos adicionais para validar as hipóteses considerdas, mediante o emprego de mostras simuladas, obtendo resultados satisfactorios.

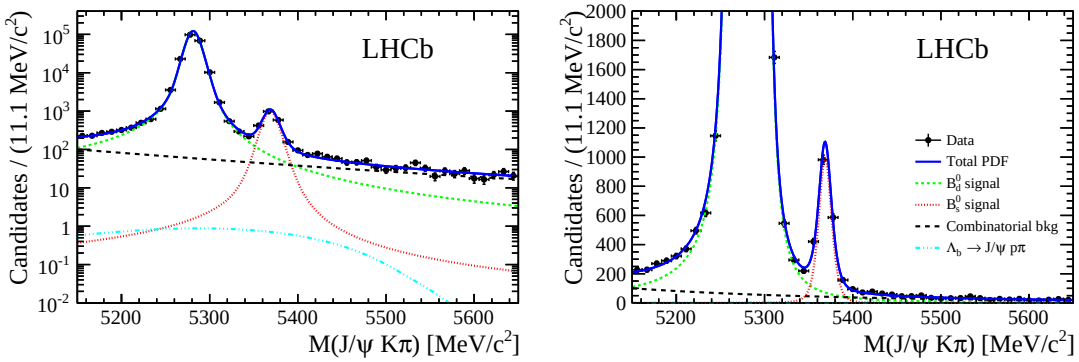

Figura 9.2: Proxección da suma dos vinte axustes en escala logarítmica (esquerda) e lineal (dereita) no eixo y. A lenda mostrada no plot dereito aplícase tamén ó plot esquerdo.

9.3.4 Análise angular e asimetrías CP

Os ángulos de decaemento considerados nesta análise, θ_K, θ_μ e φ_h, están definidos na base de helicidade. O ángulo polar θ_K (θ_μ) defínese como o ángulo entre o momento do kaón (μ^+) e a dirección oposta ó momento do mesón B_s^0 no sistema de centro de masas $K\pi$ ($\mu^+\mu^-$). O ángulo azimutal entre os planos de decaemento do sistema $K\pi$ e $\mu^+\mu^-$ é φ_h, definido a partires dunha rotación do lado do pión do plano do sistema $K\pi$ ó lado do μ^+ do plano do sistema $\mu^+\mu^-$. A rotación é positiva na dirección do sistema $\mu^+\mu^-$ no sistema

en reposo do mesón B_s^0. Estas definicións aplícanse tanto para decaementos do mesón B_s^0 como do mesón $\overline{B}_s^0$, así como para decaementos $B^0 \to J/\psi K^{*0}$.

Para determinar as compoñentes CP, as amplitudes calculadas no sistema de helicidade son transformadas en "amplitudes transversais", onde aquelas asociadas á ónda P (sistema $K\pi$ con espín $J = 1$) escríbense como A_0, $A_\parallel$ e $A_\perp$, e aquelas asociadas á onda D (sistema $K\pi$ con espín $J = 2$) escríbense como A_{20}, $A_{2\parallel}$ e $A_{2\perp}$. O módulo da amplitude transversal A_x ten un módulo $|A_x|$ e unha fase forte δ_x, e adóptase a convención $|A_0|^2+|A_\parallel|^2+|A_\perp|^2+|A_S|^2 = 1$. As mostras de $K^+\pi^-$ e $K^-\pi^+$ son separadas e axustadas mediante un fit simultáneo.

Os parámetros de onda S, $|A_S|^2$ e δ_S, son definidos independentemente para cada bin, co obxectivo de non incluir ninguna dependencia da masa $K\pi$ no axuste. Se a onda D fose incluída (a cal é únicamente considerada na evaluación de incertidumes sistemáticas, e non incluída no axuste final), é necesario definir parámetros adicionais para a onda D coma os previamente definidos para a onda S, para absorber as variacións nos diferentes bins de masa $K\pi$. Aínda así, certos termos dependentes da masa e asociados á interferencia entre ondas, seguen a estar presentes. Ditos termos correspóndese cun certo conxunto de integrais complexas, a partir das cales os chamados factores C_{ij} son calculados numéricamente, fixando unha certa hipótese para os propagadores de masa. Ditos factores son posteriormente incluídos como parámetros fixos no axuste, incluíndo no mesmo a información relativa á interferencia entre ondas. Os modelos dos propagadores de masa son elixidos a partir dunha proba sobre os datos reais, e como resultado, unha parametrización de LASS é empregada para a onda S, unha combinación isóbara de $K*(892)^0$ e $K*_1(1410)^0$ para a onda P, e unha distribución relativista de Breit-Wigner, correspondente á resonancia $K*_2(1430)^0$, para a onda P.

Os efectos da aceptancia angular son modelados mediante o emprego dun conxunto de pesos de normalización, obtidos de sucesos simulados do canle $B^0 \to J/\psi K^{*0}$. Ditos pesos son posteriormente refinados, onde a mostra simulada é pesada para corresponderse coas distribucións cinemáticas dos estados finais en datos reais, corrixindo así por imperfeccións na simulación do detector. Emprégase un procedemento iterativo para (re-)pesar ditas mostras simuladas.

Para cada un dos tres estados finais de polarización (0, $\parallel$, $\perp$) considerados para o sistema $J/\psi K\pi$, unha asimetría CP é obtida. Sen embargo, dita asimetría precisa de seres correxida para ter en conta a aceptancia do detector e mailas diferencias na interacción entre as partículas do estado final e o propio detector (asimetría de detección), así como a asimetría de producción $B_s^0 - \overline{B}_s^0$, e a dilución debida as oscilacións $B_s^0 - \overline{B}_s^0$ (factor de dilución).

Finalmente, lévase a cabo un axuste simultáneo nos catro bins de masa do espectro $K\pi$ arredor da masa nominal do mesón $\overline{K}^{*0}$, onde as amplitudes de onda P e as fases fortes son consideradas comúns en todo o rango de masa, mentres que os parámetros de onda S son obtidos de forma separada para cada bin. As proxeccións angulares do axuste móstranse na Figura 9.3. Os resultados obtidos para as fraccións de polarización e as

asimetrías CP son

$$
\begin{aligned}
f_0 &= 0.497 \;{}^{+0.024}_{-0.025}\ (\text{stat}) \pm 0.025\ (\text{syst}),\\
f_\parallel &= 0.179 \;{}^{+0.027}_{-0.026}\ (\text{stat}) \pm 0.013\ (\text{syst}),\\
A^0_{CP}(B^0_s \to J/\psi \overline{K}^{*0}) &= -0.048 \pm 0.057\ (\text{stat}) \;{}^{+0.019}_{-0.020}\ (\text{syst}),\\
A^\parallel_{CP}(B^0_s \to J/\psi \overline{K}^{*0}) &= 0.171 \pm 0.152\ (\text{stat}) \;{}^{+0.028}_{-0.027}\ (\text{syst}),\\
A^\perp_{CP}(B^0_s \to J/\psi \overline{K}^{*0}) &= -0.049 \;{}^{+0.095}_{-0.096}\ (\text{stat}) \pm 0.025\ (\text{syst}).
\end{aligned}
$$

Comparáronse ditos resultados con aqueles obtidos nun análise previo realizado por LHCb dos decaimentos $B^0 \to J/\psi\rho^0$: as asimetrías CP directas están en bo acordo, sen embargo, as diferencias observadas non son suficientemente significativas como para deducir información algunha no senso da rotura de $SU(3)$.

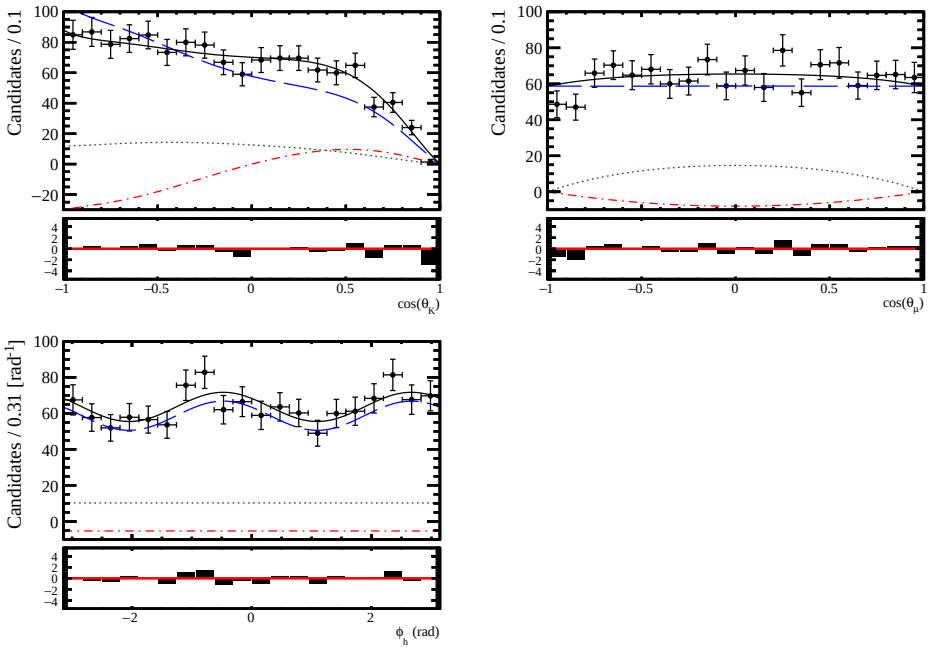

Figura 9.3: Proxeccións angulares do modelo empregado no axuste sobre datos axustados do decaimento $B^0_s \to J/\psi\overline{K}^{*0}$. Azul sólido: total. Azul discontinuo: onda P + interferancia P-P. Verde punteado: onda S. Vermello punteado-discontinuo: interferencia S-P.

9.3.5 Fraccións de ramificación

Obtivéronse dúas fraccións de ramificación normalizadas: una respecto á canle $B^0_s \to J/\psi\phi$ (ideal para o estudo de contaminación por pingüíns), e outra respecto á canle $B^0 \to J/\psi K^{*0}$ (ideal para a cancelación de incertidumes sistemáticas durante a evaluación de eficiencias). Por último, obtense unha media pesada tendo en conta ámbolos dous resultados.

Os cocientes de eficiencias son obtidos a partires das mostras simuladas, de forma separada para 2011 e 2012. Os requerimentos empregados para seleccionar a canle de normalización $B_s^0 \to J/\psi\phi$ son moi similares a aqueles empregados para seleccionar os decaementos $B_s^0 \to J/\psi\overline{K}^{*0}$. Sen embargo, no caso da canle de normalización $B^0 \to J/\psi K^{*0}$, empréganse exactamente a mesma selección que para a canle $B_s^0 \to J/\psi\overline{K}^{*0}$. Ademáis, debido á similitude do estado final entre as dúas canles no caso anterior, as incertidumes sistemáticas asociadas ás discrepancias entre mostras de datos reais e datos simulados cancélanse. Pero, como a eficiencia depende da distribución angular dos productos do decaemento, hai que aplicar correccións debido ás diferencias entre as amplitudes angulares entre datos reais e simulados.

Tras realizar a normalización á canle $B^0 \to J/\psi K^{*0}$, onde o cociente é multiplicado pola fracción de ramificación do canle $B^0 \to J/\psi K^{*0}$ obtido no experimento Belle e as diferencias nas tasas de producción dos pares B^+B^- e $B^0\overline{B}^0$ na resonancia $\Upsilon(4S)$ son tidas en conta, e tras realizar a súa vez a normalización á canle $B_s^0 \to J/\psi\phi$, ámbolos resultados son combinados nunha media pesada e correlacionada para obter un valor final de $\mathcal{B}(B_s^0 \to J/\psi\overline{K}^{*0})$. Dito valor é

$$\mathcal{B}(B_s^0 \to J/\psi\overline{K}^{*0}) = (4.14 \pm 0.18(\text{stat}) \pm 0.26(\text{syst}) \pm 0.24(f_d/f_s)) \times 10^{-5},$$

o cal atópase en bo acordo cos resultados previamente obtidos por LHCb e mais coas estimacións do SM.

9.3.6 Incertidumes sistemáticas

As fontes de incertidume sistemática máis relevantes consideradas nesta análise son:

- Fondos específicos: falta de coñecemento do modelo dos decaementos.
- Técnica do ${}_s\mathcal{P}lot$: correlacións entre $M(J/\psi K\pi)$ e $\cos(\theta_\mu)$.
- Factores C_{ij}: elección dun certo modelo de propagador para cada onda.
- Contribución de onda D: negación da contribución por onda D no axuste.
- Modelo de masa: fixado dos valores de certos parámetros obtidos nos MC.
- Contaminacións no axuste, como conclusión dos estudos de validación con mostras simuladas.
- Aceptancia angular: estadísticas de MC limitadas e correccións entre datos reais e simulados.
- Asimetrías CP: asimetrías de detección e producción.
- Fraccións de ramificación: emprego de parámetros externos nos cálculos.

Da lista anterior, hai dúas fontes dominantes de incertidume sistemática: o tamaño das mostras simuladas empregadas para a estimación dos pesos de normalización na aceptancia angular, e as correlacións entre a masa dos catro corpos e o coseno do ángulo de helicidade θ_μ.

9.4 Contaminación por pingüíns na fase ϕ_s

A contaminación por pingüíns á fase ϕ_s medida nos decaementos $B_s^0 \to J/\psi\phi$, $\Delta\phi_{s,i}$, é parametrizada polo tamaño relativo das amplitudes do diagrama de pingüín con respecto ó diagrama de árbore, a_i, que ten asociada unha diferencia de fase forte θ_i e onde a diferencia de fase feble ven dada polo ángulo γ do triángulo unitario (UT). Os devanditos parámetros de pingüín a_i e θ_i poden obterse a partires de tres por dous parámetros (dous por cada un dos tres estados de polarización i): H_i, relacionado coa fracción de ramificación e coas fraccións de polarización, e as asimetrías CP directas A_i^{CP}.

Para cada un dos tres estados de polarización, realízase un axuste de mínimos cadrados. Isto quere dicir que, esencialmente, as correlacións entre os parámetros experimentais son ignoradas. Os tamaños relativos a_i son afectados únicamente polas correccións non factorizables de rotura de $SU(3)$, as cales están moi suprimidas en comparación coas súas contrapartes factorizables. Debido á falta de estudos existentes sobre dito asunto, asúmese no axuste unha simetría $SU(3)$ perfecta. Así pois, os parámetros de pingüín conlevan á unha contaminación por pingüíns á fase $\phi_s(B_s^0 \to J/\psi\phi)$ de

$$\begin{aligned}
\Delta\phi_{s,0}^{J/\psi\phi} &= \quad 0.003^{+0.084}_{-0.011}\,(\text{stat})^{+0.014}_{-0.009}\,(\text{syst})^{+0.047}_{-0.030}\,(|\mathcal{A}_i'/\mathcal{A}_i|) = \quad 0.003^{+0.097}_{-0.033}\,, \\
\Delta\phi_{s,\parallel}^{J/\psi\phi} &= \quad 0.031^{+0.047}_{-0.037}\,(\text{stat})^{+0.010}_{-0.013}\,(\text{syst})^{+0.032}_{-0.032}\,(|\mathcal{A}_i'/\mathcal{A}_i|) = \quad 0.031^{+0.058}_{-0.051}\,, \\
\Delta\phi_{s,\perp}^{J/\psi\phi} &= -0.045^{+0.012}_{-0.012}\,(\text{stat})^{+0.007}_{-0.008}\,(\text{syst})^{+0.017}_{-0.024}\,(|\mathcal{A}_i'/\mathcal{A}_i|) = -0.045^{+0.022}_{-0.028}\,.
\end{aligned}$$

A información previamente desenvolvida sobre os parámetros de pingüín obtida a partires da información das asimetrías CP e das fracciones de ramificación en decaementos $B_s^0 \to J/\psi\overline{K}^{*0}$ pode combinarse con aquela obtida polo canle $B^0 \to J/\psi\rho^0$, relacionado mediante unha rotación de $SU(3)$, and previamente estudado por LHCb. Asumindo unha perfecta simetría de sabor $SU(3)$ e negando as contribucións de topoloxías de decaemento adicionais, o axuste combinado (mostrado na Figura 9.4) resulta nunha contaminación por pingüíns á fase $\phi_s(B_s^0 \to J/\psi\phi)$ de

$$\begin{aligned}
\Delta\phi_{s,0}^{J/\psi\phi} &= 0.000^{+0.009}_{-0.011}\,(\text{stat})^{+0.004}_{-0.009}\,(\text{syst}) = 0.000^{+0.010}_{-0.014}\,, \\
\Delta\phi_{s,\parallel}^{J/\psi\phi} &= 0.001^{+0.010}_{-0.014}\,(\text{stat})^{+0.007}_{-0.008}\,(\text{syst}) = 0.001^{+0.012}_{-0.016}\,, \\
\Delta\phi_{s,\perp}^{J/\psi\phi} &= 0.003^{+0.010}_{-0.014}\,(\text{stat})^{+0.007}_{-0.008}\,(\text{syst}) = 0.003^{+0.012}_{-0.016}\,.
\end{aligned}$$

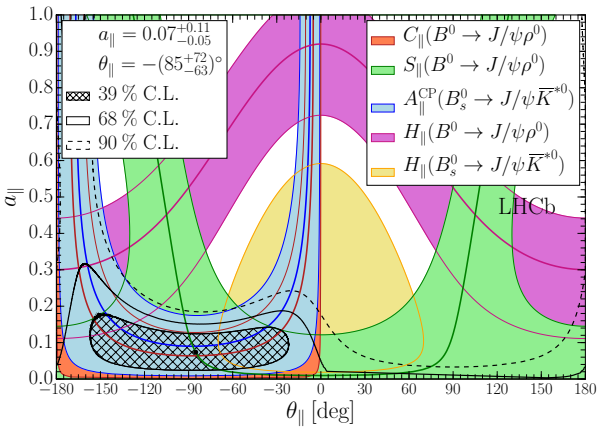

Figura 9.4: Determinación dos parámetros de pingüín a_i and θ_i a través da intersección de contornos derivados da información das asimetrías CP e máis das fracción de ramificación nas canles $B_s^0 \to J/\psi\overline{K}^{*0}$ e $B^0 \to J/\psi\rho^0$. A liña escura na rexión interior representa o contorno asociado co valor central da cantidade correspondente. Os contornos dos niveis de confianza obtidos a partires dun axuste ós datos están superpostos. Móstrase únicamente a gráfica para o estado de polarización paralelo.

9.5 O modo de decaemento $A_1^0 \to \mu^+\mu^-$

Os primeiros pasos da procura dos decaementos $A_1^0 \to \mu^+\mu^-$ nunha certa rexión do espectro de masa de dous muóns, onde A_1^0 é o bosón de Higgs lixeiro e CP impar no NMSSM, son descritos nos seguintes parágrafos. Ata o día de hoxe, leváronse únicamente a cabo estudos da selección de sucesos e do modelo de masa. Nun futuro, levaranse a cabo tanto o cálculo de límites superiores no valor de $\mathcal{B}(A_1^0 \to \mu^+\mu^-)$ mediante o emprego da técnica CLs, como a obtención das eficiencias de simulación e como o estudo de posíbeis fontes de incertidume sistemática.

Os sucesos de datos reais son seleccionados de dous conxuntos de datos de LHCb, obtidos a partires de colisións pp e cunha luminosidade total integrada de 2.97 fb^{-1}. Ditos conxuntos correspóndense con 0.98 (1.99) fb^{-1} de datos obtidos durante 2011 (2012) a unha enerxía de centro de masas de 7 (8) TeV. Seis grupos de conxuntos de mostras simuladas son tamén empregadas nesta análise: un primeiro grupo conteñe tres conxuntos de mostras de decaementos simulados do mesón Υ ($\Upsilon(1S) \to \mu^+\mu^-$, $\Upsilon(2S) \to \mu^+\mu^-$ e $\Upsilon(3S) \to \mu^+\mu^-$), un segundo grupo conteñe dous conxuntos de mostras de decaementos simulados $A_1^0 \to \mu^+\mu^-$, baixo dúas hipotéses de masa diferentes para o bosón A_1^0 (10 GeV/c^2 e 12 GeV/c^2), e un terceiro grupo consiste nun único conxunto de mostras simuladas de sucesos Drell-Yan, cun umbral de masa de 5 GeV/c^2. Cada conxunto está composto por un par de mostras, representativas dos datos tomados durante 2011 (2012). O número total de sucesos simulados son aproximadamente 6 M por canle de decaemento do mesón Υ, 0.2 M por modo de decaemento do bosón A_1^0 e 2 M de sucesos DY.

9.5.1 Selección de sucesos

Nesta análise é desexable evitar a aparición de falsos picos motivados pola estrutura de masa da mostra de adestramento elexida no momento de construir un certo discriminante multi-variábel. Por dita razón, emprégase o método uBoost, onde discriminantes multi-variábel BDT son adestrados de xeito que a súa resposta manteña unha eficiencia plana en masa. Este tipo de discriminantes coñécense co nome de UBDT. A selección de sucesos consiste en dúas partes: un conxunto de requerimentos baseado en cortes para reducir o tamaño da mostra de datos reais a unha escala manexable, seguido do emprego dun discriminante multi-variábel UBDT, co obxectivo de eliminar calqueira tipo de compoñente de fondo posíbel, mantendo sempre unha alta eficiencia de sinal consistente en pares de muóns producidos moi preto do vértice primario, muóns "prompt". Esta análise non está restrinxida a ningunha liña particular de trigger, é dicir, con que un suceso pase unha das liñas de trigger de LHCb é suficiente.

O conxunto de requirementos baseado en cortes está composto por cortes en ventá de masa, cortes cinemáticos e requerimentos nas variábeis de identificación de muóns. O rango de masa do espectro de dous muóns considerado vai de $5.5\,\mathrm{GeV}/c^2$ a $15\,\mathrm{GeV}/c^2$. Unha primeira estimación da eficiencia de sinal (rexeitamento do fondo) deste requerimentos é calculada empregando unha mostra simulada de decaementos $A_1^0 \to \mu^+\mu^-$ baixo unha hipótese de masa do bosón A_1^0 de 10 GeV/c^2 (unha mostra de datos reais de pares de muóns da mesma carga eléctrica, SS, $\mu^\pm\mu^\pm$), obtendo unha eficiencia (rexeitamento) do 95% (75%).

Un discriminante UBDT é construído separadamente para as mostras de 2011 e 2012. Unha mostra simulada de sinal de sucesos DY e unha mostra de fondo de datos reais de muóns SS son empregadas, e seleccionadas usando o mesmo conxunto de requerimentos previamente descrito. Ámbalas dúas mostras son elixidas como resultado dun estudo intensivo de diversas opcións posíbeis. O discriminante UBDT é adestrado empregando as devanditas mostras e variabéis cinemáticas e de illamento de trazas de muóns como variábeis discriminantes. A resposta da UBDT, mostrada na Figura 9.5, non presenta indicios de falsos picos nin de adestramento excesivo. Sen embargo, aínda é necesario decidir se optimizar un posíbel corte na resposta da UBDT ou sinxelamente realizar o axuste de masa en bins da mesma.

9.5.2 Modelo de masa

As resonancias de pares de muóns son modeladas empregando unha distribución completa de Hipatia, onde unha formulación máis exacta con difuminación gaussiana permite a separación dos termos de esparexemento múltiple (MS) e de resolución espacial. Así mesmo, realízase primeira unha proba inicial de axuste de masa en bins de p_T, empregando pares de muóns dunha mostra simulada de 2011. Dito espectro de masa de pares de muóns consiste en tres resonancias do mesón Υ (1S, 2S e 3S), un pico de masa do bosón A_1^0 baixo a hipótese de masa de 12 GeV/c^2, e unha compoñente de fondo exponencial. Atopouse que o termo de MS correspóndese co punto de inicio de rampa (definido para esta proba

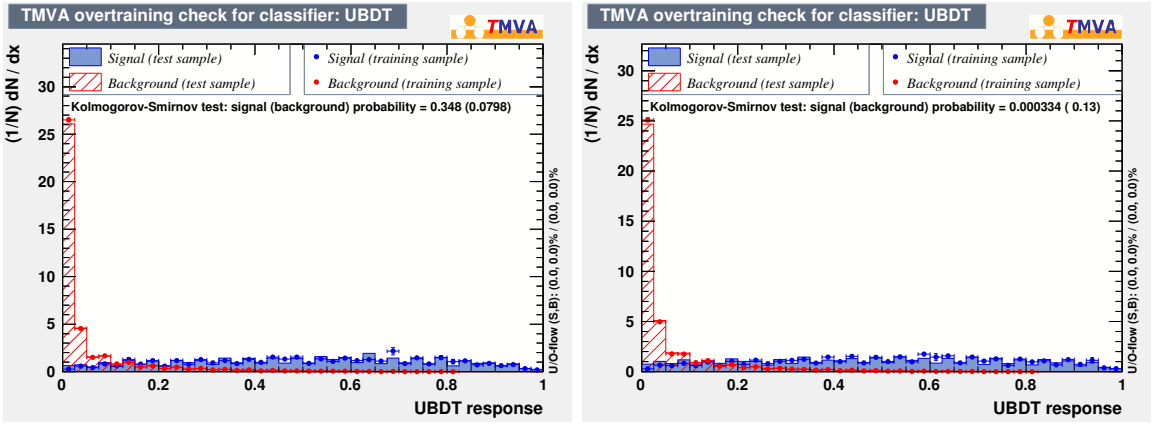

Figura 9.5: Responsa da UBDT ás distribucións de sinal e fondo de mostras de 2011 (esquerda) e 2012 (dereita).

como o punto correspondente ó 1% da distribución) da distribución evento a evento do error na masa.

Despois deste axuste de proba (ver Figura 9.6), realízase unha comparación entre as cantidades de sinal de A_1^0 obtidas no axuste e o número real de sucesos simulados de A_1^0, na procura de posíbeis dependencias do modelo empregado. Atópase unha forte dependencia do devandito modelo coa masa invariante dos pares de múons, seguramente debida ó modelado pouco preciso de certos parámetros da distribución de Hipatia. Realizaranse estudos para obter dependencias máis precisas dos devanditos parámetros do modelo de masa proposto.

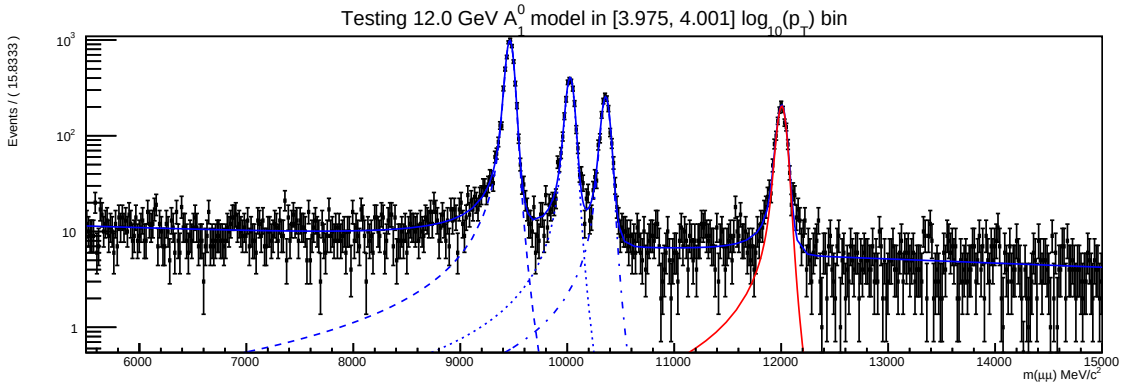

Figura 9.6: Axuste á masa invariante dos pares de muóns procedentes de mostras simuladas de 2011, nun dos bins de p_T.

Appendices

Appendix A

Multivariate analysis procedure

A.1 Mass fit for BDTG optimisation

Invariant mass fit results at the BDTG optimal threshold cut (0.2 for 2011 conditions, 0.12 for 2012 conditions) obtained during the $F({}_s\mathcal{W}eights)$ optimisation described in Chapter 4.1.4 are presented in Figure A.1 and Figure A.2 for 2011 and 2012 conditions respectively. The mass model used for this optimisation procedure consists of two Crystal-Ball [119] (signal parametrisation) and an exponential function (background parametrisation). This fit is performed in a single $M(J/\psi K\pi)$ bin and using real data samples.

A.2 BDTG correlation matrices

Correlation matrices for BDTG discriminating variables for both signal and background samples are shown in Figure A.3 under 2011 conditions, and in Figure A.4 under 2012 conditions.

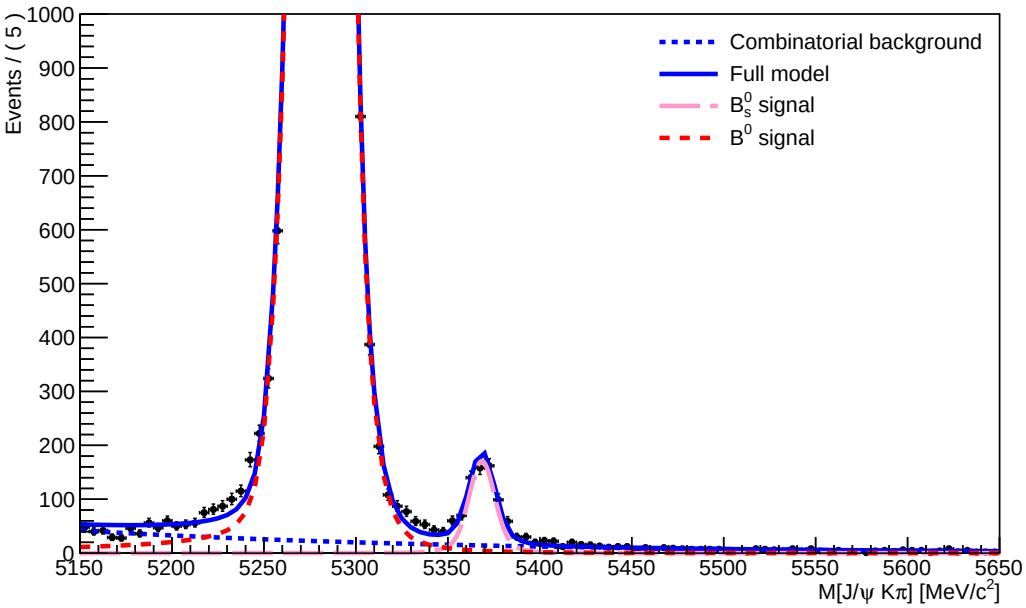

Figure A.1: Invariant mass fit projection in $M(J/\psi K\pi)$ mass under 2011 conditions (B_s^0 candidates $= 658 \pm 29$, B^0 candidates $= 70192 \pm 282$, background events $= 1555 \pm 58$).

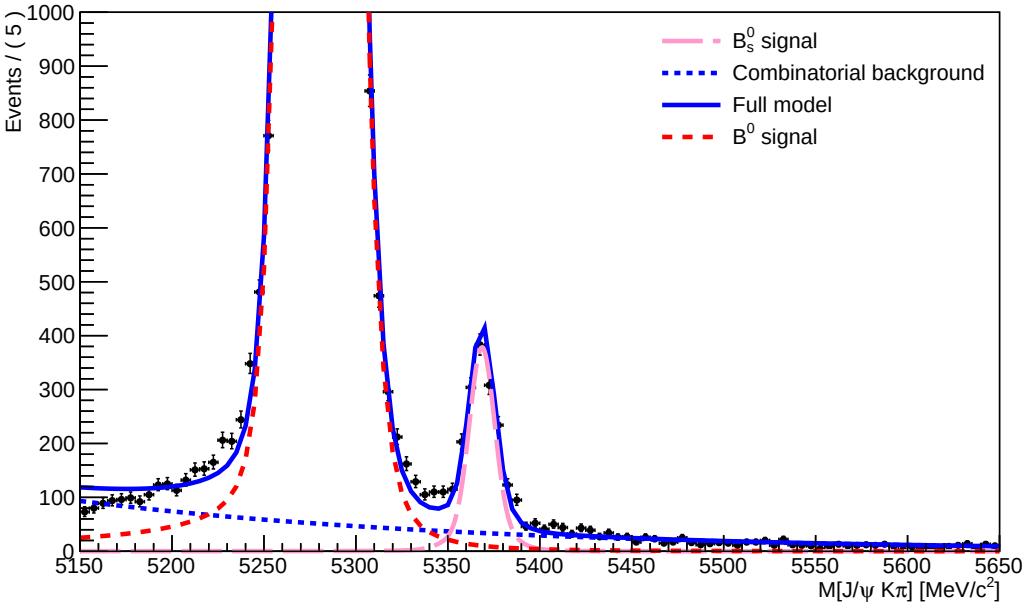

Figure A.2: Invariant mass fit projection in $M(J/\psi K\pi)$ mass under 2012 conditions (B_s^0 candidates $= 1469 \pm 43$, B^0 candidates $= 154240 \pm 417$, background events $= 3629 \pm 89$).

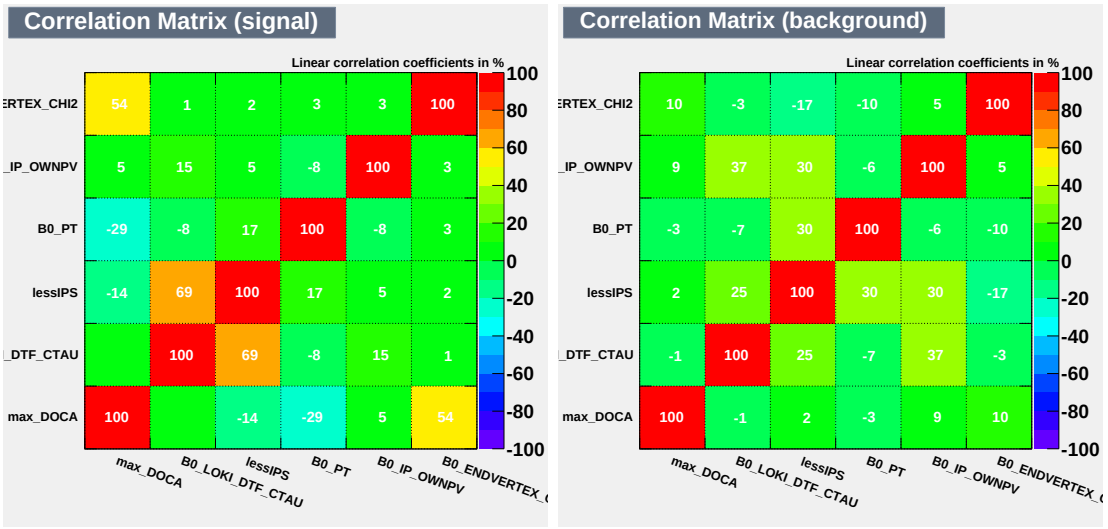

Figure A.3: Correlation matrices for BDTG discriminating variables under 2011 conditions. Left: signal sample. Right: background sample.

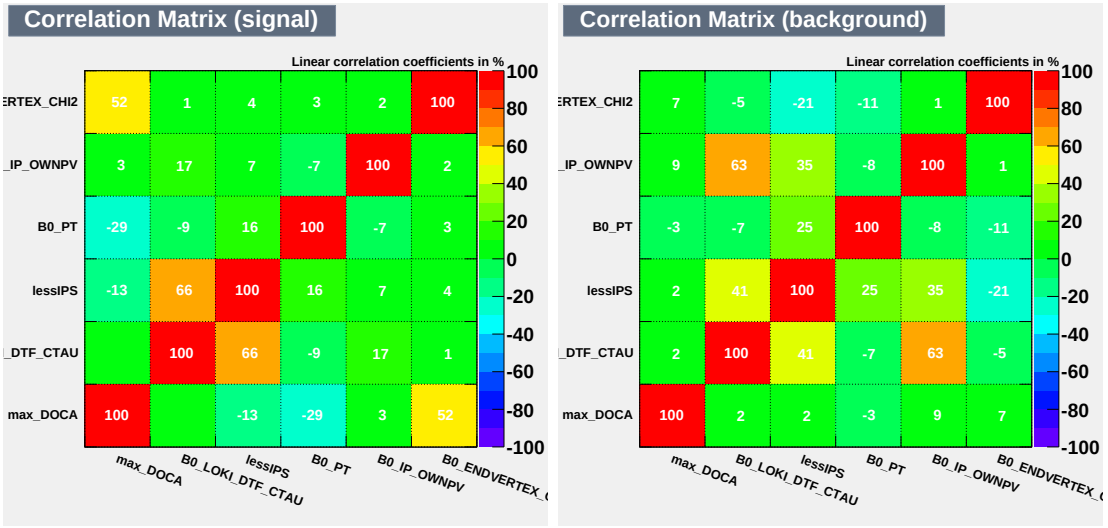

Figure A.4: Correlation matrices for BDTG discriminating variables under 2012 conditions. Left: signal sample. Right: background sample.

A.3 Distributions of BDTG discriminating variables

Distributions of discriminating variables used in the MVA procedure from real data and simulated data are compared. These comparisons are used to study the validity of these variables in simulation, in order to decide if a re-weighting is necessary. Background-subtracted (weighted histograms using ${}_s\mathcal{W}eights$ calculated from an invariant mass fit using the model described in Chapter 4.3.1) from real data samples and signal from simulated data samples are used, selected with the final selection described in Table 4.2. Comparisons (see Figure A.5, Figure A.6, Figure A.7 and Figure A.9) are done for both 2011 and 2012 conditions, using B_s^0 and B^0 candidates separately as yields for the ${}_s\mathcal{W}eights$ calculation. These comparisons between the shape of the distributions of discriminating variables for real and simulated data are purely qualitative. As conclusion, no re-weighting is applied. A final comparison of BDTG distributions between background-subtracted (using only those ${}_s\mathcal{W}eights$ calculated considering B^0 candidates as yield events) and signal from simulated $B^0 \to J/\psi K^{*0}$ decays, is done for both 2011 and 2012 conditions (see Figure A.10 and Figure A.11). Also, a comparison between signal samples from simulated $B_s^0 \to J/\psi \overline{K}^{*0}$ and $B^0 \to J/\psi K^{*0}$ data channels is shown in Figure A.12.

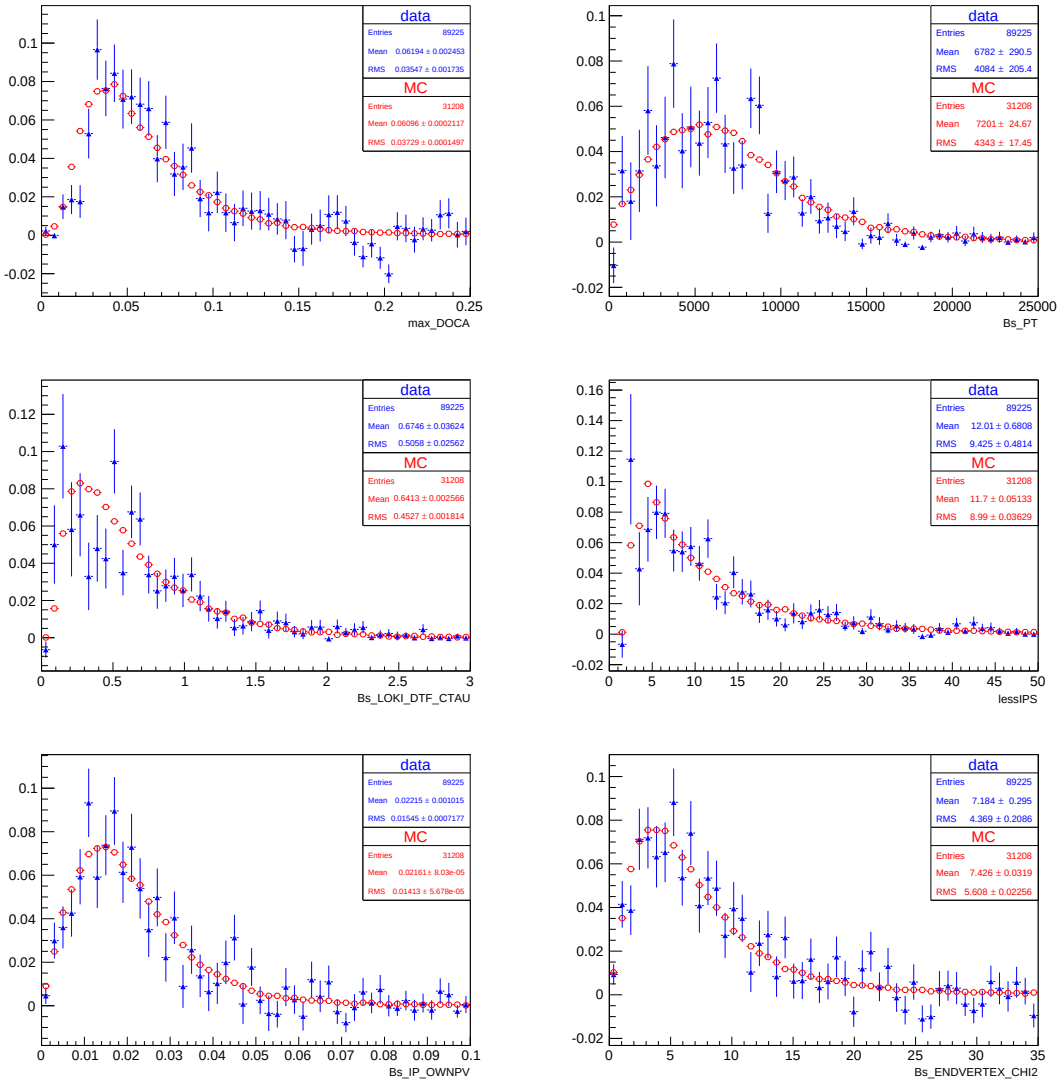

Figure A.5: Comparison of distributions of discriminating variables in background-subtracted (B_s^0) 2011 data (blue) and simulated signal (B_s^0) for 2011 conditions (red), normalised to the same area.

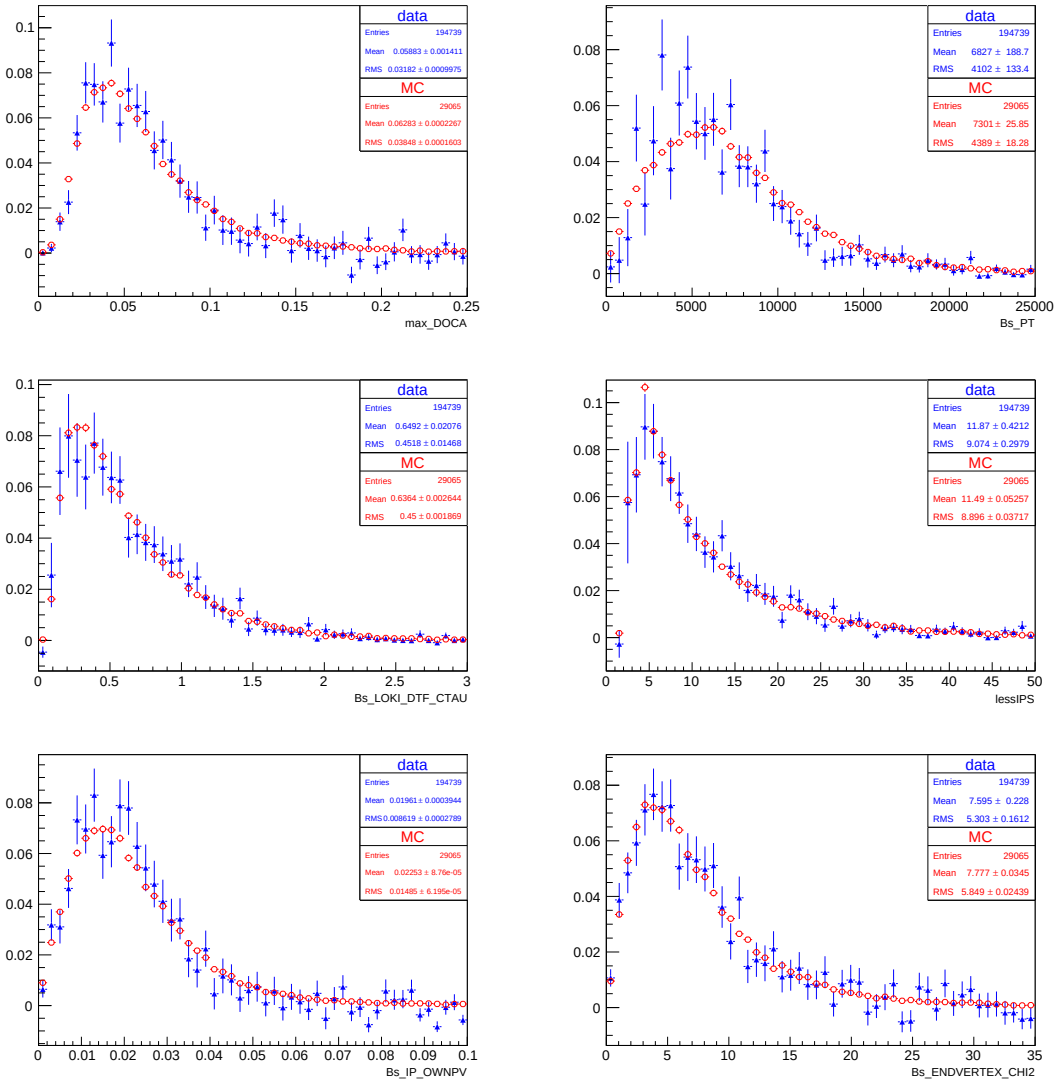

Figure A.6: Comparison of distributions of discriminating variables in background-subtracted (B_s^0) 2012 data (blue) and simulated signal (B_s^0) for 2012 conditions (red), normalised to the same area.

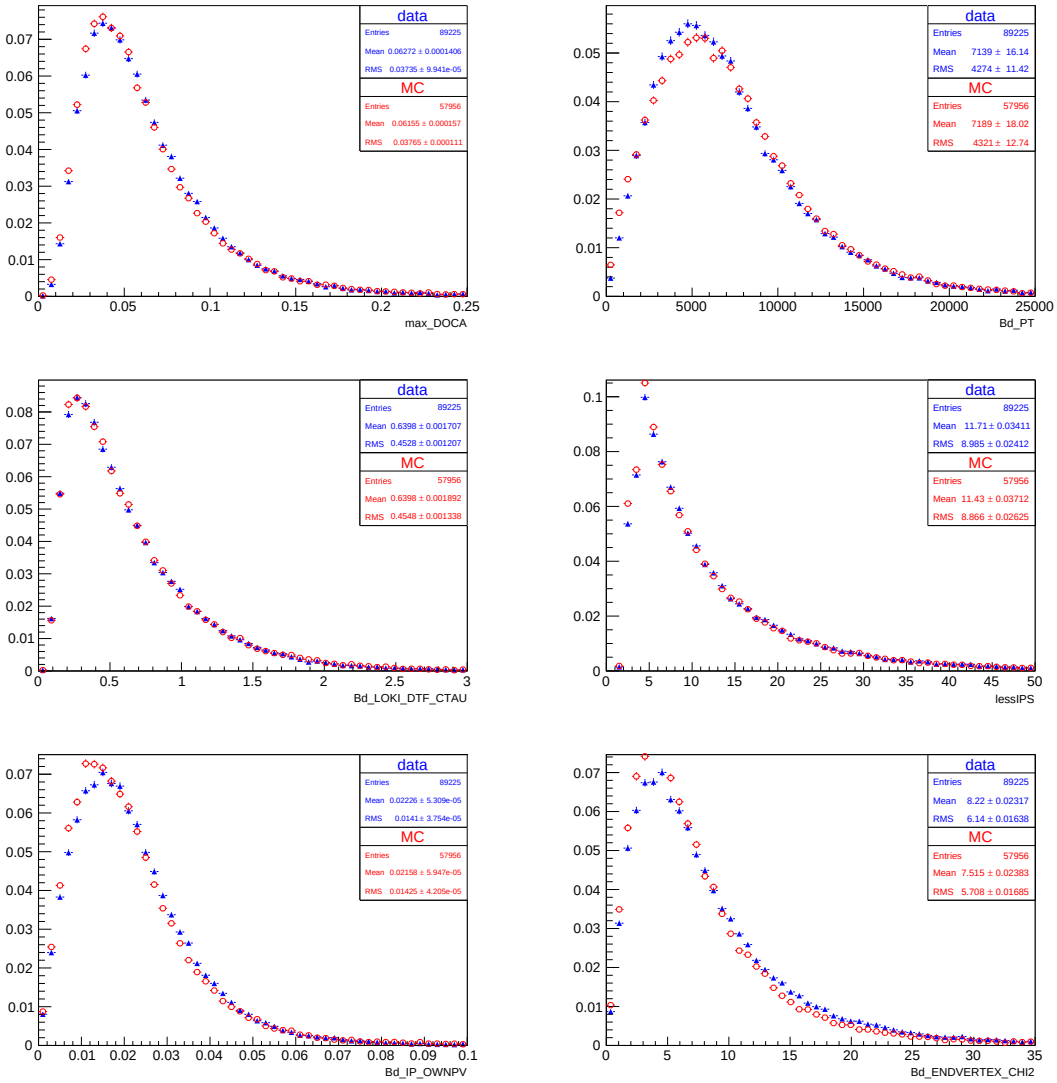

Figure A.7: Comparison of distributions of discriminating variables in background-subtracted (B^0) 2011 data (blue) and simulated signal (B^0) for 2011 conditions (red), normalised to the same area.

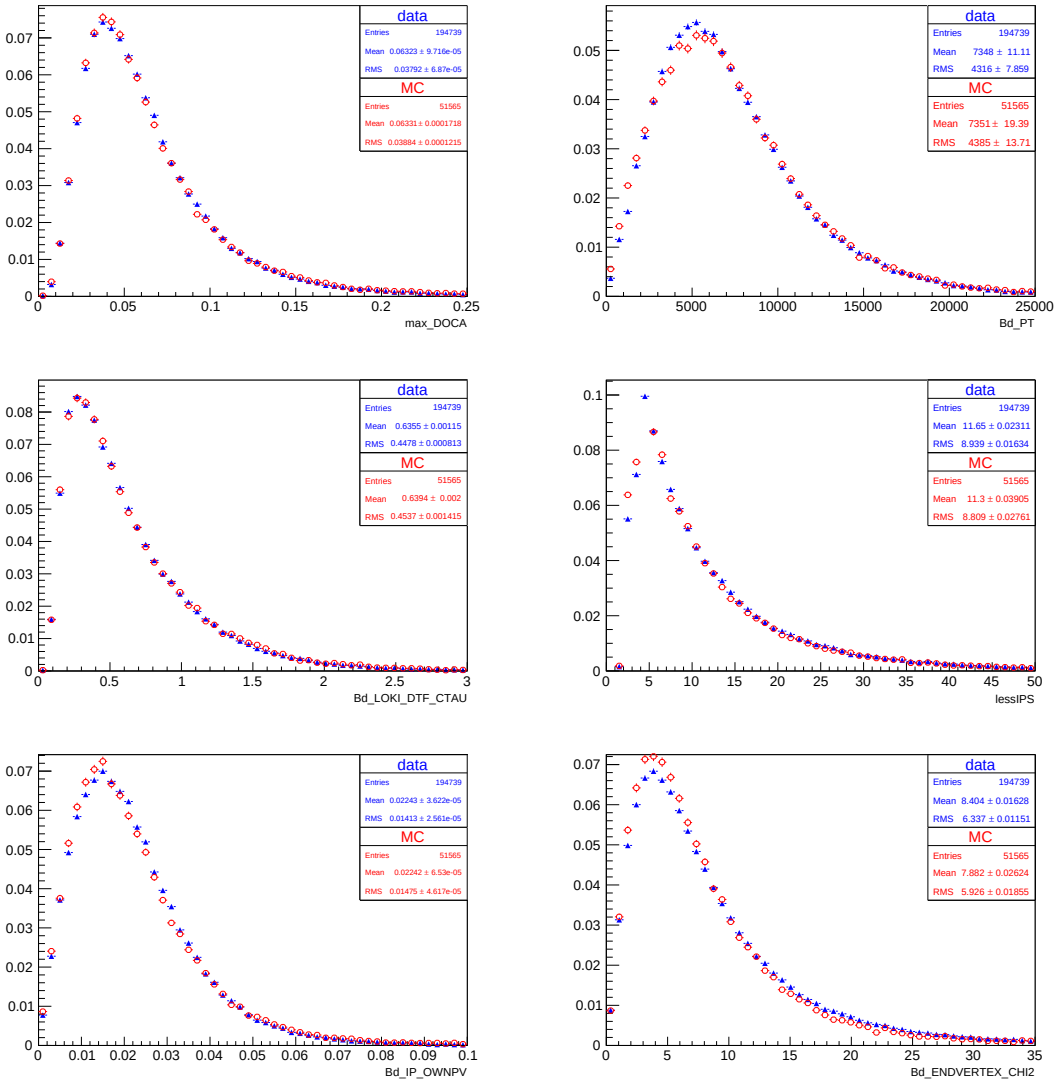

Figure A.8: Comparison of distributions of discriminating variables in background-subtracted (B^0) 2012 data (blue) and simulated signal (B^0) for 2012 conditions (red), normalised to the same area.

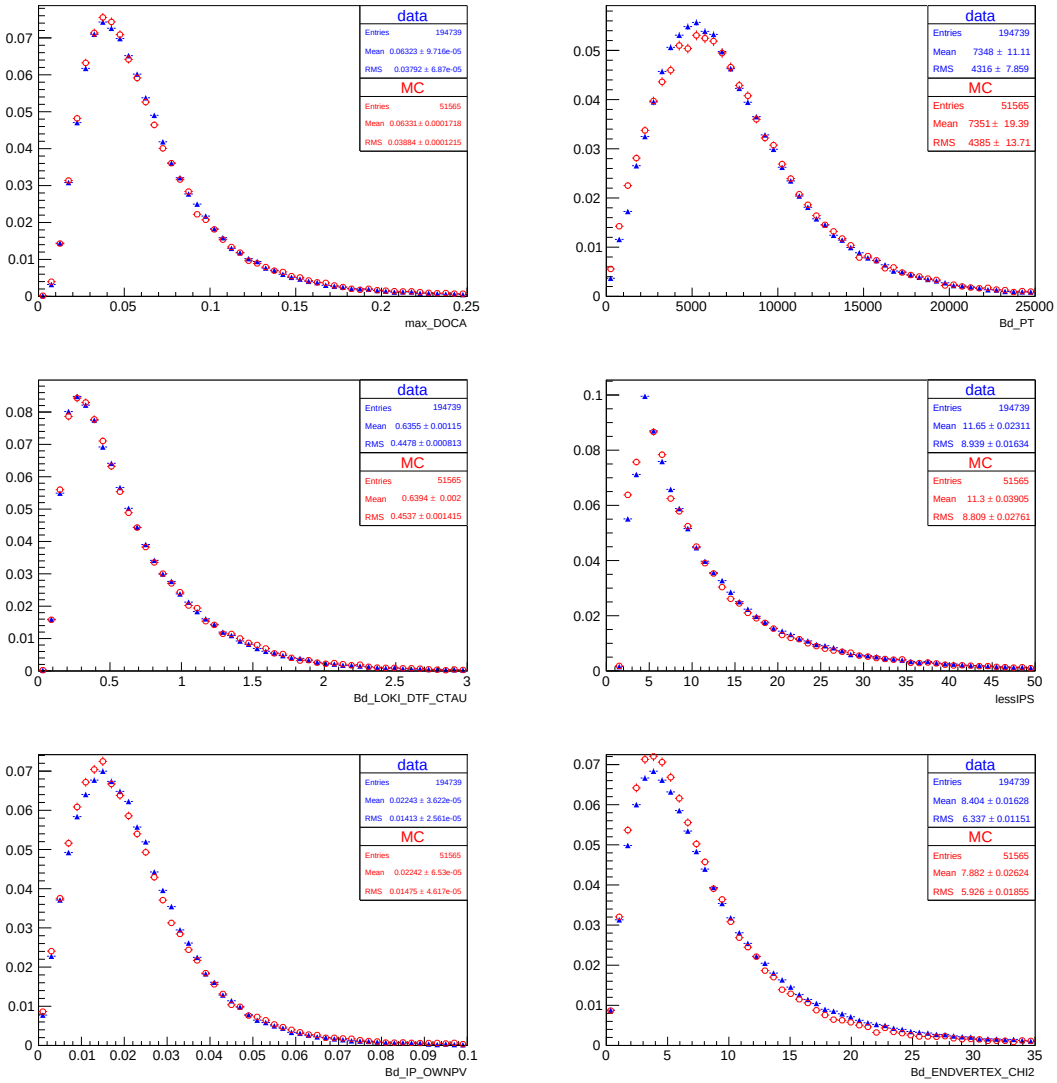

Figure A.9: Comparison of distributions of discriminating variables in background-subtracted (B^0) 2012 data (blue) and simulated signal (B^0) for 2012 conditions (red), normalised to the same area.

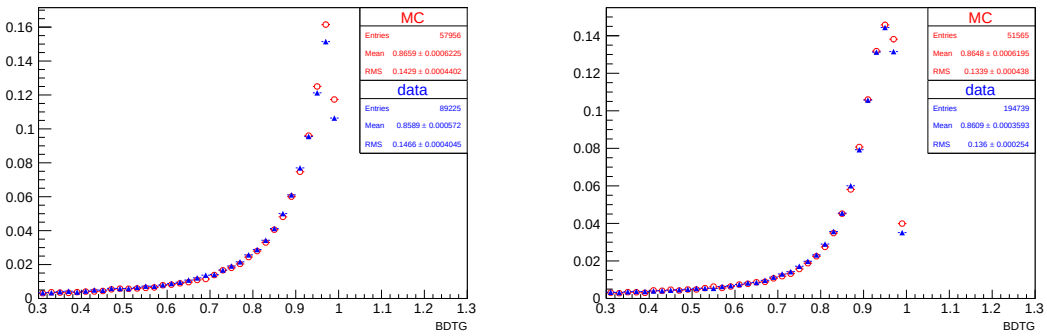

Figure A.10: Comparison of distribution of BDTG response in background-subtracted (B^0) 2011 data (blue) and simulated signal (B^0) (red) for 2011 conditions on the left and 2012 conditions on the right, normalised to the same area.

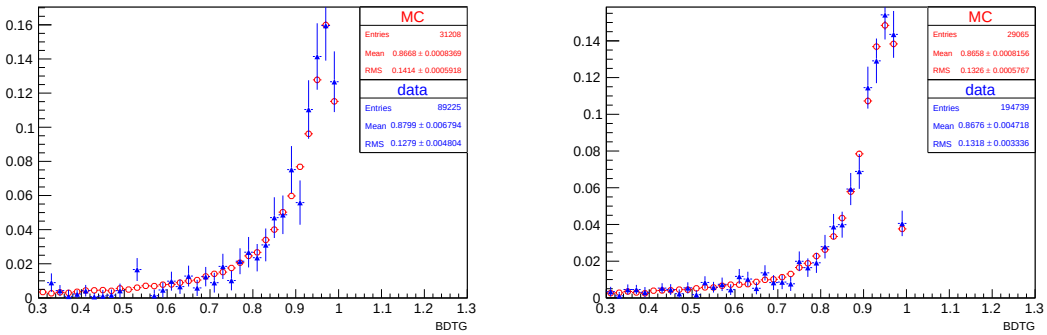

Figure A.11: Comparison of distribution of BDTG response in background-subtracted (B_s^0) 2012 data (blue) and simulated signal (B^0) (red) for 2011 conditions on the left and 2012 conditions on the right, normalised to the same area.

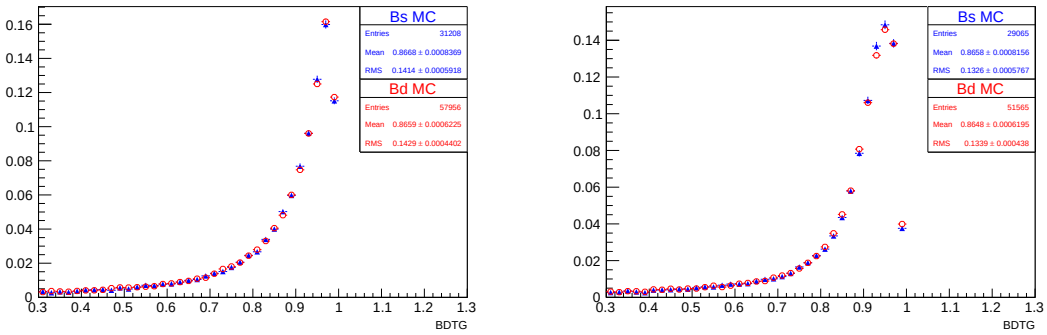

Figure A.12: Comparison of distribution of BDTG response in simulated B_s^0 (blue) and B^0 (red) signals for 2011 conditions on the left and 2012 conditions on the right, normalised to the same area.

Appendix B

Mass model studies and mass fit results

B.1 Accuracy studies of the mass model

In order to see the accuracy of the mass model in the region of interest, the model prediction fraction of $B^0 \to J/\psi K^{*0}$ that leak into the $\pm 40\,\mathrm{MeV}/c^2$ around B_s^0 is compared to that obtained in simulation (both with and without MC-*truth*). The values obtained are summarized in Table B.1. A systematic is added according to this effect.

Table B.1: Fit predictions in simulation for the fraction of $B^0 \to J/\psi K^{*0}$ events that leak into the $\pm 40\,\mathrm{MeV}/c^2$ window around the B_s^0, compared to the actual fraction found in MC. The estimates are made for a_2 free, and for a_2 set to infinity. The two approaches coincide for the MC-*truth* sample because a_2 fits to $> 14\sigma$.

	Free a_2	$a_2 = \infty$	Current value
MC-*truth* requirement	2.55 ± 0.57	2.55 ± 0.57	3.24 ± 0.20
No matching requirement	5.74 ± 0.80	3.35 ± 0.12	5.48 ± 0.25

B.2 Non-resolution effects modelled by the Hypatia distribution

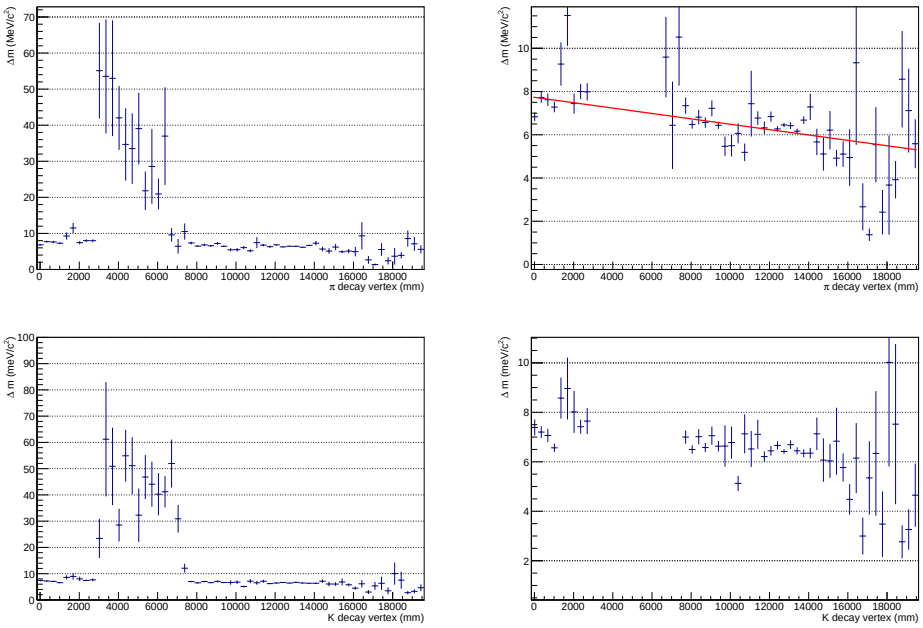

Figure B.1: Average difference between measured $M(J/\psi K\pi)$ and true mass, Δm, as a function of the pion (top) and kaon (middle) decay vertex z position. Simulated samples where MC-*truth* required over kaons and pions when needed, are used. The plots on the left show large dispersion for decay vertices in the range 2.5 to 7 meters. The plots on the right show a zoom in the region of moderate ΔM, where a slow linear decrease of ΔM as a function of the z position can be seen. The Hypatia distribution does not model those effects from first principles, but only with a phenomenological parameterisation.

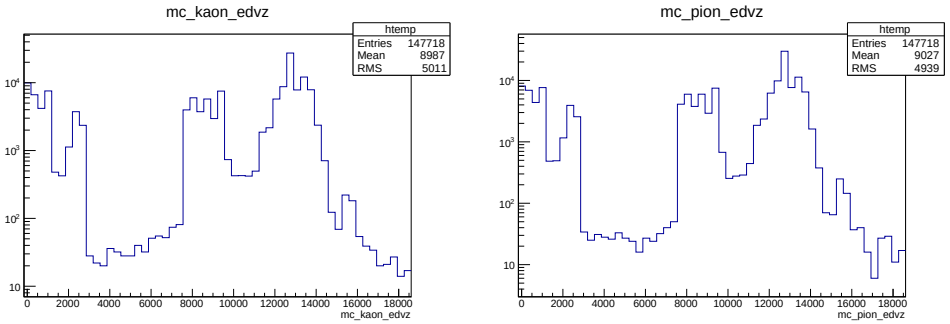

Figure B.2: Distribution of the end vertex position for MC-*truth* kaons and pions.

B.3 Simultaneous fit with shared common values

A simultaneous fit where the mean and sigma of the B_s^0 and B^0 Hypatia functions were shared over the 20 categories is performed. From this simultaneous fit, the following numbers

$$N_{B^0} = 208601 \pm 462\,, \tag{B.1}$$
$$N_{B_s^0} = 1786 \pm 48\,, \tag{B.2}$$

are obtained, where the number of B_s^0 and B^0 events correspond to the sum over the 20 bins. Here the uncertainties are statistical only. By further calculating the ratio, the value

$$\frac{N_{B_s^0}}{N_{B^0}} = (8.56 \pm 0.23) \times 10^{-3}\,. \tag{B.3}$$

is obtained. Then, comparing these results to the ones obtained in the nominal configuration of 20 independent fits (see Chapter 4.3.2), a difference can be computed, δ, between the nominal values and the ones from the simultaneous fit, such as

$$\delta N_{B^0} = 43\,, \tag{B.4}$$
$$\delta N_{B_s^0} = 13\,, \tag{B.5}$$
$$\delta \left(\frac{N_{B_s^0}}{N_{B_d^0}} \right) = 0.06 \times 10^{-3}\,, \tag{B.6}$$

where the latter corresponds to a shift of $\sim 25\%$ of the statistical uncertainty on $N_{B_s^0}/N_{B^0}$.

Using the set of ${}_s\mathcal{W}eights$ computed from the simultaneous fit, also the angular fit results can be compared. Table B.2 gives the comparison of the corresponding results.

Since constraining the mean and sigma of the B_s^0 and B^0 Hypatia functions would require to estimate an associated systematic uncertainty, and due to the fact that the gain on the statistical uncertainties is null or negligible with compatible central values, the 20 independent fit is kept as the nominal mass fit model. In addition, due to the

higher momentum of the kaon and pion final state particles for higher values of the $m_{K\pi}$ bin, one can expect the mean and sigma of the B_s^0 and B^0 to slightly increase as a function of the $m_{K\pi}$ bin.

Table B.2: Comparison between the angular fit results obtained after applying ${}_s\mathcal{W}eights$ either computed from the nominal 20 independent fits, or using a simultaneous fit with the mean and sigma of the B_s^0 and B^0 Hypatia functions shared over the 20 bins. Here the A_{CP} values are blinded with the same blinding string in both fits.

Parameter	Nominal value	Simultaneous	δ	δ/σ
A_0^{CP}	$0.175^{+0.062}_{-0.062}$	$0.155^{+0.064}_{-0.064}$	0.021	0.321
A_S^{CP}	$-0.269^{+0.090}_{-0.086}$	$-0.271^{+0.089}_{-0.088}$	0.002	0.021
$A_\parallel^{CP}$	$-0.445^{+0.159}_{-0.155}$	$-0.375^{+0.155}_{-0.155}$	−0.070	−0.451
$A_\perp^{CP}$	$0.075^{+0.099}_{-0.098}$	$0.069^{+0.100}_{-0.100}$	0.007	0.067
F_S_826_861	$0.526^{+0.084}_{-0.092}$	$0.507^{+0.092}_{-0.095}$	0.018	0.198
F_S_861_896	$0.103^{+0.033}_{-0.027}$	$0.115^{+0.033}_{-0.030}$	−0.012	−0.363
F_S_896_931	$0.064^{+0.052}_{-0.035}$	$0.063^{+0.043}_{-0.035}$	0.001	0.014
F_S_931_966	$0.698^{+0.064}_{-0.074}$	$0.693^{+0.071}_{-0.077}$	0.005	0.061
$\delta_\parallel$	$-2.585^{+0.175}_{-0.181}$	$-2.633^{+0.169}_{-0.171}$	0.048	0.279
$\delta_\perp$	$-0.081^{+0.115}_{-0.116}$	$-0.079^{+0.116}_{-0.118}$	−0.002	−0.017
δ_S_826_861	$0.296^{+0.147}_{-0.149}$	$0.334^{+0.153}_{-0.155}$	−0.038	−0.245
δ_S_861_896	$-0.495^{+0.214}_{-0.187}$	$-0.602^{+0.178}_{-0.166}$	0.107	0.621
δ_S_896_931	$-2.083^{+0.216}_{-0.338}$	$-2.088^{+0.259}_{-0.339}$	0.005	0.016
δ_S_931_966	$-2.319^{+0.156}_{-0.169}$	$-2.318^{+0.163}_{-0.172}$	−0.001	−0.004
f_0	$0.484^{+0.026}_{-0.026}$	$0.473^{+0.026}_{-0.027}$	0.011	0.400
$f_\parallel$	$0.181^{+0.029}_{-0.028}$	$0.191^{+0.029}_{-0.029}$	−0.010	−0.351

Appendix C

Angular analysis

C.1 Full decay rate

The full decay rate is shown in this section up to D-wave, and including the C_{SP}, C_{SD} and C_{PD} factors. $c\theta_K$ stands for $\cos(\theta_K)$ and $c\theta_l$ for $\cos(\theta_\mu)$.

$$
\begin{aligned}
\int_{K\pi\text{bin}} \frac{d\Gamma(\Omega, m_{K\pi})}{d\Omega} dm_{K\pi} \propto{}& \frac{3}{4}\frac{|A_0|^2 c\theta_K^2\left(-c\theta_l^2+1\right)}{\pi} \\
&+ \frac{\sqrt{15}C_{PD}|A_0||A_{2\parallel}|c\theta_K\left(6c\theta_K^2-2\right)\left(-c\theta_l^2+1\right)\cos\left(\delta_{20}\right)}{8\pi} \\
&+ \frac{3}{4}\frac{\sqrt{10}C_{PD}|A_0||A_{2\parallel}|c\theta_K^2 c\theta_l\sqrt{-c\theta_K^2+1}\sqrt{-c\theta_l^2+1}\cos\left(\delta_{2\parallel}\right)\cos\left(\phi\right)}{\pi} \\
&- \frac{3}{4}\frac{\sqrt{10}C_{PD}|A_0||A_{2\perp}|c\theta_K^2 c\theta_l\sqrt{-c\theta_K^2+1}\sqrt{-c\theta_l^2+1}\sin\left(\delta_{2\perp}\right)\sin\left(\phi\right)}{\pi} \\
&+ \frac{\sqrt{3}C_{SP}|A_0||A_S|c\theta_K\left(-c\theta_l^2+1\right)\cos\left(\delta_S\right)}{2\pi} \\
&+ \frac{3}{4}\frac{\sqrt{2}|A_0||A_\parallel|c\theta_K c\theta_l\sqrt{-c\theta_K^2+1}\sqrt{-c\theta_l^2+1}\cos\left(\delta_\parallel\right)\cos\left(\phi\right)}{\pi} \\
&- \frac{3}{4}\frac{\sqrt{2}|A_0||A_\perp|c\theta_K c\theta_l\sqrt{-c\theta_K^2+1}\sqrt{-c\theta_l^2+1}\sin\left(\delta_\perp\right)\sin\left(\phi\right)}{\pi} \\
&+ \frac{5}{64}\frac{|A_{2\parallel}|^2\left(-c\theta_l^2+1\right)\left(-36c\theta_K^2\left(-c\theta_K^2+1\right)+12c\theta_K^2+4\right)}{\pi} \\
&+ \frac{5}{16}\frac{\sqrt{6}|A_{2\parallel}||A_{2\parallel}|c\theta_K c\theta_l\sqrt{-c\theta_K^2+1}\left(6c\theta_K^2-2\right)\sqrt{-c\theta_l^2+1}\left(\sin\left(\delta_{20}\right)\sin\left(\delta_{2\parallel}\right)+\cos\left(\delta_{20}\right)\cos\left(\delta_{2\parallel}\right)\right)\cos\left(\phi\right)}{\pi} \\
&- \frac{5}{16}\frac{\sqrt{6}|A_{2\parallel}||A_{2\perp}|c\theta_K c\theta_l\sqrt{-c\theta_K^2+1}\left(6c\theta_K^2-2\right)\sqrt{-c\theta_l^2+1}\left(-\sin\left(\delta_{20}\right)\cos\left(\delta_{2\perp}\right)+\sin\left(\delta_{2\perp}\right)\cos\left(\delta_{20}\right)\right)\sin\left(\phi\right)}{\pi} \\
&+ \frac{\sqrt{5}C_{SD}|A_{2\parallel}||A_S|\left(6c\theta_K^2-2\right)\left(-c\theta_l^2+1\right)\left(\sin\left(\delta_{20}\right)\sin\left(\delta_S\right)+\cos\left(\delta_{20}\right)\cos\left(\delta_S\right)\right)}{8\pi}
\end{aligned}
$$

$$
\begin{aligned}
&+\frac{\sqrt{30}C_{PD}|A_{2\parallel}||A_{\parallel}|c\theta_l\sqrt{-c\theta_K^2+1}\left(6c\theta_K^2-2\right)\sqrt{-c\theta_l^2+1}\left(\sin\left(\delta_{20}\right)\sin\left(\delta_{\parallel}\right)+\cos\left(\delta_{20}\right)\cos\left(\delta_{\parallel}\right)\right)\cos\left(\phi\right)}{16\pi}\\
&-\frac{\sqrt{30}C_{PD}|A_{2\parallel}||A_{\perp}|c\theta_l\left(-6c\theta_K^2+2\right)\sqrt{-c\theta_K^2+1}\sqrt{-c\theta_l^2+1}\left(\sin\left(\delta_{20}\right)\cos\left(\delta_{\perp}\right)-\sin\left(\delta_{\perp}\right)\cos\left(\delta_{20}\right)\right)\sin\left(\phi\right)}{16\pi}\\
&+\frac{15}{16}\frac{|A_{2\parallel}|^2c\theta_K^2\left(-c\theta_K^2+1\right)\left(2c\theta_l^2\cos^2\left(\phi\right)+2\sin^2\left(\phi\right)\right)}{\pi}\\
&+\frac{15}{4}\frac{|A_{2\parallel}||A_{2\perp}|c\theta_K^2\left(-c\theta_K^2+1\right)\left(-c\theta_l^2+1\right)\left(-\sin\left(\delta_{2\parallel}\right)\cos\left(\delta_{2\perp}\right)+\sin\left(\delta_{2\perp}\right)\cos\left(\delta_{2\parallel}\right)\right)\sin\left(\phi\right)\cos\left(\phi\right)}{\pi}\\
&+\frac{\sqrt{30}C_{SD}|A_{2\parallel}||A_S|c\theta_Kc\theta_l\sqrt{-c\theta_K^2+1}\sqrt{-c\theta_l^2+1}\left(\sin\left(\delta_{2\parallel}\right)\sin\left(\delta_S\right)+\cos\left(\delta_{2\parallel}\right)\cos\left(\delta_S\right)\right)\cos\left(\phi\right)}{4\pi}\\
&+\frac{3}{8}\frac{\sqrt{5}C_{PD}|A_{2\parallel}||A_{\parallel}|c\theta_K\left(-c\theta_K^2+1\right)\left(2c\theta_l^2\cos^2\left(\phi\right)+2\sin^2\left(\phi\right)\right)\left(\sin\left(\delta_{2\parallel}\right)\sin\left(\delta_{\parallel}\right)+\cos\left(\delta_{2\parallel}\right)\cos\left(\delta_{\parallel}\right)\right)}{\pi}\\
&-\frac{3}{4}\frac{\sqrt{5}C_{PD}|A_{2\parallel}||A_{\perp}|c\theta_K\left(-c\theta_K^2+1\right)\left(-c\theta_l^2+1\right)\left(\sin\left(\delta_{2\parallel}\right)\cos\left(\delta_{\perp}\right)-\sin\left(\delta_{\perp}\right)\cos\left(\delta_{2\parallel}\right)\right)\sin\left(\phi\right)\cos\left(\phi\right)}{\pi}\\
&+\frac{15}{16}\frac{|A_{2\perp}|^2c\theta_K^2\left(-c\theta_K^2+1\right)\left(-2c\theta_l^2\cos^2\left(\phi\right)+2c\theta_l^2+2\cos^2\left(\phi\right)\right)}{\pi}\\
&-\frac{\sqrt{30}C_{SD}|A_{2\perp}||A_S|c\theta_Kc\theta_l\sqrt{-c\theta_K^2+1}\sqrt{-c\theta_l^2+1}\left(\sin\left(\delta_{2\perp}\right)\cos\left(\delta_S\right)-\sin\left(\delta_S\right)\cos\left(\delta_{2\perp}\right)\right)\sin\left(\phi\right)}{4\pi}\\
&+\frac{3}{4}\frac{\sqrt{5}C_{PD}|A_{2\perp}||A_{\parallel}|c\theta_K\left(-c\theta_K^2+1\right)\left(-c\theta_l^2+1\right)\left(\sin\left(\delta_{2\perp}\right)\cos\left(\delta_{\parallel}\right)-\sin\left(\delta_{\parallel}\right)\cos\left(\delta_{2\perp}\right)\right)\sin\left(\phi\right)\cos\left(\phi\right)}{\pi}\\
&+\frac{3}{8}\frac{\sqrt{5}C_{PD}|A_{2\perp}||A_{\perp}|c\theta_K\left(-c\theta_K^2+1\right)\left(\sin\left(\delta_{2\perp}\right)\sin\left(\delta_{\perp}\right)+\cos\left(\delta_{2\perp}\right)\cos\left(\delta_{\perp}\right)\right)\left(-2c\theta_l^2\cos^2\left(\phi\right)+2c\theta_l^2+2\cos^2\left(\phi\right)\right)}{\pi}\\
&+\frac{|A_S|^2\left(-c\theta_l^2+1\right)}{4\pi}\\
&+\frac{\sqrt{6}C_{SP}|A_S||A_{\parallel}|c\theta_l\sqrt{-c\theta_K^2+1}\sqrt{-c\theta_l^2+1}\left(\sin\left(\delta_S\right)\sin\left(\delta_{\parallel}\right)+\cos\left(\delta_S\right)\cos\left(\delta_{\parallel}\right)\right)\cos\left(\phi\right)}{4\pi}\\
&-\frac{\sqrt{6}C_{SP}|A_S||A_{\perp}|c\theta_l\sqrt{-c\theta_K^2+1}\sqrt{-c\theta_l^2+1}\left(-\sin\left(\delta_S\right)\cos\left(\delta_{\perp}\right)+\sin\left(\delta_{\perp}\right)\cos\left(\delta_S\right)\right)\sin\left(\phi\right)}{4\pi}\\
&+\frac{3}{16}\frac{|A_{\parallel}|^2\left(-c\theta_K^2+1\right)\left(2c\theta_l^2\cos^2\left(\phi\right)+2\sin^2\left(\phi\right)\right)}{\pi}\\
&-\frac{3}{4}\frac{|A_{\parallel}||A_{\perp}|\left(-c\theta_K^2+1\right)\left(-c\theta_l^2+1\right)\left(\sin\left(\delta_{\parallel}\right)\cos\left(\delta_{\perp}\right)-\sin\left(\delta_{\perp}\right)\cos\left(\delta_{\parallel}\right)\right)\sin\left(\phi\right)\cos\left(\phi\right)}{\pi}\\
&+\frac{3}{16}\frac{|A_{\perp}|^2\left(-c\theta_K^2+1\right)\left(-2c\theta_l^2\cos^2\left(\phi\right)+2c\theta_l^2+2\cos^2\left(\phi\right)\right)}{\pi}
\end{aligned}
\tag{C.1}
$$

C.2 Angular fit results for $B^0 \to J/\psi K^{*0}$

LHCb published a measurement of the polarisation fractions and strong phases of $B^0 \to J/\psi K^{*0}$ decays in four $m_{K\pi}$ bins, around the $K^*(892)^0$ nominal mass, using 1 fb^{-1} of real data of pp collisions [133]. A comparison of this measurement with the results obtained in

the present analysis by performing a sFit to the weighted angular distributions using the ${}_s\mathcal{W}eights$ for the B^0 signal extracted from the mass fit (see Chapter 4.3.2), is presented. A good agreement between the results obtained in the present analysis and those in the $B^0 \to J/\psi K^{*0}$ paper, as reported in Table C.1, are found. The agreement between the two analyses when allowing for possible CP asymmetries is also checked. The results are presented in Table C.2.

Table C.1: Parameters resulting from the angular fit performed simultaneously in 4 $m_{K\pi}$ bins around the $K^*(892)^0$ nominal mass. The uncertainties in the first and second columns are statistical. In the third column, the uncertainties are obtained by adding in quadrature the systematic and statistical uncertainties. The last column gives the difference between the 2 results in units of the total uncertainty σ_{tot}, which is the sum in quadrature of the uncertainties in the second and third columns.

Parameter	Results with 3 fb^{-1}	$B^0 \to J/\psi K^{*0}$ paper [133], 1 fb^{-1}	|difference|/σ_{tot}
f_0	0.552 ± 0.002	0.572 ± 0.014	1.405
$f_\parallel$	0.225 ± 0.002	0.227 ± 0.012	0.137
$\delta_\parallel$	-2.93 ± 0.01	-2.94 ± 0.04	0.19
$\delta_\perp$	2.93 ± 0.01	2.94 ± 0.03	0.29
F_S_826_861	0.090 ± 0.004	0.115 ± 0.021	1.170
δ_S_826_861	3.17 ± 0.06	3.09 ± 0.08	0.78
F_S_861_896	0.025 ± 0.002	0.049 ± 0.008	2.941
δ_S_861_896	2.54 ± 0.04	2.66 ± 0.08	1.36
F_S_896_931	0.032 ± 0.003	0.052 ± 0.011	1.742
δ_S_896_931	1.71 ± 0.02	1.94 ± 0.09	2.53
F_S_931_966	0.109 ± 0.007	0.105 ± 0.016	0.221
δ_S_931_966	1.39 ± 0.02	1.53 ± 0.11	1.30

Table C.2: Parameters resulting from the angular fit performed simultaneously in 4 $m_{K\pi}$ bins around the $K^*(892)^0$ nominal mass. The uncertainties in the first and second columns are statistical. In the third column, the uncertainties are obtained by adding in quadrature the systematic and statistical uncertainties. The last column gives the difference between the 2 results in units of the total uncertainty σ_{tot}, wich is the sum in quadrature of the uncertainties in the second and third columns.

Parameter	Results with 3 fb^{-1}	$B^0 \to J/\psi K^{*0}$ paper [133], 1 fb^{-1}	difference/σ_{tot}
A_0^{CP}	0.010 ± 0.004	-	-
A_S^{CP}	0.061 ± 0.026	-	-
$A_\parallel^{CP}$	0.033 ± 0.009	-	-
$A_\perp^{CP}$	0.005 ± 0.009	-	-
f_0	0.552 ± 0.002	0.572 ± 0.014	1.405
$f_\parallel$	0.225 ± 0.002	0.227 ± 0.012	0.137
$\delta_\parallel$	-2.93 ± 0.01	-2.94 ± 0.04	0.19
$\delta_\perp$	2.93 ± 0.01	2.94 ± 0.03	0.29
F_S_826_861	0.090 ± 0.004	0.115 ± 0.021	1.156
δ_S_826_861	3.17 ± 0.06	3.09 ± 0.08	0.76
F_S_861_896	0.025 ± 0.002	0.049 ± 0.008	2.940
δ_S_861_896	2.54 ± 0.04	2.66 ± 0.08	1.37
F_S_896_931	0.032 ± 0.003	0.052 ± 0.011	1.743
δ_S_896_931	1.71 ± 0.02	1.94 ± 0.09	2.52
F_S_931_966	0.109 ± 0.007	0.105 ± 0.016	0.234
δ_S_931_966	1.39 ± 0.02	1.53 ± 0.11	1.30

C.3 Angular acceptance splitted by data-taking year periods

Table C.3: Uncorrected normalisation weights comparision between 2011 and 2012 simulated samples, for $1^{\text{st}} K\pi$ bin, negative kaons. The weights are not normalised w.r.t. ξ_{00}.

	k	2011	2012	abs. difference (σ)
1	00	+1.0000 ± 0.0000	+1.0000 ± 0.0000	+0.0000 ± 0.0000 (+0.0 σ)
2	($\parallel\parallel$)	+1.4271 ± 0.0404	+1.3441 ± 0.0412	-0.0831 ± 0.0577 (-1.4 σ)
3	($\perp\perp$)	+1.4552 ± 0.0422	+1.3835 ± 0.0435	-0.0717 ± 0.0606 (-1.2 σ)
4	($\parallel\perp$)	+0.0175 ± 0.0267	+0.0004 ± 0.0278	-0.0170 ± 0.0385 (-0.4 σ)
5	(0 $\parallel$)	+0.0074 ± 0.0159	-0.0164 ± 0.0159	-0.0238 ± 0.0225 (-1.1 σ)
6	(0 $\perp$)	+0.0016 ± 0.0147	+0.0053 ± 0.0150	+0.0037 ± 0.0210 (+0.2 σ)
7	SS	+1.2287 ± 0.0252	+1.2230 ± 0.0270	-0.0057 ± 0.0369 (-0.2 σ)
8	(S$\parallel$)	-0.0557 ± 0.0238	-0.0143 ± 0.0247	+0.0414 ± 0.0343 (+1.2 σ)
9	(S$\perp$)	+0.0176 ± 0.0223	+0.0044 ± 0.0228	-0.0132 ± 0.0319 (-0.4 σ)
10	S0	-0.8697 ± 0.0355	-0.8734 ± 0.0364	-0.0038 ± 0.0508 (-0.1 σ)

Table C.4: Uncorrected normalisation weights comparision between 2011 and 2012 simulated samples, for $2^{\text{nd}} K\pi$ bin, negative kaons. The weights are normalised w.r.t. ξ_{00}.

	k	2011	2012	abs. difference (σ)
1	00	+1.0000 ± 0.0000	+1.0000 ± 0.0000	+0.0000 ± 0.0000 (+0.0 σ)
2	($\parallel\parallel$)	+1.4204 ± 0.0205	+1.4352 ± 0.0220	+0.0148 ± 0.0301 (+0.5 σ)
3	($\perp\perp$)	+1.4261 ± 0.0211	+1.4600 ± 0.0232	+0.0338 ± 0.0313 (+1.1 σ)
4	($\parallel\perp$)	-0.0029 ± 0.0133	+0.0208 ± 0.0147	+0.0237 ± 0.0198 (+1.2 σ)
5	(0 $\parallel$)	-0.0215 ± 0.0079	-0.0062 ± 0.0086	+0.0153 ± 0.0117 (+1.3 σ)
6	(0 $\perp$)	-0.0010 ± 0.0074	-0.0179 ± 0.0080	-0.0170 ± 0.0110 (-1.5 σ)
7	SS	+1.2351 ± 0.0129	+1.2436 ± 0.0140	+0.0085 ± 0.0191 (+0.4 σ)
8	(S$\parallel$)	-0.0407 ± 0.0120	-0.0380 ± 0.0131	+0.0027 ± 0.0178 (+0.1 σ)
9	(S$\perp$)	+0.0080 ± 0.0112	-0.0275 ± 0.0122	-0.0355 ± 0.0165 (-2.1 σ)
10	S0	-0.8364 ± 0.0178	-0.8168 ± 0.0192	+0.0196 ± 0.0262 (+0.7 σ)

Table C.5: Uncorrected normalisation weights comparision between 2011 and 2012 simulated samples, for $3^{\text{rd}} K\pi$ bin, negative kaons. The weights are normalised w.r.t. ξ_{00}.

	k	2011	2012	abs. difference (σ)
1	00	+1.0000 ± 0.0000	+1.0000 ± 0.0000	+0.0000 ± 0.0000 (+0.0 σ)
2	($\parallel\parallel$)	+1.4321 ± 0.0210	+1.4655 ± 0.0226	+0.0334 ± 0.0308 (+1.1 σ)
3	($\perp\perp$)	+1.4364 ± 0.0215	+1.4932 ± 0.0236	+0.0567 ± 0.0319 (+1.8 σ)
4	($\parallel\perp$)	-0.0268 ± 0.0137	+0.0015 ± 0.0149	+0.0283 ± 0.0203 (+1.4 σ)
5	(0 $\parallel$)	-0.0075 ± 0.0083	-0.0178 ± 0.0088	-0.0102 ± 0.0121 (-0.8 σ)
6	(0 $\perp$)	-0.0027 ± 0.0076	-0.0011 ± 0.0082	+0.0016 ± 0.0112 (+0.1 σ)
7	SS	+1.2416 ± 0.0131	+1.2668 ± 0.0143	+0.0252 ± 0.0194 (+1.3 σ)
8	(S$\parallel$)	-0.0496 ± 0.0125	-0.0257 ± 0.0134	+0.0238 ± 0.0183 (+1.3 σ)
9	(S$\perp$)	+0.0109 ± 0.0116	+0.0005 ± 0.0124	-0.0104 ± 0.0170 (-0.6 σ)
10	S0	-0.8101 ± 0.0185	-0.7869 ± 0.0200	+0.0233 ± 0.0272 (+0.9 σ)

Table C.6: Uncorrected normalisation weights comparision between 2011 and 2012 simulated samples, for $4^{\text{th}} K\pi$ bin, negative kaons. The weights are normalised w.r.t. ξ_{00}.

	k	2011	2012	abs. difference (σ)
1	00	+1.0000 ± 0.0000	+1.0000 ± 0.0000	+0.0000 ± 0.0000 (+0.0 σ)
2	($\parallel\parallel$)	+1.4959 ± 0.0383	+1.4351 ± 0.0386	-0.0608 ± 0.0544 (-1.1 σ)
3	($\perp\perp$)	+1.5152 ± 0.0398	+1.4691 ± 0.0404	-0.0461 ± 0.0567 (-0.8 σ)
4	($\parallel\perp$)	-0.0058 ± 0.0241	-0.0167 ± 0.0256	-0.0109 ± 0.0352 (-0.3 σ)
5	(0 $\parallel$)	-0.0192 ± 0.0147	+0.0196 ± 0.0160	+0.0387 ± 0.0218 (+1.8 σ)
6	(0 $\perp$)	-0.0094 ± 0.0131	-0.0026 ± 0.0144	+0.0068 ± 0.0194 (+0.4 σ)
7	SS	+1.2762 ± 0.0238	+1.2575 ± 0.0248	-0.0188 ± 0.0343 (-0.5 σ)
8	(S$\parallel$)	-0.0403 ± 0.0225	-0.0652 ± 0.0236	-0.0250 ± 0.0326 (-0.8 σ)
9	(S$\perp$)	-0.0140 ± 0.0202	-0.0055 ± 0.0215	+0.0085 ± 0.0295 (+0.3 σ)
10	S0	-0.7764 ± 0.0334	-0.7371 ± 0.0352	+0.0393 ± 0.0485 (+0.8 σ)

Table C.7: Uncorrected normalisation weights comparision between 2011 and 2012 simulated samples, for $1^{\text{st}} K\pi$ bin, positive kaons. The weights are normalised w.r.t. ξ_{00}.

	k	2011	2012	abs. difference (σ)
1	00	+1.0000 ± 0.0000	+1.0000 ± 0.0000	+0.0000 ± 0.0000 (+0.0 σ)
2	($\parallel\parallel$)	+1.3882 ± 0.0402	+1.3429 ± 0.0400	-0.0454 ± 0.0566 (-0.8 σ)
3	($\perp\perp$)	+1.4017 ± 0.0408	+1.3476 ± 0.0417	-0.0542 ± 0.0584 (-0.9 σ)
4	($\parallel\perp$)	-0.0412 ± 0.0258	-0.0238 ± 0.0265	+0.0173 ± 0.0369 (+0.5 σ)
5	(0 $\parallel$)	+0.0036 ± 0.0160	-0.0065 ± 0.0165	-0.0101 ± 0.0230 (-0.4 σ)
6	(0 $\perp$)	-0.0133 ± 0.0143	-0.0084 ± 0.0153	+0.0049 ± 0.0210 (+0.2 σ)
7	SS	+1.1869 ± 0.0244	+1.1771 ± 0.0251	-0.0098 ± 0.0350 (-0.3 σ)
8	(S$\parallel$)	-0.0160 ± 0.0237	-0.0621 ± 0.0243	-0.0461 ± 0.0339 (-1.4 σ)
9	(S$\perp$)	-0.0112 ± 0.0219	-0.0494 ± 0.0224	-0.0382 ± 0.0313 (-1.2 σ)
10	S0	-0.8410 ± 0.0344	-0.9145 ± 0.0352	-0.0734 ± 0.0493 (-1.5 σ)

Table C.8: Uncorrected normalisation weights comparision between 2011 and 2012 simulated samples, for $2^{\text{nd}} K\pi$ bin, positive kaons. The weights are normalised w.r.t. ξ_{00}.

	k	2011	2012	abs. difference (σ)
1	00	+1.0000 ± 0.0000	+1.0000 ± 0.0000	+0.0000 ± 0.0000 (+0.0 σ)
2	($\parallel\parallel$)	+1.4152 ± 0.0206	+1.4043 ± 0.0215	-0.0109 ± 0.0298 (-0.4 σ)
3	($\perp\perp$)	+1.4477 ± 0.0217	+1.4307 ± 0.0224	-0.0170 ± 0.0312 (-0.5 σ)
4	($\parallel\perp$)	-0.0183 ± 0.0137	+0.0012 ± 0.0144	+0.0195 ± 0.0198 (+1.0 σ)
5	(0 $\parallel$)	+0.0006 ± 0.0081	-0.0243 ± 0.0084	-0.0249 ± 0.0117 (-2.1 σ)
6	(0 $\perp$)	+0.0013 ± 0.0074	+0.0008 ± 0.0078	-0.0005 ± 0.0108 (-0.0 σ)
7	SS	+1.2241 ± 0.0130	+1.2196 ± 0.0136	-0.0045 ± 0.0188 (-0.2 σ)
8	(S$\parallel$)	-0.0366 ± 0.0124	-0.0295 ± 0.0126	+0.0071 ± 0.0176 (+0.4 σ)
9	(S$\perp$)	-0.0036 ± 0.0113	+0.0078 ± 0.0119	+0.0113 ± 0.0164 (+0.7 σ)
10	S0	-0.8729 ± 0.0178	-0.8589 ± 0.0186	+0.0140 ± 0.0258 (+0.5 σ)

Table C.9: Uncorrected normalisation weights comparision between 2011 and 2012 simulated samples, for $3^{\text{rd}} K\pi$ bin, positive kaons. The weights are normalised w.r.t. ξ_{00}.

	k	2011	2012	abs. difference (σ)
1	00	+1.0000 ± 0.0000	+1.0000 ± 0.0000	+0.0000 ± 0.0000 (+0.0 σ)
2	($\parallel\parallel$)	+1.4456 ± 0.0210	+1.4428 ± 0.0221	-0.0028 ± 0.0305 (-0.1 σ)
3	($\perp\perp$)	+1.4923 ± 0.0221	+1.4292 ± 0.0225	-0.0631 ± 0.0315 (-2.0 σ)
4	($\parallel\perp$)	+0.0176 ± 0.0138	-0.0062 ± 0.0143	-0.0238 ± 0.0199 (-1.2 σ)
5	(0 $\parallel$)	-0.0232 ± 0.0083	-0.0107 ± 0.0086	+0.0125 ± 0.0120 (+1.0 σ)
6	(0 $\perp$)	+0.0003 ± 0.0076	+0.0028 ± 0.0080	+0.0025 ± 0.0110 (+0.2 σ)
7	SS	+1.2430 ± 0.0131	+1.2409 ± 0.0138	-0.0021 ± 0.0190 (-0.1 σ)
8	(S$\parallel$)	-0.0176 ± 0.0125	-0.0344 ± 0.0128	-0.0168 ± 0.0179 (-0.9 σ)
9	(S$\perp$)	+0.0072 ± 0.0115	-0.0120 ± 0.0121	-0.0192 ± 0.0167 (-1.2 σ)
10	S0	-0.8071 ± 0.0185	-0.7979 ± 0.0195	+0.0092 ± 0.0269 (+0.3 σ)

Table C.10: Uncorrected normalisation weights comparision between 2011 and 2012 simulated samples, for $4^{\text{th}} K\pi$ bin, positive kaons. The weights are normalised w.r.t. ξ_{00}.

	k	2011	2012	abs. difference (σ)
1	00	+1.0000 ± 0.0000	+1.0000 ± 0.0000	+0.0000 ± 0.0000 (+0.0 σ)
2	($\parallel\parallel$)	+1.4757 ± 0.0381	+1.4851 ± 0.0406	+0.0094 ± 0.0557 (+0.2 σ)
3	($\perp\perp$)	+1.4837 ± 0.0394	+1.5136 ± 0.0420	+0.0298 ± 0.0576 (+0.5 σ)
4	($\parallel\perp$)	-0.0242 ± 0.0256	+0.0011 ± 0.0256	+0.0253 ± 0.0362 (+0.7 σ)
5	(0 $\parallel$)	-0.0135 ± 0.0146	+0.0112 ± 0.0157	+0.0247 ± 0.0214 (+1.2 σ)
6	(0 $\perp$)	+0.0025 ± 0.0137	+0.0164 ± 0.0142	+0.0138 ± 0.0198 (+0.7 σ)
7	SS	+1.2726 ± 0.0241	+1.2563 ± 0.0250	-0.0164 ± 0.0347 (-0.5 σ)
8	(S$\parallel$)	-0.0711 ± 0.0224	-0.0287 ± 0.0236	+0.0424 ± 0.0325 (+1.3 σ)
9	(S$\perp$)	+0.0340 ± 0.0208	+0.0251 ± 0.0220	-0.0090 ± 0.0303 (-0.3 σ)
10	S0	-0.7038 ± 0.0347	-0.6836 ± 0.0361	+0.0202 ± 0.0501 (+0.4 σ)

C.4 Convergence of the iterative procedure

Table C.11: Corrected angular acceptance weights for the simulated samples after each iteration. $1^{\text{st}} K\pi$ bin, positive kaons. The upper half of the table shows the value of each normalisation weight after each iteration. The iteration number is denoted by the column on the right. The two middle rows show the statistical uncertainty on each normalisation weight and the significance of its change defined as $(\xi_k^{\text{uncorr}} - \xi_k^{\text{final}})/\sigma_k^{\text{final}}$, respectivelly. The lower half of the table shows the change on the value of each normalisation weight after each iteration divided by its statistical error. This essentially shows the convergence of each weight. The normalisation weights converge when the changes gradually tend to zero. All the normalisation weights are normalised with respect to ξ_{00}.

	2 ($\parallel\parallel$)	3 ($\perp\perp$)	4 ($\parallel\perp$)	5 (0 $\parallel$)	6 (0 $\perp$)	7 (SS)	8 (S$\parallel$)	9 (S$\perp$)	10 (S0)
0	+1.3666	+1.3759	+0.0329	-0.0012	+0.0110	+1.1822	-0.0380	-0.0295	-0.8761
1	+1.3842	+1.3934	+0.0350	+0.0028	+0.0092	+1.1929	-0.0418	-0.0293	-0.9053
2	+1.3812	+1.3901	+0.0347	+0.0030	+0.0095	+1.1911	-0.0420	-0.0291	-0.9222
3	+1.3803	+1.3891	+0.0346	+0.0030	+0.0096	+1.1905	-0.0420	-0.0291	-0.9262
4	+1.3797	+1.3885	+0.0345	+0.0030	+0.0096	+1.1902	-0.0420	-0.0291	-0.9280
5	+1.3794	+1.3882	+0.0345	+0.0030	+0.0096	+1.1900	-0.0420	-0.0291	-0.9287
σ	+0.0290	+0.0299	+0.0190	+0.0116	+0.0107	+0.0180	+0.0173	+0.0160	+0.0241
diff/σ	+0.45	+0.42	+0.09	+0.37	-0.13	+0.44	-0.24	+0.03	-2.14
1	+0.623	+0.599	+0.113	+0.345	-0.167	+0.614	-0.225	+0.011	-1.187
2	-0.105	-0.110	-0.015	+0.016	+0.024	-0.103	-0.009	+0.011	-0.682
3	-0.031	-0.033	-0.005	+0.004	+0.006	-0.031	-0.002	+0.003	-0.168
4	-0.020	-0.021	-0.002	+0.002	+0.002	-0.020	-0.000	+0.001	-0.072
5	-0.010	-0.011	-0.001	+0.001	+0.001	-0.010	-0.000	+0.000	-0.031

Table C.12: Corrected angular acceptance weights after each iteration. $2^{\text{nd}} K\pi$ bin, positive kaons.

	2 ($\parallel\parallel$)	3 ($\perp\perp$)	4 ($\parallel\perp$)	5 (0 $\parallel$)	6 (0 $\perp$)	7 (SS)	8 (S$\parallel$)	9 (S$\perp$)	10 (S0)
0	+1.4100	+1.4396	+0.0090	-0.0112	-0.0010	+1.2220	-0.0332	+0.0018	-0.8663
1	+1.4086	+1.4386	+0.0081	-0.0101	-0.0025	+1.2211	-0.0320	+0.0002	-0.8822
2	+1.4053	+1.4352	+0.0081	-0.0101	-0.0025	+1.2191	-0.0321	+0.0002	-0.8930
3	+1.4035	+1.4334	+0.0080	-0.0101	-0.0025	+1.2180	-0.0321	+0.0002	-0.8978
4	+1.4025	+1.4323	+0.0080	-0.0101	-0.0025	+1.2174	-0.0321	+0.0002	-0.8999
5	+1.4020	+1.4318	+0.0080	-0.0101	-0.0025	+1.2171	-0.0321	+0.0002	-0.9009
σ	+0.0149	+0.0156	+0.0099	+0.0059	+0.0055	+0.0094	+0.0088	+0.0082	+0.0127
diff/σ	-0.54	-0.50	-0.10	+0.19	-0.26	-0.52	+0.13	-0.20	-2.69
1	-0.096	-0.063	-0.090	+0.190	-0.277	-0.090	+0.135	-0.204	-1.236
2	-0.222	-0.217	-0.007	+0.000	+0.008	-0.212	-0.002	+0.004	-0.835
3	-0.123	-0.120	-0.003	+0.001	+0.003	-0.118	-0.000	+0.002	-0.375
4	-0.068	-0.067	-0.002	+0.001	+0.001	-0.066	+0.000	+0.001	-0.168
5	-0.035	-0.034	-0.001	+0.000	+0.001	-0.034	+0.000	+0.000	-0.077

Table C.13: Corrected angular acceptance weights after each iteration. $3^{\text{rd}} K\pi$ bin, positive kaons.

	2 (||||)	3 ($\perp\perp$)	4 (||$\perp$)	5 (0 ||)	6 (0 $\perp$)	7 (SS)	8 (S||)	9 (S$\perp$)	10 (S0)
0	+1.4443	+1.4624	-0.0064	-0.0173	-0.0015	+1.2420	-0.0255	-0.0019	-0.8028
1	+1.4446	+1.4625	-0.0065	-0.0155	-0.0014	+1.2421	-0.0237	-0.0019	-0.8404
2	+1.4377	+1.4553	-0.0066	-0.0153	-0.0014	+1.2377	-0.0236	-0.0019	-0.8572
3	+1.4341	+1.4516	-0.0066	-0.0153	-0.0014	+1.2355	-0.0236	-0.0019	-0.8647
4	+1.4323	+1.4496	-0.0066	-0.0152	-0.0014	+1.2343	-0.0235	-0.0020	-0.8683
5	+1.4313	+1.4486	-0.0066	-0.0152	-0.0014	+1.2337	-0.0235	-0.0020	-0.8700
σ	+0.0152	+0.0158	+0.0099	+0.0060	+0.0055	+0.0095	+0.0090	+0.0083	+0.0129
diff/σ	-0.85	-0.87	-0.02	+0.35	+0.00	-0.87	+0.22	-0.01	-5.01
1	+0.022	+0.009	-0.018	+0.304	+0.006	+0.014	+0.207	+0.002	-2.798
2	-0.449	-0.454	-0.003	+0.027	-0.002	-0.458	+0.008	-0.005	-1.274
3	-0.232	-0.235	-0.001	+0.012	-0.001	-0.237	+0.005	-0.002	-0.583
4	-0.123	-0.125	-0.000	+0.006	-0.000	-0.126	+0.003	-0.001	-0.278
5	-0.061	-0.062	-0.000	+0.003	-0.000	-0.063	+0.001	-0.000	-0.131

Table C.14: Corrected angular acceptance weights after each iteration. $4^{\text{th}} K\pi$ bin, positive kaons.

	2 (||||)	3 ($\perp\perp$)	4 (||$\perp$)	5 (0 ||)	6 (0 $\perp$)	7 (SS)	8 (S||)	9 (S$\perp$)	10 (S0)
0	+1.4802	+1.4981	+0.0120	-0.0016	-0.0092	+1.2648	-0.0507	+0.0297	-0.6941
1	+1.4945	+1.5122	+0.0158	+0.0043	-0.0105	+1.2753	-0.0484	+0.0282	-0.7533
2	+1.4853	+1.5024	+0.0156	+0.0045	-0.0105	+1.2693	-0.0484	+0.0281	-0.7748
3	+1.4802	+1.4970	+0.0155	+0.0045	-0.0105	+1.2659	-0.0484	+0.0280	-0.7850
4	+1.4775	+1.4942	+0.0155	+0.0045	-0.0105	+1.2642	-0.0484	+0.0280	-0.7898
5	+1.4762	+1.4929	+0.0154	+0.0045	-0.0105	+1.2633	-0.0484	+0.0280	-0.7921
σ	+0.0281	+0.0290	+0.0184	+0.0109	+0.0100	+0.0176	+0.0165	+0.0152	+0.0242
diff/σ	-0.14	-0.18	+0.19	+0.58	-0.14	-0.08	+0.14	-0.12	-3.92
1	+0.512	+0.489	+0.207	+0.559	-0.136	+0.609	+0.146	-0.100	-2.369
2	-0.323	-0.332	-0.009	+0.011	+0.000	-0.340	-0.003	-0.006	-0.863
3	-0.181	-0.186	-0.005	+0.004	+0.000	-0.191	-0.000	-0.005	-0.414
4	-0.093	-0.096	-0.002	+0.001	-0.000	-0.098	+0.000	-0.003	-0.198
5	-0.046	-0.047	-0.001	+0.001	-0.000	-0.048	+0.000	-0.001	-0.095

Table C.15: Corrected angular acceptance weights after each iteration. $1^{\text{st}} K\pi$ bin, negative kaons.

	2 (‖‖)	3 (⊥⊥)	4 (‖⊥)	5 (0 ‖)	6 (0 ⊥)	7 (SS)	8 (S‖)	9 (S⊥)	10 (S0)
0	+1.3878	+1.4212	-0.0094	-0.0039	-0.0034	+1.2260	-0.0361	+0.0114	-0.8714
1	+1.3650	+1.3944	-0.0076	-0.0019	-0.0022	+1.2127	-0.0382	+0.0088	-0.8721
2	+1.3637	+1.3927	-0.0075	-0.0017	-0.0023	+1.2118	-0.0384	+0.0087	-0.8908
3	+1.3632	+1.3921	-0.0074	-0.0017	-0.0023	+1.2114	-0.0384	+0.0087	-0.8953
4	+1.3628	+1.3916	-0.0074	-0.0016	-0.0023	+1.2111	-0.0384	+0.0087	-0.8972
5	+1.3626	+1.3913	-0.0074	-0.0016	-0.0023	+1.2110	-0.0384	+0.0087	-0.8980
σ	+0.0288	+0.0298	+0.0193	+0.0114	+0.0105	+0.0183	+0.0170	+0.0158	+0.0266
diff/σ	-0.87	-0.99	+0.10	+0.20	+0.10	-0.82	-0.14	-0.17	-1.05
1	-0.789	-0.886	+0.093	+0.177	+0.113	-0.722	-0.124	-0.160	-0.025
2	-0.044	-0.058	+0.008	+0.013	-0.011	-0.050	-0.009	-0.006	-0.687
3	-0.018	-0.021	+0.002	+0.003	-0.003	-0.019	-0.002	-0.002	-0.168
4	-0.015	-0.016	+0.001	+0.002	-0.001	-0.015	-0.001	-0.001	-0.071
5	-0.008	-0.009	+0.000	+0.001	-0.000	-0.009	-0.000	-0.000	-0.030

Table C.16: Corrected angular acceptance weights after each iteration. $2^{\text{nd}} K\pi$ bin, negative kaons.

	2 (‖‖)	3 (⊥⊥)	4 (‖⊥)	5 (0 ‖)	6 (0 ⊥)	7 (SS)	8 (S‖)	9 (S⊥)	10 (S0)
0	+1.4273	+1.4419	-0.0082	-0.0143	+0.0089	+1.2391	-0.0394	-0.0086	-0.8272
1	+1.4112	+1.4270	-0.0090	-0.0134	+0.0096	+1.2291	-0.0371	-0.0077	-0.8601
2	+1.4082	+1.4239	-0.0090	-0.0132	+0.0097	+1.2271	-0.0370	-0.0076	-0.8709
3	+1.4065	+1.4222	-0.0090	-0.0131	+0.0097	+1.2260	-0.0369	-0.0076	-0.8757
4	+1.4056	+1.4212	-0.0090	-0.0131	+0.0097	+1.2253	-0.0369	-0.0076	-0.8779
5	+1.4051	+1.4207	-0.0090	-0.0131	+0.0097	+1.2250	-0.0369	-0.0076	-0.8789
σ	+0.0149	+0.0155	+0.0098	+0.0058	+0.0055	+0.0094	+0.0088	+0.0082	+0.0126
diff/σ	-1.48	-1.36	-0.08	+0.21	+0.15	-1.48	+0.29	+0.11	-3.95
1	-1.074	-0.954	-0.083	+0.165	+0.133	-1.054	+0.263	+0.110	-2.513
2	-0.205	-0.202	+0.001	+0.029	+0.010	-0.213	+0.014	+0.002	-0.843
3	-0.113	-0.112	+0.001	+0.012	+0.004	-0.118	+0.007	+0.000	-0.378
4	-0.063	-0.062	+0.000	+0.005	+0.001	-0.065	+0.004	+0.000	-0.169
5	-0.032	-0.032	+0.000	+0.002	+0.001	-0.033	+0.002	-0.000	-0.078

Table C.17: Corrected angular acceptance weights after each iteration. $3^{\text{rd}} K\pi$ bin, negative kaons.

	2 (||||)	3 ($\perp\perp$)	4 (||$\perp$)	5 (0 ||)	6 (0 $\perp$)	7 (SS)	8 (S||)	9 (S$\perp$)	10 (S0)
0	+1.4478	+1.4631	+0.0134	-0.0123	+0.0019	+1.2535	-0.0383	+0.0060	-0.7992
1	+1.4428	+1.4577	+0.0143	-0.0103	+0.0022	+1.2506	-0.0372	+0.0057	-0.8426
2	+1.4363	+1.4510	+0.0143	-0.0101	+0.0021	+1.2464	-0.0370	+0.0055	-0.8596
3	+1.4329	+1.4474	+0.0144	-0.0100	+0.0020	+1.2442	-0.0369	+0.0054	-0.8673
4	+1.4311	+1.4456	+0.0144	-0.0100	+0.0020	+1.2430	-0.0368	+0.0054	-0.8709
5	+1.4302	+1.4446	+0.0144	-0.0099	+0.0020	+1.2425	-0.0368	+0.0054	-0.8726
σ	+0.0153	+0.0158	+0.0101	+0.0060	+0.0056	+0.0096	+0.0091	+0.0084	+0.0130
diff/σ	-1.15	-1.16	+0.09	+0.40	+0.01	-1.14	+0.17	-0.07	-5.41
1	-0.329	-0.341	+0.084	+0.339	+0.051	-0.296	+0.122	-0.033	-3.196
2	-0.422	-0.424	+0.005	+0.033	-0.023	-0.435	+0.025	-0.021	-1.282
3	-0.220	-0.221	+0.002	+0.014	-0.011	-0.227	+0.013	-0.009	-0.584
4	-0.117	-0.118	+0.001	+0.007	-0.005	-0.121	+0.007	-0.004	-0.278
5	-0.058	-0.059	+0.000	+0.003	-0.003	-0.060	+0.003	-0.002	-0.131

Table C.18: Corrected angular acceptance weights after each iteration. $4^{\text{th}} K\pi$ bin, negative kaons.

	2 (||||)	3 ($\perp\perp$)	4 (||$\perp$)	5 (0 ||)	6 (0 $\perp$)	7 (SS)	8 (S||)	9 (S$\perp$)	10 (S0)
0	+1.4670	+1.4933	+0.0110	-0.0008	+0.0062	+1.2673	-0.0521	-0.0100	-0.7577
1	+1.4627	+1.4865	+0.0104	+0.0018	+0.0056	+1.2658	-0.0507	-0.0070	-0.7988
2	+1.4538	+1.4773	+0.0102	+0.0023	+0.0054	+1.2602	-0.0502	-0.0073	-0.8201
3	+1.4488	+1.4721	+0.0101	+0.0025	+0.0053	+1.2570	-0.0500	-0.0074	-0.8301
4	+1.4463	+1.4695	+0.0101	+0.0026	+0.0053	+1.2554	-0.0499	-0.0075	-0.8348
5	+1.4450	+1.4682	+0.0101	+0.0027	+0.0052	+1.2546	-0.0498	-0.0075	-0.8370
σ	+0.0273	+0.0283	+0.0176	+0.0108	+0.0096	+0.0172	+0.0162	+0.0147	+0.0232
diff/σ	-0.81	-0.89	-0.05	+0.32	-0.10	-0.74	+0.14	+0.17	-3.28
1	-0.156	-0.241	-0.034	+0.233	-0.064	-0.090	+0.090	+0.203	-1.695
2	-0.323	-0.321	-0.010	+0.048	-0.018	-0.321	+0.027	-0.020	-0.892
3	-0.182	-0.180	-0.004	+0.021	-0.010	-0.182	+0.014	-0.007	-0.423
4	-0.094	-0.093	-0.002	+0.010	-0.005	-0.094	+0.007	-0.003	-0.202
5	-0.046	-0.046	-0.001	+0.005	-0.002	-0.046	+0.003	-0.002	-0.096

Table C.19: Physics results after each iteration. The initial fit result using uncorrected normalisation weights is the one labeled as 0. The last column shows the difference in σ between the last iteration fit (column 5) and the initial one (column 0). The column before the last one shows the difference in σ between the last iteration (column 5) and the one before (column 4). The table points out that at each itearation step the change in the physics parameters converge to a certain value, which is the desired behaviour.

Parameter	0	1	2	3	4	5	diff / σ_{last}	diff / σ_{tot}
$\lvert A_0\rvert^2$	+0.5529	+0.5546	+0.5548	+0.5546	+0.5544	+0.5544 ± 0.0018	+0.0000	+0.8333
δ_{S1}	+3.1497	+3.1675	+3.1754	+3.1766	+3.1770	+3.1772 ± 0.0698	+0.0029	+0.4457
δ_{S2}	+2.5337	+2.4951	+2.4774	+2.4688	+2.4649	+2.4631 ± 0.0453	-0.0398	-1.7053
δ_{S3}	+1.7068	+1.6120	+1.5678	+1.5470	+1.5373	+1.5328 ± 0.0182	-0.2500	-10.1754
δ_{S4}	+1.3852	+1.3132	+1.2823	+1.2678	+1.2607	+1.2575 ± 0.0198	-0.1616	-7.1742
$\delta_{\parallel} - \delta_0$	-2.9315	-2.9427	-2.9479	-2.9504	-2.9516	-2.9522 ± 0.0120	-0.0504	-1.7542
$\lvert A_{\perp}\rvert^2$	+0.2222	+0.2217	+0.2217	+0.2218	+0.2219	+0.2219 ± 0.0021	+0.0000	-0.1429
$\delta_{\perp} - \delta_0$	+2.9319	+2.9279	+2.9256	+2.9244	+2.9239	+2.9236 ± 0.0097	-0.0313	-0.8646
y^{2011}_{bin1}	+7195.8738	+7195.8737	+7195.8737	+7195.8737	+7195.8737	+7195.8737 ± 84.7958	+0.0000	-0.0000
y^{2011}_{bin2}	+26516.1665	+26516.1665	+26516.1665	+26516.1665	+26516.1665	+26516.1665 ± 162.9504	+0.0000	+0.0000
y^{2011}_{bin3}	+23801.3486	+23801.3486	+23801.3486	+23801.3486	+23801.3486	+23801.3486 ± 154.2746	+0.0000	+0.0000
y^{2011}_{bin4}	+7519.1705	+7519.1705	+7519.1705	+7519.1705	+7519.1705	+7519.1705 ± 86.7079	+0.0000	+0.0000
y^{2012}_{bin1}	+15251.3720	+15251.3720	+15251.3719	+15251.3719	+15251.3719	+15251.3719 ± 123.4931	+0.0000	-0.0000
y^{2012}_{bin2}	+56345.7174	+56345.7173	+56345.7173	+56345.7173	+56345.7178	+56345.7173 ± 237.3697	-0.0000	-0.0000
y^{2012}_{bin3}	+50422.9949	+50422.9949	+50422.9949	+50422.9949	+50422.9951	+50422.9949 ± 224.5478	-0.0000	+0.0000
y^{2012}_{bin4}	+15879.3672	+15879.3672	+15879.3672	+15879.3672	+15879.3672	+15879.3672 ± 125.9676	+0.0000	+0.0000
F_{S1}	+0.0996	+0.0879	+0.0852	+0.0842	+0.0838	+0.0836 ± 0.0040	-0.0500	-3.7209
F_{S2}	+0.0287	+0.0252	+0.0237	+0.0232	+0.0229	+0.0228 ± 0.0019	-0.0526	-2.9500
F_{S3}	+0.0355	+0.0328	+0.0322	+0.0320	+0.0320	+0.0320 ± 0.0028	+0.0000	-1.2069
F_{S4}	+0.1119	+0.1058	+0.1061	+0.1062	+0.1062	+0.1063 ± 0.0069	+0.0145	-0.7671

C.5 Normalisation weights

Table C.20: Corrected normalisation weights for the simulated samples. $1^{\text{st}}K\pi$ bin.

	k	ξ_k/ξ_1 for K^+	ξ_k/ξ_1 for K^-
1	(0 $\parallel$)	$+0.0030 \pm 0.0116$	-0.0016 ± 0.0114
2	(SS)	$+1.1900 \pm 0.0180$	$+1.2110 \pm 0.0183$
3	(S0)	-0.9287 ± 0.0241	-0.8980 ± 0.0266
4	(00)	$+1.0000$	$+1.0000$
5	($\parallel\parallel$)	$+1.3794 \pm 0.0290$	$+1.3626 \pm 0.0288$
6	(S$\perp$)	-0.0291 ± 0.0160	$+0.0087 \pm 0.0158$
7	(S$\parallel$)	-0.0420 ± 0.0173	-0.0384 ± 0.0170
8	($\parallel\perp$)	-0.0345 ± 0.0190	$+0.0074 \pm 0.0193$
9	($\perp\perp$)	$+1.3882 \pm 0.0299$	$+1.3913 \pm 0.0298$
10	(0 $\perp$)	-0.0096 ± 0.0107	$+0.0023 \pm 0.0105$

Table C.21: Corrected normalisation weights for the simulated samples. $2^{\text{nd}}K\pi$ bin.

	k	ξ_k/ξ_1 for K^+	ξ_k/ξ_1 for K^-
1	(0 $\parallel$)	-0.0101 ± 0.0059	-0.0131 ± 0.0058
2	(SS)	$+1.2171 \pm 0.0094$	$+1.2250 \pm 0.0094$
3	(S0)	-0.9009 ± 0.0127	-0.8789 ± 0.0126
4	(00)	$+1.0000$	$+1.0000$
5	($\parallel\parallel$)	$+1.4020 \pm 0.0149$	$+1.4051 \pm 0.0149$
6	(S$\perp$)	$+0.0002 \pm 0.0082$	-0.0076 ± 0.0082
7	(S$\parallel$)	-0.0321 ± 0.0088	-0.0369 ± 0.0088
8	($\parallel\perp$)	-0.0080 ± 0.0099	$+0.0090 \pm 0.0098$
9	($\perp\perp$)	$+1.4318 \pm 0.0156$	$+1.4207 \pm 0.0155$
10	(0 $\perp$)	$+0.0025 \pm 0.0055$	-0.0097 ± 0.0055

Table C.22: Corrected normalisation weights for the simulated samples. $3^{\text{rd}}K\pi$ bin.

	k	ξ_k/ξ_1 for K^+	ξ_k/ξ_1 for K^-
1	(0 $\parallel$)	-0.0152 ± 0.0060	-0.0099 ± 0.0060
2	(SS)	$+1.2337 \pm 0.0095$	$+1.2425 \pm 0.0096$
3	(S0)	-0.8700 ± 0.0129	-0.8726 ± 0.0130
4	(00)	$+1.0000 \pm 0.0000$	$+1.0000 \pm 0.0000$
5	($\parallel\parallel$)	$+1.4313$	$+1.4302$
6	(S$\perp$)	-0.0020 ± 0.0083	$+0.0054 \pm 0.0084$
7	(S$\parallel$)	-0.0235 ± 0.0090	-0.0368 ± 0.0091
8	($\parallel\perp$)	$+0.0066 \pm 0.0099$	-0.0144 ± 0.0101
9	($\perp\perp$)	$+1.4486 \pm 0.0158$	$+1.4446 \pm 0.0158$
10	(0 $\perp$)	$+0.0014 \pm 0.0055$	-0.0020 ± 0.0056

Table C.23: Corrected normalisation weights for the simulated samples. 4^{th} $K\pi$ bin.

k		ξ_k/ξ_1 for K^+	ξ_k/ξ_1 for K^-
1	(0 $\parallel$)	$+0.0045 \pm 0.0109$	$+0.0027 \pm 0.0108$
2	(SS)	$+1.2633 \pm 0.0176$	$+1.2546 \pm 0.0172$
3	(S0)	-0.7921 ± 0.0242	-0.8370 ± 0.0232
4	(00)	$+1.0000$	$+1.0000$
5	($\parallel\parallel$)	$+1.4762 \pm 0.0281$	$+1.4450 \pm 0.0273$
6	(S$\perp$)	$+0.0280 \pm 0.0152$	-0.0075 ± 0.0147
7	(S$\parallel$)	-0.0484 ± 0.0165	-0.0498 ± 0.0162
8	($\parallel\perp$)	-0.0154 ± 0.0184	-0.0101 ± 0.0176
9	($\perp\perp$)	$+1.4929 \pm 0.0290$	$+1.4682 \pm 0.0283$
10	(0 $\perp$)	$+0.0105 \pm 0.0100$	-0.0052 ± 0.0096

C.6 Angular acceptance plots

Figure C.1: 2D projections of the 3D efficiency function $1^{\text{st}} K\pi$ bin, positive kaons.

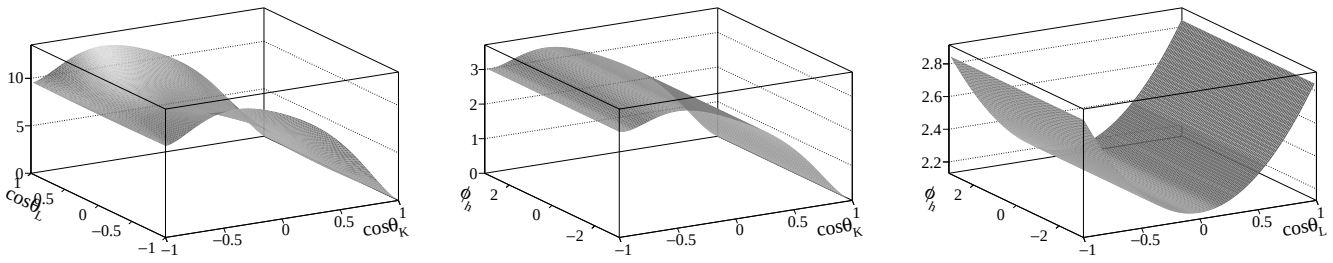

Figure C.2: 2D projections of the 3D efficiency function $2^{\text{ned}} K\pi$ bin, positive kaons.

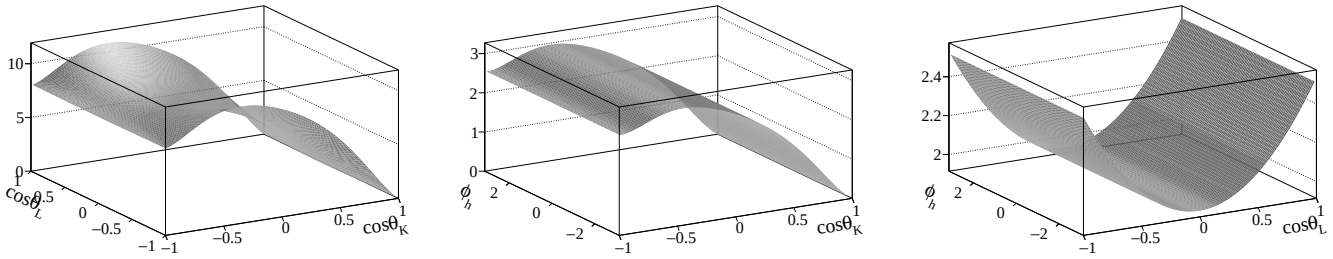

Figure C.3: 2D projections of the 3D efficiency function $3^{\text{rd}} K\pi$ bin, positive kaons.

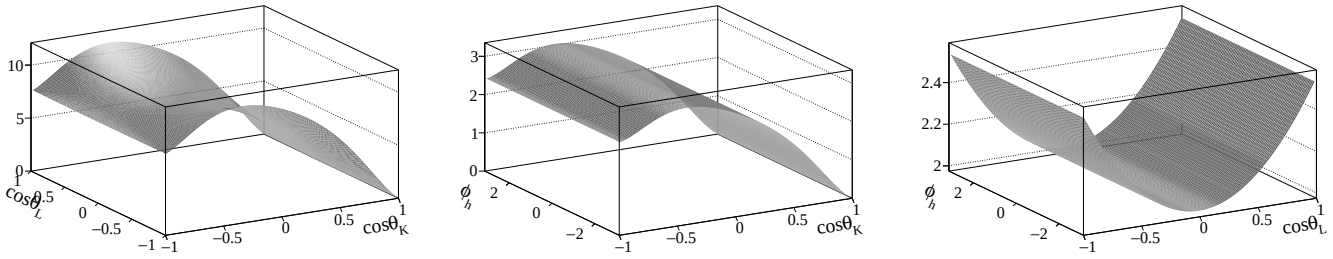

Figure C.4: 2D projections of the 3D efficiency function $4^{\text{th}} K\pi$ bin, positive kaons.

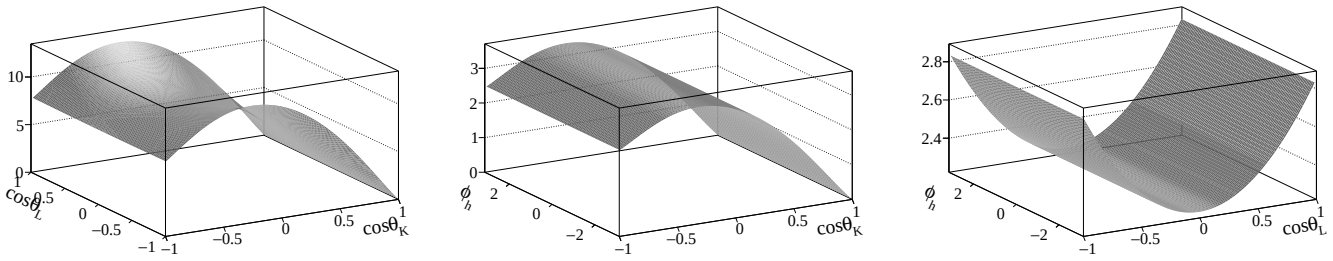

Figure C.5: 2D projections of the 3D efficiency function $1^{\text{st}} K\pi$ bin, negative kaons.

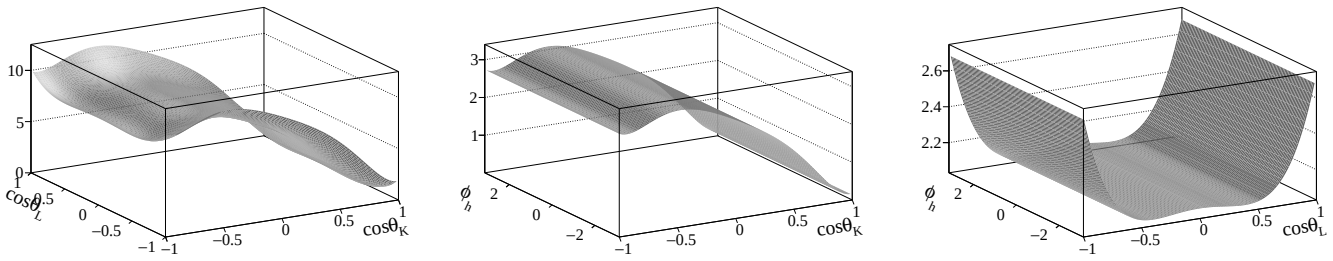

Figure C.6: 2D projections of the 3D efficiency function $2^{\text{ned}} K\pi$ bin, negative kaons.

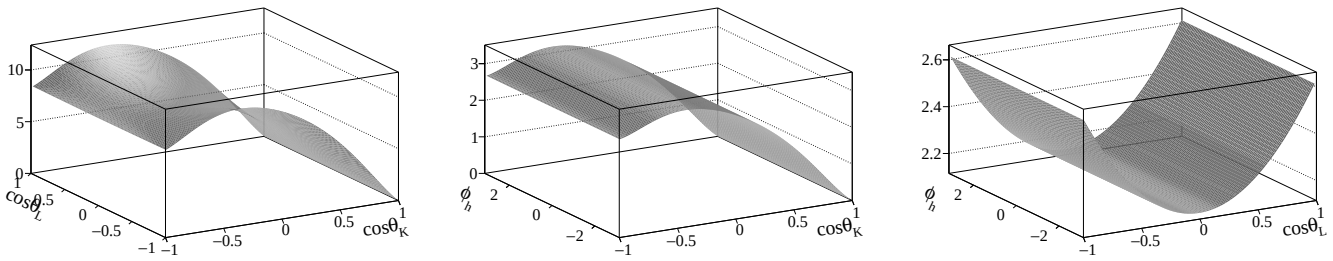

Figure C.7: 2D projections of the 3D efficiency function $3^{\text{rd}} K\pi$ bin, negative kaons.

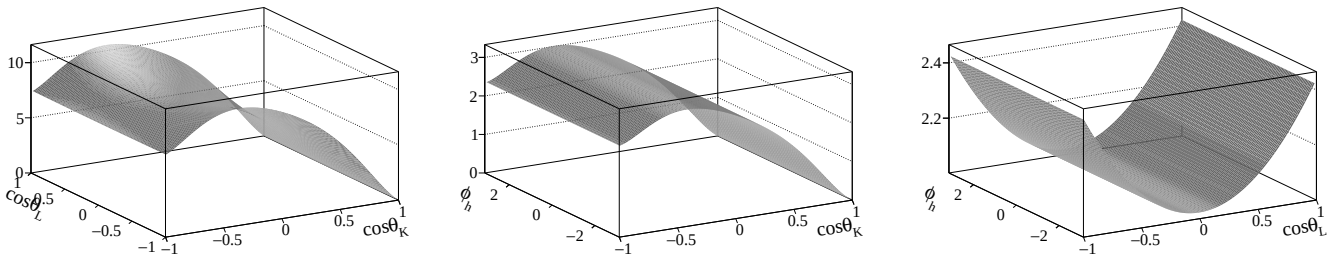

Figure C.8: 2D projections of the 3D efficiency function $4^{\text{th}} K\pi$ bin, negative kaons.

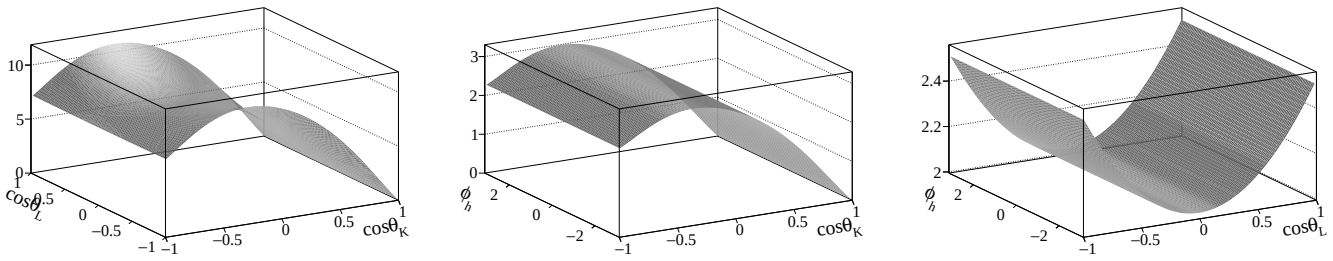

Appendix D

Measurement of $\mathcal{B}(B_s^0 \to J/\psi \overline{K}^{*0})$

D.1 Correlated weighted average

The branching fractions (4.59) and (4.63) can be written in the following way,

$$\mathcal{B}(B_s^0 \to J/\psi \overline{K}^{*0})_d = \alpha X_d, \tag{D.1}$$

$$\mathcal{B}(B_s^0 \to J/\psi \overline{K}^{*0})_\phi = \alpha X_\phi, \tag{D.2}$$

where α is a common factor given by

$$\alpha = N_{B_s^0 \to J/\psi K\pi} \times \frac{f_d}{f_s}. \tag{D.3}$$

The two different factors X_d and X_ϕ are

$$X_d = \frac{1}{N_{B^0 \to J/\psi K\pi}} \times \frac{\varepsilon^{MC}_{B^0 \to J/\psi K^{*0}}}{\varepsilon^{MC}_{B_s^0 \to J/\psi \overline{K}^{*0}}} \times \frac{\kappa_{B^0 \to J/\psi K^{*0}}}{\kappa_{B_s^0 \to J/\psi \overline{K}^{*0}}} \times \mathcal{B}(B^0 \to J/\psi K^{*0}), \tag{D.4}$$

$$\begin{aligned} X_\phi &= \frac{\mathcal{B}(\phi \to K^+K^-)}{\mathcal{B}(\overline{K}^{*0} \to K^-\pi^+)} \times \frac{1}{N_{B_s^0 \to J/\psi K^+K^-}} \times \frac{\varepsilon^{MC}_{B_s^0 \to J/\psi\phi}}{\varepsilon^{MC}_{B_s^0 \to J/\psi \overline{K}^{*0}}} \times \frac{\kappa_{B_s^0 \to J/\psi\phi}}{\kappa_{B_s^0 \to J/\psi \overline{K}^{*0}}} \times \\ &\times \frac{f_s}{f_d} \mathcal{B}(B_s^0 \to J/\psi\phi). \end{aligned} \tag{D.5}$$

There are two sources of correlations between X_d and X_ϕ:

- A correlation between $\kappa_{B^0 \to J/\psi K^{*0}}$ and $\kappa_{B_s^0 \to J/\psi \overline{K}^{*0}}$, which is taken into account calculating a correlation factor between the ratios $\frac{\kappa_{B^0 \to J/\psi K^{*0}}}{\kappa_{B_s^0 \to J/\psi \overline{K}^{*0}}}$ and $\frac{\kappa_{B_s^0 \to J/\psi\phi}}{\kappa_{B_s^0 \to J/\psi \overline{K}^{*0}}}$.

- A correlation between $\frac{\varepsilon^{MC}_{B^0 \to J/\psi K^{*0}}}{\varepsilon^{MC}_{B_s^0 \to J/\psi \overline{K}^{*0}}}$ and $\frac{\varepsilon^{MC}_{B_s^0 \to J/\psi\phi}}{\varepsilon^{MC}_{B_s^0 \to J/\psi \overline{K}^{*0}}}$, due to $\varepsilon^{MC}_{B_s^0 \to J/\psi \overline{K}^{*0}}$. These efficiencies cannot be treated separately (hence the ratios) because of the systematic uncertainty due to PIDCalib corrections (see Chapter 4.5.1). In consequence, both ratios are considered 100% correlated.

In the calculation of X_ϕ, $\frac{f_s}{f_d}\mathcal{B}(B_s^0 \to J/\psi\phi)$ instead of $\mathcal{B}(B_s^0 \to J/\psi\phi)$ is considered in order to avoid correlations due to the common factor α. Thus, both $\mathcal{B}(B_s^0 \to J/\psi\overline{K}^{*0})_d$ and $\mathcal{B}(B_s^0 \to J/\psi\overline{K}^{*0})_\phi$ can be combined into a weighted average $\mathcal{B}(B_s^0 \to J/\psi\overline{K}^{*0})$ using the method of least squares,

$$\mathcal{B}(B_s^0 \to J/\psi\overline{K}^{*0}) = \alpha(wX_d + (1-w)X_\phi), \tag{D.6}$$

$$w = \frac{\sigma^2(X_\phi) - \rho\sigma(X_d)\sigma(X_\phi)}{\sigma^2(X_\phi) + \sigma^2(X_d) - 2\rho\sigma(X_d)\sigma(X_\phi)}, \tag{D.7}$$

where ρ is the total correlation factor between X_d and X_ϕ, and α is left as an uncorrelated common factor. The uncertainty for this weighted average can be calculated separately in terms of the statistical and systematic uncertainty sources,

$$\begin{aligned}\sigma_i^2(\mathcal{B}(B_s^0 \to J/\psi\overline{K}^{*0})) &= \Big[\frac{\mathcal{B}(B_s^0 \to J/\psi\overline{K}^{*0})}{\alpha}\sigma_i(\alpha)\Big]^2 + \\ &+ \alpha^2\frac{(1-\rho_i^2)\sigma_i^2(X_d)\sigma_i^2(X_\phi)}{\sigma_i^2(X_\phi) + \sigma_i^2(X_d) - 2\rho_i\sigma_i(X_d)\sigma_i(X_\phi)},\end{aligned} \tag{D.8}$$

where i = stat, syst. The non-diagonal terms of the covariance matrix, $\rho_i\sigma_i(X_d)\sigma_i(X_\phi)$, which contain the correlations, still need to be calculated. For this purpose, the two correlations described before are evaluated separately:

1. The correlation coefficient between the efficiency ratios was assumed to be 100% (henceforth, $\frac{\varepsilon^{MC}_{B^0 \to J/\psi K^{*0}}}{\varepsilon^{MC}_{B_s^0 \to J/\psi\overline{K}^{*0}}} = \varepsilon_{ds}$ and $\frac{\varepsilon^{MC}_{B_s^0 \to J/\psi\phi}}{\varepsilon^{MC}_{B_s^0 \to J/\psi\overline{K}^{*0}}} = \varepsilon_{\phi s}$ for simplicity), so the relative uncertainty of the product $\varepsilon_{ds}\varepsilon_{\phi s}$ can be written as

$$\frac{\sigma^2(\varepsilon_{ds}\varepsilon_{\phi s})}{(\varepsilon_{ds}\varepsilon_{\phi s})^2} = \frac{\sigma^2(\varepsilon_{ds})}{\varepsilon_{ds}^2} + \frac{\sigma^2(\varepsilon_{\phi s})}{\varepsilon_{\phi s}^2} + 2\frac{\sigma(\varepsilon_{ds})\sigma(\varepsilon_{\phi s})}{\varepsilon_{ds}\varepsilon_{\phi s}}. \tag{D.9}$$

2. The correlation factor between the κ ratios can be obtained in terms of one of the ratios and the individual κ factors. For simplicitly, the abbreviation $\kappa_{B_s^0 \to J/\psi\phi} = \kappa_\phi$, $\kappa_{B^0 \to J/\psi K^{*0}} = \kappa_d$, and $\kappa_{B_s^0 \to J/\psi\overline{K}^{*0}} = \kappa_s$ is used. Then,

$$\frac{\kappa_{B^0 \to J/\psi K^{*0}}}{\kappa_{B_s^0 \to J/\psi\phi}} = \frac{\kappa_{B^0 \to J/\psi K^{*0}}}{\kappa_{B_s^0 \to J/\psi\overline{K}^{*0}}}\left(\frac{\kappa_{B_s^0 \to J/\psi\phi}}{\kappa_{B_s^0 \to J/\psi\overline{K}^{*0}}}\right)^{-1} \implies \frac{\kappa_d}{\kappa_\phi} = \frac{(\kappa_d/\kappa_s)}{(\kappa_\phi/\kappa_s)}.$$

Therefore,

$$\frac{\sigma^2(\kappa_d/\kappa_\phi)}{(\kappa_d/\kappa_\phi)^2} = \frac{\sigma^2(\kappa_d/\kappa_s)}{(\kappa_d/\kappa_s)^2} + \frac{\sigma^2(\kappa_\phi/\kappa_s)}{(\kappa_\phi/\kappa_s)^2} - 2\frac{\sigma(\kappa_d/\kappa_s)\sigma(\kappa_\phi/\kappa_s)}{(\kappa_d/\kappa_s)(\kappa_\phi/\kappa_s)}\rho_{(\frac{\kappa_d}{\kappa_s},\frac{\kappa_\phi}{\kappa_s})}. \tag{D.10}$$

Taking into account that κ_ϕ and κ_d are uncorrelated, the previous expression can be also written as

$$\frac{\sigma^2(\kappa_d/\kappa_\phi)}{(\kappa_d/\kappa_\phi)^2} = \frac{\sigma^2(\kappa_d)}{\kappa_d^2} + \frac{\sigma^2(\kappa_\phi)}{\kappa_\phi^2}. \tag{D.11}$$

Similarly,

$$\frac{\sigma^2(\kappa_\phi/\kappa_s)}{(\kappa_\phi/\kappa_s)^2} = \frac{\sigma^2(\kappa_s)}{\kappa_s^2} + \frac{\sigma^2(\kappa_\phi)}{\kappa_\phi^2}. \tag{D.12}$$

Combining the three previous equations, the correlation between the κ ratios can be put now in terms of known quantities,

$$2\frac{\sigma(\kappa_d/\kappa_s)\sigma(\kappa_\phi/\kappa_s)}{(\kappa_d/\kappa_s)(\kappa_\phi/\kappa_s)}\rho_{(\frac{\kappa_d}{\kappa_s},\frac{\kappa_\phi}{\kappa_s})} = \frac{\sigma(\kappa_s)^2}{\kappa_s^2} - \frac{\sigma(\kappa_d)^2}{\kappa_d^2} + \frac{\sigma^2(\kappa_d/\kappa_s)}{(\kappa_d/\kappa_s)^2}. \tag{D.13}$$

Taking into account both sources of correlation, the correlation coefficient between X_d and X_ϕ can be obtained from the following relation[1],

$$\frac{\sigma_i(X_d)\sigma_i(X_\phi)}{X_d X_\phi}\rho_i = \frac{\sigma_i(\kappa_d/\kappa_s)\sigma_i(\kappa_\phi/\kappa_s)}{(\kappa_d/\kappa_s)(\kappa_\phi/\kappa_s)}\rho_{i(\frac{\kappa_d}{\kappa_s},\frac{\kappa_\phi}{\kappa_s})} + \frac{\sigma_i(\varepsilon_{ds})\sigma_i(\varepsilon_{\phi s})}{\varepsilon_{ds}\varepsilon_{\phi s}}. \tag{D.14}$$

Replacing the first term of the right hand side with (D.13), a final expression for $\rho_i\sigma_i(X_d)\sigma_i(X_\phi)$ can be obtained,

$$\rho_i\sigma_i(X_d)\sigma_i(X_\phi) = \frac{X_d X_\phi}{2}\left[\frac{\sigma_i^2(\kappa_s)}{\kappa_s^2} - \frac{\sigma_i^2(\kappa_d)}{\kappa_d^2} + \frac{\sigma_i^2(\kappa_d/\kappa_s)}{(\kappa_d/\kappa_s)^2} + 2\frac{\sigma_i(\varepsilon_{ds})\sigma_i(\varepsilon_{\phi s})}{\varepsilon_{ds}\varepsilon_{\phi s}}\right] \tag{D.15}$$

where i = stat, syst, or if the purpose is to calculate (D.7), i = total. Finally, the difference in production rates for the B^+B^- and $B^0\overline{B}^0$ pairs at the $\Upsilon(4S)$ resonance is also taken into account as an uncorrelated factor.

The values obtained for (D.6), (D.8) and (D.7) are, respectively (using as input the values presented in Chapter 4.5):

$$\begin{aligned}
\mathcal{B}(B_s^0 \to J/\psi\overline{K}^{*0}) &= 4.13745577504 \times 10^{-5}, && \text{(D.16)}\\
\sigma_{stat}(\mathcal{B}(B_s^0 \to J/\psi\overline{K}^{*0})) &= 1.77056679811 \times 10^{-6}, && \text{(D.17)}\\
\sigma_{syst}(\mathcal{B}(B_s^0 \to J/\psi\overline{K}^{*0})) &= 2.54663301208 \times 10^{-6}, && \text{(D.18)}\\
w &= 0.27972545803, && \text{(D.19)}
\end{aligned}$$

where the sources of statistical uncertainty are the yields and the κ ratios (which also have a systematic contribution). An additional uncertainty due to $\frac{fd}{fs}$, which can be directly calculated as $\mathcal{B}(B_s^0 \to J/\psi\overline{K}^{*0}) \times \frac{\sigma(f_d/f_s)}{f_d/f_s}$ since it is contained in the common factor α, is

$$\sigma_{\frac{fd}{fs}}(\mathcal{B}(B_s^0 \to J/\psi\overline{K}^{*0})) = 2.39620990832 \times 10^{-6}. \tag{D.20}$$

[1] If two measurements of the same observable are obtained through the expresions $y_1 = a_1 b_1$ and $y_2 = a_2 b_2$, where a_1 and b_1 are not correlated ($\rho_{a_1 b_1} = 0$), a_2 and b_2 are also not correlated ($\rho_{a_2 b_2} = 0$), and the only non-zero correlation coefficients are $\rho_{a_1 a_2}$ and $\rho_{b_1 b_2}$, then the following relation holds,

$$\frac{\rho_{y_1 y_2}\sigma_{y_1}\sigma_{y_2}}{y_1 y_2} = \frac{\rho_{a_1 a_2}\sigma_{a_1}\sigma_{a_2}}{a_1 a_2} + \frac{\rho_{b_1 b_2}\sigma_{b_1}\sigma_{b_2}}{b_1 b_2}.$$

All these numbers leads to a final expression (4.64),

$$\mathcal{B}(B_s^0 \to J/\psi \overline{K}^{*0}) = (4.14 \pm 0.18(\text{stat}) \pm 0.26(\text{syst}) \pm 0.24(\frac{f_d}{f_s})) \times 10^{-5}. \qquad \text{(D.21)}$$

D.2 Efficiencies obtained in simulation

Two contributions are evaluated to get the global efficiency:

- $\varepsilon_{\text{offline}}$ is the efficiency of the offline reconstruction cuts, including final selection cuts described in Chapter 4.1 for the normalisation to the $B^0 \to J/\psi K^{*0}$ channel, and those in Table 4.32 for the normalisation to the $B_s^0 \to J/\psi\phi$ mode. Efficiencies of particle identification cuts are corrected using the PIDCalib package, where a systematic due to the choice of a certain binning scheme for the PID calibration samples is taken into account.

- $\varepsilon_{\text{TRIG/SEL}}$ is the efficiency of the trigger for events that would be offline selected by final selection cuts. As stated in Chapter 4.1.3, this analysis is not restricted to any particular trigger line, i.e. an event should just pass at least one of the LHCb trigger lines.

Both efficiencies are computed separately for both magnet polarities to check for possible differences. A global efficiency, $\varepsilon_{\text{TOT/GEN}}$, is computed from these two contributions. These values are shown in Table D.1. The value of $\varepsilon_{\text{offline}}$ in $B_s^0 \to J/\psi\phi$ simulated data is roughly two times bigger than the corresponding value of the same efficiency in $B_s^0 \to J/\psi\overline{K}^{*0}$ simulated data. The largest source of difference lies in the combined event reconstruction and final selection cuts (including MC-*truth*) efficiency. In addition, a minor source of difference between the $B_s^0 \to J/\psi\overline{K}^{*0}$ and $B_s^0 \to J/\psi\phi$ efficiencies is coming from the cuts on particle identification variables of daughter hadrons. The ratio

Table D.1: Efficiencies calculated from simulation.

	Polarity	Year	$\varepsilon_{\text{offline}}$ (%)	$\varepsilon_{\text{TRIG/SEL}}$ (%)	$\varepsilon_{\text{TOT/GEN}}$ (%)
$B^0 \to J/\psi K^{*0}$	down	2011	4.065 ± 0.045	85.64 ± 0.22	3.481 ± 0.039
	up	2011	4.021 ± 0.048	85.59 ± 0.22	3.441 ± 0.042
	down	2012	3.762 ± 0.041	84.16 ± 0.25	3.166 ± 0.035
	up	2012	3.708 ± 0.042	83.92 ± 0.25	3.112 ± 0.036
$B_s^0 \to J/\psi\phi$	down	2011	8.239 ± 0.096	84.659 ± 0.075	6.975 ± 0.081
	up	2011	8.154 ± 0.096	84.624 ± 0.075	6.900 ± 0.081
	down	2012	7.631 ± 0.097	83.337 ± 0.081	6.360 ± 0.081
	up	2012	7.538 ± 0.096	83.490 ± 0.082	6.294 ± 0.081
$B_s^0 \to J/\psi\overline{K}^{*0}$	down	2011	4.369 ± 0.051	85.32 ± 0.30	3.728 ± 0.045
	up	2011	4.367 ± 0.059	85.49 ± 0.30	3.733 ± 0.052
	down	2012	4.075 ± 0.052	83.96 ± 0.33	3.421 ± 0.046
	up	2012	3.951 ± 0.056	84.09 ± 0.32	3.323 ± 0.049

of final efficiencies in simulation, ε_{TOT}, is, for 2011 (2012) conditions:

$$\frac{\varepsilon_{\text{TOT}}^{B^0 \to J/\psi K^{*0}}}{\varepsilon_{\text{TOT}}^{B_s^0 \to J/\psi \overline{K}^{*0}}} = 0.929 \pm 0.012 \ (0.927 \pm 0.012), \tag{D.22}$$

$$\frac{\varepsilon_{\rm TOT}^{B_s^0\to J/\psi\phi}}{\varepsilon_{\rm TOT}^{B_s^0\to J/\psi\overline{K}^{*0}}} = 1.991 \pm 0.025 \ (1.986 \pm 0.027), \tag{D.23}$$

where $\varepsilon_{\rm TOT}$ is obtained after data from both magnet polarities is multiplied by each MC generator efficiency $\varepsilon_{\rm GEN}$ and averaged taking into account the percentage of each polarity contained in the total sample: 61.01 $\pm$ 0.04 % of magnet down and (38.99 $\pm$ 0.04)% of magnet up for 2011 conditions, and (49.68 $\pm$ 0.02)% of magnet down and (50.32 $\pm$ 0.02)% of magnet up for 2012 conditions. These averaged efficiencies are shown in Table D.2.

Table D.2: Averaged global efficiencies computed from Table D.1.

	Year	$\varepsilon_{\rm GEN}$ (%)	$\varepsilon_{\rm TOT}$ (%)
$B^0 \to J/\psi K^{*0}$	2011	15.82 $\pm$ 0.16	0.5482 $\pm$ 0.0046
	2012	16.10 $\pm$ 0.16	0.5052 $\pm$ 0.0040
$B_s^0 \to J/\psi\phi$	2011	16.91 $\pm$ 0.17	1.1742 $\pm$ 0.0099
	2012	17.11 $\pm$ 0.17	1.0823 $\pm$ 0.0098
$B_s^0 \to J/\psi\overline{K}^{*0}$	2011	15.81 $\pm$ 0.16	0.5898 $\pm$ 0.0054
	2012	16.17 $\pm$ 0.16	0.5451 $\pm$ 0.0054

Appendix E

Angular plots

Figure E.1: Angular PDF plots on top of the fitted sWeighted data for $B_s^0 \to J/\psi \overline{K}^{*0}$. Blue solid: total. Blue dashed: P-wave + P-P interference. Green dotted: S-wave. Red dotted-dashed: S-P interference.

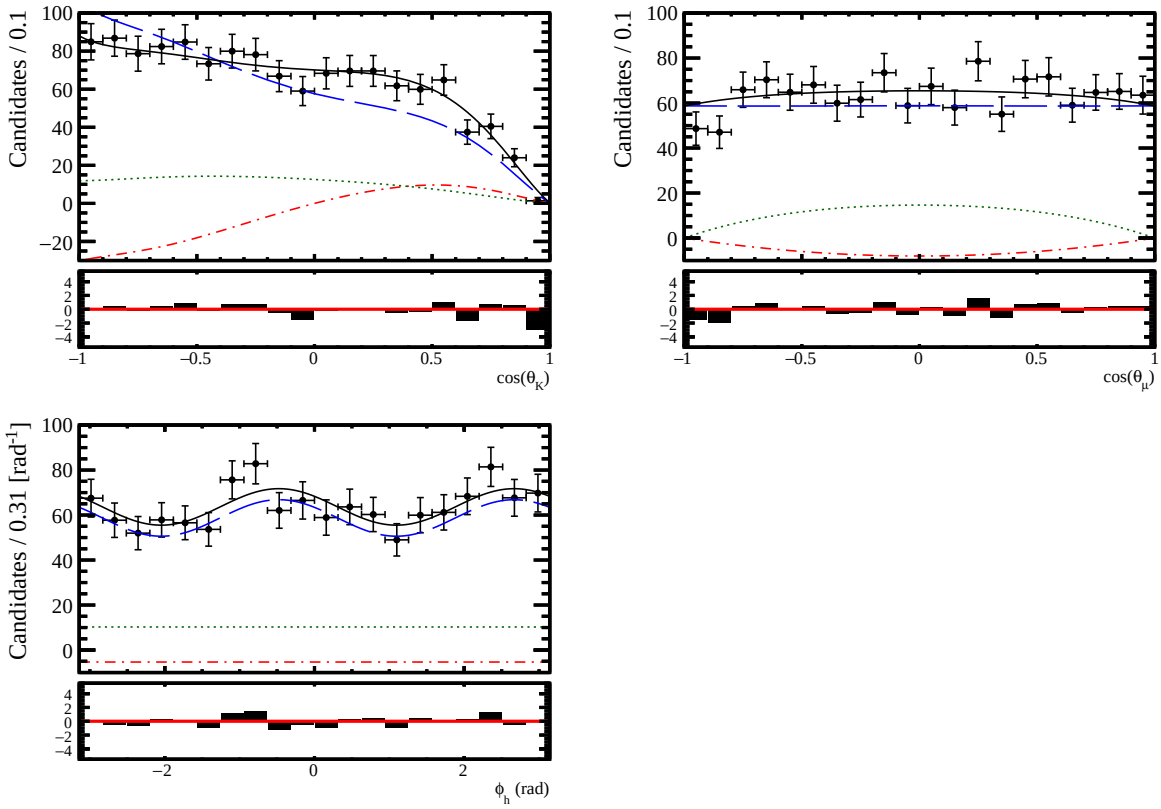

Figure E.2: Angular PDF plots on top of the fitted sWeighted data for $B_s^0 \to J/\psi \overline{K}^{*0}$ $m_{K\pi}$ bins 1 (top) and 2 (bottom). Blue solid: total. Blue dashed: P-wave + P-P interference. Green dotted: S-wave. Red dotted-dashed: S-P interference.

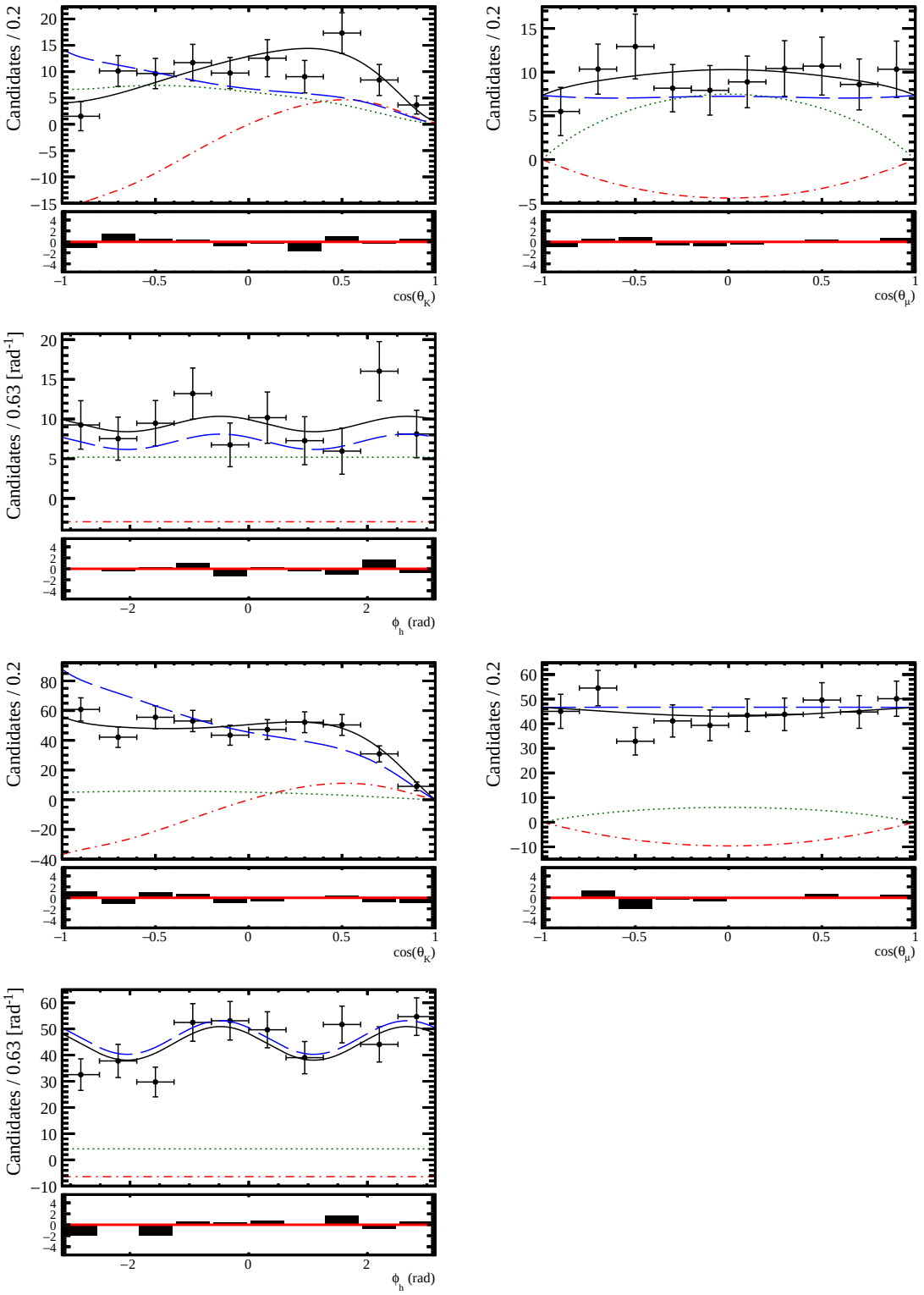

Figure E.3: Angular PDF plots on top of the fitted sWeighted data for $B_s^0 \to J/\psi \overline{K}^{*0}$ $m_{K\pi}$ bins 3 (top) and 4 (bottom). Blue solid: total. Blue dashed: P-wave + P-P interference. Green dotted: S-wave. Red dotted-dashed: S-P interference.

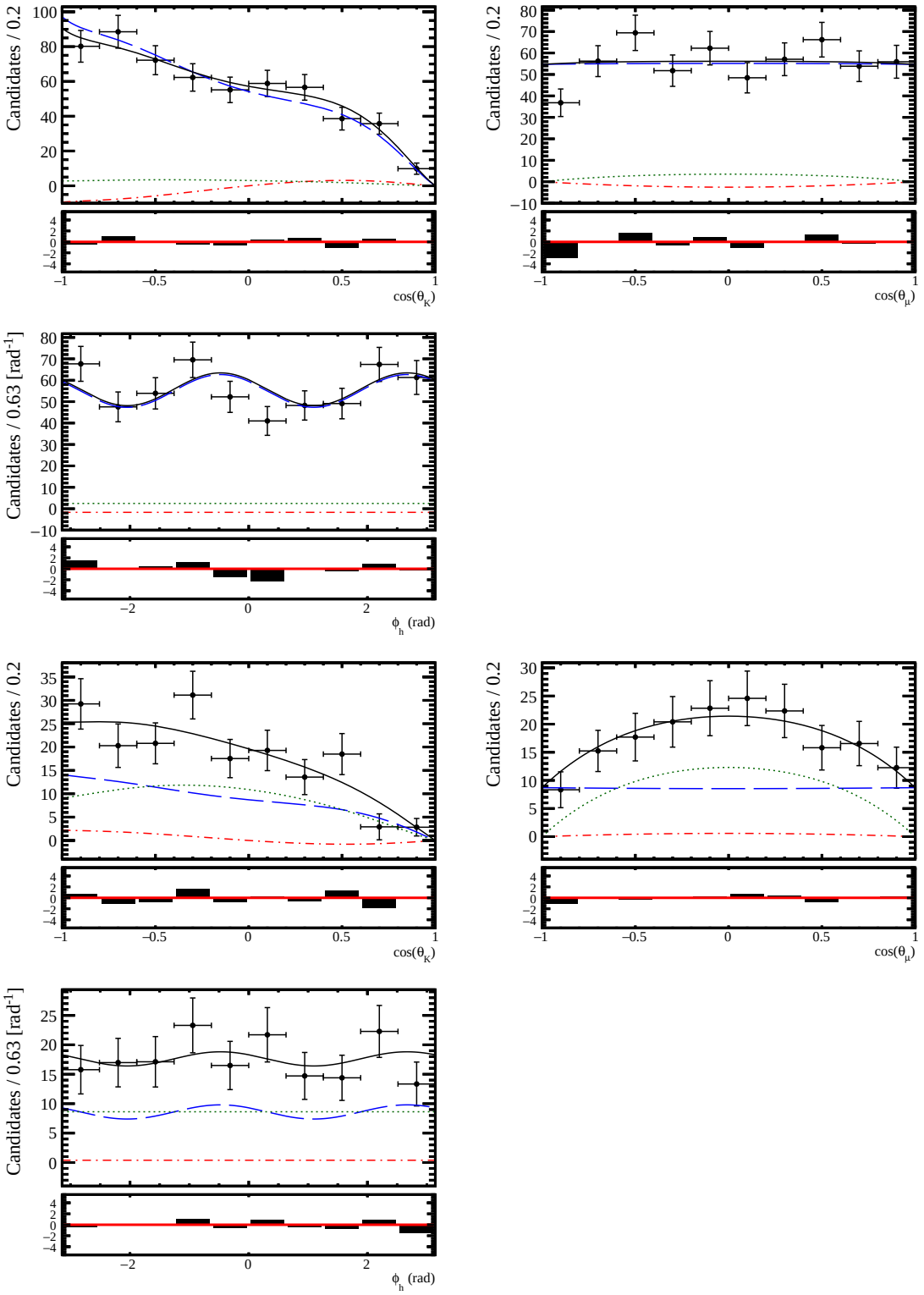

Figure E.4: Angular PDF plots on top of the fitted sWeighted data for $B^0 \to J/\psi K^{*0}$. Blue solid: total. Blue dashed: P-wave + P-P interference. Green dotted: S-wave. Red dotted-dashed: S-P interference.

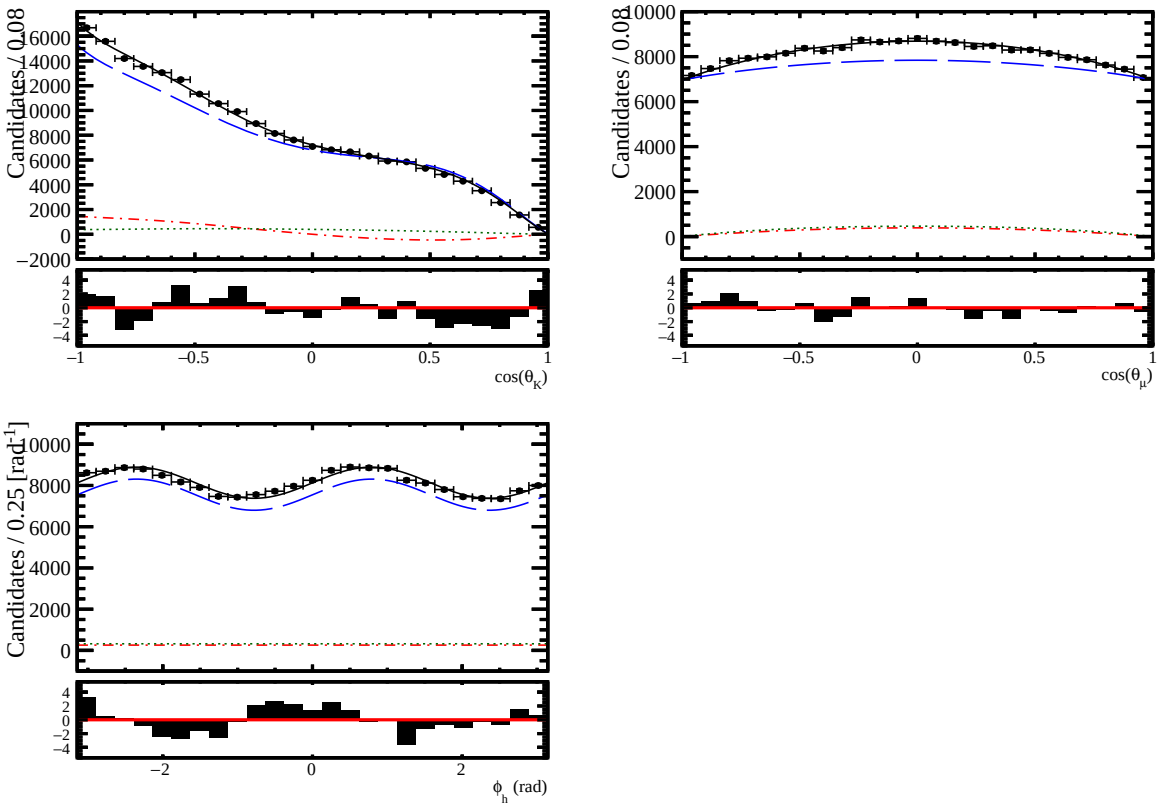

Figure E.5: Angular PDF plots on top of the fitted sWeighted data for $B^0 \to J/\psi K^{*0}$ $m_{K\pi}$ bins 1 (top) and 2 (bottom). Blue solid: total. Blue dashed: P-wave + P-P interference. Green dotted: S-wave. Red dotted-dashed: S-P interference.

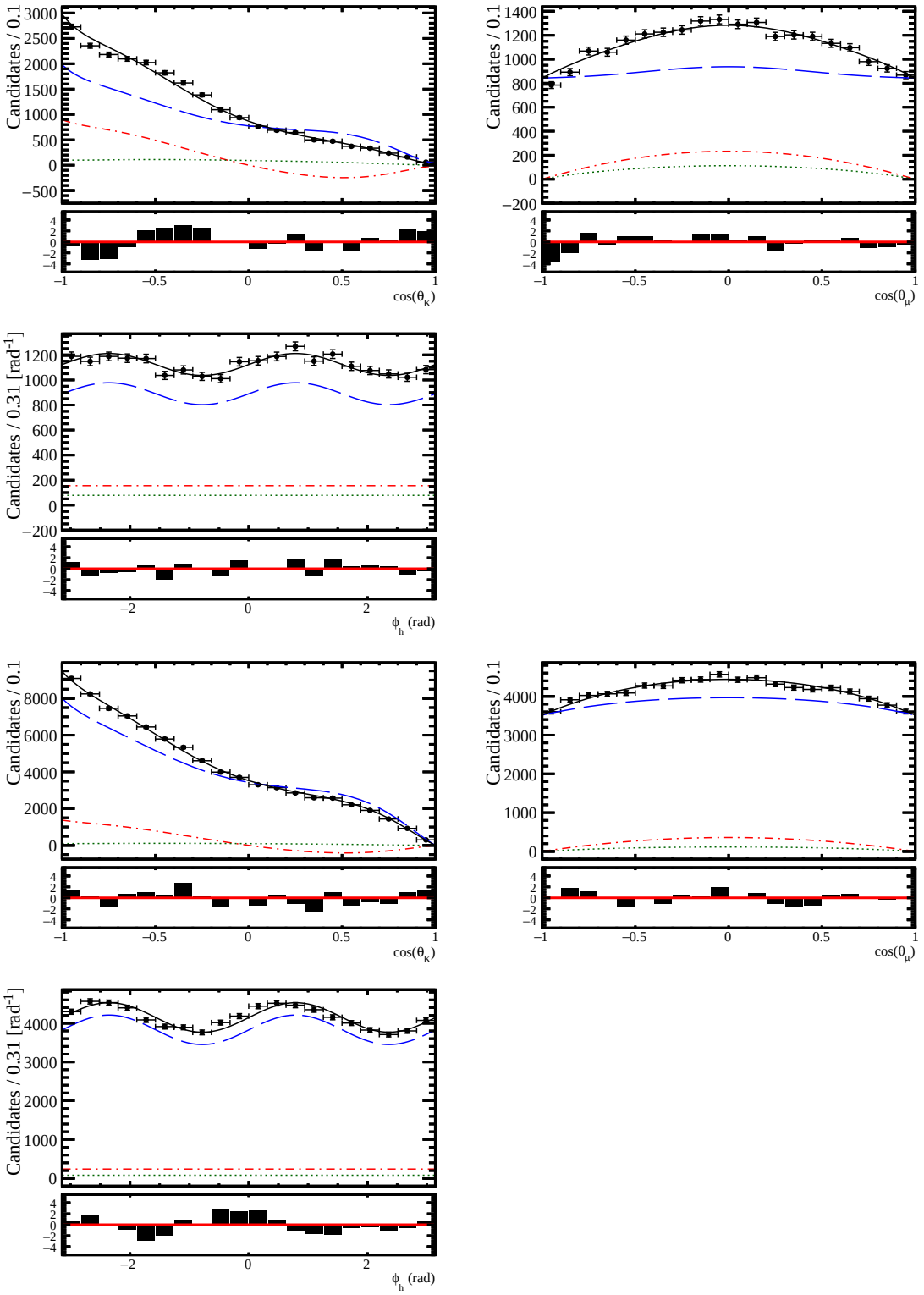

Figure E.6: Angular PDF plots on top of the fitted sWeighted data for $B^0 \to J/\psi K^{*0}$ $m_{K\pi}$ bins 3 (top) and 4 (bottom). Blue solid: total. Blue dashed: P-wave + P-P interference. Green dotted: S-wave. Red dotted-dashed: S-P interference.

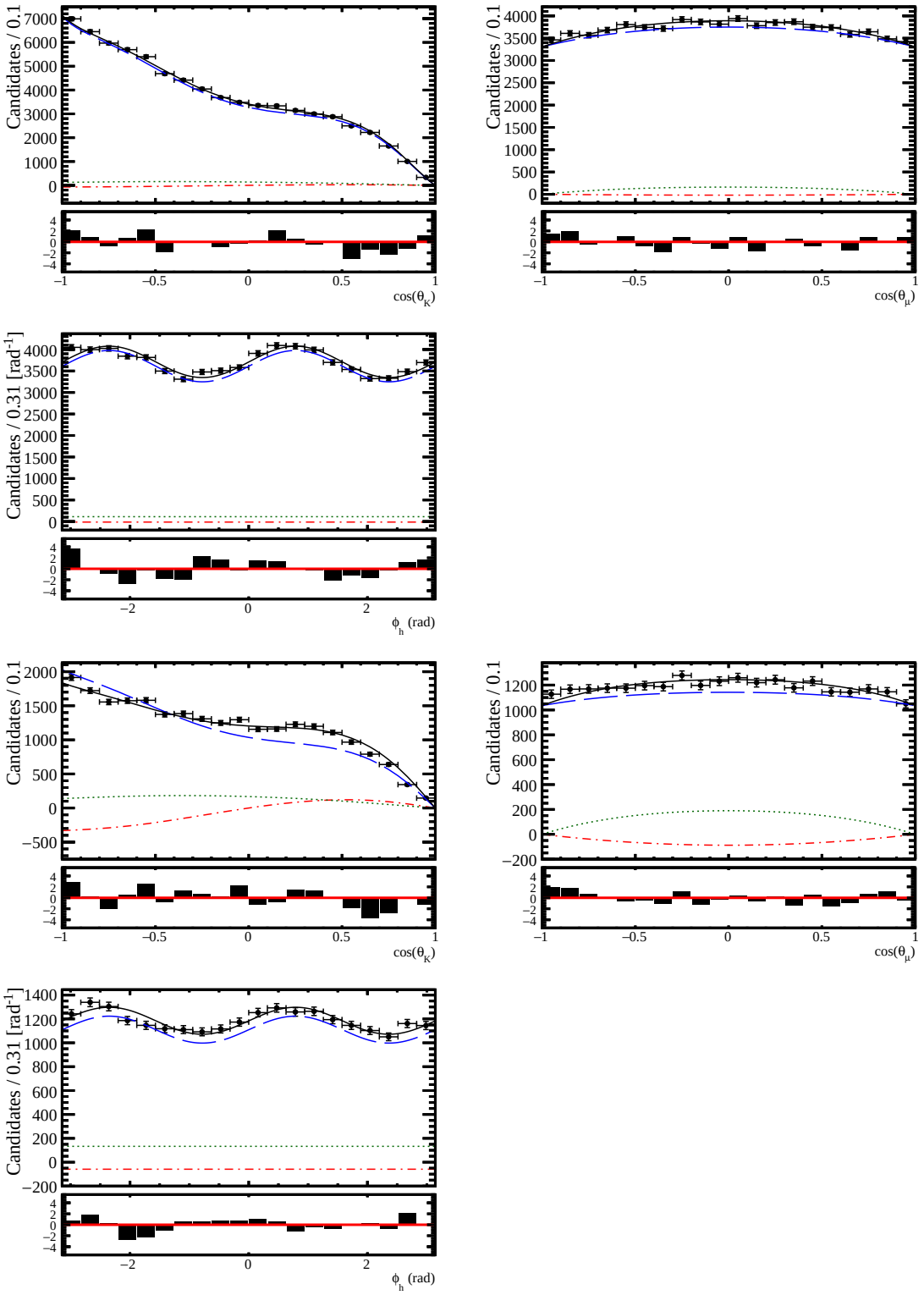

Figure E.7: Angular PDF plots on top of the fitted sWeighted data for $B_s^0 \to J/\psi \overline{K}^{*0}$. Black solid line: total. Blue dashed line: P-wave even component. Blue dotted line: P-wave odd + even-odd interference component. Green dotted line: S-wave component. Red dotted-dashed line: S-P interference component.

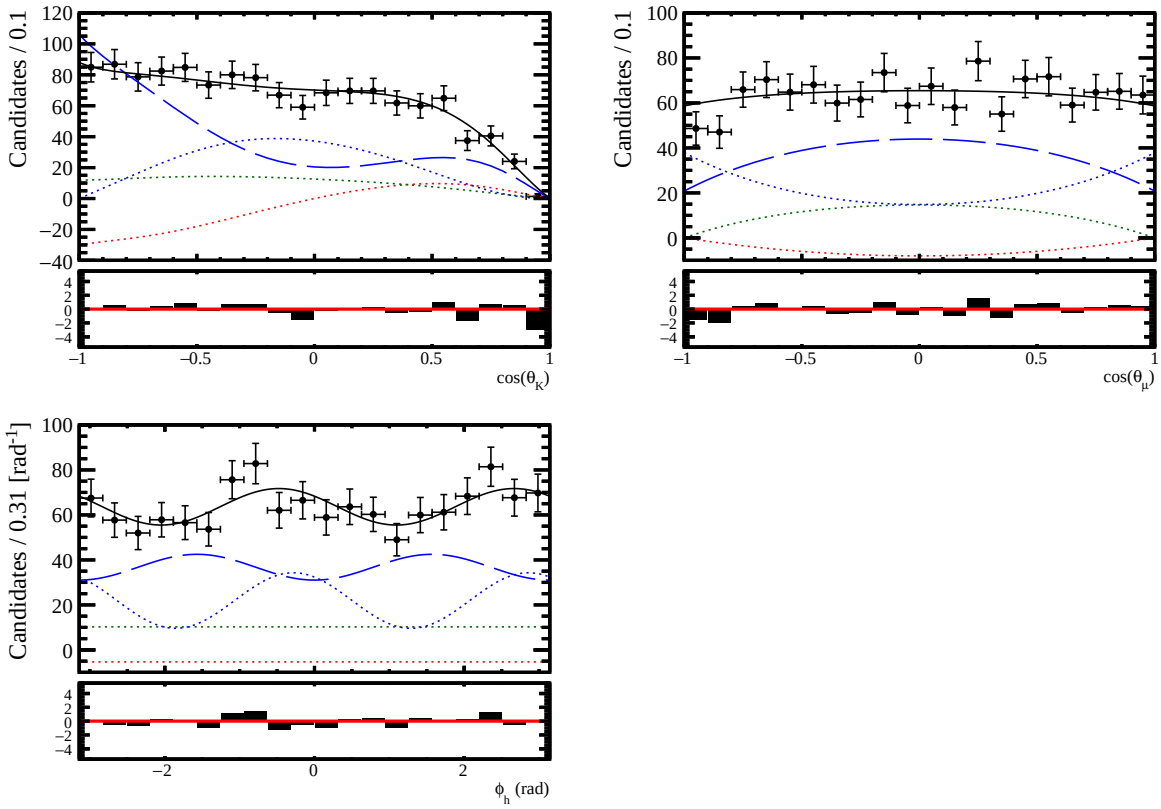

Figure E.8: Angular PDF plots on top of the fitted sWeighted data for $B_s^0 \to J/\psi \overline{K}^{*0}$ $m_{K\pi}$ bins 1 (top) and 2 (bottom). Black solid line: total. Blue dashed line: P-wave even component. Blue dotted line: P-wave odd + even-odd interference component. Green dotted line: S-wave component. Red dotted-dashed line: S-P interference component.

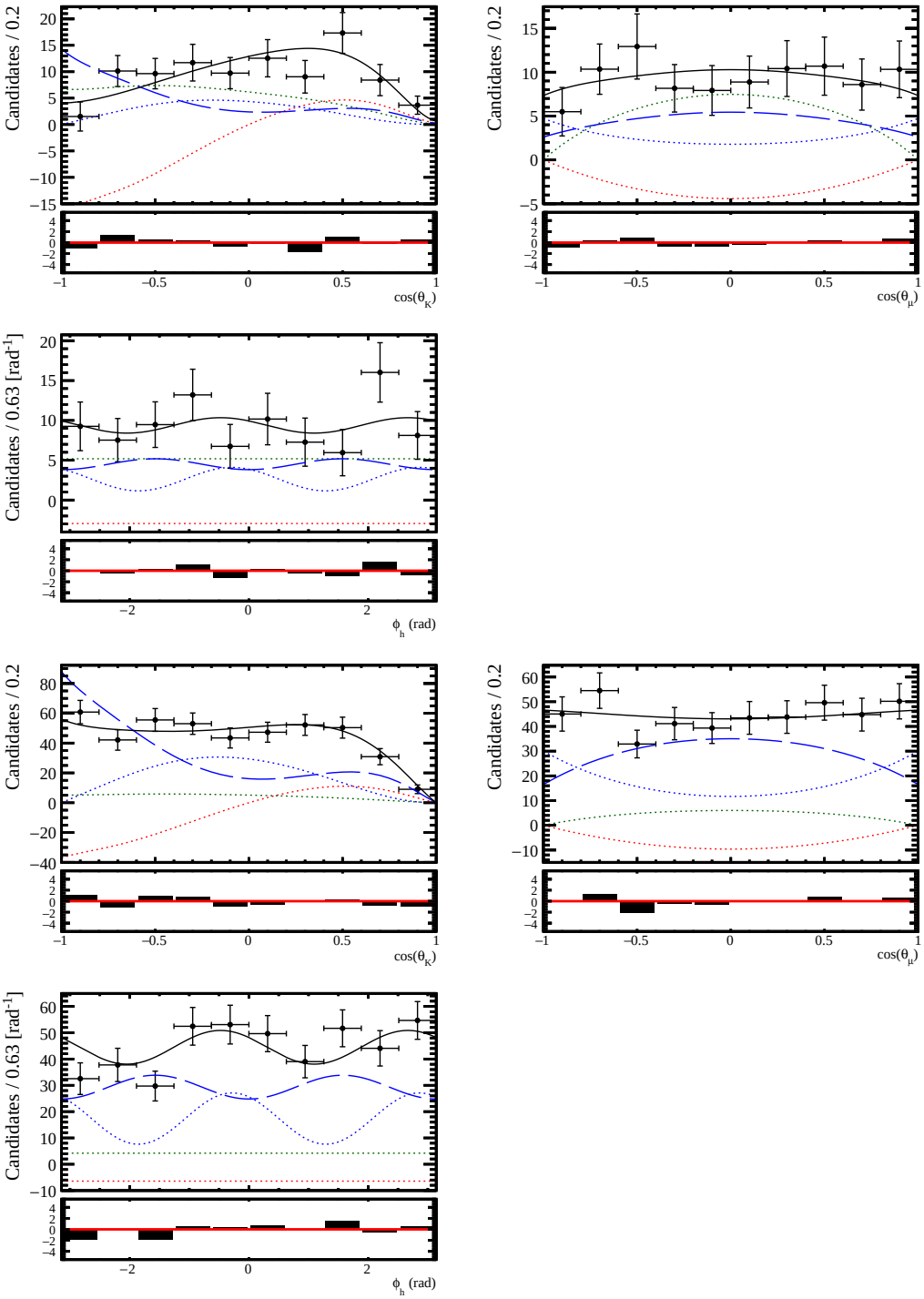

Figure E.9: Angular PDF plots on top of the fitted sWeighted data for $B_s^0 \to J/\psi \overline{K}^{*0}$ $m_{K\pi}$ bins 3 (top) and 4 (bottom). Black solid line: total. Blue dashed line: P-wave even component. Blue dotted line: P-wave odd + even-odd interference component. Green dotted line: S-wave component. Red dotted-dashed line: S-P interference component.

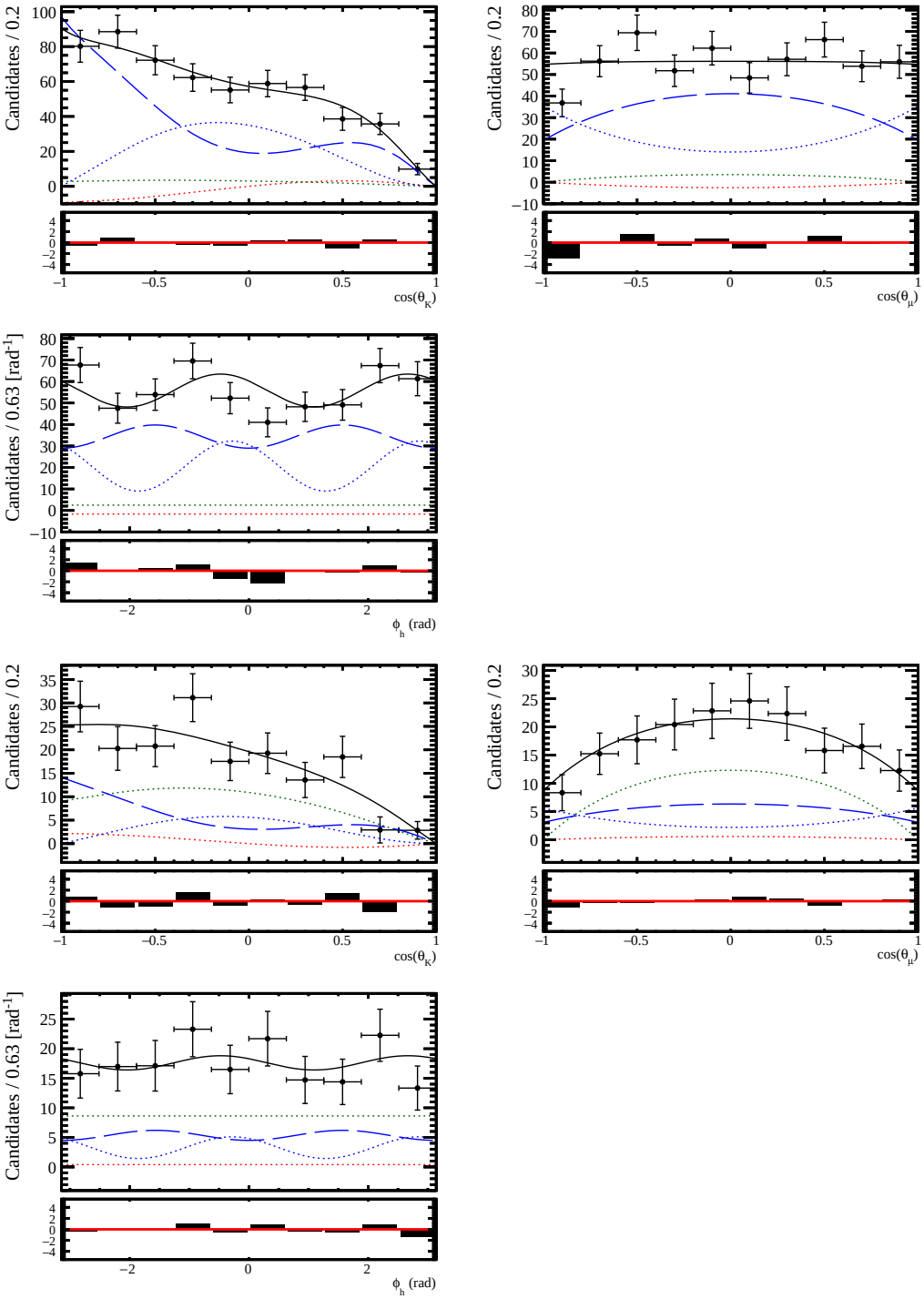

Figure E.10: Angular PDF plots on top of the fitted sWeighted data for $B_s^0 \to J/\psi \overline{K}^{*0}$. Black solid line: total. Blue dashed line: P-wave even component. Blue dotted line: P-wave odd + even-odd interference component. Green dotted line: S-wave component. Red dotted-dashed line: S-P interference component.

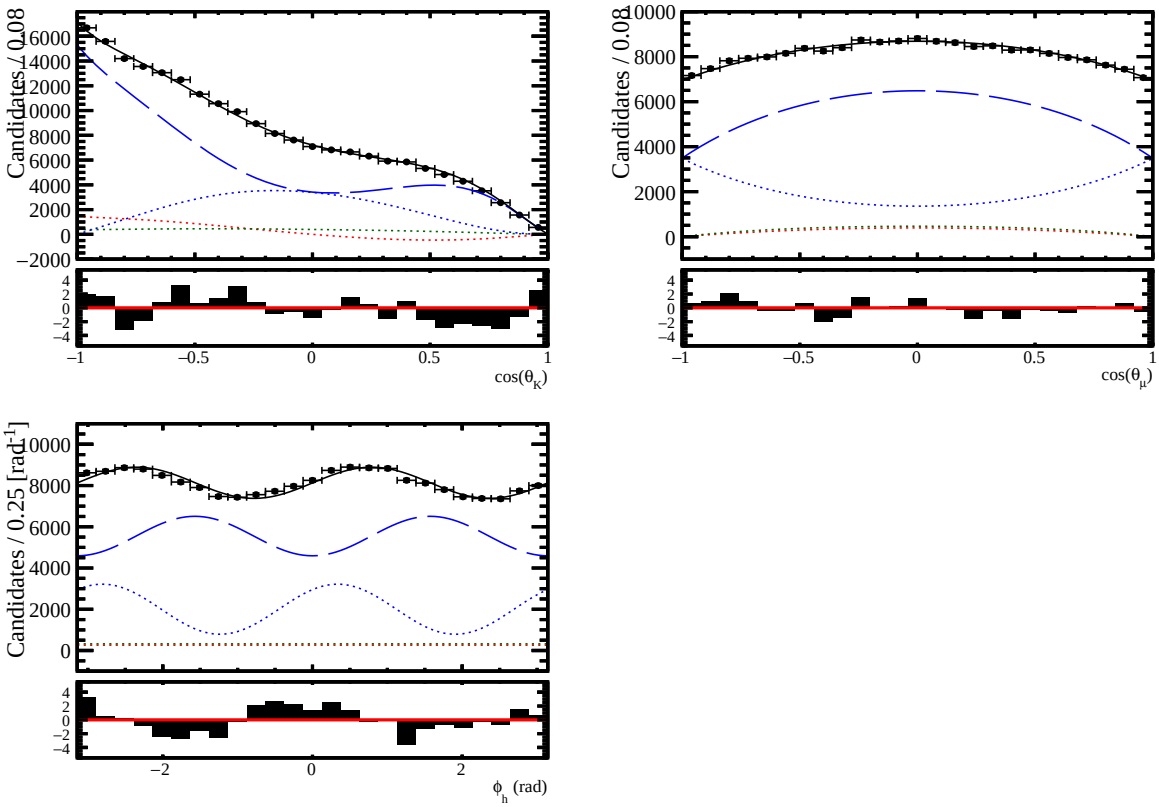

Figure E.11: Angular PDF plots on top of the fitted sWeighted data for $B_s^0 \to J/\psi \overline{K}^{*0}$ $m_{K\pi}$ bins 1 (top) and 2 (bottom). Black solid line: total. Blue dashed line: P-wave even component. Blue dotted line: P-wave odd + even-odd interference component. Green dotted line: S-wave component. Red dotted-dashed line: S-P interference component.

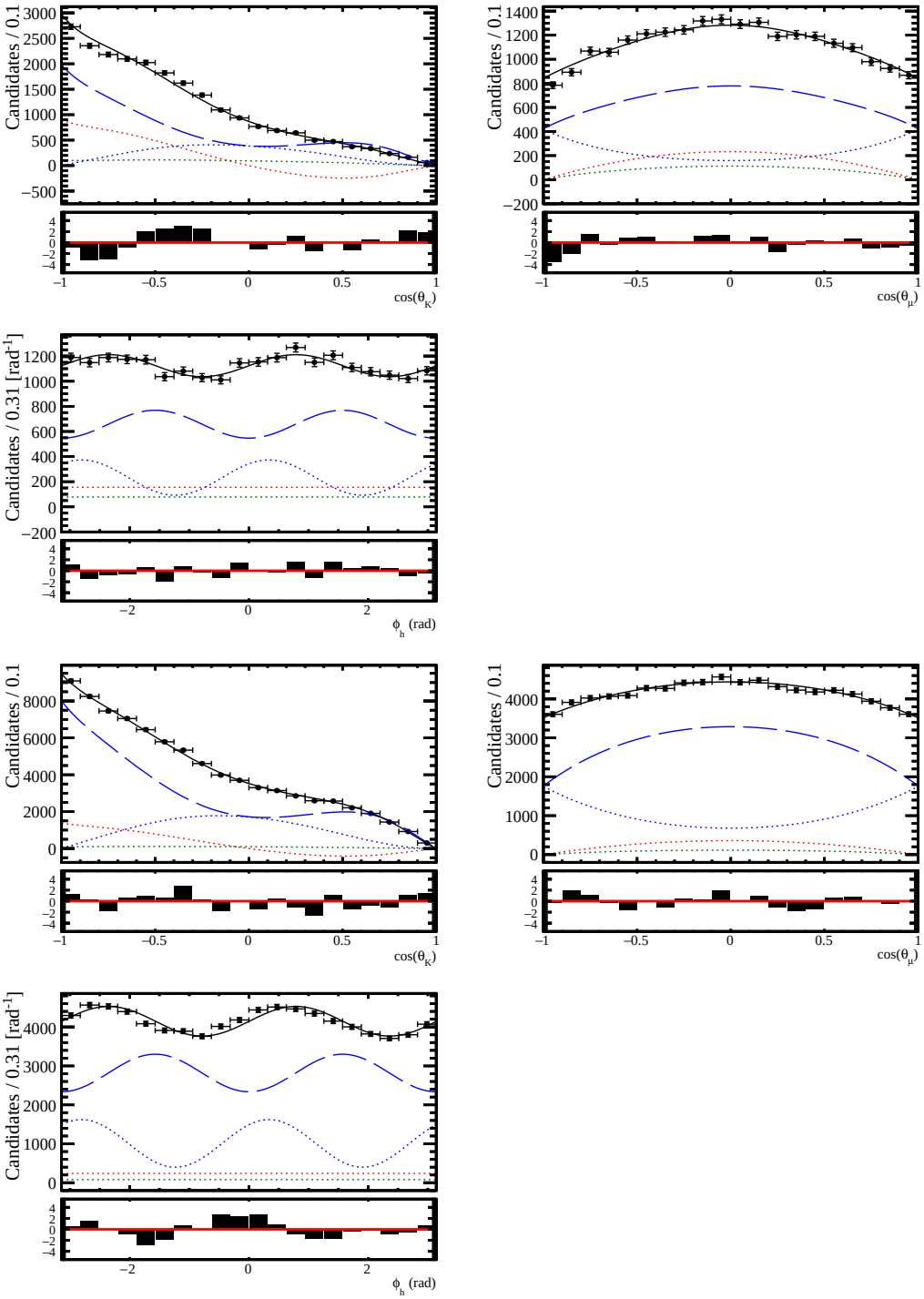

Figure E.12: Angular PDF plots on top of the fitted sWeighted data for $B_s^0 \to J/\psi \overline{K}^{*0}$ $m_{K\pi}$ bins 3 (top) and 4 (bottom). Black solid line: total. Blue dashed line: P-wave even component. Blue dotted line: P-wave odd + even-odd interference component. Green dotted line: S-wave component. Red dotted-dashed line: S-P interference component.

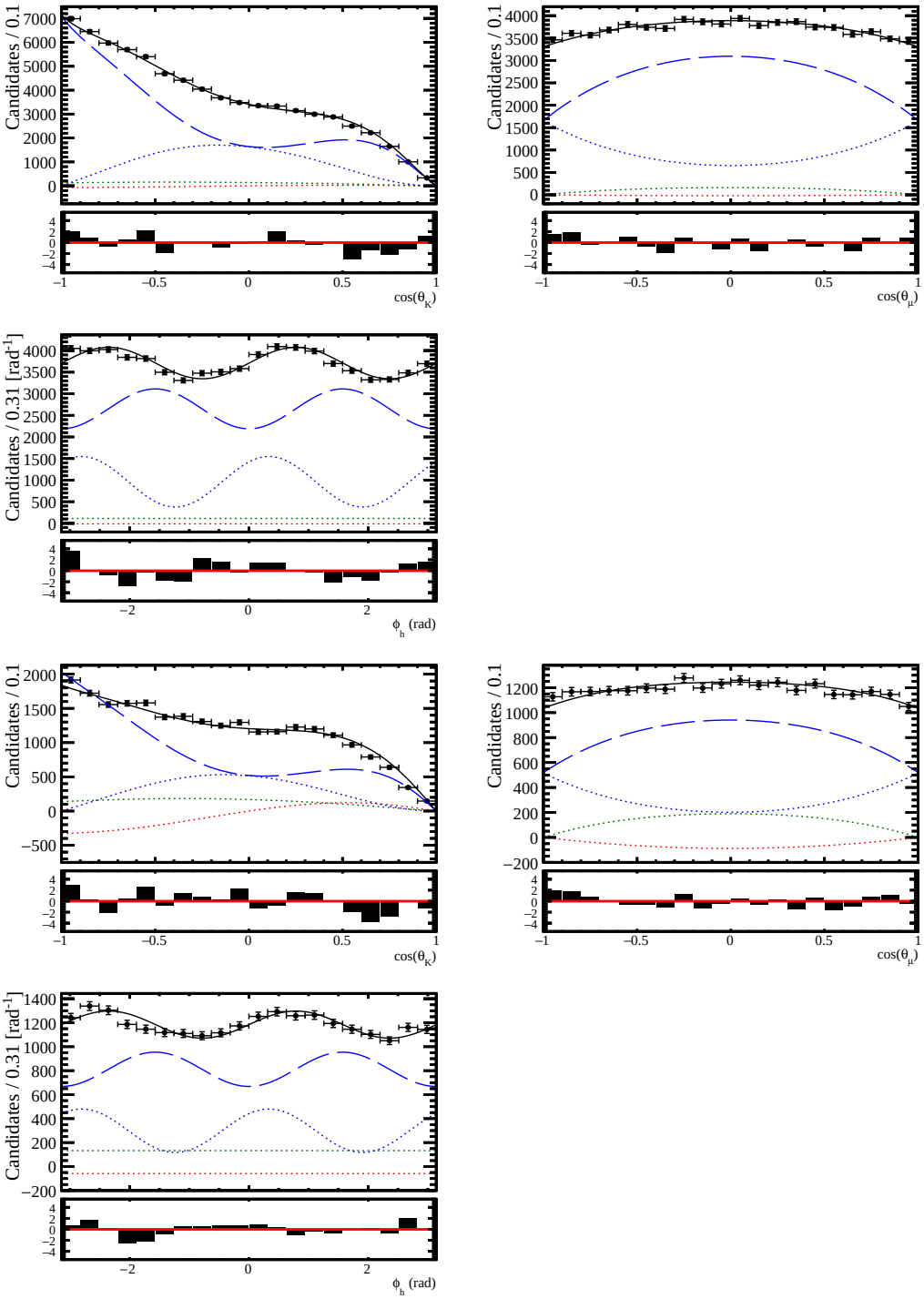

Appendix F

Fit validation with toy studies

F.1 Toy studies for the mass fit model

The fit model described in Chapter 4.3.1 is used to generate an ensemble of 1000 pseudo-experiments. In each pseudoexperiment, the yield of the B_s^0, B^0 and combinatorial background event categories are randomly generated from a Poisson distribution, or "poissonized", with values corresponding to the ones extracted from a fit performed to the $\mu^+\mu^- K\pi$ invariant mass and given in Table 4.11 to Table 4.15. For the peaking backgrounds, their yields are poissonized according to the expected values given in Table 4.10.

Since the $B^0 \to J/\psi\pi^+\pi^-$, $B_s^0 \to J/\psi\pi^+\pi^-$, $B_s^0 \to J/\psi K^+K^-$ and $\Lambda_b^0 \to J/\psi pK^-$ peaking backgrounds are subtracted using negative weights in the nominal fit model, when generating the pseudoexperiments, a poissonized number, N_j, of events are randomly drawn from the corresponding simulated sample and added to the generated sample. The corresponding event weights are set to unity. In a second step, another poissonized number, $N_j^{'}$, of events are randomly drawn and added to the generated sample. The weights applied to these events are defined as

$$w_j = -\frac{N_j}{N_j^{'}}\,. \tag{F.1}$$

This way the weighted sum of events for each of the three subtracted peaking background event categories will be statistically equal to zero. The event weights applied to all other event categories are set to unity. Note that during the generation process, it is ensured that each event drawn from the $B^0 \to J/\psi\pi^+\pi^-$, $B_s^0 \to J/\psi\pi^+\pi^-$, $B_s^0 \to J/\psi K^+K^-$ and $\Lambda_b^0 \to J/\psi pK^-$ peaking background simulated samples are unique. Here, N_j and $N_j^{'}$ are randomly generated according to a Poisson distribution of mean equal to the expected value of the corresponding subtracted peaking background j.

Following the mass fit model, in each pseudoexperiment, the data sample is divided into 20 categories corresponding to the four $m_{K\pi}$ bins times the five $\cos(\theta_\mu)$ bins as defined in Chapter 4.3.1. The values of the fixed shape parameters are extracted from all the simulation information available for signal, separately in each $m_{K\pi}$ bin, and assumed to be identical for each $\cos(\theta_\mu)$ bin. Due to the limited size of the available simulated samples

and to the small expected yields compared to the signal one, the peaking backgrounds shape parameters are extracted from simulation in the entire $m_{K\pi}$ range. The value of the combinatorial background shape parameter is directly taken from the results of the fit to data, as given in Chapter 4.3.2.

The nominal PDF is used to fit each of the 1000 pseudoexperiments. Several combinations are tested trying to maximise the number of floated parameters in order to reduce systematic uncertainties without impairing on the fit ability to discriminate the different event species. As a result, all the tails parameters of the Hypatia function describing the B^0 and B_s^0 mass shapes are fixed, while both the corresponding mean and resolution parameters are let free to vary in the fit. All the peaking background shape parameters are fixed. The yields of B_s^0, B^0 and combinatorial background event categories are free to vary in the fit. It was found that, due to its small value, the yield of the $\Lambda_b^0 \to J/\psi p\pi^-$ event category could not be freely determined in the fit. However, as described in ref. [113], when using the ${}_s\mathcal{P}lot$ technique in the case where one or more event categories have their yields fixed in the maximum likelihood fit, the estimate of the x-distributions considered, ${}_s\tilde{\mathrm{M}}_\mathrm{n}$, which is obtained as the sum of the ${}_s\mathcal{W}eights$, needs to be corrected. The correction consists in adding to the ${}_s\tilde{\mathrm{M}}_\mathrm{n}$ distribution the normalised distributions of each fixed category scaled by the factor $c_\mathrm{n} = N_\mathrm{n} - \sum_j \mathrm{V}_{\mathrm{n}j}$, where V is the covariance matrix resulting from the fit and N the expected yield of category n. This procedure implies that the x-distributions of the fixed categories are well known. Since this is not the case for the angular distribution of the $\Lambda_b^0 \to J/\psi p\pi^-$ background, in order to avoid fixing the corresponding yields, Gaussian constraints are applied when performing the fit to the mass. As a consequence, and following the procedure described in ref. [161], when performing the fit to each pseudoexperiment, the mean values of the gaussian constraints applied the $\Lambda_b^0 \to J/\psi p\pi^-$ yield are randomly generated according to the constraint PDFs.

Depending on the $m_{K\pi}$ category, some small biases appearing for the B_s^0 signal yields can be observed. When computing the branching fractions, the fitted yields are not corrected for the biases. Instead, the later are included in the systematic uncertainties, where the biases appearing in each individual $m_{K\pi}$ and $\cos(\theta_\mu)$ bins are added in quadrature. Note that the fit convergence rate is 100%. Adding the biases on the B_s^0 and B^0 yields appearing for each of the 20 bins, the following numbers

$$\mathrm{bias}_{N_{B^0}} = -11.7\,, \tag{F.2}$$

$$\mathrm{bias}_{N_{B_s^0}} = \quad 5.3\,, \tag{F.3}$$

are obtained, which are then added into the systematics on the yields, after symmetrizing their values, and further propagated to the systematic on the ratio between $N_{B_s^0}$ and N_{B^0}.

F.2 Toy studies for the angular fit model

Since the A^{CP} parameters were blind at this step, and their expected values close to zero, the nominal 1000 pseudoexperiments are generated with all A^{CP} parameters equal to zero.

The corresponding toy studies are described in Chapter F.2.1. Toy simulation generated with non-zero A^{CP} values were also studied, as described in Chapter F.2.2.

F.2.1 Toys with zero A^{CP} values

First, possible biases in the nominal fit configuration are studied by performing a sFit to the weighted angular distributions using the ${}_s\mathcal{W}eights$ for the B_s^0 event category extracted from a mass fit to each of the 1000 pseudoexperiments, as described in Appendix F.1. Then, in order to disentangle the effect of biases from the weighting and possible intrinsic fit model biases, a second toy study is done by performing a classic fit to the true B_s^0 angular distributions generated for each of the 1000 pseudoexperiments. In addition, the comparison between the results of these two toy studies allows to validate the scaling of the ${}_s\mathcal{W}eights$ procedure applied in order to get proper uncertainties, as described in Chapter 4.3.1.

Following the angular fit model, for both studies, the fit is performed simultaneously to 16 categories defined by the two data-taking periods, the kaon charge and the four $m_{K\pi}$ bins. All parameters are common among the 16 categories, except for the S-wave parameters (i.e. the fractions of amplitudes F_S and the strong phase δ_S), which are split among the four $m_{K\pi}$ bins. Each of the 16 B_s^0 angular parameters are allowed to vary in the fit. Table F.1 gives the results of the toy study with the nominal fit configuration where sFits to the weighted angular distributions are performed, showing the mean and width as returned by a fit to the corresponding pull distribution of each floated parameter in the B_s^0 angular fit model. Even though some small biases arise on the S-wave parameters, no significant bias is observed compared to the corresponding statistical uncertainty. Table F.2 gives the results of the toy study where classic fits are performed to the true B_s^0 angular distributions, showing the mean and width as returned by a fit to the corresponding pull distribution of each floated parameter in the B_s^0 angular fit model.

In order to compare the results between these two toy studies, the parameter $\Delta(\text{true}-\text{sWeight})$ is defined, the difference between the fitted value from the classic fit and the sFit, as

$$\Delta(\text{true} - \text{sWeight}) = (a_i^{f,\text{true dist.}} - a_i^{f,\text{sWeighted dist.}}), \tag{F.4}$$

and the total uncertainty $\sigma_{\text{tot.}}$ as

$$\sigma_{\text{tot.}} = \sqrt{(\sigma_i^{f,\text{true dist.}})^2 + (\sigma_i^{f,\text{sWeighted dist.}})^2}, \tag{F.5}$$

where $a_i^{f,\text{true dist.}}$ and $\sigma_i^{f,\text{true dist.}}$ are the value of the fitted parameter a_i and its associated uncertainty as extracted from a fit to the true B_s^0 angular distributions, while $a_i^{f,\text{sWeighted dist.}}$ and $\sigma_i^{f,\text{sWeighted dist.}}$ are the fitted value and uncertainty as extracted from the sWeighted angular distributions. In case that no additional biases originating from the ${}_s\mathcal{W}eights$ arise, then $\Delta(\text{true} - \text{sWeight})/\sigma_{\text{tot.}}$ should be equal to zero and $\sigma_i^{f,\text{true dist.}}/\sigma_i^{f,\text{sWeighted dist.}}$ should be equal one in the case where the scaling of the ${}_s\mathcal{W}eights$ to get proper uncertainties is correct. Table F.3 gives the results of the comparison between the two toy studies. These results are in agreement with the expected values of 0

Table F.1: Means and widths of pull distributions of all the floated parameters entering in the B_s^0 angular fit model from the toy studies when the fit is performed to the sWeighted angular distributions.

a_i (B_s^0)	$\mu(\text{pull}_i)$	$\sigma(\text{pull}_i)$	a_i^t	bias	$\mu(\sigma_i^f)$
A_0^{CP}	-0.060 ± 0.033	1.027 ± 0.024	0.000	-0.003	0.055
A_S^{CP}	0.038 ± 0.033	1.014 ± 0.025	0.000	0.004	0.106
$A_\parallel^{CP}$	0.016 ± 0.033	1.016 ± 0.024	0.000	0.002	0.156
$A_\perp^{CP}$	-0.062 ± 0.034	1.029 ± 0.023	0.000	-0.005	0.088
f_0	0.017 ± 0.033	1.025 ± 0.027	0.497	0.000	0.028
$f_\parallel$	-0.035 ± 0.033	1.020 ± 0.027	0.179	-0.001	0.027
$\delta_\parallel$	0.061 ± 0.034	1.056 ± 0.027	-2.700	0.010	0.160
$\delta_\perp$	-0.069 ± 0.034	1.059 ± 0.027	-0.010	-0.007	0.108
F_S_826_861	0.047 ± 0.035	1.078 ± 0.028	0.475	0.005	0.109
F_S_861_896	0.110 ± 0.033	0.971 ± 0.024	0.080	0.003	0.032
F_S_896_931	0.195 ± 0.033	1.010 ± 0.027	0.044	0.007	0.035
F_S_931_966	0.126 ± 0.034	1.047 ± 0.029	0.523	0.015	0.115
δ_S_826_861	0.061 ± 0.034	1.056 ± 0.027	0.540	0.010	0.156
δ_S_861_896	-0.069 ± 0.034	1.059 ± 0.027	-0.530	-0.017	0.244
δ_S_896_931	-0.108 ± 0.032	0.996 ± 0.020	-1.460	-0.022	0.208
δ_S_931_966	0.043 ± 0.035	1.063 ± 0.027	-1.760	0.006	0.136

and 1 for $\Delta(\text{true} - \text{sWeight})/\sigma_{\text{tot.}}$ and $\sigma_i^{f,\text{true dist.}}/\sigma_i^{f,\text{sWeighted dist.}}$, respectively, which validate the sFit procedure. Another conclusion is that the small biases observed on the B_s^0 yields from the toy study do not affect the extraction of the parameters of interest in the sFit to the angular distributions. Note that the fit convergence rate is close to 100%.

Table F.2: Means and widths of pull distributions of all the floated parameters entering the B_s^0 angular fit model from the toy studies when the fit is performed to the true B_s^0 angular distributions.

a_i (B_s^0)	$\mu(\text{pull}_i)$	$\sigma(\text{pull}_i)$	a_i^t	bias	$\mu(\sigma_i^f)$
A_0^{CP}	0.008 ± 0.031	0.974 ± 0.026	0.000	0.000	0.056
A_S^{CP}	-0.007 ± 0.033	1.022 ± 0.025	0.000	-0.001	0.100
$A_\parallel^{CP}$	0.003 ± 0.032	0.987 ± 0.024	0.000	0.000	0.147
$A_\perp^{CP}$	0.011 ± 0.032	0.998 ± 0.024	0.000	0.001	0.094
f_0	-0.023 ± 0.031	0.970 ± 0.028	0.497	-0.001	0.023
$f_\parallel$	-0.030 ± 0.033	1.007 ± 0.028	0.179	-0.001	0.026
$\delta_\parallel$	0.034 ± 0.032	0.979 ± 0.027	-2.700	0.005	0.161
$\delta_\perp$	-0.020 ± 0.032	1.003 ± 0.027	-0.010	-0.002	0.108
F_S_826_861	0.054 ± 0.031	0.970 ± 0.028	0.475	0.006	0.109
F_S_861_896	0.198 ± 0.031	0.961 ± 0.022	0.080	0.006	0.031
F_S_896_931	0.313 ± 0.033	1.011 ± 0.026	0.044	0.010	0.031
F_S_931_966	0.048 ± 0.031	0.962 ± 0.030	0.523	0.005	0.100
δ_S_826_861	0.034 ± 0.032	0.979 ± 0.027	0.540	0.005	0.145
δ_S_861_896	-0.020 ± 0.032	1.003 ± 0.027	-0.530	-0.005	0.229
δ_S_896_931	-0.104 ± 0.034	1.043 ± 0.020	-1.460	-0.022	0.212
δ_S_931_966	0.022 ± 0.035	1.071 ± 0.028	-1.760	0.003	0.124

Table F.3: Validation of the sFit procedure.

a_i (B_s^0)	$\Delta(\text{true} - \text{sWeight})/\sigma_{\text{tot.}}$	$\sigma_i^{f,\text{true dist.}}/\sigma_i^{f,\text{sWeighted dist.}}$
A_0^{CP}	0.048	1.023
A_S^{CP}	-0.032	0.940
$A_\parallel^{CP}$	-0.010	0.943
$A_\perp^{CP}$	0.050	1.063
f_0	-0.028	0.843
$f_\parallel$	0.005	0.955
$\delta_\parallel$	-0.019	1.005
$\delta_\perp$	0.036	0.993
F_S_826_861	0.005	0.997
F_S_861_896	0.061	0.987
F_S_896_931	0.062	0.888
F_S_931_966	-0.064	0.869
δ_S_826_861	-0.022	0.925
δ_S_861_896	0.037	0.938
δ_S_896_931	0.001	1.021
δ_S_931_966	-0.017	0.914

F.2.2 Toys with non-zero A^{CP} values

In order to test the possibility of non-zero A^{CP} values in the data, additional studies where the A^{CP} were generated with values different from zero are performed. Since the computing time required to test one configuration of parameter values is long, toy studies performed here are simplified compared to the procedure described in Chapter F.2.1.

First ten sets of non-zero A^{CP} values are randomly generated from a uniform distribution in the range $A_i^{CP} \in [-0.6, 0.6]$. The corresponding values are given in Table F.4. In a second step, ten large samples of B_s^0 angular distributions were generated from the B_s^0 nominal PDFs according to each set of A^{CP} values, where the number of generated events corresponds to 1000 times the expected number of B_s^0 events in the data. Finally a classic fit to the B_s^0 angular distributions is performed. This is justified by the fact that the A^{CP} values are not correlated to the mass distribution and by the fact that the weighting procedure do not add any additional bias on the angular parameters, as shown in Chapter F.2.1. All the B_s^0 angular parameters are free to vary in each of the ten fits performed here.

Table F.4: Definitions of the sets of randomly generated A^{CP} values.

Set	A_0^{CP}	$A_\parallel^{CP}$	$A_\perp^{CP}$	A_S^{CP}
0	−0.0768	−0.5689	−0.3779	0.5178
1	0.0596	−0.0776	0.5373	−0.0183
2	−0.0956	−0.2036	−0.2154	−0.4147
3	−0.3544	0.1431	0.2386	−0.4561
4	−0.2404	−0.2798	−0.0178	0.1593
5	0.1454	0.0350	0.3819	0.2196
6	−0.4385	0.0163	−0.0017	0.1042
7	−0.3787	0.3424	0.2637	−0.2898
8	0.4248	−0.0069	0.0554	−0.1112
9	0.4159	−0.5044	−0.3876	0.5636

The corresponding results for the sets 0 to 4 and 5 to 9 are given in Table F.5 and Table F.6, respectively. For clarity, only the results on the A^{CP} parameters are presented. Any significant bias for all the A^{CP} parameters in each of the ten fitting configurations are not observed. Note that due to the large size of the generated samples the statistical uncertainties corresponding to the A^{CP} parameters are divided by a factor of roughly 30 compared to the nominal ones. Therefore it can be concluded that the fit model is stable and exhibit no intrinsic bias for A^{CP} values in the range $A_i^{CP} \in [-0.6, 0.6]$.

Table F.5: Results of the toy study for sets 0 to 4 of non-zero values of A^{CP}.

A^{CP} set	a_i (B_s^0)	a_i^t	$a_i^f \pm \sigma_i^f$	$(a_i^f - a_i^t)/\sigma_i^f$
0	A_0^{CP}	-0.0768	-0.0745 ± 0.0017	1.369
	A_S^{CP}	0.5178	0.5184 ± 0.0043	0.139
	$A_\parallel^{CP}$	-0.3779	-0.3777 ± 0.0036	0.056
	$A_\perp^{CP}$	-0.5689	-0.5698 ± 0.0021	-0.438
1	A_0^{CP}	0.0596	0.0592 ± 0.0015	-0.277
	A_S^{CP}	-0.0183	-0.0190 ± 0.0029	-0.236
	$A_\parallel^{CP}$	0.5373	0.5354 ± 0.0038	-0.498
	$A_\perp^{CP}$	-0.0776	-0.0807 ± 0.0025	-1.217
2	A_0^{CP}	-0.0956	-0.0974 ± 0.0015	-1.160
	A_S^{CP}	-0.4147	-0.4151 ± 0.0030	-0.144
	$A_\parallel^{CP}$	-0.2154	-0.2086 ± 0.0041	1.682
	$A_\perp^{CP}$	-0.2036	-0.2044 ± 0.0025	-0.340
3	A_0^{CP}	-0.3544	-0.3533 ± 0.0015	0.729
	A_S^{CP}	-0.4561	-0.4547 ± 0.0031	0.463
	$A_\parallel^{CP}$	0.2386	0.2341 ± 0.0040	-1.135
	$A_\perp^{CP}$	0.1431	0.1419 ± 0.0025	-0.460
4	A_0^{CP}	-0.2404	-0.2432 ± 0.0015	-1.863
	A_S^{CP}	0.1593	0.1604 ± 0.0033	0.337
	$A_\parallel^{CP}$	-0.0178	-0.0154 ± 0.0041	0.591
	$A_\perp^{CP}$	-0.2798	-0.2768 ± 0.0024	1.245

Table F.6: Results of the toy study for sets 5 to 9 of non-zero values of A^{CP}.

A^{CP} set	a_i (B_s^0)	a_i^t	$a_i^f \pm \sigma_i^f$	$(a_i^f - a_i^t)/\sigma_i^f$
5	A_0^{CP}	0.1454	0.1450 ± 0.0015	-0.258
	A_S^{CP}	0.2196	0.2200 ± 0.0028	0.153
	$A_\parallel^{CP}$	0.3819	0.3776 ± 0.0039	-1.088
	$A_\perp^{CP}$	0.0350	0.0375 ± 0.0025	0.991
6	A_0^{CP}	-0.4385	-0.4385 ± 0.0015	-0.017
	A_S^{CP}	0.1042	0.1059 ± 0.0032	0.544
	$A_\parallel^{CP}$	-0.0017	-0.0028 ± 0.0041	-0.259
	$A_\perp^{CP}$	0.0163	0.0158 ± 0.0025	-0.182
7	A_0^{CP}	-0.3787	-0.3788 ± 0.0016	-0.036
	A_S^{CP}	-0.2898	-0.2855 ± 0.0030	1.443
	$A_\parallel^{CP}$	0.2637	0.2671 ± 0.0039	0.874
	$A_\perp^{CP}$	0.3424	0.3437 ± 0.0024	0.534
8	A_0^{CP}	0.4248	0.4244 ± 0.0015	-0.243
	A_S^{CP}	-0.1112	-0.1127 ± 0.0032	-0.472
	$A_\parallel^{CP}$	0.0554	0.0511 ± 0.0041	-1.051
	$A_\perp^{CP}$	-0.0069	-0.0065 ± 0.0025	0.163
9	A_0^{CP}	0.4159	0.4127 ± 0.0016	-1.989
	A_S^{CP}	0.5636	0.5671 ± 0.0036	0.980
	$A_\parallel^{CP}$	-0.3876	-0.3818 ± 0.0037	1.570
	$A_\perp^{CP}$	-0.5044	-0.4998 ± 0.0023	2.040

Appendix G

Weakly decaying *b*-fractions

There is a relation [162] between $f_{\Lambda_b^0}$ and f_d ($p_T \in [1.5, 40]\,\mathrm{GeV}/c$),

$$\frac{f_{\Lambda_b^0}}{f_d}(p_T) = a + \exp(b + c \times p_T[\,\mathrm{GeV}/c]), \tag{G.1}$$

with

$$\begin{aligned} a &= +0.151 \pm 0.016\ ^{+0.024}_{-0.025}, \\ b &= -0.573 \pm 0.040\ ^{+0.101}_{-0.097}, \\ c &= -0.095 \pm 0.007 \pm 0.014[\,\mathrm{GeV}/c]^{-1}, \end{aligned}$$

where the correlation matrix of the parameters is

$$\rho(a, b, c) = \begin{pmatrix} 1 & 0.55 & -0.73 \\ 0.55 & 1 & -0.03 \\ -0.73 & -0.03 & 1 \end{pmatrix}.$$

Assuming that

$$f_u = f_d \quad , \quad f_u + f_d + f_s + f_{\Lambda_b^0} = 1, \tag{G.2}$$

one can obtain a distribution of $f_{\Lambda_b^0}/f_d$ in real data by evaluating (G.1) event per event. From this distribution, an average for this ratio is estimated from its mean value and root mean square. Considering real data for 2012 conditions, the following value is obtained

$$\frac{f_{\Lambda_b^0}}{f_d} = 0.441 \pm 0.112. \tag{G.3}$$

Using $\frac{f_s}{f_d}$ from [149],

$$\frac{f_s}{f_d} = 0.259 \pm 0.015, \tag{G.4}$$

final expressions for all the hadronisation factors can be obtained ($f_d = f_u$),

$$f_d = \left(2 + \frac{fs}{fd} + \frac{f_{\Lambda_b^0}}{f_d}\right)^{-1} \quad , \quad \sigma^2(f_d) = f_d^4\left(\sigma^2\left(\frac{f_{\Lambda_b^0}}{f_d}\right) + \sigma^2\left(\frac{f_s}{f_d}\right)\right), \tag{G.5}$$

$$f_s = \frac{fs/fd}{(2 + fs/fd + f_{\Lambda_b^0}/f_d)} \quad , \quad \sigma^2(f_s) = {f_s}^2\Big(\frac{\sigma^2(f_s/f_d)}{(f_s/f_d)^2} + \frac{\sigma^2(f_d)}{f_d^2}\Big), \tag{G.6}$$

$$f_{\Lambda_b^0} = \frac{f_{\Lambda_b^0}/fd}{(2 + fs/fd + f_{\Lambda_b^0}/f_d)} \quad , \quad \sigma^2(f_{\Lambda_b^0}) = {f_{\Lambda_b^0}}^2\Big(\frac{\sigma^2(f_{\Lambda_b^0}/f_d)}{(f_{\Lambda_b^0}/f_d)^2} + \frac{\sigma^2(f_d)}{f_d^2}\Big), \tag{G.7}$$

leading to the following estimations,

$$f_d = f_u = 0.370 \pm 0.016, \tag{G.8}$$

$$f_s = 0.0959 \pm 0.0068, \tag{G.9}$$

$$f_{\Lambda_b^0} = 0.163 \pm 0.042. \tag{G.10}$$

Appendix H

List of footnotes with hyperlinks

- CERN, European Organization for Nuclear Research: http://home.cern/ (page 15)
- The LHCb Collaboration: http://lhcb.web.cern.ch/lhcb/ (page 15)
- The Nobel Prize in Physics 2013: François Englert and Peter Higgs (page 17)
  - http://www.nobelprize.org/nobel_prizes/physics/laureates/2013/
  - https://www.nobelprize.org/nobel_prizes/physics/laureates/2013/popular-physicsprize2013.pdf
  - http://www.nobelprize.org/
- GAES, LHCb Silicon Tracker Construction: http://www.usc.es/gaes/STconstruction.html (page 24)
- The Boole project: http://lhcb-release-area.web.cern.ch/LHCb-release-area/DOC/boole/ (page 30)
- The Moore project: http://lhcb-release-area.web.cern.ch/LHCb-release-area/DOC/moore/ (page 30)
- The Brunel project: http://lhcb-release-area.web.cern.ch/LHCb-release-area/DOC/brunel/ (page 30)
- The DaVinci project: http://lhcb-release-area.web.cern.ch/LHCb-release-area/DOC/davinci/ (page 31)
- The Bender project: http://lhcb-release-area.web.cern.ch/LHCb-release-area/DOC/bender/ (page 31)
- The Erasmus project: http://lhcb-release-area.web.cern.ch/LHCb-release-area/DOC/erasmus/ (page 31)
- The Panoramix project: http://lhcb-release-area.web.cern.ch/LHCb-release-area/DOC/panoramix/ (page 32)
- The Stripping project: http://lhcb-release-area.web.cern.ch/LHCb-release-area/DOC/stripping/ (page 32)
- LHCb database tags (page 64)
  - CondDB: https://twiki.cern.ch/twiki/bin/view/LHCb/CondDBHowTo
  - DDDB: https://lhcb-comp.web.cern.ch/lhcb-comp/Frameworks/DetDesc/default.htm)
- Monte Carlo re-weighting using Yandex software: https://github.com/arogozhnikov/hep_ml (page 134)

Bibliography

[1] S. L. Glashow, *Partial-symmetries of weak interactions*, Nuclear Physics **22** (1961), no. 4 579 .

[2] A. Salam, *Weak and Electromagnetic Interactions*, Conf. Proc. **C680519** (1968) 367.

[3] Weinberg, Steven, *A Model of Leptons*, Phys. Rev. Lett. **19** (1967) 1264.

[4] D. J. Griffiths, *Introduction to elementary particles; 2nd rev. version*, Physics textbook, Wiley, New York, NY, 2008.

[5] P. Álvarez Cartelle, *Study of the penguin-dominated decay $B_s^0 \to K^{*0}\overline{K}^{*0}$ at LHCb*, PhD thesis, Santiago de Compostela U., Sep, 2014, Presented 21 Nov 2014.

[6] Lee, T. D. and Yang, C. N. , *Question of Parity Conservation in Weak Interactions*, Phys. Rev. **104** (1956) 254.

[7] Wu, C. S. and Ambler, E. and Hayward, R. W. and Hoppes, D. D. and Hudson, R. P. , *Experimental Test of Parity Conservation in Beta Decay*, Phys. Rev. **105** (1957) 1413.

[8] Christenson, J. H. and Cronin, J. W. and Fitch, V. L. and Turlay, R. , *Evidence for the 2π Decay of the K_2^0 Meson*, Phys. Rev. Lett. **13** (1964) 138.

[9] A. Riotto, *Theories of baryogenesis*, in *Proceedings, Summer School in High-energy physics and cosmology: Trieste, Italy, June 29-July 17, 1998*, pp. 326–436, 1998. arXiv:hep-ph/9807454.

[10] Andrei D. Sakharov, *Violation of CP invariance, C asymmetry, and baryon asymmetry of the universe*, Soviet Physics Uspekhi **34** (1991), no. 5 392.

[11] N. Cabibbo, *Unitary symmetry and leptonic decays*, Phys. Rev. Lett. **10** (1963), no. CERN-TH-342 531.

[12] M. Kobayashi and T. Maskawa, *CP-Violation in the renormalizable theory of weak interaction*, Prog. Theor. Phys. **49** (1973) 652.

[13] Heavy Flavor Averaging Group (HFAG), Y. Amhis *et al.*, *Averages of b-hadron, c-hadron, and τ-lepton properties as of summer 2014*, arXiv:1412.7515.

[14] M. Artuso, G. Borissov, and A. Lenz, *CP Violation in the B_s^0 System*, arXiv:1511.09466.

[15] C. Bambi and A. D. Dolgov, *Introduction to particle cosmology: the standard model of cosmology and its open problems*, Unitext for physics, Springer, Berlin, 2016.

[16] J. Charles *et al.*, *Predictions of selected flavour observables within the Standard Model*, Phys. Rev. **D84** (2011) 033005, arXiv:1106.4041, with updated results and plots available at http://ckmfitter.in2p3.fr.

[17] Wolfenstein, L. , *Parametrization of the Kobayashi-Maskawa Matrix*, Phys. Rev. Lett. **51** (1983) 1945.

[18] LHCb, B. Adeva *et al.*, *Roadmap for selected key measurements of LHCb*, arXiv:0912.4179.

[19] K. De Bruyn and R. Fleischer, *A Roadmap to Control Penguin Effects in $B_d^0 \to J/\psi K_S^0$ and $B_s^0 \to J/\psi\phi$*, JHEP **03** (2015) 145, arXiv:1412.6834.

[20] S. Faller, R. Fleischer, and T. Mannel, *Precision Physics with $B_s^0 \to J/\psi\phi$ at the LHC: The Quest for New Physics*, Phys. Rev. **D79** (2009) 014005, arXiv:0810.4248.

[21] R. Fleischer, *In Pursuit of New Physics in the B System*, Nucl. Phys. Proc. Suppl. **163** (2007) 171, arXiv:hep-ph/0607241.

[22] X. Liu, W. Wang, and Y. Xie, *Penguin pollution in $B \to J/\psi V$ decays and impact on the extraction of the $B_s - \bar{B}_s$ mixing phase*, Phys. Rev. **D89** (2014), no. 9 094010, arXiv:1309.0313.

[23] P. Frings, U. Nierste, and M. Wiebusch, *Penguin contributions to CP phases in $B_{d,s}$ decays to charmonium*, Phys. Rev. Lett. **115** (2015), no. 6 061802, arXiv:1503.00859.

[24] LHCb, R. Aaij *et al.*, *Precision measurement of CP violation in $B_s^0 \to J/\psi K^+K^-$ decays*, Phys. Rev. Lett. **114** (2015), no. 4 041801, arXiv:1411.3104.

[25] Particle Data Group, J. Beringer *et al.*, *Review of particle physics*, Phys. Rev. **D86** (2012) 010001.

[26] S. Faller *et al.*, *The Golden Modes $B^0 \to J/\psi K_(S, L)$ in the Era of Precision Flavour Physics*, Phys. Rev. **D79** (2009) 014030, arXiv:0809.0842.

[27] LHCb, CMS, V. Khachatryan *et al.*, *Observation of the rare $B^0_s \to \mu^+\mu^-$ decay from the combined analysis of CMS and LHCb data*, Nature **522** (2015) 68, arXiv:1411.4413.

[28] A. J. Buras, *Minimal flavour violation and beyond: Towards a flavour code for short distance dynamics*, Acta Phys. Polon. **B41** (2010) 2487, arXiv:1012.1447.

[29] S. Stone, *New physics from flavour*, PoS **ICHEP2012** (2013) 033, arXiv:1212.6374.

[30] D. M. Straub, *New Physics Searches in Flavour Physics*, Nuovo Cim. **C035N1** (2012) 249, arXiv:1107.0266.

[31] Ellis, J. and Gunion, J. F. and Haber, H. E. and Roszkowski, L. and Zwirner, F. , *Higgs bosons in a nonminimal supersymmetric model*, Phys. Rev. D **39** (1989) 844.

[32] P. Fayet and S. Ferrara, *Supersymmetry*, Phys. Rept. **32** (1977) 249.

[33] R. N. Hodgkinson, *Supersymmetric Higgs singlet effects on FCNC observables*, AIP Conf. Proc. **1078** (2009) 375, arXiv:0810.0034.

[34] P. Ilten *et al.*, *Proposed Inclusive Dark Photon Search at LHCb*, Phys. Rev. Lett. **116** (2016), no. 25 251803, arXiv:1603.08926.

[35] U. Haisch and J. F. Kamenik, *Searching for new spin-0 resonances at LHCb*, Phys. Rev. **D93** (2016), no. 5 055047, arXiv:1601.05110.

[36] CMS, S. Chatrchyan *et al.*, *Search for a light pseudoscalar Higgs boson in the dimuon decay channel in pp collisions at $\sqrt{s} = 7$ TeV*, Phys. Rev. Lett. **109** (2012) 121801, arXiv:1206.6326.

[37] Lyndon Evans and Philip Bryant, *LHC Machine*, Journal of Instrumentation **3** (2008), no. 08 S08001.

[38] CKMfitter Group, J. Charles *et al.*, *CP violation and the CKM matrix: Assessing the impact of the asymmetric B factories*, Eur. Phys. J. **C41** (2005) 1, arXiv:hep-ph/0406184.

[39] LHCb, R. Aaij *et al.* , *Measurement of the b-quark production cross-section in 7 and 13 TeV pp collisions*, Phys. Rev. Lett. **118** (2017), no. 5 052002, arXiv:1612.05140.

[40] M. Borsato, *Study of the $B^0 \to K^{*0}e^+e^-$ decay with the LHCb detector and development of a novel concept of PID detector: the Focusing DIRC*, PhD thesis, Paris U., IV, 2015, Presented 08 Sep 2015.

[41] M. Grabalosa, *Flavour Tagging developments within the LHCb experiment*, PhD thesis, Barcelona U., Mar, 2012, Presented 15 May 2012.

[42] X. Cid Vidal, *Search for the rare decays $B^0_{(s)} \to \mu^+\mu^-$ and $K^0_S \to \mu^+\mu^-$ with 1 fb^{-1} at LHCb*, PhD thesis, Santiago de Compostela U., Jul, 2012, Presented 26 Oct 2012.

[43] D. Evangelho Vieira, *Amplitude Analysis of $D^+ \to K^-K^+\pi^+$ Decay with LHCb 2012 Data and RF-foil Simulations for the LHCb Upgrade*, PhD thesis, Rio de Janeiro Federal U., Nov, 2015, Presented 14 Dec 2015.

[44] M. Deckenhoff, *Scintillating Fibre and Silicon Photomultiplier Studies for the LHCb upgrade*, PhD thesis, Dortmund U., Dec, 2015, Presented 23 Feb 2016.

[45] C. Lefèvre, *The CERN accelerator complex. Complexe des accélérateurs du CERN*, Dec, 2008.

[46] O. S. Brüning *et al.*, *LHC Design Report*, CERN, Geneva, 2004.

[47] The ATLAS Collaboration, *The ATLAS Experiment at the CERN Large Hadron Collider*, Journal of Instrumentation **3** (2008), no. 08 S08003.

[48] The CMS Collaboration, *The CMS experiment at the CERN LHC*, Journal of Instrumentation **3** (2008), no. 08 S08004.

[49] ATLAS, G. Aad *et al.*, *Observation of a new particle in the search for the Standard Model Higgs boson with the ATLAS detector at the LHC*, Phys. Lett. **B716** (2012) 1, arXiv:1207.7214.

[50] CMS, S. Chatrchyan *et al.*, *Observation of a new boson at a mass of 125 GeV with the CMS experiment at the LHC*, Phys. Lett. **B716** (2012) 30, arXiv:1207.7235.

[51] The ALICE Collaboration, *The ALICE experiment at the CERN LHC*, Journal of Instrumentation **3** (2008), no. 08 S08002.

[52] The LHCb Collaboration, *The LHCb Detector at the LHC*, Journal of Instrumentation **3** (2008), no. 08 S08005.

[53] LHCb, R. Aaij *et al.*, *Observation of $J/\psi p$ Resonances Consistent with Pentaquark States in $\Lambda_b^0 \to J/\psi K^- p$ Decays*, Phys. Rev. Lett. **115** (2015) 072001, arXiv:1507.03414.

[54] LHCb, R. Aaij *et al.*, *Amplitude analysis of $B^+ \to J/\psi\phi K^+$ decays*, arXiv:1606.07898.

[55] LHCb, R. Aaij *et al.*, *Observation of $J/\psi\phi$ structures consistent with exotic states from amplitude analysis of $B^+ \to J/\psi\phi K^+$ decays*, arXiv:1606.07895.

[56] LHCb, R. Aaij *et al.*, *Observation of the resonant character of the $Z(4430)^-$ state*, Phys. Rev. Lett. **112** (2014), no. 22 222002, arXiv:1404.1903.

[57] LHCb, R. Aaij *et al.*, *Measurements of long-range near-side angular correlations in $\sqrt{s_{NN}} = 5$ TeV proton-lead collisions in the forward region*, arXiv:1512.00439.

[58] LHCb, R. Aaij *et al.*, *Observation of Z production in proton-lead collisions at LHCb*, JHEP **09** (2014) 030, arXiv:1406.2885.

[59] LHCb, R. Aaij *et al.*, *Study of J/ψ production and cold nuclear matter effects in pPb collisions at $\sqrt{s_{NN}} = 5$ TeV*, JHEP **02** (2014) 072, arXiv:1308.6729.

[60] LHCb, R. Aaij *et al.*, *Study of Υ production and cold nuclear matter effects in pPb collisions at $\sqrt{s_{NN}}$=5 TeV*, JHEP **07** (2014) 094, arXiv:1405.5152.

[61] LHCb, R. Aaij *et al.*, *Study of $\psi(2S)$ production and cold nuclear matter effects in pPb collisions at $\sqrt{s_{NN}} = 5$ TeV*, JHEP **03** (2016) 133, arXiv:1601.07878.

[62] The TOTEM Collaboration, *The TOTEM Experiment at the CERN Large Hadron Collider*, Journal of Instrumentation **3** (2008), no. 08 S08007.

[63] The LHCf Collaboration, *The LHCf detector at the CERN Large Hadron Collider*, Journal of Instrumentation **3** (2008), no. 08 S08006.

[64] MoEDAL Collaboration, J. Pinfold *et al.*, *Technical Design Report of the MoEDAL Experiment*, Tech. Rep. CERN-LHCC-2009-006. MoEDAL-TDR-001, Jun, 2009.

[65] T. Sjöstrand *et al.*, *An Introduction to PYTHIA 8.2*, Comput. Phys. Commun. **191** (2015) 159, arXiv:1410.3012.

[66] J. Pumplin *et al.*, *New generation of parton distributions with uncertainties from global QCD analysis*, JHEP **07** (2002) 012, arXiv:hep-ph/0201195.

[67] R. Lindner, *LHCb layout_2. LHCb schema_2*, LHCb Collection., Feb, 2008.

[68] LHCb Collaboration, S. Amato *et al.*, *LHCb magnet: Technical Design Report*, Technical Design Report LHCb, CERN, Geneva, 2000.

[69] LHCb Collaboration, Barbosa-Marinho *et al.*, *LHCb VELO (VErtex LOcator): Technical Design Report*, Technical Design Report LHCb, CERN, Geneva, 2001.

[70] LHCb Collaboration, R. Antunes-Nobrega *et al.*, *LHCb reoptimized detector design and performance: Technical Design Report*, Technical Design Report LHCb, CERN, Geneva, 2003.

[71] LHCb Collaboration, P. R. Barbosa-Marinho *et al.*, *LHCb inner tracker: Technical Design Report*, Technical Design Report LHCb, CERN, Geneva, 2002.

[72] LHCb Collaboration, P. R. Barbosa-Marinho *et al.*, *LHCb outer tracker: Technical Design Report*, Technical Design Report LHCb, CERN, Geneva, 2001.

[73] LHCb Collaboration, S. Amato *et al.*, *LHCb RICH: Technical Design Report*, Technical Design Report LHCb, CERN, Geneva, 2000.

[74] LHCb Collaboration, S. Amato *et al.*, *LHCb calorimeters: Technical Design Report*, Technical Design Report LHCb, CERN, Geneva, 2000.

[75] LHCb Collaboration, P. R. Barbosa-Marinho and others. *LHCb muon system: Technical Design Report*, Technical Design Report LHCb, CERN, Geneva, 2001.

[76] LHCb Collaboration, R. Antunes-Nobrega *et al.*, *LHCb trigger system: Technical Design Report*, Technical Design Report LHCb, CERN, Geneva, 2003.

[77] LHCb HLT project, J. Albrecht, V. V. Gligorov, G. Raven, and S. Tolk, *Performance of the LHCb High Level Trigger in 2012*, J. Phys. Conf. Ser. **513** (2014) 012001, arXiv:1310.8544.

[78] LHCb Collaboration, P. R. Barbosa-Marinho *et al.*, *LHCb online system, data acquisition and experiment control: Technical Design Report*, Technical Design Report LHCb, CERN, Geneva, 2001.

[79] I. Belyaev *et al.*, *Handling of the generation of primary events in Gauss, the LHCb simulation framework*, 2010.

[80] LHCb Collaboration, R. Antunes-Nobrega *et al.*, *LHCb computing: Technical Design Report*, Technical Design Report LHCb, CERN, Geneva, 2005.

[81] Clemencic, M. and others, *The LHCb Simulation Application, Gauss: Design, Evolution and Experience*, Journal of Physics: Conference Series **331** (2011), no. 3 032023.

[82] J. Bellm *et al.*, *Herwig++ 2.7 Release Note*, arXiv:1310.6877.

[83] M. Dobbs and J. B. Hansen, *The HepMC C++ Monte Carlo event record for High Energy Physics*, Comput. Phys. Commun. **134** (2001) 41.

[84] D. J. Lange, *The evtgen particle decay simulation package*, Nuclear Instruments and Methods in Physics Research Section A: Accelerators, Spectrometers, Detectors and Associated Equipment **462** (2001), no. 1–2 152 , BEAUTY2000, Proceedings of the 7th Int. Conf. on B-Physics at Hadron Machines.

[85] P. Golonka and Z. Was, *PHOTOS Monte Carlo: a precision tool for QED corrections in Z and W decays*, The European Physical Journal C - Particles and Fields **45** (2006), no. 1 97.

[86] S. Agostinelli *et al.*, *Geant4 - a simulation toolkit*, Nuclear Instruments and Methods in Physics Research Section A: Accelerators, Spectrometers, Detectors and Associated Equipment **506** (2003), no. 3 250 .

[87] C. Eck *et al.*, *LHC computing Grid: Technical Design Report*, Technical Design Report LCG, CERN, Geneva, 2005.

[88] A. Casajus and others, *DIRAC distributed secure framework*, Journal of Physics: Conference Series **219** (2010), no. 4 042033.

[89] LHCb, R. Aaij *et al.*, *LHCb Detector Performance*, Int. J. Mod. Phys. **A30** (2015), no. 07 1530022, arXiv:1412.6352.

[90] R. Aaij *et al.*, *Performance of the LHCb Vertex Locator*, JINST **9** (2014) 09007, arXiv:1405.7808.

[91] L. Anderlini *et al.*, *The PIDCalib package*, Tech. Rep. LHCb-PUB-2016-021. CERN-LHCb-PUB-2016-021, CERN, Geneva, Jul, 2016.

[92] Cherenkov, P. A. , *Visible emission of clean liquids by action of γ radiation*, Doklady Akademii Nauk SSSR **2** (1934) 451+.

[93] LHCb RICH Group, M. Adinolfi *et al.*, *Performance of the LHCb RICH detector at the LHC*, Eur. Phys. J. **C73** (2013) 2431, arXiv:1211.6759.

[94] F. Archilli *et al.*, *Performance of the Muon Identification at LHCb*, JINST **8** (2013) P10020, arXiv:1306.0249.

[95] R. Aaij *et al.*, *The LHCb Trigger and its Performance in 2011*, JINST **8** (2013) P04022, arXiv:1211.3055.

[96] LHCb, *LHCb dimuon and charm mass distributions*, LHCb-CONF-2016-005, CERN-LHCb-CONF-2016-005, 2016.

[97] LHCb, R. Aaij *et al.*, *Implications of LHCb measurements and future prospects*, Eur. Phys. J. **C73** (2013), no. 4 2373, arXiv:1208.3355.

[98] LHCb collaboration, R. Aaij *et al.*, *Measurement of $\sigma(pp \to b\bar{b}X)$ at $\sqrt{s} = 7$ TeV in the forward region*, Phys. Lett. **B694** (2010) 209, arXiv:1009.2731.

[99] T. Gershon, *Updated sensitivity projections for the LHCb Upgrade*, Tech. Rep. LHCb-PUB-2013-015. CERN-LHCb-PUB-2013-015, CERN, Geneva, Sep, 2013.

[100] LHCb Collaboration, *Letter of Intent for the LHCb Upgrade*, Tech. Rep. CERN-LHCC-2011-001. LHCC-I-018, Mar, 2011.

[101] LHCb Collaboration, *LHCb Tracker Upgrade Technical Design Report*, Tech. Rep. CERN-LHCC-2014-001. LHCB-TDR-015, Feb, 2014.

[102] LHCb Collaboration, *LHCb PID Upgrade Technical Design Report*, Tech. Rep. CERN-LHCC-2013-022. LHCB-TDR-014, Nov, 2013.

[103] LHCb Collaboration, *LHCb Trigger and Online Upgrade Technical Design Report*, Tech. Rep. CERN-LHCC-2014-016. LHCB-TDR-016, May, 2014.

[104] LHCb Collaboration, *LHCb VELO Upgrade Technical Design Report*, Tech. Rep. CERN-LHCC-2013-021. LHCB-TDR-013, Nov, 2013.

[105] Ballabriga, R. and others, *Characterization of the Medipix3 pixel readout chip*, Journal of Instrumentation **6** (2011), no. 01 C01052.

[106] K. Akiba *et al.*, *Characterisation of Medipix3 Silicon Detectors in a Charged-Particle Beam*, JINST **11** (2016), no. 01 P01011, arXiv:1509.02387.

[107] LHCb, S. De Capua, *The LHCb VELO Upgrade*, LHCb-TALK-2016-229, Aug, 2016.

[108] S. Faller, R. Fleischer, and T. Mannel, *Precision Physics with $B_s^0 \to J/\psi\phi$ at the LHC: The Quest for New Physics*, Phys. Rev. **D79** (2009) 014005, arXiv:0810.4248.

[109] X. Liu, W. Wang, and Y. Xie, *Penguin pollution in $B \to J/\psi V$ decays and impact on the extraction of the $B_s - \bar{B}_s$ mixing phase*, Phys. Rev. **D89** (2014) 094010, arXiv:1309.0313.

[110] K. De Bruyn and R. Fleischer, *A Roadmap to Control Penguin Effects in $B_d^0 \to J/\psi K_S^0$ and $B_s^0 \to J/\psi\phi$*, JHEP **1503** (2015) 145, arXiv:1412.6834.

[111] P. Frings, U. Nierste, and M. Wiebusch, *Penguin contributions to CP phases in $B_{d,s}$ decays to charmonium*, Phys. Rev. Lett. **115** (2015), no. 6 061802, arXiv:1503.00859.

[112] LHCb, R. Aaij *et al.*, *Measurement of the CP-violating phase β in $B^0 \to J/\psi\pi^+\pi^-$ decays and limits on penguin effects*, Phys. Lett. **B742** (2015) 38, arXiv:1411.1634.

[113] M. Pivk and F. R. Le Diberder, *SPlot: A Statistical tool to unfold data distributions*, Nucl. Instrum. Meth. **A555** (2005) 356, arXiv:physics/0402083.

[114] LHCb, R. Aaij *et al.*, *Measurement of CP violation parameters and polarisation fractions in $B_s^0 \to J/\psi \overline{K}^{*0}$ decays*, JHEP **11** (2015) 082, arXiv:1509.00400.

[115] LHCb, R. Aaij *et al.*, *Measurement of the $B_s^0 \to J/\psi \bar{K}^{*0}$ branching fraction and angular amplitudes*, Phys. Rev. **D86** (2012) 071102, arXiv:1208.0738.

[116] A. Hoecker *et al.*, *TMVA - Toolkit for Multivariate Data Analysis*, tech. rep., CERN, Mar, 2007. arXiv:physics/0703039.

[117] Particle Data Group, K. A. Olive *et al.*, *Review of Particle Physics*, Chin. Phys. **C38** (2014) 090001.

[118] Y. Xie, *Figure of merit for $B_s^0 \to KK$ event selection optimization*, LHCb internal WG presentation. https://indico.cern.ch/conferenceDisplay.py?confId=236950.

[119] M. Oreglia, *A Study of the Reactions $\psi' \to \gamma\gamma\psi$*, PhD thesis, SLAC, 1980.

[120] LHCb, R. Aaij *et al.*, *LHCb Detector Performance*, Tech. Rep. 07, 2015. doi: 10.1142/S0217751X15300227.

[121] LHCb, R. Aaij *et al.*, *Measurement of $\sigma(pp \to b\bar{b}X)$ at $\sqrt{s} = 7$ TeV in the forward region*, Phys. Lett. **B694** (2010) 209, arXiv:1009.2731.

[122] LHCb, R. Aaij *et al.*, *Study of the kinematic dependences of Λ_b^0 production in pp collisions and a measurement of the $\Lambda_b^0 \to \Lambda_c^+ \pi^-$ branching fraction*, JHEP **08** (2014) 143, arXiv:1405.6842.

[123] LHCb, *Updated average f_s/f_d b-hadron production fraction ratio for 7 TeV pp collisions*, LHCb-CONF-2013-011, Jul, 2013.

[124] LHCb, R. Aaij *et al.*, *Measurement of the resonant and CP components in $\overline{B}^0 \to J/\psi\pi^+\pi^-$ decays*, Phys. Rev. **D90** (2014), no. 1 012003, arXiv:1404.5673.

[125] LHCb, R. Aaij *et al.*, *Measurement of resonant and CP components in $\bar{B}_s^0 \to J/\psi\pi^+\pi^-$ decays*, Phys. Rev. **D89** (2014), no. 9 092006, arXiv:1402.6248.

[126] LHCb, R. Aaij *et al.*, *Amplitude analysis and the branching fraction measurement of $\bar{B}_s^0 \to J/\psi K^+K^-$*, Phys. Rev. **D87** (2013), no. 7 072004, arXiv:1302.1213.

[127] L. Zhang and S. Stone, *Time-dependent Dalitz-plot formalism for $B_{(s)}^0 \to J/\psi h^+h^-$*, Phys. Lett. **B719** (2013) 383, arXiv:1212.6434.

[128] LHCb, R. Aaij *et al.*, *Study of the production of Λ_b^0 and $\overline{B}^0$ hadrons in pp collisions and first measurement of the $\Lambda_b^0 \to J/\psi p K^-$ branching fraction*, Chin. Phys. **C40** (2016), no. 1 011001, arXiv:1509.00292.

[129] L. Amoroso, *Richerche intorno alla curve die redditi*, Ann. Mat. Pura. Appl. **21** (1925) 123.

[130] LHCb collaboration, R. Aaij *et al.*, *Observation of the $\Lambda_b^0 \to J/\psi p\pi^-$ decay*, JHEP **07** (2014) 103, arXiv:1406.0755.

[131] D. Martinez Santos and F. Dupertuis, *Mass distributions marginalized over per-event errors*, Nucl. Instrum. Meth. **A764** (2014) 150, arXiv:1312.5000.

[132] Y. Xie, *sFit: a method for background subtraction in maximum likelihood fit*, arXiv:0905.0724.

[133] LHCb collaboration, R. Aaij *et al.*, *Measurement of the polarisation amplitudes in $B^0 \to J/\psi K^*(892)^0$ decays*, Phys. Rev. **D88** (2013) 052002, arXiv:1307.2782.

[134] LHCb collaboration, R. Aaij *et al.*, *Measurement of the $B_s^0 \to J/\psi \bar{K}^{*0}$ branching fraction and angular amplitudes*, Phys. Rev. **D86** (2012) 071102(R), arXiv:1208.0738.

[135] Y. Xie, *Some physics and technical issues in analysis of the decay $B_s^0 \to J\psi K^+K^-$*, LHCb-INT-2012-017.

[136] D. Aston *et al.*, *A Study of $K^-\pi^+$ Scattering in the Reaction $K^-p \to K^-\pi^+n$ at 11* GeV/c, Nucl. Phys. **B296** (1988) 493.

[137] J. Bressieux *et al.*, *Evidence for the resonant character of the $Z(4430)^- \to \psi(2S)\pi^-$ mass peak observed in $B^0 \to \psi(2S)K^+\pi^-$ decays, and determination of the $Z(4430)^-$ spin-parity*, LHCb-ANA-2013-053.

[138] M. Needham and G. Cowan, *Observation of $\overline{B}_s \to \psi(2S)K^+\pi^-$*, LHCb-ANA-2013-091.

[139] R. Aaij *et al.*, *Tagged time-dependent analysis of $B_s^0 \to J/\psi K^+K^-$ decays with 1 fb^{-1}*, LHCb-ANA-2012-067.

[140] LHCb collaboration, Y. Xie, *Iterative method to improve simulation-based detector efficiency description in angular analysis*, LHCb-INT-2013-010.

[141] LHCb collaboration, R. Aaij *et al.*, *First observation of CP violation in the decays of B_s^0 mesons*, Phys. Rev. Lett. **110** (2013) 221601, arXiv:1304.6173.

[142] LHCb collaboration, R. Aaij *et al.*, *Measurement of the $\bar{B}^0$–B^0 and $\bar{B}_s^0$–B_s^0 production asymmetries in pp collisions at $\sqrt{s} = 7$ TeV*, Phys. Lett. **B739** (2014) 218, arXiv:1408.0275.

[143] LHCb collaboration, R. Aaij *et al.*, *Measurement of the semileptonic CP asymmetry in B^0–$\bar{B}^0$ mixing*, arXiv:1409.8586, to appear in Phys. Rev. Lett.

[144] LHCb collaboration, R. Aaij *et al.*, *Measurement of CP asymmetry in $D^0 \to K^-K^+$ and $D^0 \to \pi^-\pi^+$ decays*, JHEP **07** (2014) 041, arXiv:1405.2797.

[145] LHCb collaboration, R. Aaij *et al.*, *Precision measurement of CP violation in $B_s^0 \to J/\psi K^+K^-$ decays*, arXiv:1411.3104, to appear in Phys. Rev. Lett.

[146] LHCb collaboration, R. Aaij *et al.*, *Measurement of CP violation and the B_s^0 meson decay width difference with $B_s^0 \to J/\psi K^+K^-$ and $B_s^0 \to J/\psi \pi^+\pi^-$ decays*, Phys. Rev. **D87** (2013) 112010, arXiv:1304.2600.

[147] Belle Collaboration, K. Abe *et al.*, *Measurements of branching fractions and decay amplitudes in $B \to J/\psi K^*$ decays*, Phys. Lett. **B538** (2002) 11, arXiv:hep-ex/0205021.

[148] Heavy Flavor Averaging Group, Y. Amhis *et al.*, *Averages of b-hadron, c-hadron, and τ-lepton properties as of early 2012*, arXiv:1207.1158, updated results and plots available at http://www.slac.stanford.edu/xorg/hfag/.

[149] LHCb collaboration, *Updated average f_s/f_d b-hadron production fraction ratio for 7 TeV pp collisions*, LHCb-CONF-2013-011.

[150] R. Fleischer, *Extracting CKM phases from angular distributions of B(d,s) decays into admixtures of CP eigenstates*, Phys. Rev. **D60** (1999) 073008, arXiv:hep-ph/9903540.

[151] K. De Bruyn *et al.*, *Branching Ratio Measurements of B_s Decays*, Phys. Rev. **D86** (2012) 014027, arXiv:1204.1735.

[152] K. De Bruyn, *Searching for penguin footprints, PhD Thesis*, VU University, Amsterdam (2015), CERN-THESIS-2015-126.

[153] A. S. Dighe, I. Dunietz, and R. Fleischer, *Extracting CKM Phases and B_s^0–$\overline{B}_s^0$ Mixing Parameters from Angular Distributions of Non-Leptonic B Decays*, Eur. Phys. J. **C6** (1999) 647, arXiv:hep-ph/9804253.

[154] A. Bharucha, D. M. Straub, and R. Zwicky, *$B \to V\ell^+\ell^-$ in the Standard Model from Light-Cone Sum Rules*, arXiv:1503.05534.

[155] CKMfitter group, J. Charles *et al.*, *Current Status of the Standard Model CKM Fit and Constraints on $\Delta F = 2$ New Physics*, Phys. Rev. **D91** (2015), no. 7 073007, arXiv:1501.05013, Online update: CKM 2014.

[156] A. L. Read, *Presentation of search results: The CL(s) technique*, J. Phys. **G28** (2002) 2693.

[157] J. Stevens and M. Williams, *uBoost: A boosting method for producing uniform selection efficiencies from multivariate classifiers*, JINST **8** (2013) P12013, arXiv:1305.7248.

[158] LHCb, R. Aaij *et al.*, *Search for hidden-sector bosons in $B^0 \to K^{*0}\mu^+\mu^-$ decays*, Phys. Rev. Lett. **115** (2015), no. 16 161802, arXiv:1508.04094.

[159] D. Martínez, J. Hernando, and F. Teubert, *LHCb potential to measure/exclure the branching ratio of the decay Bs $\to \mu^+\mu^-$*, Tech. Rep. LHCb-2007-033. CERN-LHCb-2007-033, CERN, Geneva, Apr, 2007.

[160] A. Rogozhnikov *et al.*, *New approaches for boosting to uniformity*, JINST **10** (2015), no. 03 T03002, arXiv:1410.4140.

[161] T. M. Karbach and M. Schlupp, *Constraints on Yield Parameters in Extended Maximum Likelihood Fits*, arXiv:1210.7141.

[162] LHCb collaboration, R. Aaij *et al.*, *Study of the kinematic dependences of Λ_b^0 production in pp collisions and a measurement of the $\Lambda_b^0 \to \Lambda_c^+ \pi^-$ branching fraction*, JHEP **08** (2014) 143, arXiv:1405.6842.